Density Functional Theory Investigation of the Uranium Oxides

Brincat, Nick

Award date:
2015

Awarding institution:
University of Bath

Density Functional Theory Investigation of the Uranium Oxides

Nicholas Anthony Brincat

A thesis submitted for the degree of Doctor of Philosophy

University of Bath

Department of Chemistry

February 2015

Contents

Abstract

The aim of this thesis is to provide insight into the structures and properties of the uranium oxides. As UO_2 is easily oxidised during the nuclear fuel cycle it is important to have a detailed understanding of the structures and properties of the oxidation products. Experimental work over the years has revealed many stable oxides including UO_2, U_4O_9, U_3O_7, U_2O_5, U_3O_8 and UO_3, all with a number of different polymorphs. The oxides are broadly split into two categories, fluorite-based structures with stoichiometries in the range of UO_2 to U_2O_5 and less dense layered-type structures with stoichiometries in the range of U_2O_5 to UO_3. While UO_2 is well characterised, both experimentally and computationally, there is a paucity of data concerning higher stoichiometry oxides in the literature. Experiments and simulations are emerging that deal with individual phases, however a comprehensive study that assesses the properties of all polymorphs and provides comparison over the full range of stoichiometries has been lacking from the literature

First the nuclear fuel cycle is introduced, as well as UO_2 as a nuclear fuel (Chapter 1), before the quantum mechanical methodology used throughout is explained (Chapter 2). Applying a number of different density functionals (including GGAs, meta-GGAs and hybrids) to UO_2 in Chapter 3 it emerges that the PBE + U formalism reproduces the experimentally observed properties to a good degree of accuracy, and so is selected for the rest of the simulations. Following this Chapter 4 examines defect clusters in UO_2, finding split interstitials to dominate at low stoichiometry (UO_2 – $UO_{2.0625}$), chains of 2:2:2 Willis clusters at higher stoichiometry ($UO_{2.125}$ – $UO_{2.25}$ (U_4O_9)) and split quad interstitials at higher stoichiometry ($UO_{2.33}$ (U_3O_7)). Chapter 5 is an investigation of layered U_2O_5, where it emerges that the Np_2O_5 structure is more stable than δ-U_2O_5 and all uranium ions are in the U^{5+} oxidation state. Next Chapter 6 considers layered U_3O_8, which is structurally oxygen rich U_2O_5, where it is found that U^{5+} and U^{6+} ions exist in pentagonal bipyramidal and octahedral coordination respectively. The final set of results in Chapter 7 concern the polymorphs of UO_3, where it is found that U^{6+} adopts a range of coordination environments and the predicted relative stability of each modification matches well with experiment. Finally the conclusions are presented in Chapter 8 along with plans for future work.

Acknowledgements

I would first like to thank my supervisor, Professor Steve Parker, for his support, advice and knowledge throughout my PhD. Without his help and enthusiasm this work would not have been possible. Another big thank you goes to Dr Marco Molinari, who works tirelessly to help everyone in the Parker group. His support, advice and ideas were invaluable to the completion of this thesis. I would also like to thank the rest of the Parker group, past and present, particularly Dr James Grant for his help with this thesis, Tom Shapley and Stephen Yeandel for all of their technical assistance and Nick Williams, Richard Driscoll and Joe Flitcroft for their useful discussions on uranium oxides.

I also need to thank my external supervisor, Professor Geoff Allen, for his useful advice and discussions throughout my PhD. He kept pushing me to find a stable model for the Willis cluster when I had all but given up. I would also like to acknowledge my industrial supervisor, Dr Mark Storr, for both his support and the funding from AWE.

I would also like to acknowledge the University of Bath for funding and use of the Aquila HPC facility. The Materials Chemistry Consortium must also be acknowledged for time on the HECToR and ARCHER HPC facilities, funded through the EPSRC (EP/F067496 and EP/L000202). HECToR and ARCHER are provided by UoE HPCx Ltd, Cray Inc and NAG Ltd at the University of Edinburgh.

Finally I would like to thank my friends and family for all of their support during my PhD, especially during the final few months. I could not have finished this thesis without you all.

Publications

Ab initio Investigation of the UO_3 Polymorphs: Structural Properties and Thermodynamic Stability.
N.A. Brincat, S.C. Parker, M. Molinari, G.C. Allen and M.T. Storr, Inorganic Chemistry (2014) 53, 12253-12264

Computer simulation of defect clusters in UO_2 and their dependence on composition.
N.A. Brincat, M. Molinari, S.C. Parker, G.C. Allen and M.T. Storr, Journal of Nuclear Materials (2015) 456, 329-333

Density functional theory investigation of the layered uranium oxides U_3O_8 and U_2O_5.
N.A. Brincat, S.C. Parker, M. Molinari, G.C. Allen and M.T. Storr, Dalton Transactions (2015) 44, 2613-2622

Ab initio Investigation of the Uranium-Oxygen System, **Poster**, Plutonium Futures, Las Vegas, Nevada, USA, September 2014

Density functional theory investigation of the layered uranium oxides U_3O_8 and U_2O_5, **Talk**, Dalton Discussions 14: Advancing the chemistry of the f-elements, Edinburgh, UK, July 2014

Ab initio Investigation of Uranium Oxides & Defect Structures, **Talk**, 44th JdA, Ein Geddi, Israel, April 2014

Ab initio Investigation of Uranium Oxides & Defect Structures, **Talk**, Actinides, Karlsruhe, Germany, July 2013

Computer Modelling of Defect Structures in Actinide Oxides, **Poster**, ATALANTE, Montpellier, France, September 2012

Computer Modelling of Defect Structures in Actinide Oxides, **Poster**, Plutonium Futures, Cambridge, UK, July 2012

Chapter 1

1 Introduction

Nuclear power is, and will continue to be, an important component of our energy needs. In order to continue to provide and develop this resource to improve efficiency, reliability and safety whilst reducing environmental impact it is crucial to engage in fundamental research into the materials and processes involved. This chapter sets the context and provides some background for the potential applications and uses of the work contained within the whole thesis. First the concept of nuclear power is introduced; then the various nuclear fuels are discussed; then the uranium oxide nuclear fuel cycle is described, as the focus of this work; and finally the aims of thesis are set out. More detailed technical information for each of the materials examined can be found at the beginning of the appropriate chapter.

1.1 Nuclear Power

Although experimentation with nuclear particles began in the early 1930s, the nuclear fission process was demonstrated in 1938 by German scientist Otto Hahn [1]. The coinciding of this discovery with the start of the Second World War led to a vast amount of research into nuclear fission, particularly regarding using the huge power of the process for nuclear weapons. While weapons development and stockpiling continued long after this into the Cold War, research soon turned to using nuclear fission for power generation and the 1950s and 1960s saw the first nuclear power stations come online. By the 1970s, however, research into nuclear materials had fallen into decline amidst growing concerns of safety due to poor public perception of the technology [2]. The Three Mile Island accident of 1979 and Chernobyl disaster of 1986 confirmed these fears for many and stunted the development of nuclear programmes globally.

Today a growing awareness of the impact of CO_2 emissions, security of energy supply and diminishing fossil fuel reserves has initiated a nuclear power renaissance [3]. 18% of the UK's power is generated from nuclear power and 12% of power globally [4]. The International Atomic Energy Agency estimates that nuclear power will generate a total of between 0.8 and 2.3 million TWh of electricity worldwide over the next 90 years [5], depending on how nuclear energy policy develops, whilst the International Energy Agency projects 2382 TWh/year will be generated from nuclear power by 2030 compared to 1534 TW/h year from renewable sources [6]. Evidently nuclear power is an integral part of the energy portfolio of today and will remain so for the foreseeable future; it has the potential to produce vast amounts of electricity at a reasonable cost and with relatively little environmental impact, if waste is handled responsibly. It is the need to fulfil these goals of cheap, reliable and safe energy that inspires a growing body of research.

Nuclear power refers to the process of generating electricity from the heat produced by nuclear fission; whereby an atom is split by a smaller particle colliding with it, in this case a neutron. Fission occurs naturally in the form of radioactive decay, however power generation requires a more controlled process where the fission reaction is moderated using a combination of fuel rods and neutron-absorbing control rods. The fuel is required to contain fissile material, that is to say capable of sustaining a nuclear fission chain reaction. The ^{235}U isotope is fissile but is only present at 0.72 % natural abundance, compared to the dominant ^{238}U isotope at 99.28 %. Typically this is an insufficient concentration for fission to occur (although graphite and heavy water moderated reactors do use natural uranium fuel) and so the material must be enriched to 3.5 – 50 % ^{235}U depending on the type of reactor.

There are a variety of different nuclear reactors, however there are two main types in use today; thermal reactors use neutron absorbing materials to moderate the fission process whilst fast reactors do not contain moderators and often surround the reactor core with a neutron reflecting material. Fast reactors usually require fuel containing 20% or more fissile material and are also known as breeder reactors as they contain fertile material (isotopes that can absorb neutrons to become fissile) to breed their own fuel. Although developed earlier, thermal reactors are still the most common reactor design in use today and of these the pressurised water reactor (PWR) makes up 60% of the world's current

commercial reactors [7]. Different types of reactor have different fuel requirements, for instance using an oxide instead of a metal provides natural moderation as there is a lower density of fissile material. Not only do nuclear fuels need to be enriched to contain a suitable amount of fissile material, they must also be converted to the appropriate chemical state for reactor operation. Additionally, processes such as fuel storage and reactor operation can alter the chemical state of the fuel and conversion to other forms is then required at various stages. This group of processes is collectively known as the nuclear fuel cycle, however before discussing fuel cycles it is necessary to introduce nuclear fuels.

1.2 Nuclear Fuels

Nuclear fuels are almost exclusively actinide-based, with thorium, uranium and plutonium being the most common elements used to provide the fissile material. Early reactors were fuelled with uranium metal, which, although less abundant than thorium, requires less enrichment and can produce more fissile and fertile isotopes during reactor operation. With the advent of thermal PWRs oxide based fuels came to the forefront, with UO_2 dominating, due to their improved chemical and thermodynamic stability over metal based fuel [8]. PuO_2 is chemically more stable than UO_2 with respect to oxidation, however it is more susceptible to reduction due to formation of Pu_2O_3. More recently the development of fast reactors has prompted the use of mixed oxide (MOX) fuels, which contain U/Pu in varying ratios. U/Pu MOX offers a convenient means of utilising surplus weapons-grade plutonium stocks, although the global inventory of fissile ^{239}Pu from civilian sources alone already exceeds 160 metric tons [9]. Given it has the highest natural abundance and chemical stability of the three, ThO_2 is seeing increasing usage as a nuclear fuel in reactors, especially as the higher enrichment requirements are now easier to achieve. Thorium naturally occurs as the fertile ^{232}Th isotope, which can be used to form fissile ^{233}U, providing a convenient alternative to U-Pu fuel cycles by producing less plutonium [10]. A further advantage to this cycle is that enriched uranium cannot be extracted, thus reducing the risk of nuclear proliferation. Alternatively the Th-Pu fuel cycle can be employed, which has the additional benefit of being the only one to consume existing plutonium supplies without generating any more [11]. Despite advances in reactor and fuel technology, PWRs with UO_2 fuel continue to be the dominant reactor type. UO_2 is readily oxidised under

normal fuel cycle and reactor operating conditions. This leads to the uranium nuclear fuel cycle, the materials of which are the focus of this thesis.

1.3 The Uranium Nuclear Fuel Cycle

The nuclear fuel cycle is the term used to describe the collection of industrial processes involved in the production of electricity from nuclear power reactors. The cycle begins with the mining of uranium, which then undergoes milling, conversion, enrichment and fuel fabrication processes before entering a nuclear reactor; this is known as the "front end" of the fuel cycle. The uranium based fuel is used in a reactor for around three years and then undergoes a series of processing steps including storage (either temporary or long term), reprocessing, recycling and waste disposal; these processes are known as the fuel cycle "back end" (Figure 1.1) [12]. Uranium is highly susceptible to oxidation, forming a number of different oxides during the cycle.

Uranium is a relatively common mineral in the Earth's crust, it occurs in low concentrations in most rocks, soils and sea water, while it is primarily found in uraninite or pitchblende deposits (UO_2, U_3O_8 and UO_3 in varying proportions) [13]. It is these deposits that are traditionally extracted in either underground or open pit mines, although 46 % of the global uranium supply is now produced via *in situ* leaching, where oxygenated water is circulated through highly porous ores to dissolve the uranium oxide and bring it to the surface [14]. The extracted ore is then milled, which involves crushing and grinding before dissolving in sulphuric acid to separate the uranium from the waste rock. The concentrated uranium can then be precipitated as U_3O_8 (known in the nuclear industry as "yellowcake"), which is the commercial product sold to nuclear power facilities. The waste products from the ore are referred to as "tailings" and contain no useful nuclear material but are still slightly radioactive due to low concentrations of long-lived isotopes. They are isolated from the environment and stored in a secure location such as a mined out pit [12].

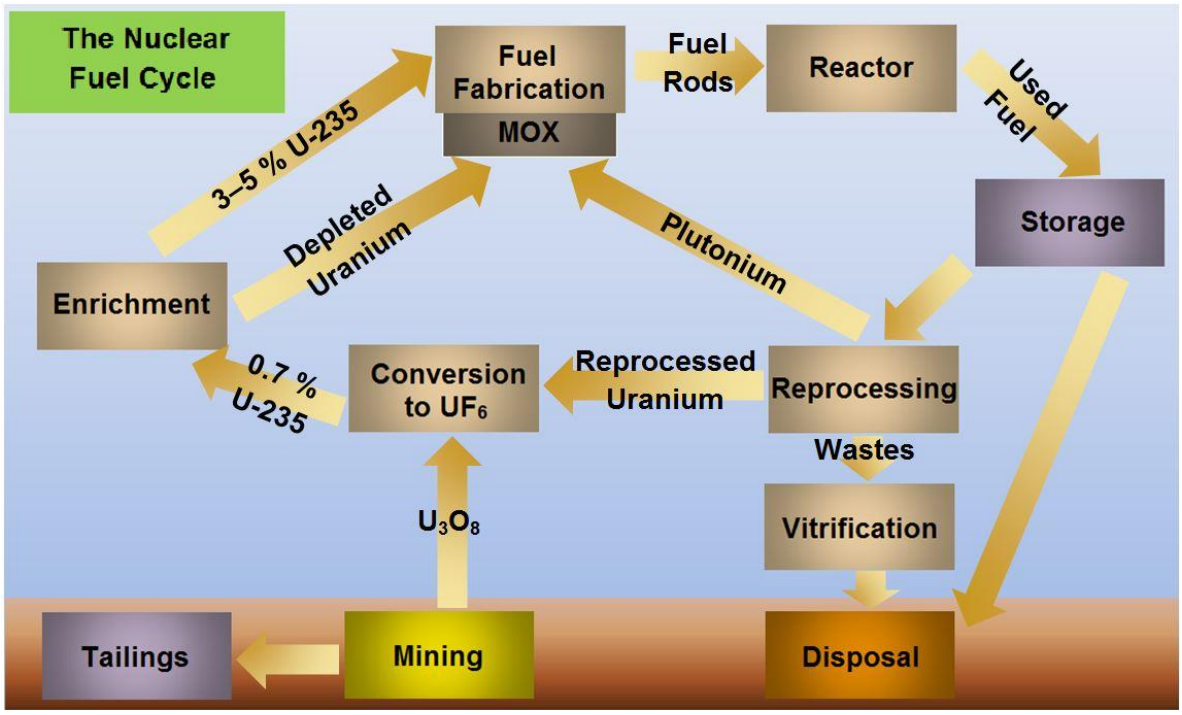

Figure 1.01 – Schematic diagram of the nuclear fuel cycle. Processes on the left make up the front end and processes on the right comprise the back end of the cycle.

U_3O_8 from a uranium mill is currently not directly usable as reactor fuel due to the low natural abundance of fissile ^{235}U (0.7 %), however a recent US Department of Energy report concluded that a heavy water moderated reactor using natural uranium fuel in the form of U_3O_8 or UO_3 is entirely feasible [15]. As 3.5 – 5% ^{235}U is required by most PWRs, enrichment must occur, which requires the uranium to be in gaseous form, via conversion to UF_6. To achieve this the uranium is first reduced to UO_2, the fuel source for existing natural uranium reactors, and then the majority is converted to UF_6 and enriched to a higher proportion of ^{235}U via centrifuge. The enriched UF_6 is then converted back to UO_2 ready to be processed into fuel [16].

Nuclear reactor fuel is then fabricated by pressing the UO_2 into pellets which are sintered at high temperature (over 1673 K) and then encased in metal tubes to form fuel rods. Fuel rods can then be arranged in a fuel assembly along with control rods (made of a moderating material that absorbs neutrons) ready for introduction to a reactor. A reactor core is made up of hundreds of fuel assemblies and the heat given off from the nuclear fission reactions is used to produce steam to drive turbines and thus generate electricity. However the high

temperatures can also have the secondary effect of oxidising the UO_2 fuel (especially in the presence of moisture or air) and producing U_3O_8 [17]. This is highly undesirable as the UO_2 expands by 36 % on oxidation to U_3O_8 due to a transition from a fluorite structure to a layered type structure which severely damages fuel rods and cladding.

Fuel is typically used for between 18 and 36 months, by which time the proportion of fissionable ^{235}U has been reduced to less than 1 %, although the total amount of uranium remaining is normally still as high as 96 % (the proportion of oxygen is not reduced and may increase as a result of oxidation). The remainder is comprised of 3 % fission waste products (e.g. caesium) and 1 % plutonium. When removed from the reactor the material is still highly radioactive and producing heat and so is immediately moved to storage ponds adjacent to the reactor until radiation levels fall significantly. After several months to five years, depending on the fuel composition, radioactivity levels will have fallen sufficiently that the material can either be transferred to ventilated dry storage or reprocessed [12].

Reprocessing involves separating the useful uranium and plutonium from the waste products, and the fuel cladding, by cutting up the fuel rods and dissolving them in acid. The actinides can be precipitated out and recycled into fresh fuel (after enrichment), significantly reducing the total amount of waste. The remaining 3 % of high-level radioactive waste can be stored as a liquid and then later solidified (vitrification) for long-term storage and eventual disposal. There are currently no disposal facilities in operation, however, as waste is in a stable, solid form and there is relatively little of it in existence. Additionally, the longer the material is stored for the easier it becomes to handle as the radioactivity falls [12].

Although not described explicitly in the discussion of the nuclear fuel cycle there are other, less stable, uranium oxides which can form during the process. These include the fluorite based U_4O_9, U_3O_7 and U_2O_5 phases as well as layered U_2O_5 [18] and are most likely to form during reactor operation and fuel storage as intermediate products of UO_2 oxidation.

1.4 The Uranium-Oxygen System

Uranium exists in U^{4+}, U^{5+} and U^{6+} oxidation states when in combination with oxygen, thus UO_2 forms the lowest available stoichiometry and UO_3 the highest. However, as shown in

Figure 1.2, the uranium-oxygen system is complex, with a large number of intermediate oxides between these two compositions and a number of different polymorphs at each stoichiometry [19]. These include U_4O_9 and U_3O_7, which are closely related to the UO_2 structure, as well as U_3O_8 and UO_3 which adopt distinct layered-type structures. Bridging the gap between these is U_2O_5, reported to have a mixture of fluorite UO_2-derived and layered-type polymorphs [18]. Over the years a considerable body of research has amassed that deals with fluorite-structured UO_2 due to its role as the primary fuel material in nuclear reactors [20-28] (further details are in Chapter 3). However the literature is lacking fundamental research into the higher uranium oxides which also play crucial roles in the fuel cycle; and in the case of U_3O_8 and UO_3 could soon be used as fuels themselves [15]. Although more work is starting to emerge on these two materials there is still a significant paucity of data on the less stable U_4O_9, U_3O_7 and U_2O_5 oxides, which could provide valuable insight into the process of oxidation in UO_2 and fluorite based structures. So there is broad scope for more detailed investigation of the different polymorphs at each stoichiometry to improve our understanding of their structures and properties.

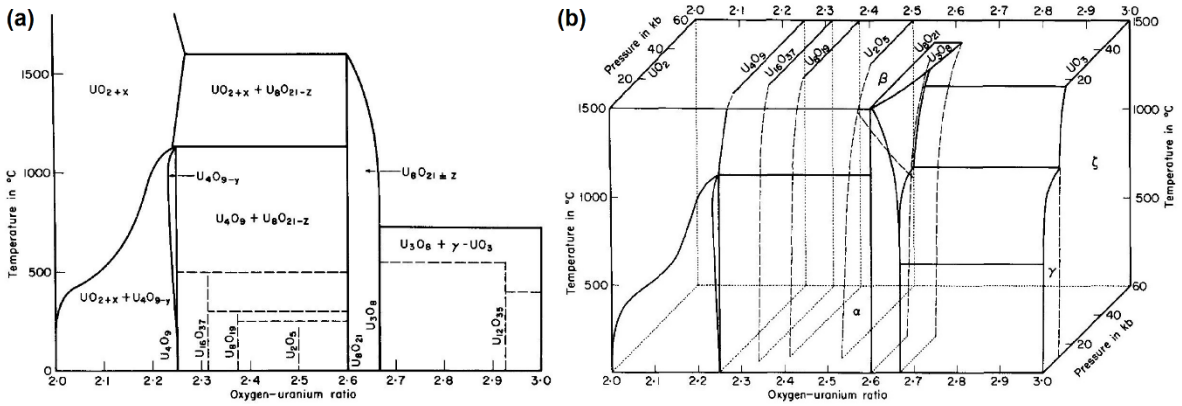

Figure 1.02 – Phase diagrams for the binary uranium oxygen system in the UO_2-UO_3 composition range [19]. (a) oxygen uranium ratio compared with temperature, (b) oxygen uranium ratio compared with temperature and pressure.

The oxidation of UO_2 occurs readily during reactor operation and fuel storage and is facilitated by accommodation of additional oxygen atoms (interstitial defects) in the fluorite lattice. At low concentrations these take the form of single interstitial oxygen atoms, however as more oxygen is added to the lattice the defects aggregate to form clusters [29]. The higher fluorite-based structures, namely U_4O_9 and U_3O_7, consist of UO_2 supercells

containing ordered arrangements of oxygen defect clusters. However, there is still considerable debate in the literature regarding which clustering scheme is present, with discrepancies between computational and experimental results [30-32]. Thus, there is a need for more detailed investigation of the fluorite-based UO_{2+x} region of the U-O phase diagram to resolve the structural features and effects on the materials properties.

1.5 Aims of Thesis

The radioactivity of uranium is a barrier to experimental work, as is the meta-stability of some of the intermediate oxides (with respect to U_3O_8 and UO_3) and so computational approaches can provide convenient alternatives. This thesis aims to examine the full set of uranium oxides using density functional theory (DFT) simulations to probe their structures and make predictions of their structural and electronic properties.

Thus the main goals are:

- Establish effective methodology for simulating UO_2 that can reproduce the experimentally observed structural, electronic and magnetic properties to a good level of accuracy. As the magnetic and electronic properties are of interest it is necessary to use DFT rather than potential based methods.
- Simulate hyperstoichiometric UO_2 to ascertain whether interstitial oxygen prefers to be isolated or form defect clusters and if the latter, which defect clusters.
- Produce models for the fluorite based U_4O_9 and U_3O_7 oxides to identify stable structures and determine which uranium charge states are present in these mixed valence systems.
- Simulate the layered uranium oxides, identifying charge states in the mixed valence systems, and make predictions of their structural, electronic and magnetic properties. In particular, data on polymorph stability and elastic properties are lacking in the literature.
- Apply the same methodology at each stoichiometry so the results are directly comparable with one another thus allowing analysis of the relative stability of each phase.

The following chapter describes the computational methodology (density functional theory) and validation of the simulations used throughout this investigation. Results of the simulations are then presented, starting with UO_2 (Chapter 3) and increasing stoichiometry to $UO_{2.0625}$ – $UO_{2.33}$ (Chapter 4), U_2O_5 (Chapter 5), U_3O_8 (Chapter 6) and UO_3 (Chapter 7). Each of these chapters begins by discussing the relevant experimental and computational work in the literature and continues with a description of the results of the simulations on structural, electronic and lattice dynamical properties. Finally the thesis concludes with a summary of the findings and discussion of potential future work arising from them Chapter 8.

Chapter 2

2 Computational Methodology

The simulation of atomic level systems can be broadly categorised into two approaches: quantum mechanical and classical methods. Within either of these frameworks there are three main simulation techniques that can be applied: static energy minimisation (EM), where an algorithm is used to update ionic positions until predefined convergence criteria are met; molecular dynamics (MD), where ions are allowed to interact for a period of time and their trajectories are determined by Newton's equations of motion and Monte Carlo (MC), where steps are randomly generated and accepted or rejected based on the effect to the system energy. The methods have their own benefits and drawbacks; MD and MC can be more useful for finding the global energy minimum of a system and including temperature effects. By comparison EM will normally find the nearest local minimum but this means it can be useful for comparing different polymorphs of the same composition.

Classical methods use a set of parameterised equations, or potentials, to describe the interactions between atoms and are derived from known physical quantities such as lattice parameters and elastic constants. Ions are considered to either have a point charge or a charge gradient (based on a core and shell of differing charge) to include polarizability. Classical techniques are ideal for large simulation cells and can provide accurate information about the behaviour of a system, despite only considering attractive and repulsive interactions between species. The main drawback though is the large amount of data from experiment (or quantum mechanical calculations) required to derive potentials and lack of explicit treatment of electrons (electronic properties cannot be calculated).

By contrast quantum mechanical methods are considered *ab initio*, or "from first principles", as they explicitly simulate the electron density of a system and derive all properties from this, so less prior information about a particular system is required. Most

crucially a set of initial atomic coordinates are needed (typically from experiment). In practice, the techniques are not yet fully '*ab initio*' but simply contain far fewer adjustable parameters than classical methods. The parameters that are present relate to the level of theory and functional to be used and hence *ab initio* methods represent a useful approach for investigating material properties with relatively little starting information. The main drawback of quantum mechanical approaches is the significant computational expense associated with considering the electrons explicitly, which drastically limits the system sizes that can be practically modelled. Traditionally most quantum mechanical studies use an EM algorithm, however as computational resources become cheaper *ab initio* MD and MC simulations are becoming more common.

After assessing the merits and drawbacks of the two types of simulation technique it was decided to use quantum mechanical simulations in this work. The system sizes are, for the most part, small enough to be modelled quantum mechanically. The large variation in uranium charge and coordination environment across the full set of oxides could be challenging to find or fit effective potentials for but can be described using a single pseudopotential (section 2.2.4). Hence this chapter is concerned with the background and theory of quantum mechanical simulation, other properties calculated in this work and validation of the methodology used.

2.1 Quantum Theory

Quantum mechanical methods aim to solve the many-body Schrödinger equation in order to calculate the electronic structure of a system. Equation 2.01 shows the time-independent form of the Schrödinger equation:

$$H\Psi = E\Psi \qquad \textbf{Equation 2.01}$$

where H is the Hamiltonian operator, E is the total energy of the system and Ψ is the electron wave function. The Hamiltonian itself can be expressed as a function of nuclear and electronic components (Equation 2.02):

$$H = T_n + T_e + V_{nn} + V_{ee} + V_{ne} \qquad \textbf{Equation 2.02}$$

where T_n and T_e are the nuclear and electronic kinetic operators and V_{nn}, V_{ee} and V_{ne} are the nuclear and electronic potentials (repulsive contributions) and the nuclear-electron interaction (Coulombic attraction of electrons to nucleus). Unfortunately, the exact solution to the Schrödinger equation can only be found for single electron systems, as the V_{ee} prevents the complete wave function from being decoupled into a set of independent equations. Thus for many-body systems the Born-Oppenheimer approximation [33] is employed, which allows the nuclear and electronic degrees of freedom to be decoupled. The approximation states that although the forces acting on the nucleus and electrons are the same the mass of the electrons is far less, so the nucleus is essentially stationary compared to the electrons (or the electrons move instantaneously relative to the nucleus). The outcome is that the nuclei can be considered as fixed charges, forming part of the external potential, and the Hamiltonian is redefined in Equation 2.03:

$$H = T_e + v_{ext}\{(\boldsymbol{R}_i)\} + V_{ee} \qquad \textbf{Equation 2.03}$$

where v_{ext} is the external potential imposed by the configuration of nuclear positions $\boldsymbol{R}_{\mathbf{i}}$.

2.1.1 Density Functional Theory

Density Functional Theory (DFT) is an electronic structure method where the N-electron wave function (and its corresponding Schrödinger equation) are replaced by the (simpler) electron density (ρ) (Equation 2.04). This exploits the principal that the ground state energy of a system can be expressed solely as a function of the ground state charge density.

$$\rho(r) = |\Psi(r_1,\ s_1; \ldots; r_{\mathrm{N}}, s_{\mathrm{N}})|^2 \qquad \textbf{Equation 2.04}$$

In Equation 2.04 r_{i} and s_{i} are the positon and spin of the electron, i. The primary advantage of this approach is that it drastically reduces the dimensionality of the problem; from the $4N$ degrees of freedom of the electron's spin-orbitals ($\mathrm{r}_1,\ \mathrm{s}_1;\ldots;\mathrm{r}_{\mathrm{N}},\ \mathrm{s}_{\mathrm{N}}$) to just three spatial coordinates, r, thus locating a solution faster.

The key mathematical element of DFT is the functional. A functional transforms a function that exists in vector space to a scalar. Thomas [34] and Fermi [35] were the first to attempt to describe an atomic system in this way, shortly after Schrödinger's equation was derived. This early work made a number of approximations, including the exclusion of exchange

and correlation effects, making it too inaccurate to be used practically. In 1930 Dirac added a local approximation for exchange [36], however a suitably accurate method for directly calculating electron density did not emerge for another 30 years.

2.1.2 The Hohenberg-Kohn Theorems

There are two principle theorems that all modern DFT depends on, both formalised and proven by Hohenberg and Kohn in 1964 [37]. The first being that the external potential (v_{ext}) is a unique functional of the electron density (ρ). A direct consequence of this is that, because v_{ext} is part of the Hamiltonian (Equation 2.03), the full many-body ground state wave function Ψ is also a unique function of ρ. In other terms, all ground state and excited state properties of an atomic system are uniquely determined by the electron density. The second theorem defines a functional for calculating total energy from an electron density (Equation 2.05).

$$E[\rho] = \int v_{ext}(r)\rho(r)dr + F[\rho] = E_{ne}[\rho] + F[\rho] \qquad \textbf{Equation 2.05}$$

As seen in Equation 2.03, the nuclear-electronic interaction can be incorporated into the external potential. The functional in Equation 2.05 produces the lowest energy for a particular system when provided with the true ground state electron density. The $F[\rho]$ term is known as the Hohenberg-Kohn functional; it is composed of a kinetic energy term $T[\rho]$ and a total energy term for interelectronic interactions $E_{ee}[\rho]$ (containing the potential energy term V_{ee},). The contribution to the total energy is the same as that of the kinetic and full electron-electron components of the Hamiltonian (Equation 2.06).

$$F[\rho] = T[\rho] + E_{ee}[\rho] \qquad \textbf{Equation 2.06}$$

$E_{ee}[\rho]$ (total interelectronic energy) is defined by a classical contribution, $J[\rho]$ (the Coulomb interaction), and a non-classical contribution, $E_{ncl}[\rho]$ (exchange and correlation contributions), according to Equation 2.07.

$$E_{ee}[\rho] = J[\rho] + E_{ncl}[\rho] \qquad \textbf{Equation 2.07}$$

$J[\rho]$ is the only explicitly known contribution to the functional at this stage, as $T[\rho]$ and E_{ncl} are still unknown. This provides an advantage over other frameworks (e.g. Hartree-Fock or Thomas-Fermi); if all functionals are known explicitly the exact solution to the

Schrödinger equation can be obtained (although this is not possible in practice) as no approximations have been made yet.

2.1.3 The Kohn-Sham Equations

The Hohenberg-Kohn theorems provide a solid foundation on which to build DFT methods, although they offer no inherent means to locate a solution. This came slightly later with the work of Kohn and Sham in 1965 [38]. Combining Equations 2.05-2.07 yields Equation 2.08.

$$E[\rho] = E_{ne}[\rho] + T[\rho] + J[\rho] + E_{ncl}[\rho] \qquad \textbf{Equation 2.08}$$

The $E_{ne}[\rho]$ term (defined in Equation 2.05) and $J[\rho]$ (the Coulomb interaction) were defined explicitly by Hohenberg and Kohn whilst the other functionals were left undefined. $T[\rho]$, the kinetic energy, is dependent on electron velocities and has a complicated relationship with the electron density, which only considers the spatial distribution of the electrons. In other words the kinetic energy is inherently non-local. Previous models failed to perform well due to their consideration of kinetic energy as entirely an explicit function of electron density [34-36]. Kohn and Sham were aware of this problem and tackled it by calculating as much of the kinetic energy as possible in an exact manner and then using an approximation to deal with the remainder.

In order to achieve this a reference system of non-interacting electrons is used. The reference system is defined such that it has an identical electron density as the real solution and is defined by Equation 2.09.

$$H_{Ref} = \sum_{i=1}^{N}\left[-\frac{1}{2}\nabla_i^2 + V_{Ref}(r_i)\right] \qquad \textbf{Equation 2.09}$$

In the Hamiltonian (H_{Ref}) V_{Ref} is the reference potential, chosen so that the ground state density for H_{Ref} is equal to the true electron density. Thus the ground state energy of the non-interacting system is the same as the ground state energy of the real system.

As there are no electron-electron interacting terms the solution to the reference system can be represented exactly by a Slater determinant comprised of single electron functions, φ_i, named Kohn-Sham orbitals. Although it seems counterintuitive to introduce wave functions

again (as the aim of using electron density was to reduce the dimensionality), because the reference system only contains non-interacting electrons, the single particle solutions can be found independently of one another (Equation 2.10).

$$\left[-\frac{1}{2}\nabla_i^2 + V_{Ref}(r_i)\right]\varphi_i = \in_i \varphi_i \qquad \textbf{Equation 2.10}$$

The kinetic energy of the non-interacting system is then defined exactly by Equation 2.11.

$$T_{Ref} = -\frac{1}{2}\sum_{i=1}^{N}\int \varphi_i^*\nabla^2\varphi_i d\tau \qquad \textbf{Equation 2.11}$$

T_{Ref} can now be incorporated into the energy expression for the real system of fully interacting electrons, defined in Equation 2.12.

$$E_{KS}[\rho] = E_{ne}[\rho] + T_{Ref}[\rho] + J[\rho] + E_{xc}[\rho] \qquad \textbf{Equation 2.12}$$

The new quantity, $E_{\mathrm{xc}}[\rho]$, is called the exchange-correlation functional and contains not only the exchange and correlation energies but also the remainder of the true kinetic energy (which incidentally arises from correlation effects between electrons). All unknown elements of the system can now be grouped into the exchange-correlation functional, according to Equation 2.13.

$$E_{xc}[\rho] = \big(T[\rho] - T_{Ref}[\rho]\big) + \big(E_{ee}[\rho] - J[\rho]\big) = T_{Corr}[\rho] + E_{ncl}[\rho] \qquad \textbf{Equation 2.13}$$

The only outstanding problem is to find a reference potential (V_{Ref}) that produces a non-interacting electronic system with the same electron density as the real system. Where $\bar{\rho}$ represents a trial density and E_0 is the true ground state energy, $E[\bar{\rho}] \geq E_0$ is true for both the reference and interacting systems; with $E[\bar{\rho}] = E_0$ only when $\bar{\rho}$ is the true electron density ρ. Consequently, when given the true electron density the energy of both systems must be at a minimum, yielding an expression for the reference potential in terms of the interacting system (Equation 2.14):

$$V_{Ref}(r) = V_{ext}(r) + \int \frac{\rho(r\prime)}{|r-r\prime|}dr' + V_{xc}(r) \qquad \textbf{Equation 2.14}$$

where $V_{\mathrm{xc}}(\mathrm{r})$ is the exchange-correlation potential determined by the functional derivative given in Equation 2.15.

$$V_{xc}(r) = \frac{\delta E_{xc}}{\delta\rho(r)} \qquad \textbf{Equation 2.15}$$

So, the system can now be solved self-consistently by generating an initial set of Kohn-Sham orbitals, which are used to calculate a reference potential (Equation 2.14), that is used to minimise the energy of the Kohn-Sham orbitals within the reference system (Equation 2.10). The process is then repeated until the system reaches convergence.

2.1.4 Approximate Exchange-Correlation Functionals

As mentioned previously, all uncertainty within Kohn-Sham DFT has been grouped into the exchange-correlation functional. Exact functionals are only known for the free electron gas, however there are a number of methods available to approximate it. There is still debate over how the best approximation is achieved; semi-empirically (e.g. B3LYP functional [39, 40]) or purely theoretically (functionals used in this work). However most current functionals are based on the local density approximation (LDA), or an extension of it, known as the generalised gradient approximation (GGA).

The Local Density Approximation

The LDA is the simplest exchange-correlation functional and is based on the uniform electron gas model [37]. In this model, the electron density is homogeneous over all space and E_{xc} is known accurately for all electron gas densities used in the calculation. The LDA exchange-correlation functional is described generically by Equation 2.16:

$$E_{xc}^{LDA}[\rho] = \int \rho(r)\varepsilon_{xc}[\rho]dr \qquad \textbf{Equation 2.16}$$

where ε_{xc} $[\rho]$ is the exchange-correlation energy density, that is to say the energy per particle of the uniform electron gas of density ρ.

The primary assumption made in the LDA is that at a point (r) in the electron distribution the value of E_{xc} will be the same as that for the homogeneous electron gas of the same density. In other terms, the LDA exchange-correlation functional is local, depending solely on the density at r ($E_{xc}[\rho(r)]$). By comparison to non-local functionals, which depend on the density at that point (local) and elsewhere ($E_{xc}[\rho(r), \rho(r')]$. The expectation is that the LDA should function poorly for chemical systems due to their variation in density. Kohn and Sham applied the LDA to limiting cases in their original paper but initially considered it too

inaccurate for practical use. Subsequent calculations employing the LDA have yielded surprisingly good results, and the LDA is regularly used in DFT calculations today.

The extension of the LDA to spin polarised systems is straightforward for the exchange energy, where the exact spin scaling is known, but further approximations must be employed for the correlation energy. The spin polarised LDA functional is thus described by Equation 2.17:

$$E_{xc}^{LSDA}[\rho_\alpha \rho_\beta] = \int dr\, \rho(r) \varepsilon_{xc}(\rho_\alpha \rho_\beta) \qquad \textbf{Equation 2.17}$$

where $\rho = \rho_\alpha + \rho_\beta$ (representing the two spin states) [41]. All modern LDA functionals can operate as either spin polarised or non-spin polarised.

The ε_{xc} term can be split into exchange and correlation components, of which correlation is smaller but more complicated to compute. The exchange part (ε_x) is the original form proposed by Dirac [36]. In modern LDA functionals the correlation portion (ε_c) is generally fitted to data from high accuracy quantum Monte Carlo simulations of the uniform electron gas at varying densities [42]. Good examples of such fits are the different functionals proposed by Vosko *et al* [43] and Perdew *et al* [44].

The LDA rests on the assumption that the exchange-correlation potential is dependent only on the local value of ρ; however, as correlation is inherently non-local the assumption can lead to a number of errors. The main inadequacy is that the LDA requires ρ(r) to vary slowly, which is not the case for strongly correlated systems (e.g. metals and semiconductors), which are calculated to overbind [45]. Overestimating binding energies leads to shorter bond lengths and smaller system volumes. Other issues include small predicted band gaps in semiconductors and incorrect ground state electronic structures, often due to false delocalisation of electrons. Despite these shortcomings the LDA generally achieves good equilibrium geometries, vibrational frequencies and charge moments and so enjoys widespread use.

The Generalised Gradient Approximation

A logical progression from the LDA, the GGA incorporates the gradient of electron density into the exchange-correlation functional, accounting for the inhomogeneity of chemical systems. The GGA exchange-correlation functional is generally defined by Equation 2.18.

$$E_{xc}^{GGA}[\rho] = \int \rho(r)\varepsilon_{xc}(\rho, |\nabla\rho|)dr \qquad \textbf{Equation 2.18}$$

In practice the GGA is achieved by applying a correction to the LDA exchange-correlation functional that is dependent only on the (reduced) density gradient. To correct the exchange portion Becke proposed a function with a single empirical parameter, fitted to experimental data for the rare gas atoms [46]. This form is used in Perdew and Wang's PW91 functional, albeit with a modification to remove the dependence on the empirical parameter [47]. Alternatively the exchange functional can be corrected using a rational function in which all components are determined computationally. This is the approach employed by Perdew, Burke and Ernzehof in the PBE functional [48]. These GGA functionals typically underbind, overestimating lattice parameters and volumes. A revised version of the PBE (PBEsol) was developed to improve equilibrium properties for densely packed solids, slightly compressing the lattice compared to the PBE [49], however it is less accurate for prediction of dissociation or cohesive energies.

Although GGA functionals attempt to account for variations in density, they are still local in the sense that they are dependent only on the properties of the density at each point, *r*. Overall, GGA functionals tend to perform better than LDA functionals, however results can vary from system to system as they are still inclined to underestimate band gaps.

Meta-GGA Functionals

Meta-GGAs go one step further than GGA functionals, adding the second derivative of electron density (the Laplacian, $\nabla^2\rho$) or, more recently, the kinetic energy density (τ_0) [50]. Inclusion of τ_0 allows meta-GGA functionals to distinguish between single orbital shape regions and orbitally overlapped regions [51]. Meta-GGA functionals reportedly predict slightly shorter lattice constants than GGA functionals and very accurate band gaps [51]. Examples include the MBJ [52], M06L [53], TPSS [54] and revisedTPSS functionals [50].

Hybrid Functionals

Whilst still falling under the DFT umbrella, hybrid functionals are distinct from the types of functional discussed thus far. They improve predicted atomisation energies, bond lengths and vibrational frequencies by incorporating a portion of exact exchange from Hartree-Fock (HF) theory with exchange and correlation from either *ab initio* or empirical sources.

The exact exchange energy functional is expressed in terms of Kohn-Sham orbitals (rather than density) and so is regarded an implicit density functional. Hybrid functionals are usually constructed as linear combinations of the HF exact exchange functional and then exchange and correlation explicit density functionals. The weighting parameters for each functional can then be fitted to experimental or more accurately calculated thermochemical data. The most common examples of hybrid functionals include B3LYP [39, 40], PBE0 [55], HSE [56] and M06 [57]. PBE0 mixes PBE and HF exchange energy in a fixed three to one ratio, alongside the full PBE correlation energy. HSE is based on PBE0 but is more efficient, using an error function screened Coulomb potential to calculate the exchange portion of the energy. It also includes a parameter to control the portion of HF exchange (α) and an adjustable parameter that controls the range of interaction (ω).

The GW Approximation

The GW approximation is slightly different to the other methods described here. A Green's function (G) is adopted in place of the electronic density, which is dynamic and non-local and also depends on the empty states in a material. An exchange-correlation operator is also used instead of an exchange-correlation potential. The method is essentially a variation of Hartree-Fock [58] in which the interaction between electrons is screened. The main advantage of the approximation over conventional DFT is vastly improved calculation of band gaps due to the inclusion of empty states. The method is, however, considerably more computationally expensive than DFT methods due to the time dependence and screened Coulomb interactions. The method has not been implemented at all in the present work, although it can be used in VASP.

Van der Waals Corrected DFT

Most local and semi-local density functionals, including those used in this thesis, do not correctly describe the van der Waals (vdW) interactions that arise from the dynamical correlations between shifting charge distributions. The issue can be addressed by including a correction term in the form of a dispersion energy to the standard Kohn-Sham DFT energy. In VASP this term is applied to the potential energy, interatomic forces and stress tensor and so it is possible to perform lattice relaxations, molecular dynamics and vibrational analysis using it. In some calculations (Chapter 7) vdW correction is employed

in the form of Grimme's D3 correction method, in which the dispersion coefficients are geometry dependent [59].

2.1.5 The Hubbard Coefficient (DFT + U)

A notable shortcoming of the way in which DFT operates is a failure to describe systems with strongly correlated (or localised) *d*- and *f*-electrons, a characteristic shared by the LDA and GGA alike. This occurs because of fractional numbers of electrons being assigned to atoms causing a self-interaction error that favours delocalised states. So they predict partially filled bands with metallic electronic structure and itinerant electrons in contrast to real properties of transition metal and rare-earth oxides (semiconductors and insulators) [60].

In order to overcome this problem, the Hubbard coefficient is introduced to account for strong on-site correlation, by treating the Coloumb interaction in a mean-field Hartree-Fock type manner [61]. The Hubbard coefficient depends on two parameters; the effective on-site Coloumb parameter (U) and the effective on-site exchange parameter (J). There are two common implementations of DFT + U; under the Dudarev scheme the individual values of U and J are insignificant, with only the difference between them (U_{eff}) appearing in the formulation [62]. Alternatively, there is the rotationally invariant approach developed by Lichtenstein where U and J are considered individually and both contribute to correcting the self-interaction error [63]. It is possible to calculate the values of U and J via linear regression or tune them to band gap of the material under investigation. Alternatively it is possible to fit them to experimentally derived values from X-ray Photoelectron Spectroscopy (XPS) experiments. This work uses the Dudarev implementation and applies the same U_{eff} (U = 4.50, J = 0.54 eV) to the *f* electrons on the uranium ions in each oxide under investigation for consistency. The value of U_{eff} used is derived for UO_2 from XPS experiments [64].

2.2 The Practical Use of DFT

Now that the electronic representation and functional based mechanics of DFT have been established, it is necessary to develop an understanding of its practical implementation, which requires a number of other factors to be defined and explained.

2.2.1 Periodic Boundary Conditions

Real systems contain enormous amounts of atoms (~10^{23} atoms) whereas in DFT simulations the limit (with the resources available at the time of writing) is ~200 atoms. Therefore to obtain meaningful results from simulations it is necessary to approximate an infinite system using a finite number of species. Periodic boundary conditions (PBC) are the most common feature of computational studies used to overcome this problem. Depending on the type of system different boundary conditions can be applied to the simulation cell: 0D molecules, 1D polymers, 2D slabs/surfaces and 3D crystals.. Particles in each box (simulation cell) move identically to their corresponding particles in other boxes, so when one leaves a box its image enters on the opposite side (Figure 2.01).

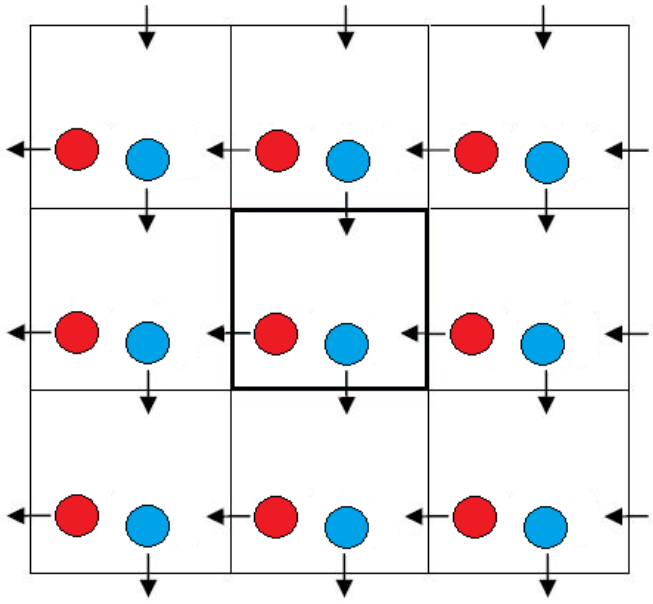

Figure 2.01 – 2D representation of periodic boundary conditions with the simulation box in bold.

2.2.2 The Reciprocal Lattice

The reciprocal lattice is a representation of the real crystal lattice but defined in reciprocal space (also known as *k* space). It is generated by applying a Fourier transform to the real space lattice, and the relationship between the real space lattice vectors (*a*, *b* and *c*) and the *k* space lattice vectors (*a**, *b** and *c**) is defined in Equation 2.19.

$$a^* = 2\pi \frac{b \times c}{a \cdot b \times c}; \quad b^* = 2\pi \frac{a \times c}{b \cdot a \times c}; \quad c^* = 2\pi \frac{a \times b}{c \cdot a \times b}; \qquad \textbf{Equation 2.19}$$

It is possible to construct the infinite reciprocal lattice from primitive cells in precisely the same manner as the real space lattice. The primitive reciprocal space cell is known as the first Brillouin zone (BZ) (Figure 2.02). The first BZ is of crucial importance to electronic calculations of periodic systems as the wave function can be completely characterised within this volume.

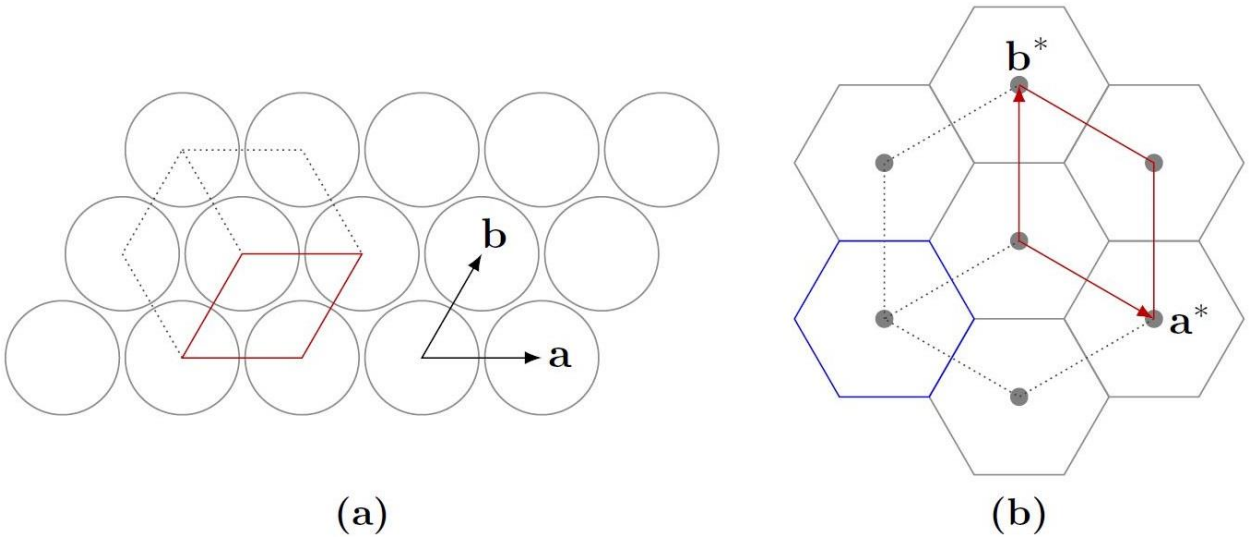

Figure 2.02 – Relationship between real space and reciprocal space using a 2D hexagonal lattice. (a) shows the real space hexagonal lattice of atoms (grey circles) with the unit cell highlighted in red. (b) shows the corresponding reciprocal lattice points (grey dots), reciprocal unit cell (red) and the first Brillouin zone (blue) [65].

2.2.3 Bloch's Theorem and Plane-wave Basis Sets

An infinite solid poses two main problems in solving the Schrödinger equation. Firstly, an infinite number of wave functions must be determined for the infinite number of electrons.

Secondly, each electron wave function spreads across the entire lattice, meaning that an infinite basis set is also needed to describe it [66]. These problems can be overcome by taking advantage of the PBCs of the system.

Bloch's theorem states the wave function of an electron (*i*) in a periodic potential may be expressed as the product of a wave-like term and a term with the same periodicity as the unit cell (Equation 2.20):

$$\psi_i(r) = e^{ik\cdot r} f_i(r) \qquad \textbf{Equation 2.20}$$

where *k* is the wave vector, lying within the first BZ and determining the direction and frequency of the wave for the wave like term. The cell-periodic part of the wave function (Equation 2.21) can now be assembled from a basis set of discrete plane waves ($e^{iG\cdot r}$). The wave vectors (G) are the set of all possible reciprocal lattice vectors, i.e. translations to identical lattice points.

$$f_i(r) = \sum_G c_i, G^{e^{iG\cdot r}} \qquad \textbf{Equation 2.21}$$

The wave function of each electron can then be written as the sum of plane waves (Equation 2.22), where the coefficients c_i, k + G define the solution.

$$\psi_i(r) = \sum_G c_i, k + G^{e^{i(k+G\cdot r)}} \qquad \textbf{Equation 2.22}$$

The set of reciprocal lattice vectors, and therefore the size of the basis set, can be limited because plane waves with higher |G| have higher kinetic energy and so contribute less to the wave function. Above some point, referred to as the cut-off energy, their effects are negligible and so the basis set can be truncated to plane waves below this energy. The limit is usually set manually in DFT calculations by varying cut-off energy and establishing at what energy convergence is reached (i.e. increasing the cut-off energy does not affect the calculated energy of the system).

Equally, if the wave function (ψ) is assumed to be a continuous function of *k*, then it will not change much with small variations in *k*; hence ψ over a region of *k* space can be represented by ψ at a single *k* point. Thus the system can be sampled with a discrete number of *k* points, removing the need for an infinite number of electrons.

It is vital to select *k* points appropriately for integrating across the first BZ in order to achieve good representations of band structures and densities of states. The present work employs the Monkhorst-Pack scheme, which distributes the *k* points evenly throughout the first BZ [67]. An example of a Monkhorst-Pack grid for a hexagonal reciprocal lattice is provided in Figure 2.03. This choice of *k* mesh means many points are related by symmetry, further reducing the number of *k* points required as ψ need only be calculated at each unique *k* point. The homogenous distribution of *k* points is described in Equation 2.23, where a^*, b^* and c^* for x_i are determined by Equation 2.24.

$$k = x_1 a^* + x_2 b^* + x_3 c^* \qquad \textbf{Equation 2.23}$$

$$x_i = \frac{l}{n_i} \qquad l = 1, \ldots, n_i \qquad \textbf{Equation 2.24}$$

The density of the *k* grid is defined by the folding parameters n_i. Conducting materials (e.g. metals and small band gap semiconductors) require a finely spaced *k* mesh and so the folding parameters are large. In contrast insulating materials (and large band gap semiconductors) need a less dense *k* point grid and so a small folding parameter is used. The grid is normally centred at the Γ point (the centre of the reciprocal lattice) however it can be shifted depending on the symmetry of the simulation cell. The present work only uses Γ centred *k* point grids but the folding parameters are changed for each material (i.e unit cell) to normalise *k* mesh density. The folding parameter selection process is discussed in section 2.4 and individual folding parameters for each oxide are provided with the relevant results.

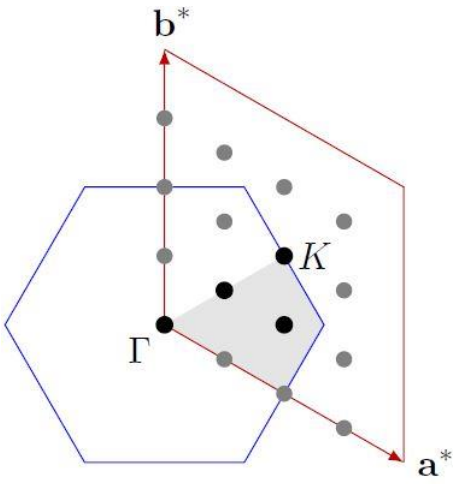

Figure 2.03 – Monkhorst-Pack *k* point grid for a hexagonal reciprocal lattice. The irreducible BZ is shaded in grey and irreducible *k* points are black. The *Γ* and *K* points are high symmetry points representing the centre of the reciprocal lattice [65].

2.2.4 Pseudopotentials

Plane-wave basis sets are usually inappropriate for expanding electronic wave functions because a large number of plane waves are required to expand the orbitals of tightly bound core electrons and represent the rapid oscillations of their wave functions. The basis of the pseudopotential approximation is that the physical properties of a system depend on the valence electrons to a far greater extent than the core electrons, thus the core electrons can remain essentially fixed. Therefore the approximation operates by replacing the core electrons and strong ionic potential with a weaker pseudopotential that acts on a set of pseudo-wave functions instead of true valence wave functions. The pseudopotential wave function, ψ_{pseudo} is the same as the all-electron wave function ψ outside a certain cut-off radius r_c (Figure 2.04) and so is only representative within this region. The smoother functions of pseudopotentials than true all-electron potentials means that fewer plane-waves are required to describe them.

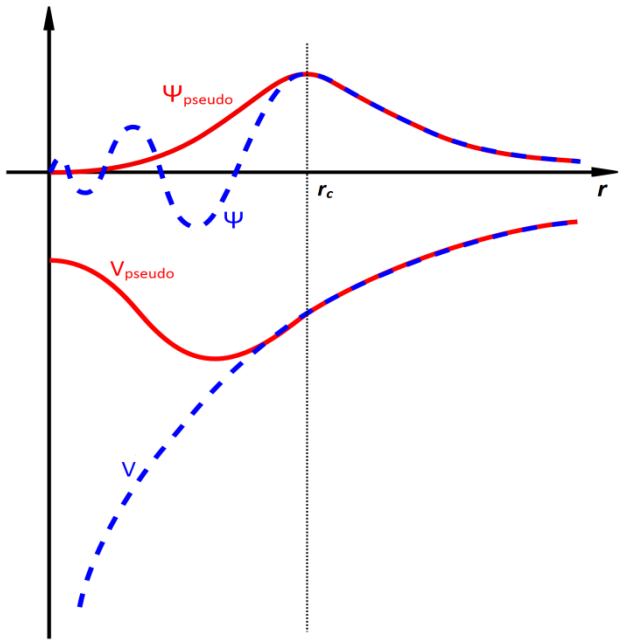

Figure 2.04 – Schematic of all-electron (blue) and pseudo- (red) potentials (v) and wave functions (Ψ). r_c is the cut-off where the values match [66].

There are a variety of types of pseudopotential [45, 68], and the form can be chosen based on the system to improve the efficiency of the calculation. Although it is possible to define them empirically, the most accurate and transferable pseudopotentials are generated using *ab initio* calculations. Pseudopotentials are categorised by softness, which is a measure of both smoothness and the magnitude of the cut-off radius. Smoother pseudopotentials need fewer basis functions, however large cut-off radii give a poorer atomic description and reduce transferability.

Ultrasoft pseudopotentials achieve large cut-off radii and high levels of smoothness by redefining the construction of the pseudopotential. The main pseudopotential is very smooth (and not norm-conserving) and has a large cut-off radius, using an auxiliary function close to each ion core to represent the rapidly varying core density.

Norm-conserving pseudopotentials have orthonormal pseudo-wave functions. They are typically more accurate and transferable than ultrasoft pseudopotentials. Additionally, they simplify the implementation because the solutions automatically reproduce the atomic valence properties.

This work uses the projecter augmented wave (PAW) method [69], the basis of which is similar to ultrasoft pseudopotentials as it uses localised auxillary functions, however it treats the full all-electron wave function. In the PAW method all the integrals are made up of smooth functions, extending in space, and localised contributions that are evaluated by radial integration over muffin-tin spheres. The 'projector' part stems from the mathematical operations used to convert the smooth pseudo-wave function back to the real wave function.

All of the types of pseudopotential described here can be implemented in VASP.

2.3 Energy Minimisation

Energy minimisation is one of the three main simulation techniques introduced at the beginning of this chapter, the others being molecular dynamics and Monte Carlo simulations. Energy minimisation simulations use the forces between atoms to adjust atomic positions to obtain the lowest energy structure; there are a number of different methods to achieve this which are discussed here. This thesis is only concerned with quantum mechanical (or *ab initio*) energy minimisation, implemented via the VASP code [70]. This section provides an overview of various minimisation techniques, and so although they are not used in the present work; steepest descents and Newton-Raphson algorithms are discussed as an introduction to the conjugate gradients and quasi-Newton methods.

All energy minimisation algorithms begin from an initial configuration, calculate the energy and forces in this state and adjust the atomic coordinates to produce a lower energy configuration, repeating until a minimum is reached. With increasingly sophisticated minimisation methods, agreement with experimental crystal structures is generally good; however there are still three main drawbacks to energy minimisation:

- An initial crystal structure is required.
- The nearest local energy minimum will almost always be found. Meaning that if multiple minima are present in the system the minimisation may only locate a local minimum as opposed to the global minimum.

- Vibrational properties are not included, so simulations always take place at 0 K and neglect zero point energy.

Consequently results are not always representative of experiments (which are not conducted at 0 K). In addition to lacking vibrational properties this can affect magnetism, for example UO_2 (discussed in Chapter 3) is paramagnetic above 30 K[71] and exhibits non-collinear antiferromagnetism below this point [24] and so DFT calculations typically consider the latter magnetic structure. The simulations presented here are assumed to either have a good initial atomic configuration (experimentally determined structure from literature) or a large number of initial configurations are trialled to improve the chances of finding the global minimum. When the atomic coordinates of different polymorphs are known, energy minimisation can be used effectively to assess their relative stabilities due to its tendency to find the closest local minimum (e.g. UO_3 in Chapter 7). By comparison using molecular dynamics or Monte Carlo simulations are more likely to locate the global minimum for a particular composition. The calculations here are performed at 0 K however the computed energies can be incorporated into further calculations to give predictions of behaviour at higher temperatures. This is not as accurate as using alternative techniques to include temperature explicitly however it can still produce thermodynamically meaningful results [72, 73] (Chapters 6 and 7). In summary, efforts have been made to reduce the impact of the known limitations of these types of simulation.

Most energy minimisation methods rely on either first or second derivatives of lattice energy (U_L) with respect to atomic positions (r), and aim to reduce this value to zero so there is no residual stress (or force) on the atoms. Equation 2.25 shows this for a first derivative.

$$\frac{\delta U_L}{\delta r} = 0 \qquad \textbf{Equation 2.25}$$

The iterative procedure required to minimise the energy is implemented by expressing the energy with a Taylor expansion in terms of basis strain (δr) using Equation 2.26.

$$U_L(r + \delta r) = U_L(r) + \frac{\delta U_L(r)}{\delta r}\delta r + \frac{1}{2!}\frac{\delta^2 U_L(r)}{\delta r^2}\delta r^2 + K \qquad \textbf{Equation 2.26}$$

The Taylor expansion shows *r* is composed of three components, giving rise to a 3*N* matrix. The more terms that are included in the expansion (*K* is used in Equation 2.26 to refer to additional terms) the more accurate the minimisation will be.

The two main strands of energy minimisation are constant volume and constant pressure calculations; the former fixing the cell dimensions but allowing movement of ions and the latter permitting both to relax. The present work uses constant pressure minimisations exclusively. They typically operate in much the same manner as constant volume minimisations, adjusting atomic coordinates to reach the energy minimum, but then apply Hooke's law to alter the lattice vectors according to the bulk lattice strain (Equation 2.27):

$$\varepsilon = C^{-1}\sigma \qquad \textbf{Equation 2.27}$$

where ε is the strain and σ is the stress, defined as the sum of applied and static pressure (Equation 2.28), and C^{-1} is the compliance matrix, or second order derivatives of lattice energy (U_L) with respect to strain. For a detailed description of constant pressure energy minimisation refer to Leach [74].

$$P_{static} = \left(\frac{1}{V}\right)\left(\frac{dU_L}{d\varepsilon}\right) \qquad \textbf{Equation 2.28}$$

Generally speaking a more complex minimisation procedure (i.e. involving second derivatives) will take fewer iterations to converge than a simpler one (i.e. first derivatives) but each step will take longer to complete. The main energy minimisation methods are now outlined, with particular emphasis on those used in this work.

2.3.1 Steepest Descent Minimisation

The steepest descent method is the simplest first order type of energy minimisation algorithm. If r_i is the initial configuration, the algorithm moves closer to the minimum with each step by moving in the direction of the residual, or 'down the energy slope' (Equation 2.29).

$$r_{i+1} = r_i + \alpha_i s_i \qquad \textbf{Equation 2.29}$$

Where s_i is the gradient vector, defined in Equation 2.30.

$$s_i = -g_i \qquad \text{where} \qquad g_i = \frac{\delta U_L}{\delta r_i} \qquad \textbf{Equation 2.30}$$

Where g_i is the gradient, however the most important consideration here though is how far to move in each step, or the magnitude of α_i. It is determined using a line search procedure that minimises the energy in the direction of the residual, so the new position will be closer to the minimum than the previous position. By definition the gradient of the energy surface at the minimum must have no component in the direction of the search. The main implication of this is that the next step will be orthogonal to the search direction (or gradient). Thus in a narrow energy well the accumulation of many small successive steps makes the algorithm quite inefficient, although it can often quickly relieve high energy features at the start of a minimisation. This is because it is possible for later steps to reintroduce error components that were already removed in previous minimisation steps. Naturally this means steepest descent methods are rarely employed in modern studies however it useful nonetheless to use them as an introduction to energy minimisation techniques.

2.3.2 Conjugate Gradient Minimisation

Conjugate gradient techniques are a natural progression from steepest descents minimisation; a steepest descent method is used for the first step (quickly moving away from high energy features) and all subsequent iterations use information from previous gradients to calculate the new displacement vector [75, 76]. The minimisation itself has the same general form as a steepest descents algorithm (Equation 2.27) however as information from previous steps must be included the calculation of the gradient vector (s_i) differs (Equation 2.31).

$$s_i = -g_i + \gamma_i s_{i-1} \qquad \text{where} \qquad \gamma_i = \frac{g_i \cdot g_i}{g_{i-1} \cdot g_{i-1}} \qquad \textbf{Equation 2.31}$$

So the gradient (g_i) is still the same as in steepest descents (first derivative of energy with respect to the atomic coordinates) but the gradient vector includes the $\gamma_i s_{i-1}$ term, which takes into account s_i and g_i from the previous step as well. The outcome of this is that the algorithm will converge well regardless of the shape of the surface so the best solution within the imposed bounds will be located. This also has the effect of eliminating the loss

of efficiency that steepest descents techniques encounter in long, narrow energy minima. As it is also a first derivatives method conjugate gradient minimisations are typically very efficient and so are one of the algorithms used for energy minimisation in the present work.

2.3.3 Newton-Raphson Minimisations

The Newton-Raphson method is another widely used energy minimisation technique, unlike the previous two discussed it uses information from both the first and second derivatives to reach the minimum [77]. This makes it more efficient, in terms of numbers of steps required for a minimisation, however each individual step may take longer due to the additional computational expense of calculating second derivatives. The general approach is to take the Taylor expansion (Equation 2.26) to the second derivative, the gradient at the iteration *i* is expressed by Equation 2.32.

$$g_i = \frac{\delta U_L}{\delta r_{i-1}} + \frac{\delta^2 U_L}{\delta r_{i-1}^2}\delta r = g_i + W_{i-1} \cdot \delta r \qquad \textbf{Equation 2.32}$$

Where W_{i-1} is the Hessian matrix and δr is the displacement of ions between iterations *i*-1 and *i*. At energy minima, where g_i equals zero, the atomic displacement is given by Equation 2.33.

$$\delta r = -g_{i-1} \cdot H_{i-1} \qquad \textbf{Equation 2.33}$$

Where H_{i-1} is the inverse Hessian matrix (W_{i-1}^{-1}), this therefore yields Equation 2.34 to calculate the new atomic positions in the Newton-Raphson minimisation scheme.

$$r_i = r_{i-1} - g_{i-1} \cdot H_{i-1} \qquad \textbf{Equation 2.34}$$

The process must still be repeated iteratively like the previous minimisation techniques. The harmonic approximation can be very similar to the real potential energy surface, in which case convergence is still rapid. Further from the minimum though the Taylor series will not approximate the surface as well and convergence could be poorer. This makes it particularly important to have a good starting configuration with Newton-Raphson minimisation. Alternatively many minimisations start with a more robust method (such as conjugate gradients) to move the system close to the minimum and then apply the Newton-Raphson method.

The calculation, and subsequent inversion, of the Hessian matrix is computationally very expensive, in spite of the extra efficiency gained from using second derivatives. This means that it is mainly used for potential-based energy minimisations and electronic structure energy minimisation codes (e.g. VASP) use either the conjugate gradients approach or employ a simplification of Newton-Raphson, the so-called quasi-Newton methods.

2.3.4 Quasi-Newton Minimisations

Quasi-Newton methods do no explicitly calculate the inverse Hessian each iteration, as it does not change much between individual steps, and so an approximated form is used. Generally this means the inverse Hessian is either recalculated after a fixed number of steps or when the changes in energy are too large for the approximation to still be valid. There are a number of different implementations of the methodology available, such as Davidon-Fletcher-Powell (DFP) [76], Broyden-Fletcher-Goldfarb-Shanno (BFGS) [78-81] or the RMM-DIIS algorithm [82].

The DFP method approximates the inverse Hessian matrix according to Equation 2.35.

$$H_i \approx H_{i-1} + \frac{\delta r \times \delta r}{\delta r \cdot \delta g} - \frac{(H_{i-1} \cdot \delta g) \times (H_{i-1} \cdot \delta g)}{\delta g \cdot H_{i-1} \cdot \delta g} \qquad \textbf{Equation 2.35}$$

Where δr = ($r_i - r_{i-1}$) and δg = ($g_i - g_{i-1}$). The alternative BFGS approach is more efficient, differing from the DFP equation by including an additional term (Equation 2.36).

$$H_i \approx H_{i-1} + \frac{\delta r \times \delta r}{\delta r \cdot \delta g} - \frac{(H_{i-1} \cdot \delta g) \times (H_{i-1} \cdot \delta g)}{\delta g \cdot H_{i-1} \cdot \delta g} + (\delta g \cdot H_{i-1} \cdot \delta g) u \times u \qquad \textbf{Equation 2.36}$$

Where the vector u is defined by Equation 2.37.

$$u = \frac{\delta r}{\delta r \cdot \delta g} - \frac{H_{i-1} \cdot \delta g}{\delta g \cdot H_{n-1} \cdot \delta g} \qquad \textbf{Equation 2.37}$$

All quasi-Newton methods depend solely on the change in forces, strains and the previous inverse Hessian matrix. Assuming that the approximation holds, with increasing iterations, the estimate of the inverse Hessian becomes closer to the true inverse Hessian matrix, and on approaching the minimum has similar accuracy to the full Newton-Raphson method. RMM-DIIS quasi-Newton is the other type of algorithm used in the present work.

2.4 Calculation of Crystalline Properties

There are a number of properties discussed in this thesis that are calculated after the structural energy minimisation, either with VASP or through an alternative code. This section outlines these properties and details how they are calculated.

2.4.1 Bulk Modulus and Elastic Constants

The bulk modulus is defined as a material's resistance to uniform compression, the two most common ways to calculate it are a finite displacement method and fitting to a Birch-Murnaghan equation of state. Each has benefits and drawbacks and both of these were tested for this thesis, using UO_2 as the sample case, and found to show good agreement with one another (within 3 %).

If only the bulk modulus is required then it can be calculated with relative computational ease by expanding and contracting the lattice from the predicted equilibrium volume and performing energy minimisations at each point; seven points were found to be sufficiently accurate in most cases. This data can then be fitted to the second or third order Birch-Murnaghan equation of state [83] to yield the bulk modulus. This approach is the less computationally intensive of the two, as the minimised equilibrium lattice can be expanded (and contracted) so the configuration will already be close to the minimum in each case and only a small number of relatively short energy minimisations are then required. However, only the bulk modulus is obtained as it cannot be used to calculate individual elastic constants.

The finite displacement method (used in the present work) operates on a unit cell which is already minimised using a separate algorithm to energy minimisation. Small finite distortions are made to the lattice parameters and the stress matrix response is calculated, thus the full elastic constant matrix (C_{11}:C_{66}) is produced and the bulk modulus derived from this. The elastic constants referred to here are the elastic stiffness constants (or elastic moduli), as opposed to the elastic compliance constants (S_{11}-S_{66}), of which C_{xx} are linear functions. The approach is based on Hooke's law, that for sufficiently small deformations the strain is directly proportional to the stress [84]. This a computationally expensive

process that calculates the full Hessian matrix, although the expense can be reduced slightly by only considering symmetry inequivalent displacements [85].

To derive the bulk modulus from the elastic constant matrix is a straightforward procedure of averaging the first nine elastic constants (C_{11}:C_{33}). Equations have also been derived for this relationship for various crystal symmetries, with more complex equations required for lower symmetries [86, 87]. The equations, however, are just symmetry-adjusted simplifications of averaging the first nine elastic constants (although in the case of orthorhombic cells the equations are more complex) and so the approaches yield identical results.

In a cubic crystal (the highest symmetry) there are only three unique elastic constants (C_{11}, C_{12} and C_{44}) and the average of the first nine constants can be simplified to Equation 2.38 (where B is the bulk modulus) [28]:

$$B = \frac{1}{3}(C_{11} + 2C_{12}) \qquad \textbf{Equation 2.38}$$

For hexagonal crystals there are five unique elastic constants (C_{11}, C_{12}, C_{13}, C_{33} and C_{55}) and the bulk modulus can be calculated using Equation 2.39 [87]:

$$B = \frac{2}{9}(C_{11} + C_{12} + C_{13} + C_{33}/2) \qquad \textbf{Equation 2.39}$$

In orthorhombic lattices there are nine independent elastic constants (C_{11}, C_{12}, C_{13}, C_{22}, C_{23} C_{33}, C_{44}, C_{55} and C_{66}) and bulk modulus is calculated according to Equation 2.40 [86]:

$$B = \frac{\Lambda}{(1+\alpha+\beta)^2} \qquad \textbf{Equation 2.40}$$

Where Λ, α and β are defined by Equations 2.41, 2.42 and 2.43 respectively:

$$\Lambda = C_{11} + 2C_{12}\alpha + C_{22}\alpha^2 + 2C_{13}\beta + C_{33}\beta^2 + 2C_{23}\alpha\beta \qquad \textbf{Equation 2.41}$$

$$\alpha = \frac{(C_{11}-C_{12})(C_{33}-C_{13})-(C_{23}-C_{13})(C_{11}-C_{13})}{(C_{33}-C_{13})(C_{22}-C_{12})-(C_{13}-C_{23})(C_{12}-C_{23})} \qquad \textbf{Equation 2.42}$$

$$\beta = \frac{(C_{22}-C_{12})(C_{11}-C_{13})-(C_{11}-C_{12})(C_{23}-C_{12})}{(C_{22}-C_{12})(C_{33}-C_{13})-(C_{12}-C_{23})(C_{13}-C_{23})} \qquad \textbf{Equation 2.43}$$

For lower symmetry crystals (e.g. monoclinic or triclinic) no equations could be found in the literature and so when these are encountered in the present work bulk moduli have been calculated by averaging the first nine elastic constants.

A further advantage of the implementation of finite displacements in VASP is that the distortions are also applied to each ion in the system (in the *x*, *y* and *z* directions) and the stress matrix response to distortions of atomic vectors and coordinates is also recorded. This allows calculation of the full set of vibrational frequencies for the system, which are a useful way of validating the stability of a structure. The presence of any imaginary (negative) vibrational frequencies indicate the lattice is dynamically unstable, a single frequency typically indicating an energy maximum in one dimension and thus a saddle point (or transition state) between two energy minima.

2.4.2 Density of States

The term density of states (DOS) refers to the occupancy and density of the electronic states in a crystalline solid. It is a function, g(E), defined as the number of electronic states per unit volume, per unit energy, for electron energies near E. The DOS is related to the band structure, showing both the occupied and unoccupied available states, arising from the overlap of atomic orbitals (or wave functions) resulting from a periodic crystalline system. So to consider it within the plane wave framework of DFT, the DOS are the total available electronic wave functions in the system [84].

The contributions from individual orbitals can be calculated (partial DOS) to reveal information on which orbitals are occupied or involved in bonding. This also yields the Fermi level (E_F) at 0 K, or electrochemical potential, which is defined at thermodynamic equilibrium as the energy level with a 50 % probability of being filled (i.e. halfway between the conduction and valence bands). g(E) = 0 for energies within the electronic band gap, a forbidden range of energy or bands, sat between the valence (highest occupied) and conductance (lowest unoccupied) bands. The location of E_F within the DOS determines the electrical behaviour of the material (Figure 2.05):

- In an insulator E_F lies within a large band gap, far from any available states. The composition of bands neighbouring the band gap determine the particular insulating

behaviour. The most common is a charge-transfer insulator where the valence band is composed of anion states and the conductance band of cation states, e.g. O 2*p* and U 5*f* in UO_3 and U_3O_8 [72, 73]. Less common are the Mott-Hubbard insulators, such as UO_2 [88], which has a strong on-site Coulomb repulsion on the uranium atoms leading to valence and conductance bands both composed predominantly of U 5*f* states.

- In a metal, or semi-metal, E_F lies within a delocalised band, and there is no electronic band gap. The high electrical conductivity of metals arises from this wide availability of partially filled states, allowing good electron mobility.
- In an intrinsic, or lightly doped, semiconductor the bands are sufficiently close to E_F that they can be populated by thermal excitation of electrons.

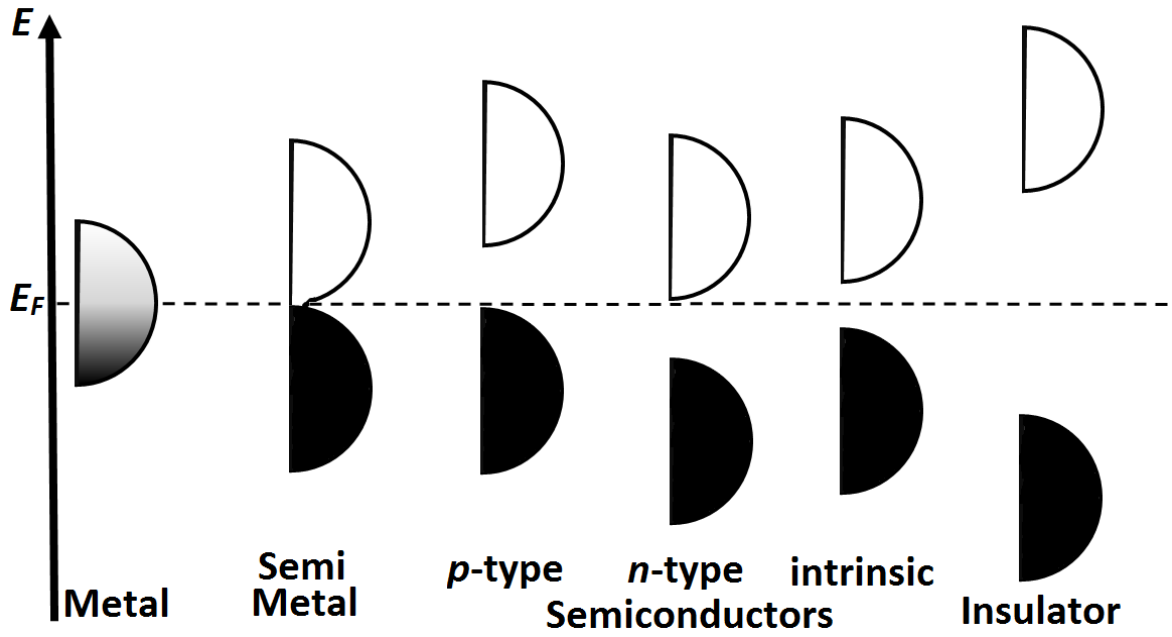

Figure 2.05 – Filling of the DOS for different types of material at equilibrium, energy is on the vertical axis and DOS is on the horizontal axis. The location of the Fermi level (E_F) is shown for each class of material [84].

The DOS is calculated in VASP by default as it is a function of the energy of the system, however to perform accurate DOS calculations there are two main approaches. The first is to perform a normal, self-consistent calculation but with a very fine *k* mesh, scaling even higher for metals. The second approach is a two-step process; first is a self-consistent energy minimisation (with normal *k* grid density) and then, taking the charge density from

the first minimisation, perform a non-self-consistent calculation (i.e. the charge density remains constant throughout). The present work employs the second of these two approaches as it less computationally expensive and gives comparable results.

2.4.3 Simulated Neutron Diffraction

Neutron diffraction (or elastic neutron scattering) is an important tool used experimentally to determine atomic and magnetic structures of materials, operating on the same principles as X-ray diffraction. A beam of neutrons emitted from a source (e.g., a nuclear fission reactor) can have their speed moderated by passing through a neutron absorbing material (e.g. graphite or heavy water). When moderated to appropriate speed the wavelength of the beam is comparable to the separation (and radii) of atoms in a crystalline lattice (~1-2 Å) and so the beam will be diffracted. The resultant diffraction pattern can be indexed (assigned Miller indices for each reflection) and then is related to the atomic (or magnetic) distribution by Fourier transform. In the present work the Powder Cell code is used to predict neutron diffraction patterns using the inverse process of applying a Fourier transform to the atomic coordinates [89]. This provides a simple visual comparison of experimental and computational crystal structures. Differences in neutron wavelength, incomplete publication of spectra and use of X-ray diffraction to determine structures can make comparing patterns from experiment and simulation difficult. Thus neutron diffraction patterns are calculated for the experimentally determined structures as well as the relaxed systems to permit straightforward comparison here.

2.4.4 Calculation of Reference Energies

For parts of this investigation of the uranium oxides it is necessary to calculate reference energies (or chemical potentials) for elemental uranium and oxygen. These include:

- Defect formation energies, which are calculated by subtracting the total energy for the pure bulk (E_{Tot}) from the total energy for the defective system (E_{Def}) and then subtracting the reference energies (E) for defective atoms. For example, for two oxygen interstitials (O_i) in UO_2 E_{Form} would be calculated as follows $E_{\mathrm{Form}} = E_{\mathrm{Def}} - E_{\mathrm{Tot}} - 2E_{\mathrm{O}}$. It should be noted that all defects are treated as charge neutral; meaning

E_{Form} represents formation of compensating electrons or holes as well as the vacant or interstitial ion.

- Formation energies for bulk materials, which are calculated by subtracting the uranium and oxygen reference energies in the correct ratio for the phase in question from the DFT calculated total energy. So for UO_2, $E_{Form} = E_{Tot} - E_U - 2E_O$

These reference energies can either be taken from experimental data or calculated *ab initio*. This section details how the two required quantities were calculated and compares the results with the experimental data.

Oxygen Gas

An O_2 molecule was placed at the centre of a 20 x 20 x 20 Å box and minimised with a 500 eV plane wave cut-off energy and a single Γ-centred k point using the PBE functional and the triplet state (electronic ground state). As O_2 is multiconfigurational (having a triplet and singlet state) there can be large differences in reported calculated energies (up to 2eV). Table 2.1 shows the predicted properties and compares them with experiment.

Table 2.1 – Calculated and observed properties of an O_2 molecule. The reference energy is calculated directly by VASP and the dissociation energy is the energy of an isolated oxygen atom minus the energy of a single atom in an oxygen molecule.

Property	Present Work		Geng [90]		Experiment
	Calculated (PBE)	Δ%	Calculated (PBE)	Δ%	
Bond length (Å)	1.23	1.9	1.22	0.8	1.21 [91]
Vibrational Frequency (cm^{-1})	1566.3	-0.9	1588.6	0.5	1580.2 [91]
Dissociation Energy (eV)	5.89	15.7	5.75	11.3	5.10 [92]
Reference Energy (E_O) (eV/O)	-4.93	-	-5.75	-	-

Good agreement is found between the calculated and observed physical properties, although the dissociation (or binding) energy is overestimated by 0.79 eV. The results also compare well with similar simulations from the literature for all properties [90]. The dissociation energy was found by calculating the energy of an isolated O atom in the centre of a 20 x 20 x 20 Å box and subtracting it from the O_2 molecule energy. Although this quantity has been calculated it has been decided to use the energy directly calculated in

VASP ($\frac{1}{2}E_{O_2}$) as the oxygen reference energy, a convention that will be maintained for uranium.

Uranium Metal

The four atom α-uranium [93] structure (*Cmcm*, shown in Figure 2.06) was used for this calculation with a plane wave energy cut-off of 500 eV using the PBE functional. A denser *k* point mesh (1.50 *k* points/Å^3) has been used than those for the oxides, as is typically necessary for metallic systems.

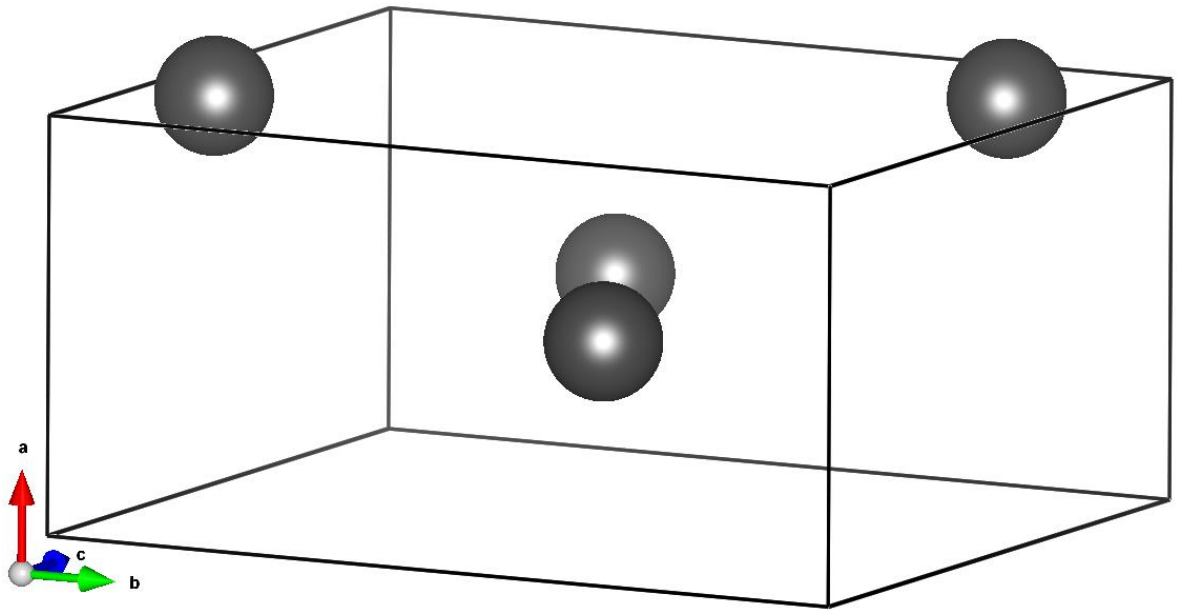

Figure 2.06 – *Cmcm* orthorhombic unit cell of α-uranium, uranium atoms shown as grey spheres.

Table 2.2 shows some of the predicted properties for PBE and PBE + U methodology and compares them with experiment. The effective Hubbard coefficient used (U_{eff}) is 3.96 eV, the value derived empirically from Kotani *et al*'s XPS experiments on UO_2 [64].

The three calculations in Table 2.2 show large differences in predicted lattice parameters and heats of formation depending on the presence of a magnetic moment or the use of a Hubbard coefficient. Although the non-magnetic systems (non-spin polarised calculations) show excellent structural agreement with experiment, the uranium oxides are magnetic systems and so it is necessary to include spin polarisation in the calculation of reference

energies. A Hubbard coefficient is necessary to reproduce the observed properties of UO_2 and so is included in the calculation of the reference energy for uranium. For these reasons the calculated reference energy (total energy from VASP per uranium ion) from the magnetic PBE + U calculation has been used as the uranium reference in this thesis. Although the properties are not as well reproduced as those of O_2 in the interest of applying consistent and fully *ab initio* methodology this calculated energy is used for the uranium reference energy. The most comparable study in the literature comes from Söderlind where lattice parameters of 2.845, 5.818 and 4.996 Å are reported [94] using the GGA (the functional and whether a Hubbard coefficient is used are not reported). No calculated energies are provided, however the calculated lattice parameters match well with the PBE and non-spin polarised PBE + U calculations here.

Table 2.2 – Calculated and observed properties of α-uranium metal.$^+$ = AFM ordering (μ_B = 2.2), * = no magnetism (μ_B = 0). The reference energy is calculated directly by VASP and the heat of formation is the energy of an isolated uranium atom minus the energy of a single atom in uranium metal.

Property		**PBE***	**Δ%**	**PBE + U***	**Δ%**	**PBE + U$^+$**	**Δ%**	**Experiment**
Lattice Parameters	*a* (Å)	2.7997	-1.3	2.9688	2.1	3.3798	19.1	2.8364 [93]
	b (Å)	5.8190	-0.8	5.9182	0.9	5.9988	2.3	5.8666
	c (Å)	4.9194	-0.3	5.1765	4.9	5.717	15.8	4.9363
Heat of Formation (eV)		-6.61	19.7	-6.67	20.8	-4.49	-18.6	-5.52 [129]
Reference Energy (E_U) (eV/U)		-11.15	-	-6.97	-	-8.43	-	-

2.5 Validation of the Models

It is important to establish that the model being used provides an accurate representation of the system of interest. One of the stated aims of this thesis is to apply a consistent simulation framework across the full set of uranium oxides. Consequently energy convergence criteria and plane wave cut-off energies must be the same and the *k* meshes close enough in density to provide good convergence for transferability between systems. Here, electronic relaxation is performed until the total energy is converged to at least 1 x 10^{-6} eV/ion and ionic relaxation until the residual Hellmann-Feynman forces on each ion are less than 0.01 eV/Å (with the exception of defect calculations). As previously stated, all

energy minimisations are at constant pressure and employ the same Hubbard coefficient on the uranium sites (U_{eff} = 3.96 eV) with the Dudarev implementation. The PBE functional is used for the bulk of the calculations in this thesis (including those presented here), although others using GGA, meta-GGA and hybrid functionals are included in section 3.1. An example set of input files for VASP (INCAR, KPOINTS and POSCAR) with annotation are included in Appendix A to provide the full computational details.

The following section details the choice of plane wave cut-off energies and *k* point grids for cubic UO_2 (12 atom cell), orthorhombic α-U_3O_8 (22 atom cell) and hexagonal α-UO_3 (4 atom cell). This demonstrates the transferability of a common set of criteria for U^{4+}, mixed U^{5+}/U^{6+} and U^{6+} systems; three different crystal symmetries and three different unit cell sizes.

2.5.1 Fluorite Cubic UO_2

Cubic UO_2 (*Fm3m a* = 5.4682) has a twelve atom unit cell and convergence has been tested over a range of *k* meshes (*3*x*3*x*3 – 10*x*10*x*10*) and plane wave cut-offs (300 – 700 eV), based on DFT studies of UO_2 in the literature [28, 90, 95-97]. The folding parameters (*N*x*N*x*N*) used to determine the *k* point grid depend on cell size and symmetry and so the *k* point density (*k* points/Å^3) has been used. Using *k*-point density rather than number ensures the results can be compared between the three different systems. Figure 2.07 displays plots of *k* point density against energy for each plane wave cut-off for UO_2.

It is clear that 300 eV is too low a cut-off energy, however the calculations converge well by 400 eV, with less than 0.02 eV spread between all of the results. The lowest *k* mesh density used (0.04 *k* points/Å^3) is consistently slightly higher in energy than the rest but convergence seems to have been reached by 0.11 *k* points/Å^3. The cell volume shows almost no change when the *k* mesh is varied but is affected by plane wave cut-off energy. Excellent convergence is achieved by 500 eV (0.02 Å^3/U atom difference between 500 and 700 eV) and good convergence is found at 400 eV (approximately 1 Å^3/U atom discrepancy with 500 – 700 eV).

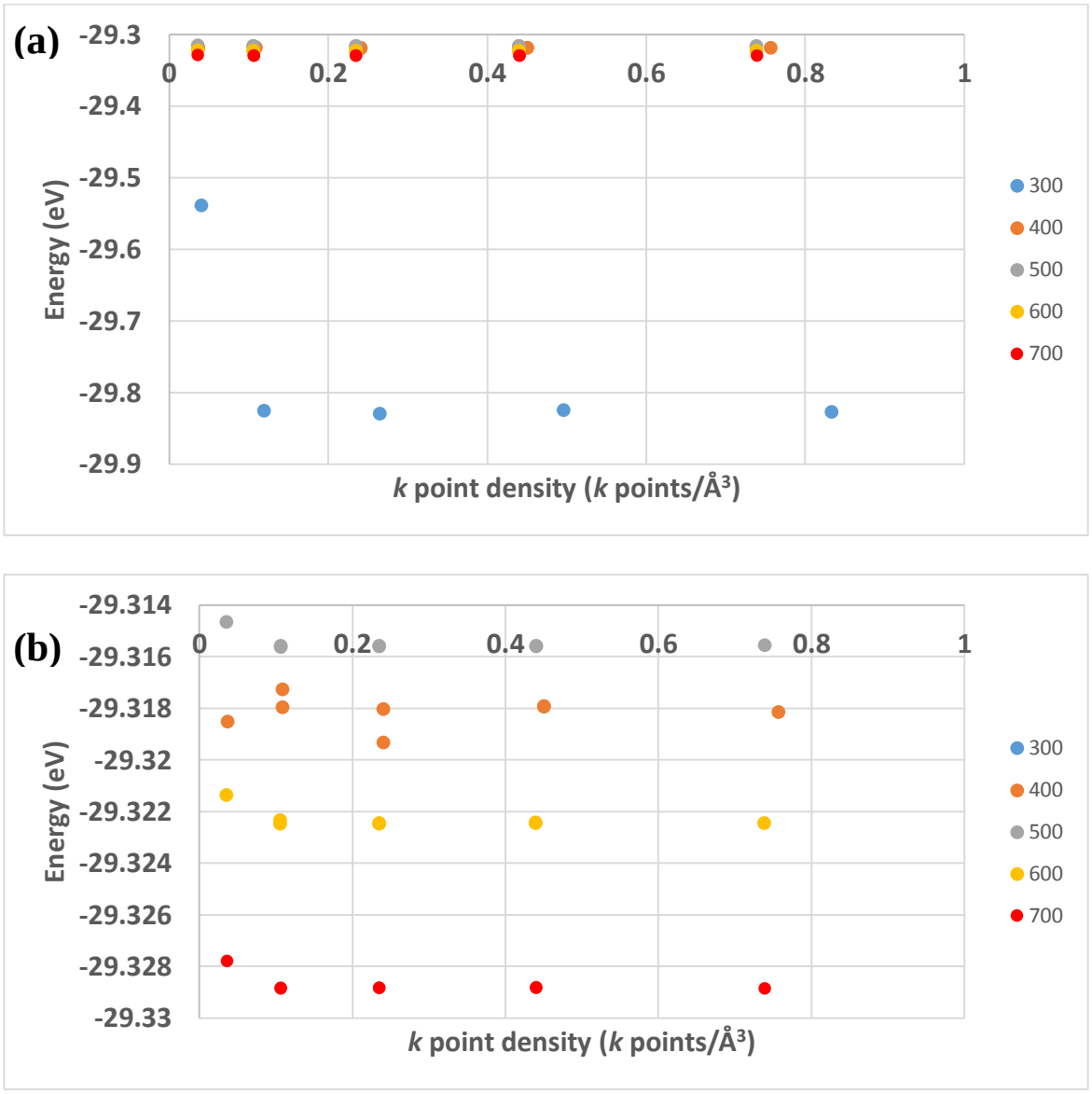

Figure 2.07 - Convergence plots for UO_2. *k* point density (*k* points/Å^3) is shown on the *x*-axis and energy per uranium ion (eV) is shown on the *y*-axis. (a) shows the full range tested, (b) is focused on the converged area.

2.5.2 Layered Orthorhombic α-U_3O_8

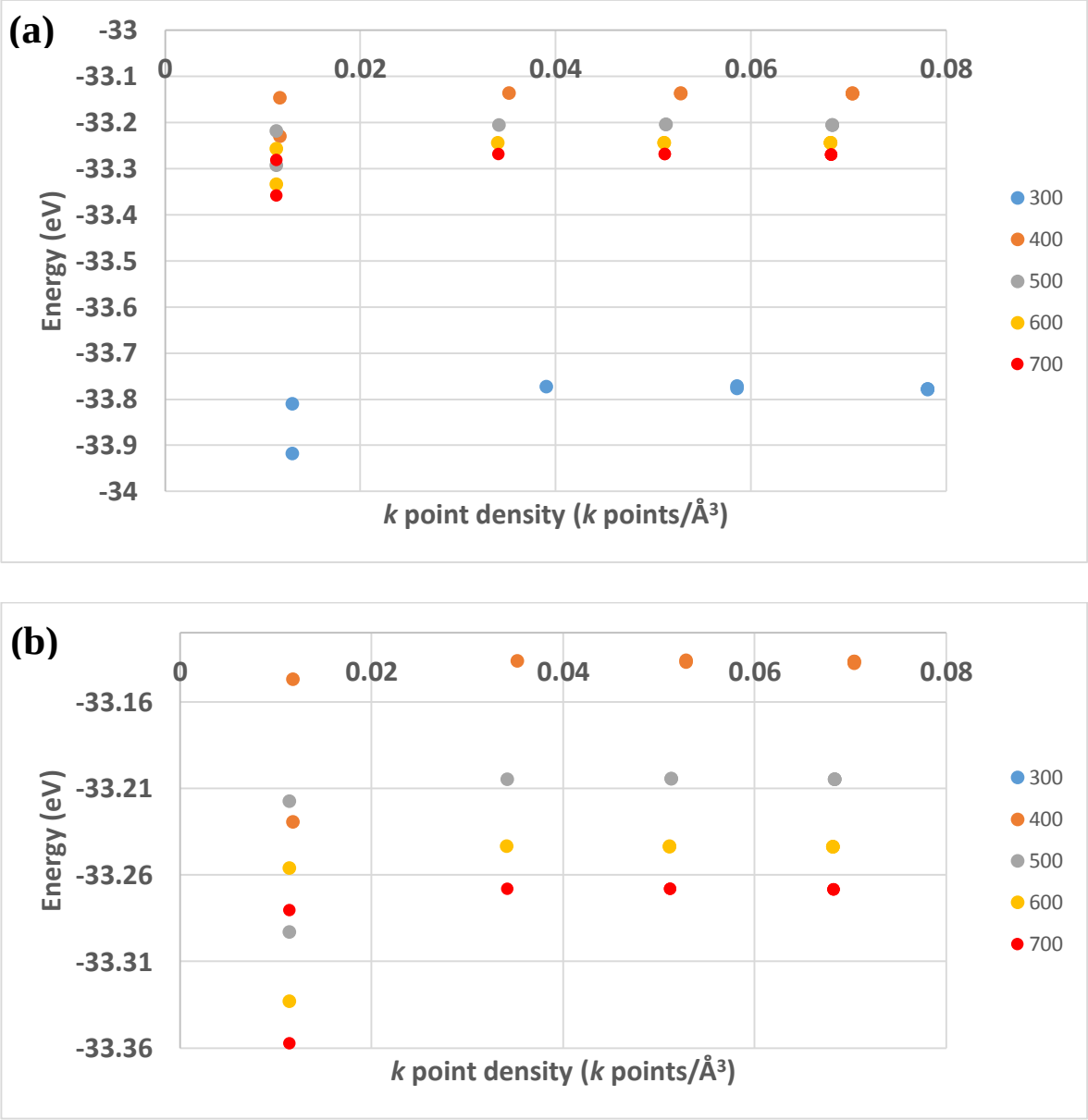

Figure 2.08 - Convergence plots for α-U_3O_8. *k* point density (*k* points/Å^3) is shown on the *x*-axis and energy per uranium ion (eV) is shown on the *y*-axis. (a) shows the full range tested, (b) is focused on the converged area.

Orthorhombic α-U_3O_8 has a 22 atom unit cell, convergence has been tested over the same range of cut-off energies as UO_2 The orthorhombic symmetry of this oxide means that different folding parameters must be used for each direction. As the folding parameters

distribute the *k* points in reciprocal space, smaller folding parameters are required for larger lattice vectors and vice versa. Figure 2.08 shows the convergence plots for α-U_3O_8.

As with UO_2, the 300 eV is too low a cut-off and the calculations are well converged above 400 eV, although best convergence is seen from 500 eV and up. A *k* mesh of 0.035 *k* points/Å^3 was the minimum density required to achieve convergence. The same is observed for the unit cell volume; where best convergence is seen above 500 eV (0.16 Å^3/U atom difference between 500 and 700 eV) but good convergence is still found from 400 eV (approximately 1.7 Å^3/U atom discrepancy with 500 – 700 eV). As with UO_2 *k* mesh density is found to have very little effect on the cell volume.

2.5.3 Hexagonal α-UO_3

Hexagonal α-UO_3 has a four atom unit cell, convergence has been tested over the same range of cut-off energies and *k* grid densities as UO_2. As $|a|=|b|$ in a hexagonal lattice, and in this case *c* is relatively close to *a* and *b*, the same folding parameters are used for each lattice vector in the α-UO_3 convergence calculations. Figure 2.09 shows the convergence plots for α-UO_3.

A 300 eV cut-off is definitely too low for α-UO_3 but good convergence is found from 500 eV and above. Again at 400 eV the results are converged but not as well converged as the higher cut-offs The two lowest density *k* meshes used have not converged, however from the third onwards (>0.73 *k* points/Å^3) good convergence is achieved. Once again *k* grid density has very little effect on the unit cell volume but cut-off energy does. The same trend of no convergence at 300 eV, convergence at 400 eV (approximately 1 Å^3/U atom discrepancy with 500 – 700 eV) and better convergence at 500 eV and above (0.07 Å^3/U atom difference between 500 and 700 eV) is found.

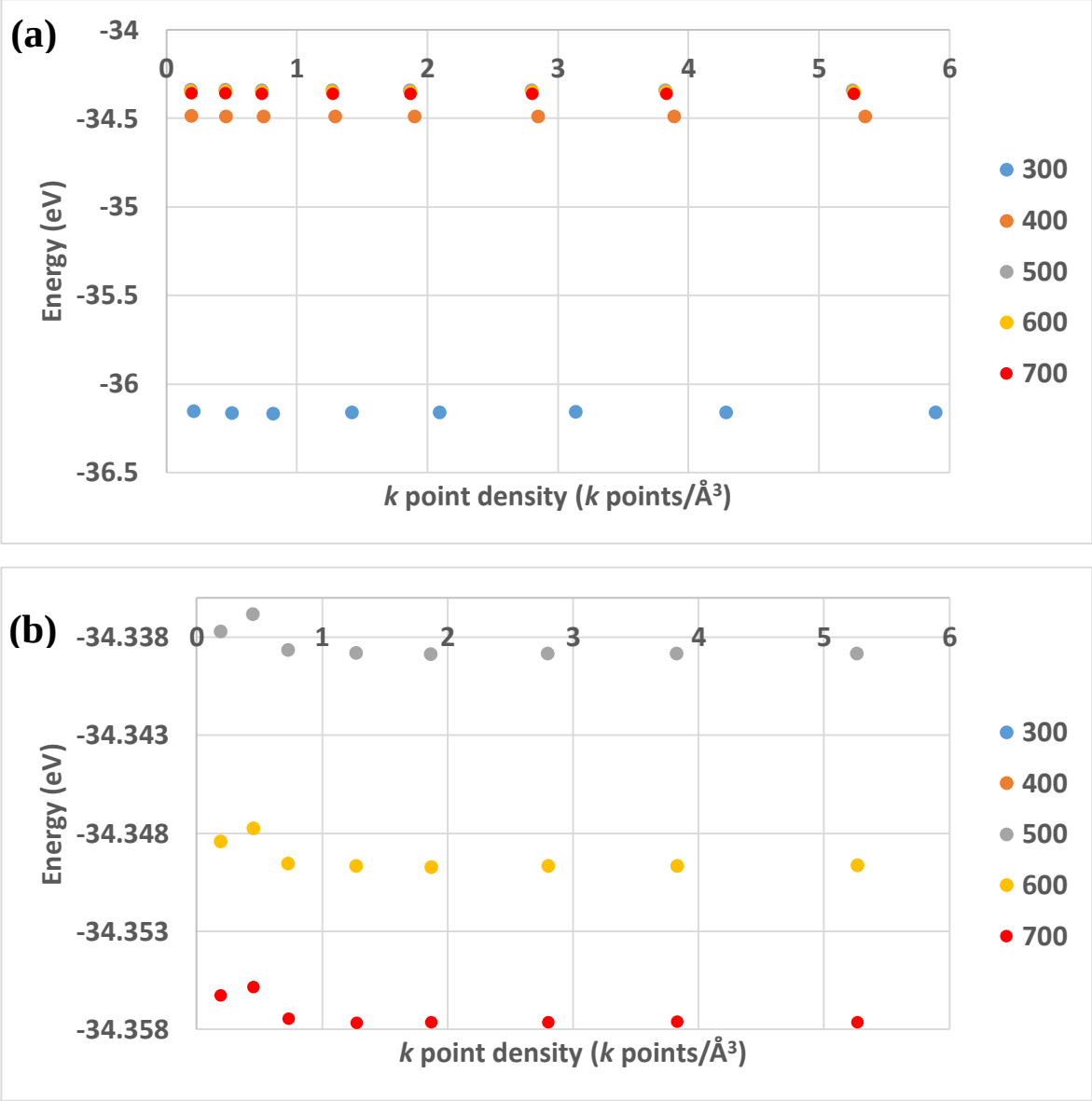

Figure 2.09 – Convergence plots for α-UO_3. *k* point density (*k* points/Å^3) is shown on the *x*-axis and energy per uranium ion (eV) is shown on the *y*-axis. (a) shows the full range tested, (b) is focused on the converged area.

2.5.4 Selection of Criteria

Based on these three systems a plane wave cut-off energy of 500 eV has been selected for all calculations and a *k* grid density of at least 0.04 *k* points/Å^3 for a large cell and 0.73 *k* points/Å^3 for a small cell. In all simulations the cells and ions were fully relaxed. These conditions showed excellent convergence for the cell energies and volumes.

Some of the oxides encountered in Chapters 5, 6 and 7 have very large unit cells (64 -128 atoms), which would require an enormous number of *k* points to reach this minimum specified density. However, as the *k* points are distributed in reciprocal space these oxides have a smaller reciprocal cell, meaning they can be modelled with fewer *k* points to achieve comparable results. For these materials (δ-U_2O_5, β-U_3O_8, and γ-UO_3) different *k* meshes have been trialled to identify the appropriate grid density (with all falling into the 0.04 – 0.73 *k* points/Å^3 range).

A number of calculations on defective systems are also presented (section 3.6 and Chapter 4) in the results. Due to the increased computational expense associated with the lattice distortion and lowered symmetry introduced by defects these phases have been simulated at lower plane wave energy cut offs (400 eV). Similar defect calculations in the literature [90, 98] use a 400eV cut-off and in section 2.5.3 it was identified to provide satisfactory convergence. The formation energy (E_{Form}) is the most important energetic quantity in these calculations, which is the relative energy with respect to the perfect (i.e. non-defective) system. Thus for these calculations the perfect reference system must be simulated using precisely the same criteria and so is also calculated using the lower plane wave cut-off energy (400 eV).

Now that transferable calculation parameters have been established it is necessary to assess how suitable they are for simulating uranium oxides, and the following chapter will deal with this. UO_2 is the most studied oxide both experimentally and computationally and so is the perfect system to gauge the effectiveness of the chosen methodology.

2.6 DFT Software and Calculation Details

As described throughout this chapter, all of the simulations presented here use DFT code VASP [70]. VASP is written using Fortran and, in addition to the energy minimisation calculations presented here, offers a considerable range of alternative functionality (e.g. *ab initio* molecular dynamics, GW calculations etc.). Appendix A contains example INCAR, POSCAR and KPOINTS input files for a twelve atom UO_2 calculation. The POSCAR file contains the lattice geometry and ionic positions and the KPOINTS file contains the *k* point coordinates and weights or mesh size for creating the grid. The INCAR is the central input

file for VASP, containing all of the information on the type of calculation and how to perform it, e.g. the type of minimisation algorithm or functional to use. All presented simulations were performed using the most recent (at the time of writing) version of VASP (5.3.5).

The calculations were all carried out using the UK national high performance computing service (ARCHER), with some earlier work being conducted on its predecessor (HECToR). The service is provided by UoE HPCx Ltd, Cray Inc and NAG Ltd at the University of Edinburgh. Access to the facility was provided via our membership of the UK's HPC Materials Chemistry Consortium, which is funded by EPSRC (EP/F067496 and EP/L000202). Test calculations were also carried out on the University of Bath's Aquila HPC facility.

To fully utilise multi-core architecture of the available HPC platforms and achieve the best efficiency parallelisation techniques have been employed. These include parallelisation and date distribution over bands (NPAR) and parallelisation over *k*-points (KPAR). NPAR is typically set to approximately $\sqrt{number\ of\ cores}$, with the best results varying slightly between systems. For KPAR the greatest efficiency is generally found for the highest available values, i.e. the smallest number of *k*-points possible assigned to each group of cores.

Chapter 3

3 Fluorite UO_2

UO_2 is the most studied uranium oxide, with a considerable amount of experimental data in the literature, and thus is an ideal system to apply the chosen methodology and evaluate the performance of different functionals to identify the most suitable one for simulating the rest of the uranium oxides. Thus this chapter aims to compare the various functionals with experimental data. However, before discussing the results the relevant previous work will be reviewed.

3.1 UO_2 Background

UO_2 is by far the best characterised of the uranium oxides, with many experimental studies of its structural [20, 21, 31, 99-102], elastic [22, 103-105], vibrational [23, 106-109], magnetic [24, 71, 108, 110, 111] and electronic [25, 112-114] properties as well as defect chemistry [26, 29, 115, 116]. There are also a large variety of computational investigations using both potential based [27, 117-121] and *ab initio* techniques [28, 95, 97, 122-125]. UO_2 maintains the cubic fluorite structure (10.97 gcm^{-3}, *Fm3m*, $a=b=c$=5.4682 Å [99]) (Figure 3.01(a)) over the entire temperature range up to its melting point of 3125 K. It is described in terms of a twelve atom unit cell containing four uranium atoms in face centred cubic positions and eight oxygen atoms, filling the tetrahedral sites. It exhibits a phase transition at high pressure to an orthorhombic cotunnite structure (11.46 gcm^{-3}, *Pnma* a=7.62, b=4.53 and c=9.05 Å) (Figure 3.01(b)) that early measurements reported to occur over the 29 – 38 GPa range [126]. More recent experiments suggest a range of 40 – 69 GPa [20], while computational work predicts a transition at ~17 GPa for stoichiometric UO_2 and ~27 for $UO_{2.03}$, suggesting the experimental samples may have been hyperstoichiometric [127]. The focus of the work described in this chapter is on the fluorite structure (hereafter

referred to simply as UO_2) as the cotunnite polymorph is not observed under normal nuclear fuel cycle conditions.

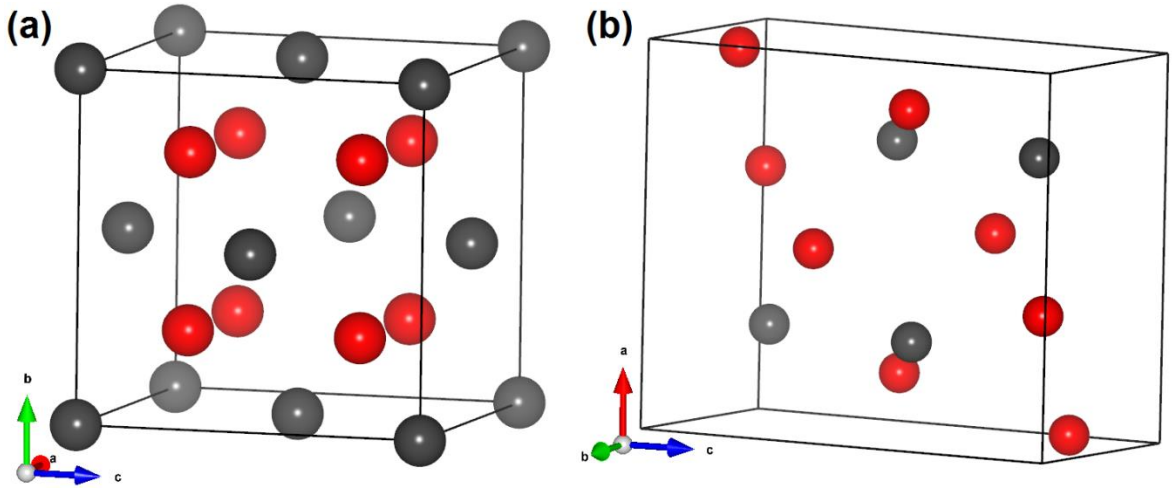

Figure 3.01 – *Fm3m* fluorite (a) and *Pnma* cotunnite (b) structures of UO_2. Uranium atoms shown as grey spheres, oxygen shown as red.

3.2 Structure and Stability

A number of different functionals have been used to simulate the twelve atom UO_2 unit cell. The predicted lattice parameters are presented in Table 3.01 along with data from experimental and computational work in the literature. All of the calculations use either ferromagnetic (FM) or simple antiferromagnetic (AFM) ordering aligned in the <010> (*b*) direction, however the effects of magnetism are explored in more depth in section 3.3.

Of the GGA formulations used, PBEsol + U predicts lattice parameters closest in line with experiments. The rTPSS meta-GGA improves on this result, which is subsequently improved slightly by the PBE0 and HSE hybrid functionals. This order is expected, given the increasingly sophisticated level of theory associated with each calculation and generally acknowledged superior performance of meta-GGAs and hybrids. The predicted lattice parameters also compare very favourably with those of Gryaznov [95] and Prodan [125].

Table 3.01 – Experimentally and computationally determined lattice parameters for UO_2. AFM and FM refer to antiferromagnetism and ferromagnetism. Calculation time refers to the full structural minimisation. Energy is presented as formation energy per uranium ion[+].

Author	Method	Lattice Parameter (Å)				E_{Form} (eV)	Magnetic Order	Calculation Time (s)
		a	Δ%	*b* = *c*	Δ%			
Desgranges [31]	neutron diffraction[‡]	5.468	-	5.468	-	-11.25 [129]	AFM	-
This Work	PBE + U	5.503	0.64	5.568	1.83	-11.03	AFM	780
	PBE + U	5.535	1.23	5.535	1.23	-10.00	FM	481
	PBE	5.423	-0.83	5.410	-1.07	-12.62	AFM	793
	PBEsol + U	5.446	-0.40	5.505	0.68	-10.62	AFM	798
	rTPSS	5.477	0.16	5.546	1.40	-	AFM	1987
	PBE0*	5.450	-0.33	5.450	-0.33	-	FM	19534
	HSE*	5.443	-0.46	5.443	-0.46	-	FM	22863
Gryaznov [95]	LSDA + U	5.418	-0.92	5.463	-0.10	-	AFM	-
	PW91 + U	5.511	0.78	5.562	1.72	-	AFM	-
	PBE + U	5.512	0.80	5.562	1.81	-	AFM	-
Prodan [128]	PBE0[#]	5.454	-0.26	5.454	-0.26	-	AFM	-
	HSE[#]	5.463	-0.10	5.463	-0.10	-	AFM	-

[‡] - neutron diffraction experiments were conducted at 293 K

* - three atom primitive cell was used due to high computational expense and so FM magnetism was used, resulting in no tetragonal distortion.

[#] - six atom unit cell was used.

[+] - $E_{\text{Form}} = E_{UO_2} - E_U - E_{O_2}$ (see section 2.4.4)

A notable artefact of the calculations is the tetragonal distortion observed in all of the AFM cells. This arises from the stacking of uranium layers with opposing magnetic moments that cause a weak attraction leading to a slight contraction of the lattice along the magnetisation axis (<010> (*b*) in this case). The phenomenon disappears in an FM calculation, where all magnetic moments align in the same direction. Prodan *et al* do not report this distortion, although they used a six atom unit cell (a 2 x 1 x 1 expansion of the primitive three atom cell) that is tetragonal in symmetry to begin with.

The additional computational expense associated with higher levels of theory is clearly apparent from Table 3.01. All GGA calculations are relatively inexpensive to run, requiring under 800 seconds to minimise. This number is doubled going to the rTPSS meta-GGA, which is still manageable but rTPSS does not compute accurate energies and so is unfortunately unsuitable. Hybrid functionals are significantly more expensive, requiring around 20 times longer to converge than GGA calculations, and that is in the three atom primitive cell with FM ordering. Thus hybrids are not viable for performing the calculations in this work as some uranium oxides have in excess of 100 atoms in their unit cells.

Although PBEsol + U predicts lattice parameters closer to experiment for UO_2, PBE + U gives the best predicted formation energy (E_{Form}) compared to experiment. PBE (with no Hubbard coefficient) overestimates E_{Form} by almost 1.5 eV, FM PBE + U underestimates by 0.22 eV and PBEsol + U underestimates by 0.63 eV. In addition, the PBE calculation results in two negative vibrational modes, as well as very high translational frequencies. As these could not be removed with small atomic displacements they indicate that the structure is unstable with this methodology. The PBE + U and PBEsol + U both have their strengths but on balance the PBE + U has been selected as the functional of choice, primarily due to its predicted E_{Form} being closest to experiment [129]. As relative stabilities of all uranium oxides treated in this thesis are to be considered it is important to accurately capture the energetics of UO_2.

The 1.83 % overestimation of the lattice parameters may be larger than in the other calculations but it is still a very good overall structural representation. This is illustrated in Figure 3.02, which shows the neutron diffraction patterns for the PBE + U predicted and experimental UO_2 structures. The peaks from the simulated structure are shifted to slightly

lower 2θ, indicative of slight overestimation of lattice parameters that becomes more apparent with increasing 2θ. The other functionals will continue to be presented for the remainder of this chapter to demonstrate their capabilities at predicting other properties.

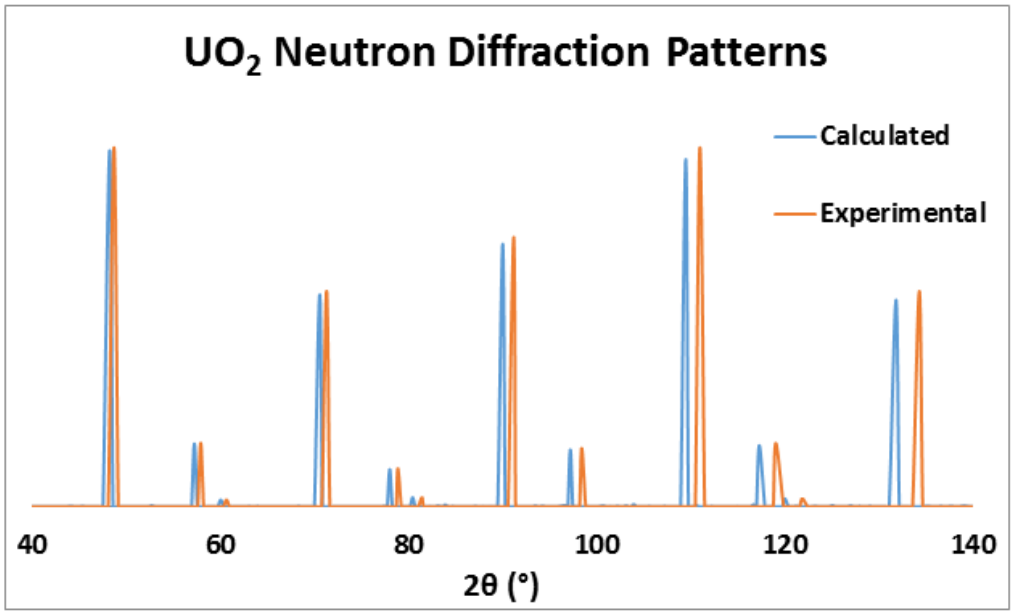

Figure 3.02 – Predicted and experimental [31] UO_2 neutron diffraction patterns.

3.3 Non-collinear Magnetism and Spin-orbit Coupling

The PBE + U model of UO_2 established in section 3.2 gave a good structural and energetic description of the system. This employed a 1*k* (i.e. one dimensional) collinear (CL) AFM magnetic ordering (Figure 3.03), however the real magnetic structure differs from this and has been the subject of much investigation over the years. In the late 60s Allen reported a 1*k* CL magnetic structure (with accompanying one dimensional Jahn-Teller (J-T) distortion of the oxygen sub-lattice) [111]. This paved the way for the proposal of non-collinear (NCL) magnetic orderings in UO_2. In a CL magnetic structure all magnetic moments align in a particular direction (magnetisation axis) whereas in NCL systems there is greater freedom of alignment, in either two or three dimensions, illustrated by Figure 3.03.

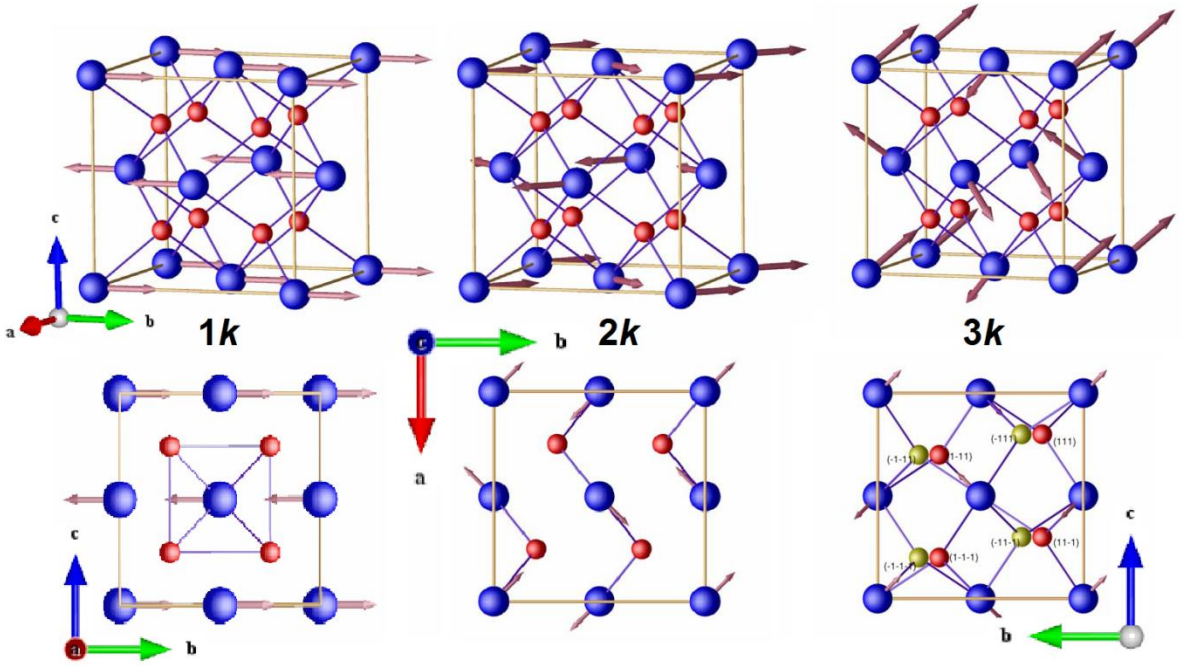

Figure 3.03 – 1*k* collinear and 2*k* and 3*k* non-collinear magnetic orderings in fluorite UO_2 [130]. The lower diagrams illustrate the 1D, 2D and 3D oxygen sublattice distortions associated with each structure. Uranium ions in blue and oxygen in red.

The magnetic ground state was later revised to NCL 2*k* [110] and subsequently 3*k* with three dimensional (3D) J-T distortion of the oxygen sublattice and magnetic moment of 1.74 μ_B [24, 101, 131]. In the 2*k* and 3*k* structures, magnetic moments align in <110> directions and <111> directions respectively. The J-T distortion is small, only 0.014 Å, however as the calculations show, this is significant enough to affect the stability relative to other magnetic orderings and sublattice distortions. Above 30.8 K UO_2 is reported to display paramagnetism [21, 71, 132], although as the methodology applied here is limited to 0 K paramagnetism in UO_2 has not been considered. DFT simulations involving paramagnetism in UO_2 have begun to emerge recently [133], employing a model for paramagnetism known as disordered local moments that involves randomly orientated magnetic moments (not dissimilar from the NCL method used here) [134].

Spin-orbit coupling (SOC) describes the interaction between an electron's spin and the magnetic field it generates by orbiting the nucleus. In many systems SOC effects are negligible, however they typically become more important with the presence of heavier (*d*- and *f*-element) nuclei as the magnetic field is stronger and so larger interactions are generated. Therefore it is important to establish the influence of SOC in UO_2. In VASP,

SOC is applied automatically with NCL magnetism and is included in all the NCL calculations presented in Table 3.02.

Table 3.02 – Comparison of different magnetic structures in UO_2 calculated using PBE + U. The total uranium magnetic moment is given in each case, calculated from a single component in 1*k*, two components in 2*k* and three components in 3*k* ordering. The distortion type refers to the number of dimensions the oxygen sublattice is distorted in. Energy is given per uranium atom relative to the CL AFM structure discussed in section 3.1.

Distortion Type	Magnetic Structure	Lattice Parameter (Å)				μ_B	Energy (eV)
		a	**Δ%**	***b* = *c***	**Δ%**		
3D	3*k*	5.468	-	5.468	-	1.74	-
None	CL AFM	5.503	0.64	5.568	1.83	1.99	0.000
	1*k*	5.545	1.41	5.547	1.44	1.56	-3.112
	2*k*	5.548	1.47	5.547	1.44	1.54	-3.116
	3*k*	5.546	1.42	5.546	1.42	1.54	-3.113
1D	1*k*	5.542	1.34	5.549	1.47	1.56	-3.112
	2*k*	5.553	1.55	5.543	1.38	1.54	-3.116
	3*k*	5.547	1.44	5.546	1.43	1.54	-3.117
2D	1*k*	5.543	1.37	5.550	1.49	1.56	-3.116
	2*k*	5.551	1.51	5.545	1.40	1.54	-3.116
	3*k*	5.546	1.42	5.547	1.43	1.54	-3.113
3D	1*k*	5.543	1.37	5.550	1.50	1.56	-3.116
	2*k*	5.553	1.55	5.544	1.38	1.54	-3.116
	3*k*	5.546	1.43	5.546	1.43	1.54	-3.117

The first major observation from the results is the significantly reduced magnetic moments in the NCL calculations compared to CL. This reportedly arises from the inclusion of SOC rather than NCL magnetism, as the interaction between spin and orbital moments serves to dampen the overall magnetic moment [122], reducing it to around 1.55 μ_B. This is an underestimate compared to the experimental value (1.74 μ_B), although not quite as significant as the overestimate of CL calculations.

It was established in section 3.2 that a CL AFM ordering produces a tetragonal distortion of the lattice along the magnetisation axis. The NCL calculation results give a more detailed impression of the effects of magnetism on unit cell distortions. All calculations feature reduced tetragonal distortions compared to the CL case, however the effect is clearly greatest for the 3*k* magnetic orderings. In two of these simulations, those with no and 3D sublattice distortions, there is no distortion of the unit cell at all and in the other two calculations (1D and 2D oxygen sublattice distortions) tetragonal distortion is only by 0.001 Å. This behaviour originates from the spatial orientation of the magnetic moments

and magnetisation axes in the various structures. In the 3*k* magnetic orderings there is no overall magnetisation component in *x*, *y* or z directions, the moments align along <111> directions, and so have equal contributions in each direction. The small deviations from cubic in the 1D and 2D oxygen distortion calculations with 3*k* ordering most likely arise from the small change in symmetry introduced by shifting the oxygen atoms in <100> or <110> directions. There is no such change when there is no sublattice distortion present or indeed with a 3D sublattice distortion with <111> displaced oxygen ions and consequently no distortion is found. Looking at the 1*k* and 2*k* magnetic orderings the smallest tetragonal distortions are found when there is no or a 3D oxygen sublattice distortion (as with the 3*k* ordering) and the largest are observed for a 2D sublattice distortion.

All of the NCL calculations show a significant stabilization (approximately 3 eV/U) compared to the CL AFM system. The variation in energy between the different magnetic structures though is very small, only 0.005 eV, indicating that most of the stabilisation arises from the inclusion of SOC rather than NCL magnetism or J-T distortions. The two most stable arrangements are 3*k* magnetic ordering with 1D and 3D oxygen sublattice distortions; 1*k* magnetic structures are generally least stable although with a 2D oxygen distortion 3*k* magnetic ordering becomes least stable.

The NCL calculations took an average of 8500 seconds to converge, around ten times longer than a CL PBE + U calculation. Although this is acceptable for a twelve atom UO_2 unit cell it will not scale well with the larger unit cells of some of the higher uranium oxides (128 atoms for γ-UO_3). Taking into account the tiny energy variations between competing magnetic structures and the fact that SOC shifts the energy by a constant amount in UO_2 (-3.1 eV/U) it has been decided that SOC will be excluded from the remainder of the calculations to allow consistent methodology to be applied to all of the oxides under investigation. However, other properties from the NCL simulations with the lowest energy will be discussed in this chapter to provide more detail.

3.4 Elastic Properties

As (experimentally at least) UO_2 is a high symmetry cubic structure there are only three unique elastic constants (C_{11}, C_{12} and C_{44}), which are well established, with numerous

experimental studies over the years. Table 3.03 summarises experimental and computational data from the literature as well as this thesis. Details of calculations of the bulk modulus can be found in section 2.4.1.

Table 3.03 – Predicted and measured elastic constants and bulk modulus of UO_2 from the literature and present work. All theoretical work uses a CL AFM magnetic structure and only the independent elastic constants for a cubic unit cell are included.

	Author	Method	Elastic Constants (GPa)			B (GPa)	Δ%
			C_{11}	C_{12}	C_{44}		
Exp.	**Fritz [22]**	Ultrasonic pulse-superposition	389.3	118.7	59.7	208.9	-
	Clausen [105]	Inelastic neutron scattering	395.0	120.0	63.0	212.0	-
	Brandt [104]	Ultrasonic attenuation	396.0	121.0	64.0	213.0	-
Calc.	**Gryaznov [95]**	LSDA + U	-	-	-	196.0	-7.24
		PW91 + U	-	-	-	183.0	-13.39
		PBE + U	-	-	-	180.0	-14.81
	Dorado [135]	PBE + U	382.0	130.0	54.0	214.0	1.28
	Devey [28]	PW91 + U	361.2	114.7	63.9	197.0	-6.77
	Prodan [128]	PBE0	-	-	-	219.0	3.64
		HSE	-	-	-	218.0	3.17
	This Work	PBE + U	409.1	118.1	62.0	215.1	1.80
		PBEsol + U	340.8	149.3	103.5	213.1	0.85
		PBE	377.6	114.8	70.0	202.4	4.21
		rTPSS	389.7	119.4	68.8	209.5	-0.85

Different experimental methods have been used to measure the elastic constants of UO_2 and show good agreement with each other. The DFT calculations also generally show good agreement with experiment, with the best performance found for the rTPSS (-0.85 %) functional. The PBE + U also performed very well in the calculations from this work (+1.80 %) and Dorado *et al* [135] (+1.28 %). Gryaznov *et al* [95] underestimate the bulk modulus by around 7 – 14 %, particularly in the GGA calculations, in contrast to the others. They used a slightly larger effective Hubbard U parameter of 4.1 eV and calculated the bulk modulus via fitting to a Birch-Murnaghan equation of state. The PW91 functional employed by Devey also leads to an underestimation of the bulk modulus (-6.77 %), arising from an underestimation of C_{11} [28]. In this study an effective Hubbard U parameter of 4 eV was employed and the bulk modulus also calculated via fitting to a Birch-Murnaghan equation of state.

The dependence of the bulk modulus on C_{11} and C_{12} means that inaccuracies in the individual elastic constants can lead to a misleadingly accurate bulk modulus. The best example of this is in the PBEsol + U calculation, where C_{11} is underestimated (-13.38 %) and C_{12} is overestimated (24.52 %), by half as much as C_{11}, and so a false accurate result is

found for the bulk modulus (+0.85 %) (due to the 2:1 ratio described in Equation 2.38). So it is apparent that, without the individual elastic constants, it is difficult to comment on the accuracy of a theoretical result for the bulk modulus. In contrast, the PBE + U calculated bulk modulus from this work is very close to the equivalent calculation in the literature and gives a good representation of the individual elastic constants compared to experiments and other calculations.

3.5 Electronic Properties

A further important concern is the calculation of density of states (DOS) and band gap of UO_2, which are both well characterised experimentally. Baer and Schoenes used XPS and Bremsstrahlung isochromat spectroscopy (BIS) measurements to determine an electronic band gap of 2.17 eV [25]. This value has subsequently been confirmed and UO_2 has been identified as a Mott-Hubbard insulator, i.e. the valence and conductance bands are both composed of uranium states (in this case 5*f*) [112]. Table 3.04 shows the predicted band gap using a number of functionals and Figure 3.04 shows the PBE + U predicted DOS for CL AFM UO_2.

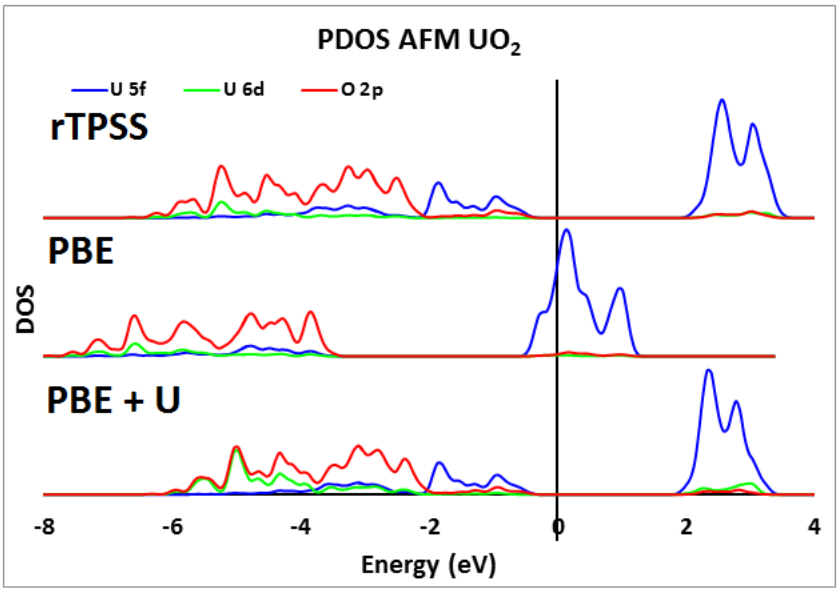

Figure 3.04 – Predicted DOS for AFM UO_2, only states that make significant contributions have been included. The spin down channel has been omitted from this diagram as it is identical to the spin up channel. The energy of the highest occupied state was set to zero eV (i.e. $E = E - E_f$).

Inspection of Table 3.04 reveals that an AFM structure is required in order to effectively reproduce the experimentally determined band gap (-10.60 %). Including SOC and NCL magnetism improves the predicted band gap (-2.30 %) but oxygen sublattice distortions do not affect it. The FM HSE result from this work is close to experiment (+1.38 %) because the amount of HF exchange (40 %) was tuned to best reproduce the structure and band gap. Accurate band gap prediction also requires at least the GGA level of theory, demonstrated by the LSDA result of Gryaznov [95] which underestimates it by 19.35 %. GGA and meta-GGA calculations reproduce the band gap most effectively overall (rTPSS result is equal to experiment), although the HF mixing ratio in the HSE functional can be varied to improve the electronic description.

Table 3.04 – Calculated and experimentally determined band gaps of UO_2. All theoretical values are for twelve atom CL AFM systems unless otherwise specified.

	Author	Method	Band Gap (eV)
Experimental	**Baer [25]**	XPS/BIS	2.17
	Yu [112]	X-ray Absorption Spectroscopy	2.10
Theoretical	**Gryaznov [95]**	LSDA + U	1.75
		PW91 + U	1.94
		PBE + U	1.94
	Dorado [135]	PBE + U	2.10
	Devey [28]	PW91 + U	2.80
	Prodan [128]	PBE0	3.13
		HSE	2.39
	This Work	PBE + U	1.94
		PBE + U (FM)	0.92
		PBE + U (NCL 1*k*)	2.19
		PBE + U (NCL 2*k*)	2.25
		PBE + U (NCL 3*k*)	2.12
		PBE	2.74
		PBEsol + U	1.81
		rTPSS	2.17
		PBE0 (three atom FM cell)	1.32
		HSE (three atom FM cell)	2.20

Only AFM orders have been included in Figure 3.04 as in FM arrangements the spin up and spin down channels differ significantly and the overall electronic structure is poorly represented. The *f-f* Mott-Hubbard insulating behaviour is well reproduced in both the PBE + U and rTPSS calculations, however the PBE (with no Hubbard coefficient) predicts the top of the valence band to be composed of O 2*p* states and the Fermi level to be in the middle of the conduction band. All calculations predict relatively minor contributions from U 6*d* states to the conduction band, although they are more significant to the lower valence

band, particularly in the rTPSS calculation. Although the rTPSS band gap is more accurate than the PBE + U, the predicted electronic structures are extremely similar so it is not necessary to use meta-GGAs to analyse electronic properties.

3.6 Isolated Point Defect Clusters

In an oxygen rich atmosphere oxygen is readily transferred from the ambient gas phase into the UO_2 lattice. This process leads to the creation of intrinsic point defects in the form of oxygen interstitials during reactor operation and long term fuel storage [30]. In this section four basic types of point defect are considered: oxygen interstitial (O_i), oxygen vacancy (V_O), uranium interstitial (U_i) and uranium vacancy (V_U); the interstitial ions are placed at the centre of oxygen sublattice cubes (known as the octahedral site due to the arrangement of six uranium ions around it). There are a variety defects not considered here, notably divacancies, trivacancies and clusters. The main interest here is oxidation of UO_2, as this is the major process associated with the material in the nuclear fuel cycle and so although hypostoichiometric UO_2 is beyond the scope of the present work, V_O and U_i are also simulated. Conversely O_i defect clusters are an integral part of the oxidation process and are discussed extensively in Chapter 4. All point defects are modelled as charge neutral clusters, that is to say the simulation cell has no net charge, and so charge compensation occurs via oxidation or reduction of the uranium ions. This is in contrast to the potential models presented for comparison which use the Mott-Littleton approximation to simulate a larger region centred on the defect [136]. Thus in the potential models the defects are essentially at infinite dilution whilst in the quantum mechanical supercell calculations there is a significant change in stoichiometry associated with the introduction of defects. Therefore the different types of point defect, as considered in this work, are expected to form according to Equations 3.01-3.04.

$$\frac{1}{2}O_{2(g)} + 2U_U^x \xrightarrow{UO_2} O_i'' + 2U_U^{\cdot} \qquad \textbf{Equation 3.01}$$

$$2U_U^x + O_O^x \xrightarrow{UO_2} V_O^{\cdot\cdot} + 2U_U' + \frac{1}{2}O_{2(g)} \qquad \textbf{Equation 3.02}$$

$$U_{(s)} + 4U_U^x \xrightarrow{UO_2} U_i^{\cdot\cdot\cdot\cdot} + 4U_U' \qquad \textbf{Equation 3.03}$$

$$5U_U^x \xrightarrow{UO_2} V_U'''' + 4U_U^{\cdot} + U_{(s)} \qquad \textbf{Equation 3.04}$$

Computational results from the literature show that O_i are the most energetically favourable point defects, the only type with a negative formation energy [8, 90, 137, 138, 120, 147] (Table 3.05). Point defects are considerably harder to study experimentally, the leading study in this area comes from Matzke, who used diffusion experiments to determine formation energies for Frenkel pairs and Schottky defects in UO_2, finding O Frenkel to be most favourable [139].

Schottky and Frenkel defects are comprised of a number of individual point defects and provide a convenient means of comparing defect properties between theory and experiment. Equations 3.05 (O Frenkel pair), 3.06 (U Frenkel pair) and 3.07 (Schottky) describe their formation.

$$O_O^x \xrightarrow{UO_2} V_O^{\cdot\cdot} + O_i'' \qquad \textbf{Equation 3.05}$$

$$U_U^x \xrightarrow{UO_2} V_U'''' + U_i^{\cdot\cdot\cdot\cdot} \qquad \textbf{Equation 3.06}$$

$$\emptyset \xrightarrow{UO_2} 2V_O^{\cdot\cdot} + V_U'''' \qquad \textbf{Equation 3.07}$$

Thus a Frenkel pair occurs when an ion, cation or anion, is displaced from its lattice site, resulting in a vacancy-interstitial pair. A Schottky defect involves a formula unit being removed from the bulk, leaving a set of vacancies. In the present work Schottky and Frenkel defects have not been modelled explicitly, their energies have been calculated from summing the appropriate individual point defect clusters.

Table 3.05 summarises predicted defect energies and compares them with experimental results for Schottky and Frenkel defects while Figure 3.05 shows the point defects in the UO_2 supercell. All point defect calculations were performed in a 96 atom UO_2 supercell. Full details of how defect formation energies are calculated can be found in section 2.4.4. Note that here point defects are considered to be charge neutral this is the same with all DFT methods shown in Table 3.05 except Crocombette *et al*, who simulate charged defects. The EM based results all consider defects at infinite dilution, using either shell or partial charge (rigid ion) models.

Table 3.05 – Predicted and experimentally determined defect formation energies (relative to pure bulk UO_2) (see section 2.4.4 for details of how formation energy is calculated). All calculations use DFT in a 96 atom cell with full relaxation of all internal parameters, constant pressure and a 400 eV plane wave energy cut-off unless otherwise specified. FP refers to Frenkel pair, Sch refers to Schottky defects. All energies presented are per defect, i.e. the total energy divided by two for FPs and total energy divided by three for Schottky energies.

Author	Method	Defect Formation Energy (eV)							Comments
		O_i	V_O	U_i	V_U	O-FP	U-FP	Sch	
DFT									
Matzke [139]	Experiment	-	-	-	-	1.50-2.00	4.80	2.00-2.30	-
Gupta [137]	PW91 + U	-1.60	5.60	8.20	6.00	2.00	7.10	5.70	Constant volume
	PW91	-2.50	6.10	6.00	4.00	1.80	5.00	5.40	
Geng [90]	LSDA + U	-2.20	7.50	8.20	9.10	2.70	8.70	8.00	500 eV cut-off
Iwasawa [138]	PBE + U	-0.44	4.46	4.70	8.45	2.01	6.58	5.79	-
Freyss [140]	GGA	-2.50	6.10	7.00	4.80	1.80	6.30	5.80	24 atom unit cell
Yu [141]	PBE + U	-2.44	5.06	4.67	2.30	1.31	3.49	4.14	500 eV/const. vol.
Dorado [142]	PBE + U	0.10	5.67	-	-	2.89	-	-	500 eV cut-off
Andersson [143]	LSDA + U	-0.50	3.84	-	-	2.17	-	7.88	144 atom cell/500 eV
Crocombette [144]	PBE + U	-1.40	5.60	-	-4.70	2.10	-	2.20	544 eV/const. vol/charged defects
This Work	PBE + U	-1.76	5.77	4.13	7.75	2.00	5.94	6.43	-
Interatomic Potentials									
Williams [145]	EM	-	-	-	-	1.70	5.20	1.70	Partial charge model
Morelon [146]	EM	-	-	-	-	1.59	6.30	2.23	Partial charge model
Jackson [147]	EM	-	-	-	-	2.38	9.70	2.45	Partial charge model
Catlow [120]	EM	-	-	-	-	2.70	9.27	3.45	Shell model
Grimes [148]	EM	-	-	-	-	3.41	6.1	4.45	Shell model

As expected, the PBE + U calculations predicted an O_i to be the most favourable point defect in UO_2. The order of defect stability, however, is not the same for every study in the literature. Consistency is found for the Schottky and Frenkel defects though, with almost every study (including experiment) finding oxygen Frenkel pairs to be most favourable, followed by Schottky defects and then uranium Frenkel pairs. Agreement with the absolute formation energies from Matzke is generally good, although the energy associated with uranium Frenkel pair and Schottky defect formation is overestimated in almost every case. The predicted oxygen Frenkel pair formation energy from this work shows very good agreement with experiment, sitting comfortably within the reported ranges.

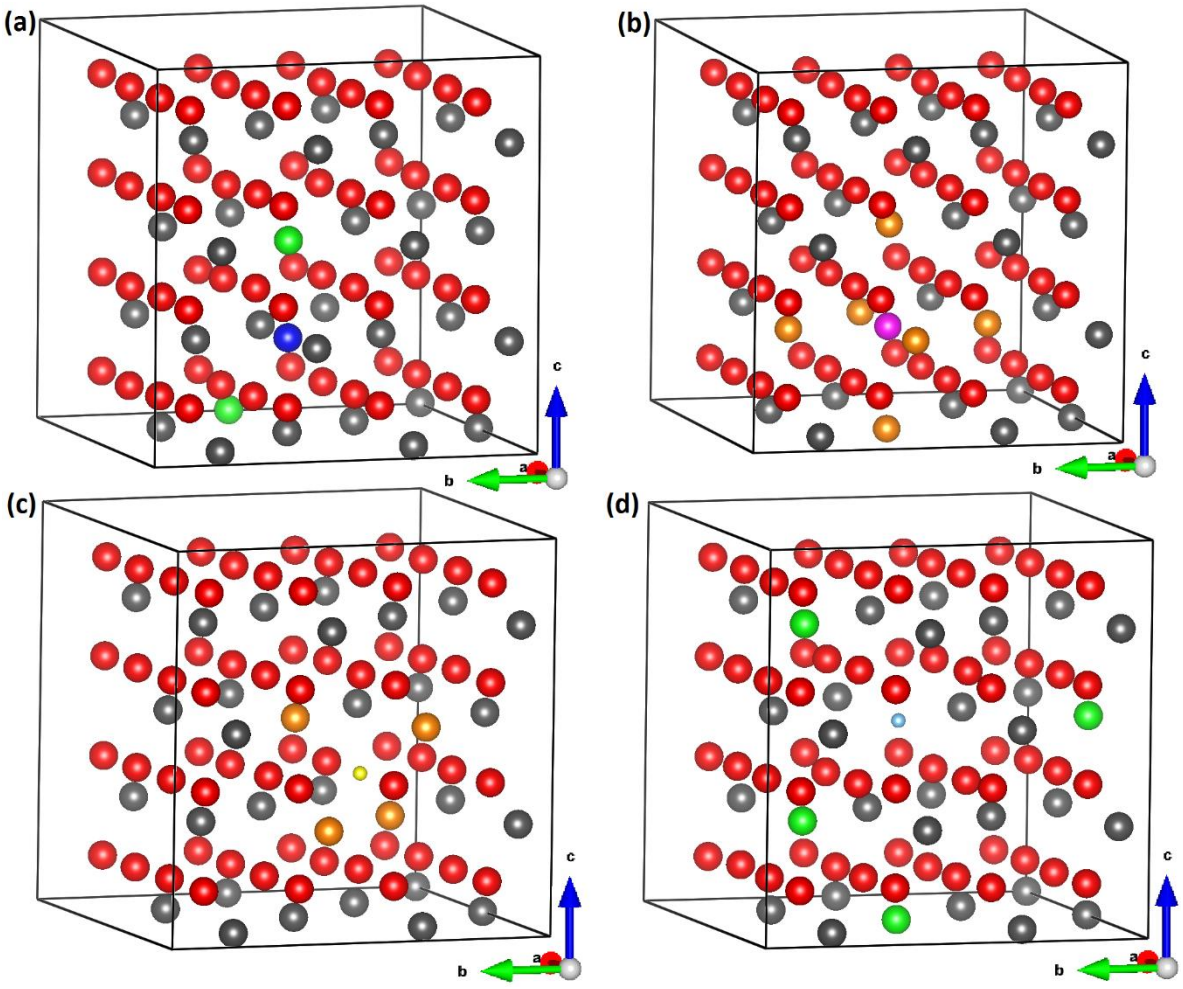

Figure 3.05 – Point defects in UO_2 supercells: (a) oxygen interstitial, (b) uranium interstitial, (c) oxygen vacancy and (d) uranium vacancy. U^{4+} are shown in grey, U^{5+} are shown in green, reduced uranium in orange, interstitial uranium in pink, uranium vacancies in light blue, lattice oxygen in red, interstitial oxygen in blue and oxygen vacancies in yellow.

The uranium Frenkel pair formation energy is overestimated but the result agrees well with the other DFT studies [137, 138, 144]. The potential based studies only present composite defect energies as they all use a charged model. Good agreement is generally found with experiment, with improved Schottky energies over the DFT calculations but comparable oxygen and uranium Frenkel pair energies. It should be noted that the partial charge models use a rigid ion, and so lack ionic polarisability, however the simulations of Williams still give the best overall agreement with experiment [145].

These point defects in a 96 atom UO_2 cell produce a change in stoichiometry to 1.94 (U_i), 1.97 (V_O), 2.03 (O_i) and 2.06 (U_i). Incorporation of point defect clusters is accompanied by local relaxation of the surrounding atoms, as well as smaller effects to the unit cell as a whole. The largest local distortion was found for the uranium vacancy, where the surrounding oxygen atoms (comprising a single sublattice cube) shift outwards by 0.270 Å along <111> directions. Uranium vacancy formation is accompanied by the surrounding uranium atoms (forming an octahedron) relaxing outwards along <100>, <010> or <001> directions by 0.215 Å. Oxygen point defects have less impact on the surrounding lattice: the V_O leads to inwards relaxation of the surrounding oxygen octahedron (<100>, <010> and <001>) by 0.102 Å and the O_i displaces the encompassing oxygen sublattice cube outwards by 0.136 Å (<111> directions). Considering the entire unit cell, it would be expected that interstitial atoms lead to expansion of the lattice and vacancies to its contraction. This holds true with the oxygen defects, an O_i gives a 0.09 % expansion and V_O a 0.29 % contraction of the simulation cell, however it is reversed for the uranium defects, U_i gives a 2.12 % contraction and V_U a 0.52 % expansion of the simulation cell. In order to understand this behaviour it is necessary to consider the charge compensation schemes in each defective system, i.e. the oxidation and reduction of the surrounding uranium atoms.

Introduction or removal of species from the UO_2 lattice will result in oxidation or reduction of uranium atoms, as there are multiple valence states available. Figure 3.05 displays the relaxed structures for each point defect system with accompanying uranium oxidation or reduction. In the case of an O_i two lattice uranium ions, one nearest neighbour and one next nearest neighbour, are oxidised to U^{5+}. A V_U behaves in a similar way, except the greater charge of this defect results in oxidation of four uranium ions to U^{5+}, two nearest neighbours and two next nearest neighbours. A slightly different picture is found for V_O

and U_i, rather than reduction to formal U^{3+} charges the charge is delocalised evenly across the nearest neighbour uranium ions to the defect: for V_O this is a tetrahedron (four ions) and for U_i this is an octahedron (six ions). This shows a resistance to reduction which fits with experiments that found the greatest extent of hypostoichiometry to be $UO_{1.98}$ [149]. As the U_i and V_O introduced here correspond to stoichiometries of 1.94 and 1.97 respectively it is possible that the defect is not dilute enough for U^{3+} to form as the compensating species. Additionally UO_2 is the lowest known oxide of uranium, there are no reports of U_2O_3 synthesis, although Pu_2O_3 is a stable oxide [150, 151], thus suggesting that U^{3+} is not a favourable species in oxides. The effect persists even when atoms are displaced to encourage stabilisation of U^{3+} or atom size is varied. Charge compensation schemes are not discussed in most of the computational work in the literature. Geng reports delocalised charge for all types of point defect using the LSDA + U [90]. Their reduced uranium ions compensating their U_i defect are distributed identically to in this thesis (six nearest neighbours, forming an octahedron) however they report three nearest neighbours and a single next nearest neighbour for the oxidised uranium ions accompanying V_U. Dorado *et al* report similar results to those found here for O_i, formation of two U^{5+}, although both next nearest neighbours. However they find two nearest neighbour uranium ions are reduced to U^{3+} when an V_O is present, in contrast to the results presented here [152].

3.7 Conclusions

Fluorite-structured UO_2 is an excellent system to assess the suitability of different functionals for simulating uranium oxides as there is a wealth of experimental data to compare with. Functionals from the GGA, meta-GGA and hybrid levels of theory were successfully employed to examine the structural, energetic, elastic, electronic and defect properties.

Hybrids were quickly abandoned due to their significant computational expense compared to the others. The rTPSS meta-GGA, although accurately computing physical and electronic properties, was also ruled out as it cannot precisely calculate energies. The PBE GGA functional was selected to carry out the bulk of the work in this thesis as it predicts

the most accurate energies and performs well for all of the other calculated properties, including point defects.

The Hubbard coefficient (U) and CL AFM ordering are required to accurately reproduce the electronic properties. SOC and NCL magnetism can also be employed to slightly improve the predicted band gap but are not necessary for an adequate description of the system. SOC serves to shift the energy by a constant amount (~3.1 eV/U) and the difference in stability of the various NCL orderings is as little as 0.005 eV.

Thus the PBE + U methodology evaluated in this chapter will be applied to the rest of the uranium oxides in this thesis to allow for direct comparison of results. It provides a good description of the UO_2 structure, although there is a slight tetragonal distortion which is inherent to simulating AFM structures with DFT. The elastic constants and bulk modulus were also well reproduced using PBE + U, giving the best overall agreement with experiments. The band gap is underestimated slightly by CL AFM PBE + U, however the Mott-Hubbard insulating state is well reproduced and the improvement in band gap using NCL magnetism does not appear to affect the relative stability to a significant extent and hence does not justify the additional computational expense. Defects were only examined using PBE + U, as they are more expensive calculations, however the results compare well with experimental and computational (both DFT and potential based) results from the literature. The defect chemistry of UO_2 is both extensive and complex, thus in the following chapter the defects formed from further oxidation of UO_2 are considered.

Chapter 4

4 Fluorite UO_{2+x}

UO_2 is particularly susceptible to oxidation and displays considerable hyperstoichiometry whilst still retaining a fluorite based structure. Defect clusters are a long acknowledged phenomenon in fluorite UO_2, with the closely related U_4O_9 phase being identified as early as the late 1940s [153] and models for the geometry of defect clusters emerging in the early 1960s [154] and developing into the 1970s [120, 155, 156]. Since then there has been considerable debate surrounding the types of oxygen defect cluster present in the fluorite-based oxides, which has only started to be resolved relatively recently. This chapter examines oxygen defect cluster stability in UO_{2+x}; from isolated clusters of oxygen interstitials in the $0.063 < x < 0.13$ region, to arrangements of multiple defect clusters at $UO_{2.25}$ (U_4O_9) and $UO_{2.33}$ (U_3O_7) stoichiometries. All of the calculations use 1*k* antiferromagnetic ordering, a plane wave cut off energy of 400 eV, *k* point density of 0.1 *k* points/Å^3 and the same PBE + U coefficients as previous calculations ($U = 4.5$, $J = 0.54$).

4.1 Isolated Defect Clusters

First to be discussed are defect cluster models for the composition range $UO_{2.063} – UO_{2.156}$, simulations of each cluster are presented and the energetically most stable identified.

4.1.1 Defect Cluster Literature Review

The first structural investigations of UO_{2+x} came from Willis, who used neutron diffraction to identify two oxygen interstitial sites which were distinct from the octahedral site at the centre of oxygen sublattice cubes. Each is displaced by approximately 1 Å from an octahedral site; O’ in <110> direction and O” along a <111> direction [154]. These experiments were later refined, determining precise ratios of O’ to O’’ and identifying the

presence of neighbouring oxygen vacancies to form a cluster of oxygen based defects [157]. These defect structures have since become known as Willis clusters with this original configuration labelled the 2:2:2 cluster, so named for its two O', two V_O and two O'', in that order (Figure 4.01 (c)). There are only two excess oxygen ions present in the cluster (O'), the O'' form as the O' displace them from lattice sites, creating two V_O in the process. Cheetham then extended defect cluster models in fluorite type structures, using neutron diffraction to identify 1:2:2 (one O', two V_O and two O'') (Figure 4.01 (a)) and 4:3:2 (four O', three V_O and two O'') clusters (Figure 4.01 (b)) in CaF_2 [158].

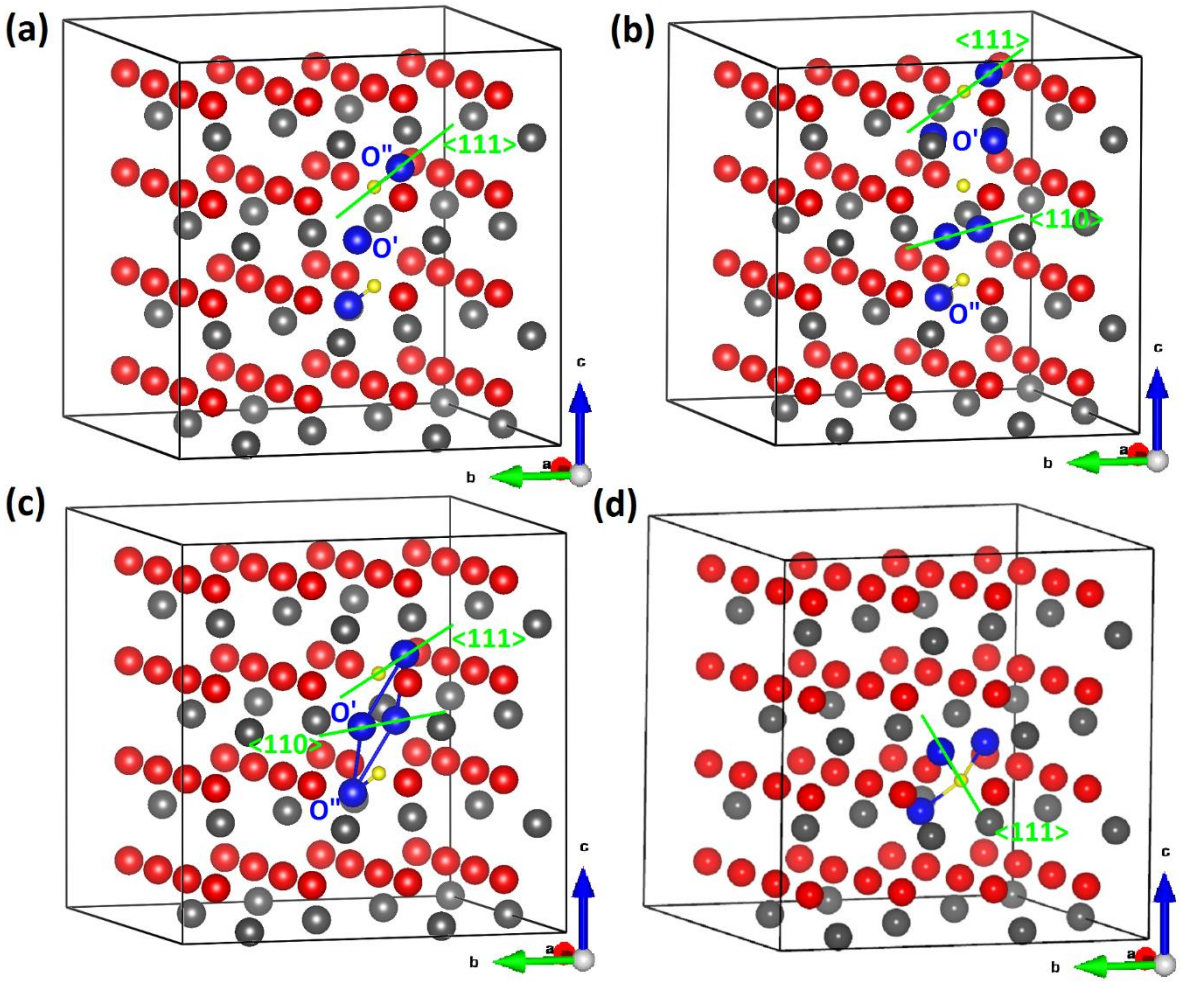

Figure 4.01 – Oxygen defect clusters in UO_2: (a) 1:2:2 Willis, (b) 4:3:2 Willis, (c) 2:2:2 Willis and (d) split di-interstitial. Uranium atoms are shown in grey, lattice oxygen in red, interstitial oxygen in blue and oxygen vacancies in yellow. Bonds have been drawn to emphasise cluster geometries.

The experimental measurements were followed by theoretical work from Catlow, initially in his PhD thesis using potential based calculations to examine defect structures in fluorite crystals (including UO_2) [155] and later in a comprehensive study of point defects and defect clusters in UO_2 [120]. The simulations predicted the 2:2:2, 1:2:2 and 4:3:2 clusters are all stable in UO_2 and proposed a clustering model for U_4O_9 based on arrangements of 4:3:2 clusters. The construction of Willis type clusters allows for many different combinations with varying amounts of V_O and O' but always having an O" interstitial at each end. More recently the 2:2:2 cluster has been assessed using DFT and found to be unstable, relaxing to a split di-interstitial cluster (Figure 4.01 (d)) [96, 118, 159, 160].

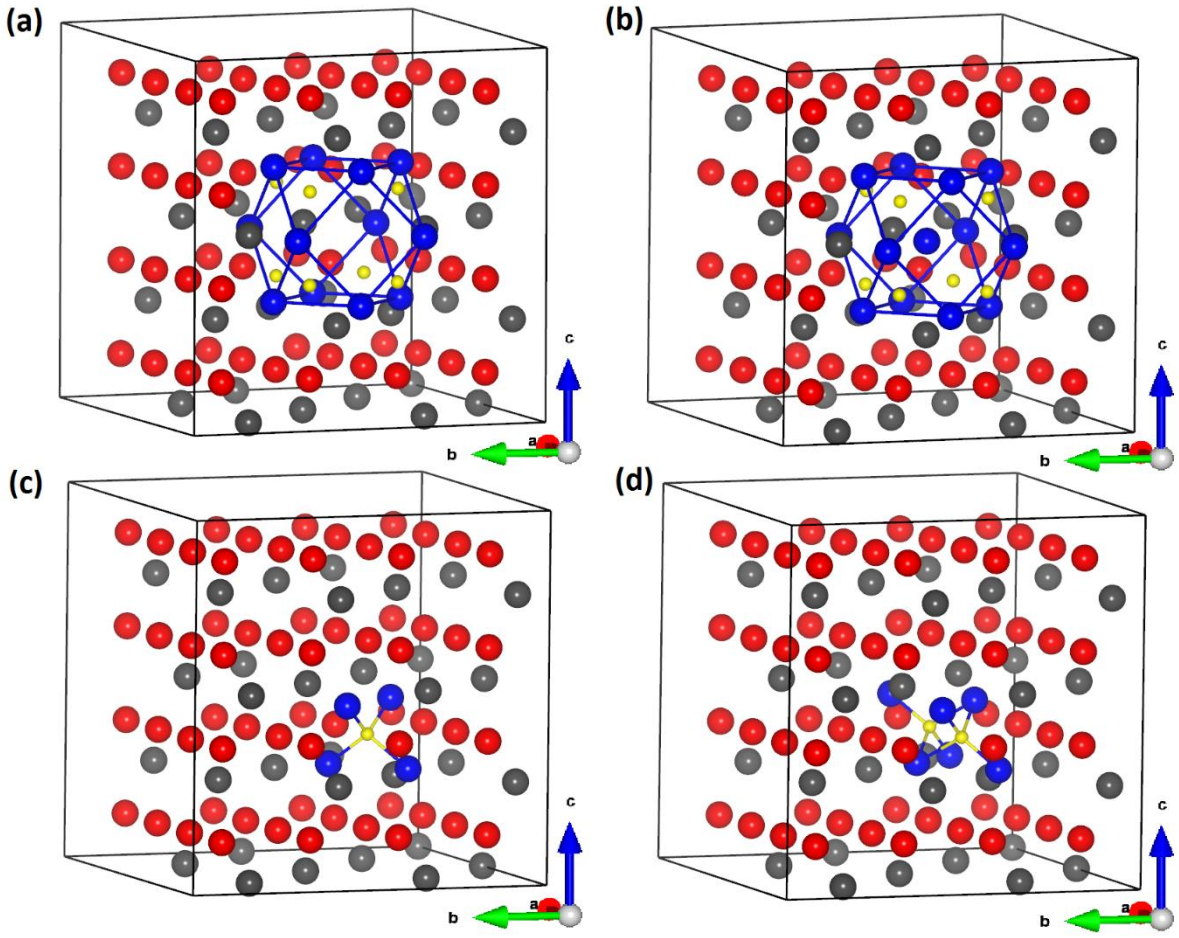

Figure 4.02 – Oxygen defect clusters in UO_2: (a) cuboctahedral (12), (b) cuboctahedral (13), (c) split tri-interstitial and (d) split quad-interstitial. Uranium atoms are shown in grey, lattice oxygen in red, interstitial oxygen in blue and oxygen vacancies in yellow. Bonds have been drawn to emphasise cluster geometries.

After the discovery of Willis clusters a new defect cluster arrangement was proposed, again in CaF_2, known as the cuboctahedral cluster (COT-12) [161]. The cluster consists of a vacant anion sublattice cube that has been replaced with a cuboctahedral cage-like structure, giving a total of four excess anions. It can also be considered as four anion interstitials placed half way between the top and bottom layers of an existing anion cube and subsequently displacing the cube outwards from the lattice sites along <110> directions (Figure 4.02 (a))). Bevan later performed neutron diffraction experiments on fluorite uranium oxides, identifying the cuboctahedral cluster, although proposing an additional oxygen ion at the centre of the structure (COT-13) (Figure 4.02 (b)) [162]. Subsequent neutron diffraction work [31] and DFT studies [32, 159, 163] have also attested to the stability of COT clusters, although presence or absence of the central O_i is still under debate.

Finally, the split interstitial group of defect clusters have emerged from theoretical work as stable in UO_2, presenting another viable clustering scheme. The first of these to be identified was the split di-interstitial cluster (I_2^x), mentioned above as the species formed on relaxation of a 2:2:2 Willis cluster [96, 118, 159, 160]. A I_2^x cluster consists of a central V_O with three O_i displaced approximately 1.6 Å in <111> directions, making an equilateral triangle whose centre is also in a <111> direction from the V_O (Figure 4.01 (d)). More recent DFT work has suggested that the 2:2:2 Willis cluster is actually a transition state between two I_2^x clusters [164]. Ensuing the I_2^x cluster a split tri-interstitial cluster (I_3^x) has been reported (Figure 4.02 (c)) which is a I_2^x cluster with the fourth <111> site occupied by an O_i, giving a total of four O_i and one V_O [90]. Geng *et al* predicted a 4:3:2 Willis cluster relaxes to a I_3^x, similarly to the 2:2:2 Willis relaxing to a I_2^x cluster [160]. In the same paper they report the 1:2:2 cluster relaxes to a point oxygen interstitial, occupying the octahedral site, and so finding no isolated Willis-type clusters to be stable. Completing the split interstitial class of defects, the split quad-interstitial cluster (I_4^x) was identified with DFT (Figure 4.02 (d)), consisting of two I_2^x on adjacent sites to give a total of six O_i and two V_O [98].

4.1.2 Stability of Isolated Defect Clusters

The use of computational techniques allows for straightforward calculation and comparison of relative stabilities, however, there is currently still debate in the literature over the most stable isolated defect clusters. Using the LSDA + U Geng *et al* predict split interstitial type clusters to be more stable than cuboctaheral clusters (both COT-12 and COT-13), with I_2^x most stable overall [90]. In contrast Andersson *et al* predict the I_4^x cluster to be most stable, followed by COT-13 and I_2^x [98], also using the LSDA + U. Both of these research groups find the isolated 2:2:2 Willis cluster to be unstable with respect to the I_2^x cluster. Hence it still remains for all types of cluster to be simulated using a single technique to compare their energies, the occurrence and distribution of U^{5+} and U^{6+} ions as well as the relationships of the clusters with other fluorite based phases of UO_{2+x}.

Table 4.01 contains the predicted formation energies of isolated defect clusters in a 96 atom UO_2 cell from this work and the literature. The formation energy is calculated by subtracting the total energy for pure UO_2 and the energy $E(\frac{n}{2}O_{2(g)})$ (where *n* is the number of additional oxygen atoms in the lattice) from the total energy for the defective phase (details in section 2.4.4). The results are presented alongside those from the literature, which use LSDA + U calculations. Figure 4.03 shows the relaxed defect structures in UO_2, along with the uranium charge compensation schemes.

Table 4.01 – Predicted formation energies per excess O_i of isolated defect clusters (see section 2.4.4 for details of formation energy calculation). Δ % refers to the change in cell volume compared to the perfect UO_2 lattice.

Cluster	Stochiometry	V_O:O_i Ratio	This Work		Geng [160, 163]		Andersson [98, 165]	
			PBE + U		LSDA + U		LSDA + U	
			E_{form} (eV)	Δ %	E_{form} (eV)	Δ %	E_{form} (eV)	Δ %
COT-12	2.125	0.66	-0.52	0.32	-1.80	-0.14	-	-
COT-13	2.156	0.62	-0.68	-0.85	-2.48	-1.61	-2.46	-
I_4^x	2.125	0.33	-0.55	-0.53	-	-	-2.60	-
I_2^x	2.063	0.33	-1.06	0.00	-2.65	-0.21	-2.34	-
I_3^x	2.094	0.25	-0.88	-0.14	-2.58	-0.42	-	-

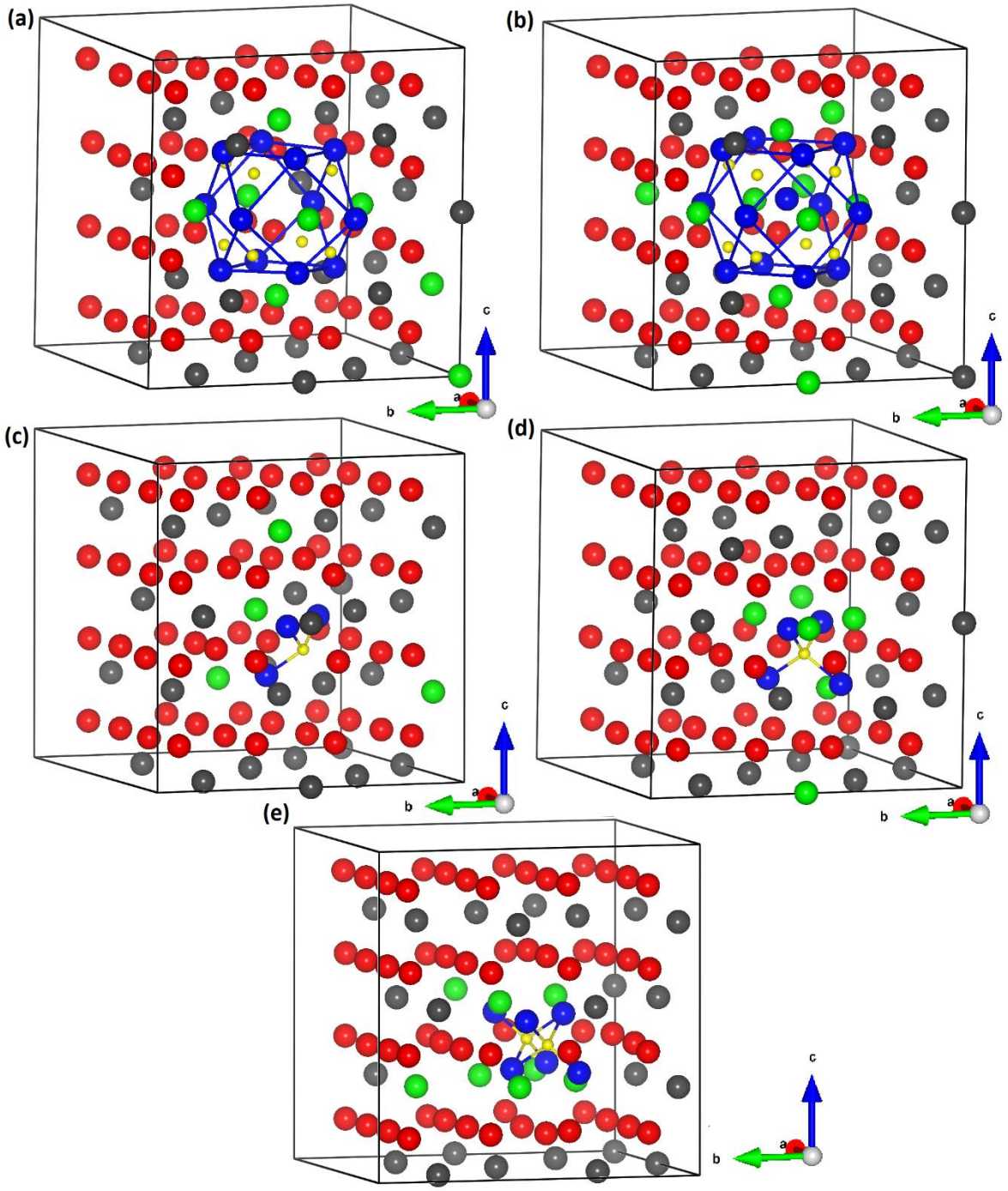

Figure 4.03 – Relaxed oxygen defect clusters in UO_2: (a) cuboctahedral (12), (b) cuboctahedral (13), (c) split di-interstitial, (d) split tri-interstitial and (f) split quad-interstitial. U^{4+} are shown in grey, U^{5+} are shown in green, lattice oxygen in red, interstitial oxygen in blue and oxygen vacancies in yellow. Bonds have been drawn to emphasise cluster geometries.

The PBE + U calculations find the order of stability to be: I_2^x > I_3^x > COT-13 > I_4^x > COT-12; this follows the order of stoichiometry from lowest to highest, with the exception of

COT-13. Unfortunately, there is incomplete literature data to compare with, however the predicted order of stability agrees with the available data from Geng [160, 163]. The order of stability predicted by Andersson is in reverse compared to the other results [98, 165]. A possible explanation is Andersson kept the volume fixed at the UO_2 cell size whereas in the PBE + U and Geng's calculations full relaxation of the ions and cells were permitted. In section 3.1.6 it was established that O_i have a more negative formation energy than V_O, however the V_O:Oi ratio in defect clusters does not show an obvious relationship with relative stability.

The results using PBE + U show that charge compensation occurs entirely by oxidation to U^{5+} in a mixture of nearest neighbour and next nearest neighbour sites and no U^{6+} is calculated. This behaviour is mirrored in the results of Andersson but Geng predicts the charge is spread over more uranium sites with $U^{4.5+}$ charge. It is possible that Geng *et al* have located meta-stable states as there are no experimental reports of delocalised charges in uranium oxides, or indeed in any other DFT studies.

The COT-13 cluster is predicted to be energetically more stable than the COT-12, behaviour which must arise from the presence of the additional O_i at its centre, as this is the only distinguishing feature. Examining Figure 4.03 (a) and (b), both clusters exert fairly minimal distortion to the surrounding uranium sublattice. Slightly more distortion is observed for the oxygen sublattice, as the ions are pushed outwards from the COT cluster (in keeping with the literature results) although it is more significant with the COT-13, which is also slightly more distorted from a perfect cuboctahedron itself. In both cases the nearest neighbour uranium ions in front of all six square faces of the cuboctahedron are oxidised to U^{5+} as well as two next nearest neighbour uranium ions for COT-12 and three for COT-13. The final COT-13 U^{5+} is a nearest neighbour ion in front of a triangular face, which causes the central O_i to shift off centre in a <111> direction towards it, as well as making this triangular face the most distorted of the cluster. The distortion of the cuboctahedron is therefore linked to the nearest neighbour charge distribution, while an insignificant distortion is found for the COT-12 cluster because of its symmetrical U^{5+} environment surrounding it. Andersson *et al* predict the same arrangement of U^{5+} ions adjacent to the square faces of the COT-13 cluster, however the remaining U^{5+} are all next nearest neighbours [165]. It is unclear precisely which sites are oxidised in Geng *et al*'s

simulations, although from the description it appears to be a mixture of nearest neighbour and next nearest neighbour sites, but with delocalised charge.

The generally greater stability of the I_2^x cluster compared to the other split interstitials most likely arises from the smaller local distortion of the oxygen sublattice and the symmetric distribution of compensating U^{5+} ions. The three nearest neighbour oxygen ions in front of the triangular cluster are pushed outwards slightly from their lattice sites (Figure 4.03 (c)), compared to six for the I_3^x cluster, in an octahedral distribution (Figure 4.03 (d)), and ten for the I_4^x cluster, in two octahedra centred on the dual vacancies (Figure 4.03 (e)). There is also very little distortion of split interstitial cluster geometries on relaxation compared to the cuboctahedral clusters. The U^{5+} distribution from the I_2^x simulation is perfectly symmetrical; featuring the nearest neighbour uranium ion directly in front of the triangular cluster, the two next nearest neighbour uranium ions in <101> directions from the first U^{5+} and a final next nearest neighbour in the same {101} plane as the first U^{5+} but two {010} planes away. The nearest neighbour uranium ion is shifted slightly off the lattice site towards the cluster whereas the others remain relatively undistorted. In the I_3^x cluster, three of the nearest neighbour uranium ions are oxidised (forming three vertices of a tetrahedron) as well as another three next nearest neighbours, giving a higher concentration of U^{5+} in close proximity to each other than in the I_2^x case. The relaxed I_4^x cluster has an even higher local concentration of U^{5+} ions, with five out of six nearest neighbour sites oxidised. Of the remaining three U^{5+} two are adjacent along the long axis of the cluster and the other is in the next {010} plane. Andersson *et al* find a more diffuse spread of U^{5+} throughout the cell, which is likely to be the reason they find the I_4^x cluster to be the most stable [165]. Certainly from the results in this thesis it seems that the stability of isolated defect clusters is linked to the U^{4+}/U^{5+} distribution, the higher the U^{5+} concentration surrounding the cluster, the lower its relative stability, possibly due to increased repulsion between the +1 effective charges of U^{5+}.

All clusters in this work, except for COT-12, were predicted to result in a slight contraction of the cell volume. This comes despite the main local distortion in each case being a repulsion of the neighbouring oxygen ions. The greatest contraction is found for the COT-13 cluster, followed by the I_4^x, I_3^x and I_2^x clusters; an order found previously by Geng *et al* [90]. This seems counterintuitive given the local sublattice expansion and the fact that more

oxygen ions have been added. However, the oxidised U^{5+} ions could exert a stronger Coulombic attraction on the surrounding oxygen ions, shortening the bonds and leading to the small lattice contractions observed in these calculations, i.e. U^{5+} as a smaller ionic radius than U^{4+}.

4.2 $UO_{2.25}$ (U_4O_9)

U_4O_9 marks the first isolatable uranium oxide phase after UO_2, however its long-debated structure is complex with a variety of different configurations proposed over the years. Most work has focused on determining the structure and thermodynamic properties and so there is a lack of research into its electronic and elastic properties. This section provides some background on U_4O_9 and details of simulations undertaken in an attempt to elucidate the structure and its relationship to the isolated defect clusters. The findings of this section have been published in the Journal of Nuclear Materials in an article entitled "*Computer simulation of defect clusters in UO_2 and their dependence on composition*" [159].

4.2.1 U_4O_9 Background

U_4O_9 is an intermediate product of UO_2 oxidation, forming at temperatures less than 673 K [17]. It crystallises in two closely related polymorphs (α- and β-) which are both structurally similar to UO_2, demonstrated by the density of 11.31 gcm^{-3} [19]. It exhibits a degree of non-stoichiometry at higher temperatures with composition typically ranging from $UO_{2.23}$ to $UO_{2.25}$ [157]. The structure has been rationalised in terms of UO_2 supercells (typically 4 x 4 x 4) containing periodic arrangements of O_i defect clusters, such as the ones discussed in the previous section. The first of these, proposed by Allen *et al*, consisted of linear chains of 2:2:2 Willis clusters aligning along <110> directions, spaced $2\sqrt{2}a_0$ apart (where a_0 is the lattice parameter of the parent UO_2 structure) [30]. This follows from a UO_{2+x} region composed of isolated 2:2:2 Willis clusters that develop into chains with increasing x [115]. This model fits well with a general Willis type clustering model as intersecting chains would result in a 4:3:2 cluster. Later came a clustering model based on cuboctahedral clusters, with Bevan *et al* using single crystal neutron diffraction to propose a structure containing COT-13 clusters, each separated by a plane of uranium ions [162].

This model has subsequently been refined by Cooper *et al* [166] and Desgranges *et al* [31], the latter suggesting a 3:1 ratio of COT-12 to COT-13 clusters. Most recently Andersson *et al*, using DFT, established a clustering model based on split interstitial clusters [98] finding the most stable configuration to be layers of I_4^x clusters [32].

The first polymorph, α-U_4O_9, is formed from heat treatment (1323 K, under vacuum) of a mixture UO_2 and U_3O_8 powder, in a ratio that gives a $UO_{2.37}$ composition on average [167]. The unit cell is rhombohedral with a = 18.9286 and α = 109.686 ° and the *R3c* space group [167] (Figure 4.04(a)). β-U_4O_9 was the first U_4O_9 polymorph to be identified and subsequently has become the most studied [157]. A stoichiometric sample can be prepared by heating UO_2 powder to 1270 K and maintaining the temperature for 30 days before slowly cooling to room temperature over twelve hours [31]. The highest resolution neutron diffraction experiments on the material indicate a cubic *I-43d* structure with a = 21.7666 Å, representing a 4 x 4 x 4 expansion of the parent UO_2 cell [31] (Figure 4.04 (b)). In both polymorphs uranium ions are in eight-, nine- and ten-fold coordination sites whilst the oxygen ions have distorted tetrahedral coordination (four-fold). The eight-coordinate uranium sites are equivalent to those in UO_2 whereas the higher coordinate sites incorporate additional oxygen from the defective superlattice into their coordination sphere.

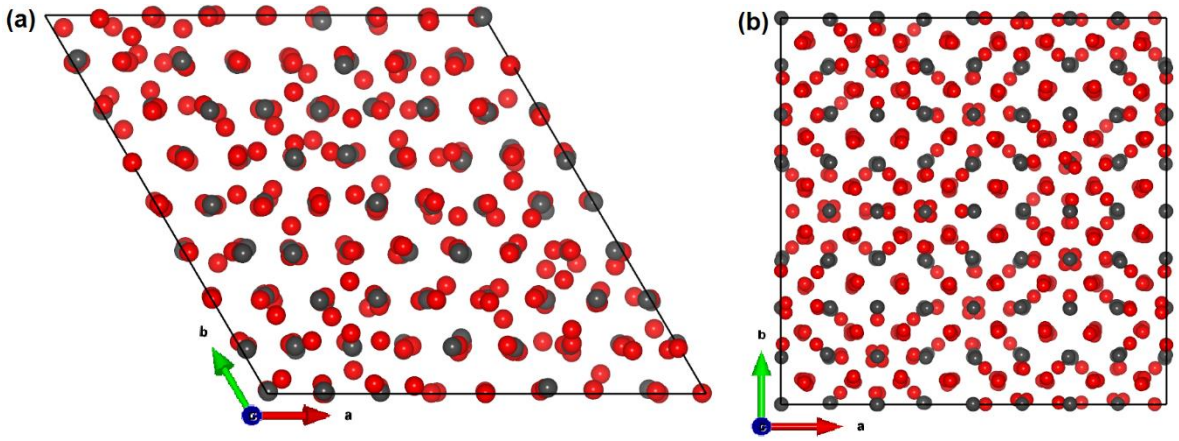

Figure 4.04 – Experimentally determined structures of U_4O_9 aligned along the *z* axis. (a) shows the α- polymorph [167], (b) displays the β- polymorph [31]. Uranium ions are shown in grey and oxygen are shown in red. The {001} plane of α-U_4O_9 (shown) is equivalent to the {111} plane in UO_2 and cubic β-U_4O_9.

The most stable phase at room temperature, β-U_4O_9, has been investigated in more depth than the α- polymorph, including studies of the heat capacity [168, 169], thermal

conductivity [170] and magnetic susceptibility [171]. More recently the charge on uranium sites has been deduced experimentally using X-ray absorption near edge structure measurements (XANES), determining an even mixture of U^{4+} and U^{5+} ions [114]. Although the DFT calculations presented earlier predicted no U^{6+} in fluorite based structures, the XANES results represent the first direct experimental evidence for this. He *et al* also used the LDSA + U to predict a band gap of 1.68 eV [172] for Andersson *et al*'s quad interstitial based U_4O_9 structure.

4.2.2 Simulation of U_4O_9 ($UO_{2.25}$)

The difficulty in simulating U_4O_9 using DFT is the very large unit cell sizes, α-U_4O_9 has 416 atoms and β-U_4O_9 has 832 atoms, 32 and 64 formula units respectively. In order to overcome this issue a similar approach has been adopted to Andersson *et al* [32], whereby a UO_2 supercell has oxygen added to it to give the correct stoichiometry.

As I_2^x defects were found to be the most stable isolated clusters from the calculations presented in section 4.1.2 these, as well as point O_i, have been selected as the building blocks of U_4O_9 stoichiometry phases. Rather than select a few arrangements in a 96 atom (2 x 2 x 2) UO_2 supercell a 48 atom (1 x 2 x 2) supercell was chosen and all 33 symmetry inequivalent arrangements of four O_i and all 11 unique configurations of two I_2^x clusters were identified using the site-occupancy disorder (SOD) program [173]. This provides a more complete scan of the stoichiometry, albeit in a smaller cell. However the most stable relaxed configurations are then doubled to give a 2 x 2 x 2 cell to confirm their stability in a larger supercell.

As a total of 44 simulations were undertaken the complete results table can be found in Appendix B, however Figure 4.05 provides a graphical representation of the full set of results, showing the formation energy with respect to UO_2 and the volume change from the UO_2 unit cell.

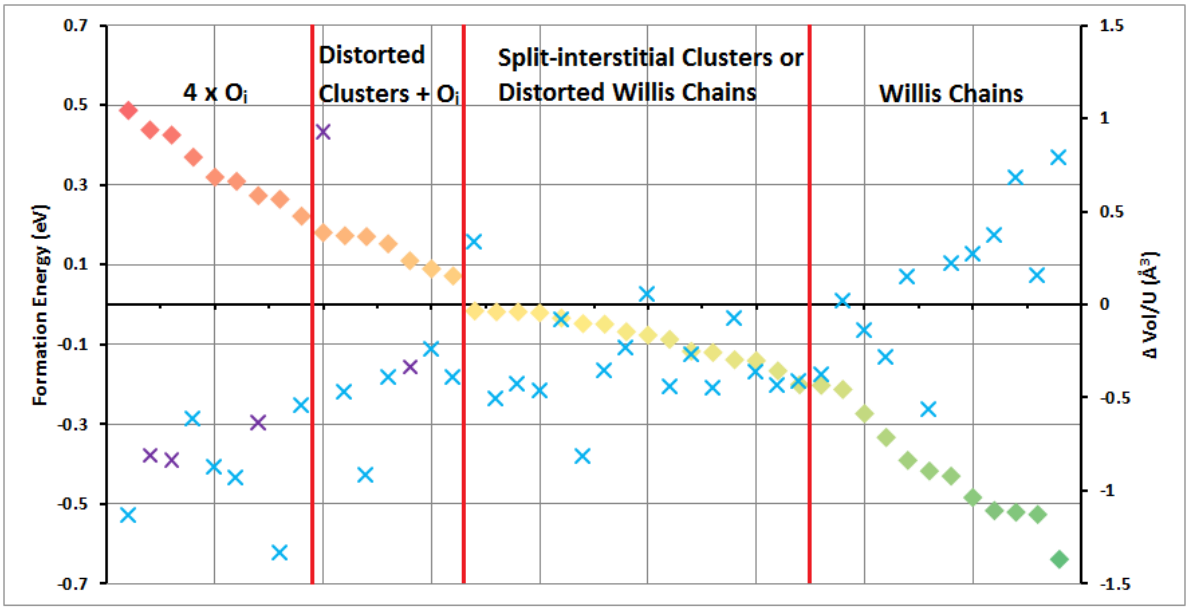

Figure 4.05 – Plot showing predicted formation energies for each calculated U_4O_9 phase (diamonds) and percentage change in volume relative to UO_2 per uranium ion (crosses). Purple cross markers indicate one or more U^{6+} ions were predicted in that system.

The simulations predict a number of different defect configurations and the stability is related to the amount of O_i bound in clusters compared to the number of isolated O_i. The least stable configurations were those that remained as four O_i (Figure 4.06 (d)); followed by a mixture of distorted clusters and isolated O_i (Figure 4.06 (c)); then split-interstitial clusters and distorted chains of 2:2:2 Willis clusters are predicted to have slightly negative formation energies; and finally undistorted chains of 2:2:2 Willis clusters (Figure 4.06 (a) and (b)) are predicted to be the most stable arrangements of defects in U_4O_9 stoichiometry phases. This comes despite the earlier confirmation that a single 2:2:2 Willis cluster relaxes to a I_2^x cluster, suggesting that 2:2:2 clusters can only exist as chains and their formation is stoichiometry dependent. The chains all feature edge-sharing 2:2:2 clusters and align along the *x*, *y* or *z* axis and can either be single (Figure 4.06 (b)) or double (Figure 4.06 (a)).

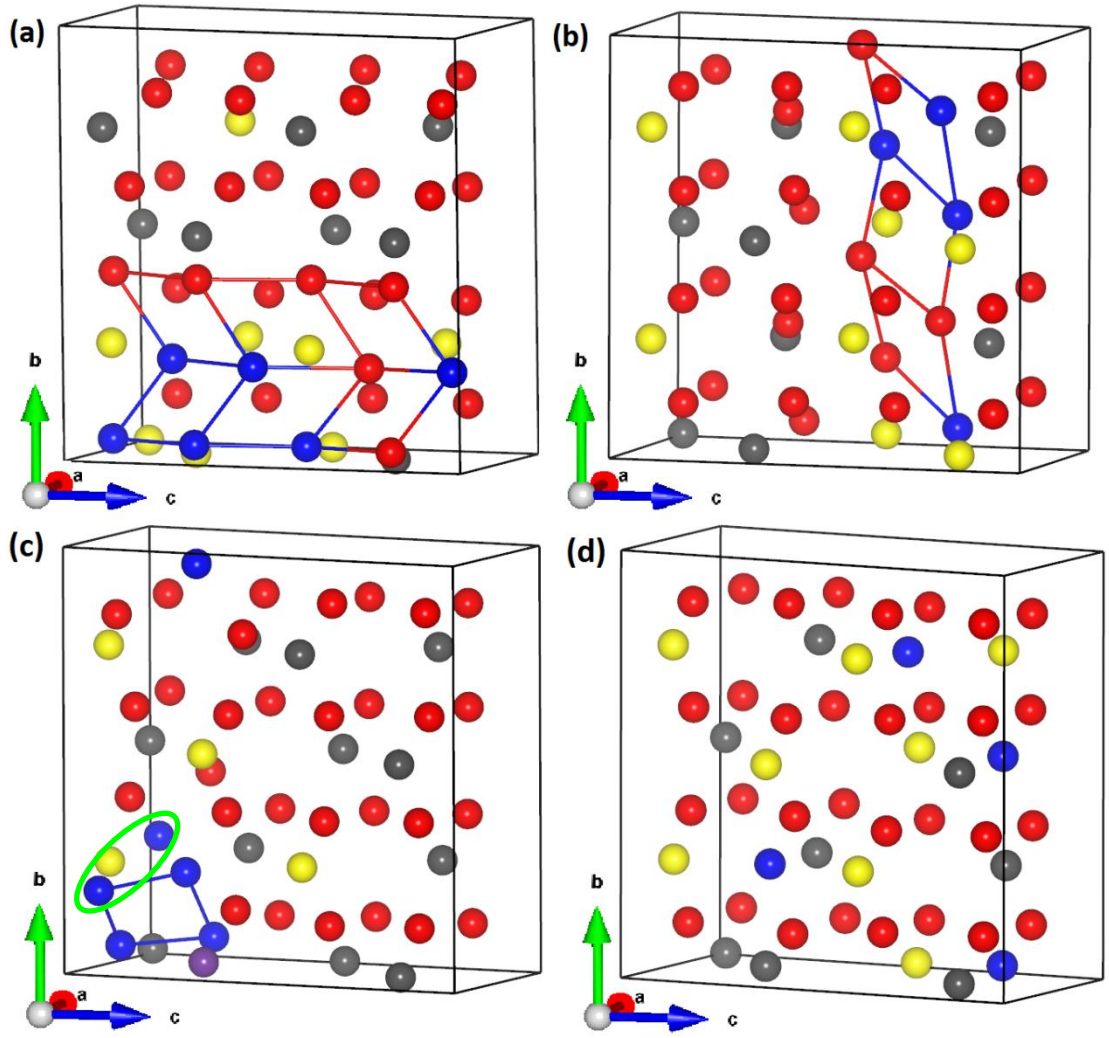

Figure 4.06 – Relaxed U_4O_9 phases (a) a double 2:2:2 Willis cluster chain, (b) a single 2:2:2 Willis cluster chain, (c) a distorted 2:2:2 Willis cluster (one unit of a chain along the *x* axis) and (d) four isolated O_i. Grey spheres are U^{4+} ions, yellow are U^{5+}, purple are U^{6+}, red are lattice oxygen (i.e from UO_2) and blue are excess oxygen introduce for the simulation.

As shown in Figures 4.05 and 4.06, in the overwhelming majority of systems the additional charge introduced by O_i is compensated by oxidation to U^{5+}; however in five of the least stable configurations one or two U^{6+} ions are predicted to form (E_{form} = 0.11-0.44 eV). These results agree well with the experimental observations that U_4O_9 contains only U^{4+} and U^{5+}. In the 2:2:2 chain systems the majority of the U^{5+} ions are nearest neighbours to the oxygen interstitials. In the energetically most stable simulations (e.g. Figure 4.06 (a)) this leads to alternating layers of 2:2:2 Willis chains and relatively undisturbed UO_2 layers, similar to the spacing described by Allen *et al* [30]. However the chains proposed by Allen

et al order along <110> directions instead of the <100> directions found here. The least stable O_i based systems, such as Figure 4.06 (d), feature almost no lattice relaxation at all, which is most likely the cause of the instability. The U^{6+} containing example shown in Figure 4.06 (c) is a slightly special case as it contains an O_i 1.443 Å from the closest 2:2:2 Willis O_i which prevents the formation of a chain by the distortion of the local oxygen sublattice. The short O-O distance is indicative of a peroxide ion (O_2^{2-}), previously predicted by Andersson *et al* in their DFT study of UO_2 oxidation [32]. Peroxide status, rather than superoxide (O_2^-), is confirmed by the lack of magnetisation on the two constituent oxygen atoms. Although peroxide ions were not identified in every system containing U^{6+} the presence of peroxide ions could be indicative of U^{6+} ions.

The coordination of uranium ions in the stable U_4O_9 simulations generally remains eight-fold for U^{4+} and U^{5+} ions, with the extent of distortion from cubic determined by the proximity to 2:2:2 cluster chains. Around U^{6+} ions the oxygen sublattice is typically more distorted and the coordination number falls to seven. Figure 4.07 shows the coordination at U^{5+} and U^{6+} sites adjacent to 2:2:2 clusters.

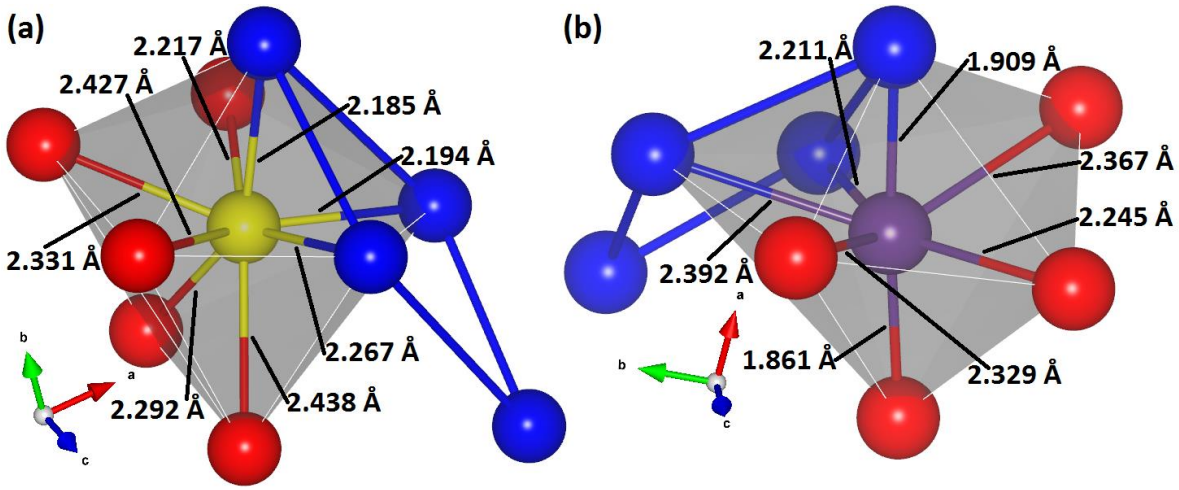

Figure 4.07 – Coordination of U^{5+} (a) and U^{6+} (b) ions neighbouring 2:2:2 clusters. Yellow spheres are U^{5+} ions, purple are U^{6+}, red are lattice oxygen (i.e from UO_2) and blue are excess oxygen introduce for the simulation.

At the U^{5+} sites, the average U-O bond length is 2.294 Å, slightly lower than the 2.368 Å observed in UO_2. Examining Figure 4.07 (a), the four in-plane oxygen ions on the left show half of an oxygen sublattice cube (aligned in the {100} plane) whilst the other four form a

flattened tetrahedron. This is not a huge departure from cubic coordination, as if the tetrahedron were completely flat (in a {100} plane) then it would be cubic once more. At U^{6+} sites (Figure 4.07 (b)) the coordination has been reduced to seven-fold with a larger local oxygen sublattice distortion. There is greater reduction of the average U-O bond length to 2.188 Å, mainly due to the emergence of two shorter, collinear axial bonds resembling the uranyl ion (UO_2^{2+}). The coordination is puckered pentagonal bipyramidal and when considered with the non-symmetrical uranyl-like bonds the U^{6+} site is strongly reminiscent of the coordination in η-UO_3 [72, 174].

There is a moderate negative correlation (r = -0.63) between U_4O_9 stability and volume change relative to the parent UO_2 lattice. The energetically least stable systems generally show a decrease in volume whereas the most stable increase. This is most likely because the less stable systems show less relaxation compared to the more stable systems, where the large oxygen sublattice distortions cause a slight cell expansion. The relatively unrelaxed lattice now contains half U^{5+} ions which exert a stronger Coloumbic attraction on the oxygen ions and thus causes a slight contraction over the whole cell for the separated defects. Consequently it is predicted that with high applied pressure 2:2:2 Willis chains would destabilise and isolated O_i or split interstitial clusters would become the dominant defect species. These results are in contrast to experiment where the U_4O_9 lattice represents a volume decrease from UO_2 of approximately 1.5 % [31]. As volume decrease is predicted for the split-interstitial based U_4O_9 systems it is possible that they are forming experimentally through a kinetically controlled process, whereas the thermodynamically most stable U_4O_9 composition is the Willis cluster chains that are accompanied by an increase in volume relative to UO_2.

Further to these structural considerations the electronic band gaps of the U_4O_9 phases have been calculated and the energetically most stable configurations are found to have a gap between 1.48 and 1.61 eV. Although there are no experimental measurements available for comparison these results compare favourably with the LSDA + U computed value of 1.68 eV from He *et al* [172].

Five of the most stable U_4O_9 systems have had their cells doubled (now a 2 x 2 x 2 supercell) and reminimised to provide more confidence that the presence of 2:2:2 Willis

clusters is not simply an artefact of simulation cell size. In each case the single or double chain of Willis clusters is retained and the predicted formation energies range from -0.47 to -0.58 eV, showing excellent agreement with calculations in 1 x 2 x 2 supercells. All relaxed cells were found to increase in volume compared to pure UO_2, also in line with the smaller supercell calculations, with the actual values varying between 0.43 and 1.12 % volume increase. The predicted band gaps are also in line with the other calculations, with a predicted range of 1.35 to 1.48 eV.

Further simulations have also been undertaken to provide comparison with the U_4O_9 systems described in the literature calculations of COT-12 based and I_4^x based phases in 2 x 2 x 2 supercells. The defect clusters in each case were placed such that there is at least one layer of typical bulk atoms separating them. Although a number of different arrangements are possible for these systems time and resource constraints have meant only single examples of each have been simulated. Both systems were found to retain their respective defect structures on minimisation but predicted to be significantly less stable than the 2:2:2 Willis chain based phases at -0.08 – - 0.11 eV. The predicted band gaps for these phases also fall within the 1.35 to 1.48 eV range found for the equivalent Willis cluster chain systems. These results give further confidence that the Willis model of U_4O_9 is the most energetically stable.

4.3 Willis Clusters at Lower Stoichiometry ($UO_{2.13}$)

Now that 2:2:2 Willis cluster chains have been identified as energetically stable entities at U_4O_9 stoichiometry it is necessary to investigate its stability range. In order to assess stability at lower stoichiometry a 1 x 2 x 2 pure UO_2 cell was added to the U_4O_9 supercell to give an overall stoichiometry of $UO_{2.125}$. The 2:2:2 Willis chains are found to remain present, retaining their geometry, and are still predicted to be the energetically most stable defect arrangements, with comparable stability to the most stable U_4O_9 configurations. This is in accordance with the initial observations of Willis, who reported the presence of the 2:2:2 cluster at $UO_{2.13}$ stoichiometry [154]. The almost identical cluster chains in the $UO_{2.125}$ systems suggest that the chains are required in order to stabilise the clusters, or in other terms Willis cluster chain stability is entirely composition dependent. Table 4.02

gives a comparison of different defective systems over the $UO_{2.0625}$-$UO_{2.25}$ stoichiometry range.

Table 4.02 – Predicted formation energies (see section 2.4.4 for details of defect formation energy calculation) and volume changes for selected defective phases over $UO_{2.0625}$-$UO_{2.25}$ stoichiometries. Formation energies are all given per excess O_i.

Supercell Size	Stoichiometry	Figure	Configuration	E_{form} (eV)	Δ Volume (%)
1 x 2 x 2	**$UO_{2.25}$ (U_4O_9)**	4.06 (d)	4 x O_i	0.49	-1.14
1 x 2 x 2	**$UO_{2.25}$ (U_4O_9)**	4.06 (c)	2:2:2/2 x O_i	0.18	0.93
1 x 2 x 2	**$UO_{2.25}$ (U_4O_9)**	4.06 (a)	Double 2:2:2 chain	-0.52	0.68
1 x 2 x 2	**$UO_{2.25}$ (U_4O_9)**	4.06 (b)	Single 2:2:2 chain	-0.53	0.16
2 x 2 x 2	**$UO_{2.25}$ (U_4O_9)**	4.06 (a) x 2	Double 2:2:2 chain	-0.58	1.12
2 x 2 x 2	**$UO_{2.25}$ (U_4O_9)**	-	2 x COT-12	-0.11	0.34
2 x 2 x 2	**$UO_{2.25}$ (U_4O_9)**	-	2x I_4^x	-0.08	-0.81
2 x 2 x 2	**$UO_{2.125}$**	4.06 (a) + UO_2 bulk	Double 2:2:2 chain	-0.68	0.32
2 x 2 x 2	**$UO_{2.125}$**	4.03 (a)	COT-12	-0.52	0.32
2 x 2 x 2	**$UO_{2.125}$**	4.03 (f)	I_4^x	-0.55	-0.53
2 x 2 x 2	**$UO_{2.0625}$**	4.03 (c)	I_2^x	-1.06	-0.00

Based on the simulations of isolated 2:2:2 Willis and I_2^x clusters, it would be expected that reduction of a $UO_{2.125}$ phase to $UO_{2.0625}$ stoichiometry would destabilise the 2:2:2 cluster. To test this, two oxygen ions were removed from the $UO_{2.125}$ cells shown in Figure 4.06 (a) and (b) to break the cluster chains and yield single and edge-sharing double 2:2:2 Willis clusters. In both of these $UO_{2.0625}$ simulations, the systems relaxed to a single I_2^x cluster in accordance with the previous simulations from this work and the literature [96, 118, 159, 160]. The stability of 2:2:2 Willis cluster chains is now confirmed as being fully dependent on the phase composition, with stoichiometries of $UO_{2.125}$ and higher required to stabilise them.

4.4 $UO_{2.33}$ (U_3O_7)

U_3O_7 is the next experimentally observed uranium oxide phase and is structurally similar to U_4O_9. In a similar fashion, different structures have been proposed over the years with the research converging on common structures more recently. As with U_4O_9, the majority of work in the literature consists of structural and thermodynamic studies with very few publications on its other properties. The present section gives some background on the material and describes the simulations used to examine structures of U_3O_7 stoichiometry.

4.4.1 U_3O_7 Background

U_3O_7 is a fluorite based oxide, with a density of 11.35 - 11.42 gcm^{-3}, slightly higher than U_4O_9 (described in section 4.2.2), in keeping with the greater oxygen content [19]. Like the other fluorite based oxides, it exhibits non-stoichiometry with four known polymorphs falling in the O/U ratio range 2.27 to 2.38 generally classed as U_3O_7 [175]. As another intermediate oxidation product, it is generally reported to form during UO_2 oxidation at high pressure [17] or when UO_2 leaches into water [176]. Similarly to U_4O_9 the structure has been rationalised in terms of 4 x 4 x 4 UO_2 supercells housing periodic arrangements of O_i defect clusters. Allen *et al* proposed the same <110> aligned 2:2:2 Willis cluster chains but spaced $\frac{3}{2}\sqrt{2}a_0$ apart from one another, where a_0 is the lattice parameter of the UO_2 unit cell [30]. Nowicki *et al* [177] and later Desgranges *et al* [31] used neutron diffraction measurements to determine a similar structure to U_4O_9, proposing ordering of cuboctahedral defect clusters. Most recently, Andersson *et al* used DFT to apply their split interstitial clustering model to U_3O_7, finding split quad interstitials to be the most stable arrangement at that stoichiometry [32].

α-U_3O_7 is obtained by slowly oxidising UO_2 in dry air at 373 K [178], neutron diffraction experiments determined it has a tetragonal unit cell with the *I4/m* space group. The O/U ratio is found to be 2.27-2.33 and the lattice parameters for the primitive cell are a=b=5.46 Å, c=5.40 Å [177]; the full cell is a 2 x 2 x 2 expansion. β-U_3O_7 can be synthesised by monitoring oxidation of UO_2 (at less than 570 K) and quenching the reaction at the appropriate stoichiometry. It crystallises in a tetragonal *I-42d* unit cell (a=b=21.5898 Å, c=22.229 Å) with an O/U ratio of 2.33 [31] (Figure 4.08). The coordination in this polymorph is the same as in U_4O_9 but with a higher proportion of nine- and ten-fold coordinate sites. The structure is significantly more disordered than U_4O_9 with increased distortion to the uranium sublattice as well. There are, however, clear channels of oxygen ions at regular fluorite anion locations running along the *x*, *y* and *z* axes (viewable along the *x* and *z* axes in Figure 4.08(a)). γ-U_3O_7, or $U_{16}O_{37}$ as it is more commonly referred to, is a further tetragonal polymorph with an O/U ratio of 2.31, but is harder to isolate than the previous two modifications [179]. It has been prepared by annealing β-U_3O_7; however as with α-U_3O_7 only the pseudo-cell parameters have been determined, a = b = 5.407 and c =

5.497 Å [19]. Finally there is high pressure U_8O_{19} (O/U ratio 2.375), also known as δ-U_3O_7, which has a density of 11.34 gcm^{-3} and is formed at pressures of at least 30 kbar and temperature greater than 673 K [180]. Again, only the pseudo-cell parameters have been determined with a = 5.378, b = 5.559, c =- 5.490 Å and β = 90.29 °. The large difference in X-ray scattering power for uranium and oxygen meant, historically at least, that single crystals were required to determine oxygen positions; however the sample instability prevents single crystal preparation [179]. Powder neutron diffraction is more effective but resolution was limited when most of these experiments were carried out and there has been relatively little work on these oxides since, with the notable exception of β-U_3O_7 [31].

The low inherent stability of U_3O_7 has limited the amount of experimental data collected on the material. Westrum *et al* recorded heat capacities for the α- and β- polymorphs [181] and free energy and enthalpy of formation have also been reported for the more stable β-U_3O_7 [129]. Beyond this, He *et al* predicted an electronic band gap of 1.59 eV using the LSDA + U [172].

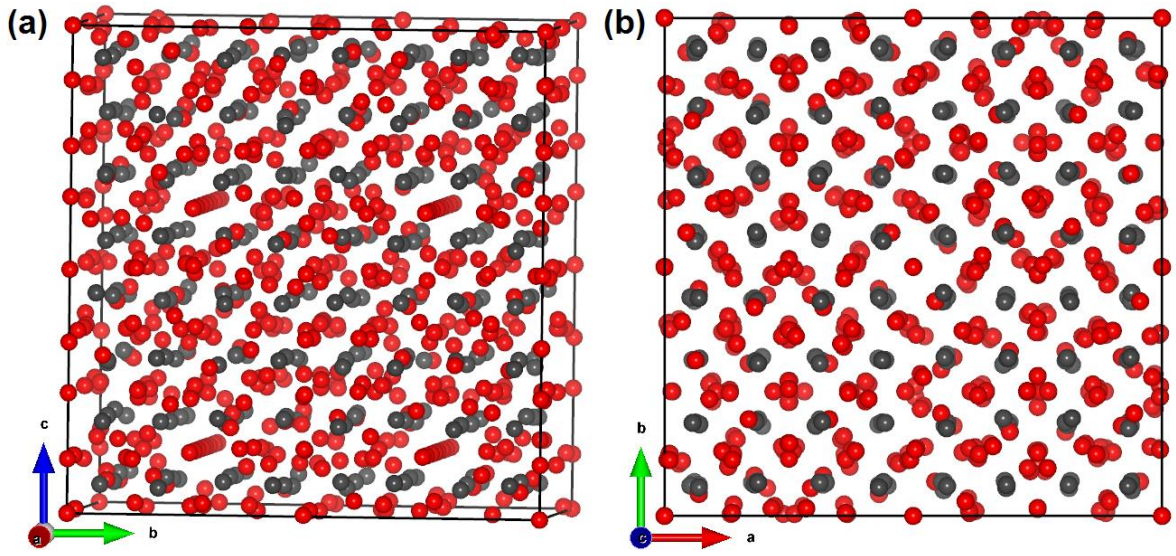

Figure 4.08 – Experimentally determined structure of β-U_3O_7 (a) slightly rotated to view fluorite oxygen channels and (b) orientated along the *z* axis [31].

4.4.2 Simulation of U_3O_7 ($UO_{2.33}$) Phases

As with U_4O_9, the experimentally determined U_3O_7 cell is prohibitively large to simulate using the DFT methods employed in this thesis at this time, but again it can be viewed as a defective fluorite structure, and so the defective supercell approach described in section 3.3.2 has also been used here. A further layer of complexity is that U_3O_7 stoichiometry requires the UO_2 cell to be expanded by a multiple of three in a least one direction. A 3 x 1 x 1 expansion yields a 36 atom cell, which is a sufficiently large number of atoms, however it only features a double layer of uranium and oxygen atoms in two dimensions which raises concerns of effects from small periodic boundary conditions. A 3 x 2 x 1 expansion gives a 72 atom cell with a double layer in only one dimension (as in the successful U_4O_9 simulations), however if all O_i and I_2^x arrangements are to be considered then over 3000 calculations must be performed.

To overcome this issue the cubic fluorite cell was re-orientated to an orthorhombic cell such that the cubic <111> direction becomes the <100> in the orthorhombic cell. The basic unit cell produced from this contains 18 atoms and so when doubled (in the *y* direction) to give a 36 atom simulation cell, either four point O_i or two I_2^x clusters must be introduced to give U_3O_7 stoichiometry. The SOD program [173] calculated a total of 26 inequivalent I_2^x configurations and 45 unique O_i arrangements, to give a considerably more manageable 71 simulations in total. Although the orthorhombic cell is smaller than the cubic one used for U_4O_9 it is still large enough to accommodate Willis cluster chains.

The relaxed pure orthorhombic UO_2 cell (36 atom) has the lattice parameters a = 7.814, b = 6.716 and c = 9.532 Å. To ensure the orthorhombic cell is equivalent to the cubic cell an identical *k*-mesh density was used and a number of properties were calculated for the orthorhombic cell. Table 4.03 contains these properties and demonstrates the strong agreement between the two cells.

Table 4.03 – Comparison of various properties of UO_2 calculated in cubic and orthorhombic cells.# refers to the number of *k*-points used in a simulation cell, ρ to the *k*-point density and *B* refers to the bulk modulus.

Symmetry	Method	*k*-points		Volume/U atom (Å^3)	E_{Form} (eV)	*B* (GPa)	Band Gap (eV)
		#	ρ (#/Å^3)				
Cubic	Experiment	-	-	40.88	-11.25	208.9	2.14
Cubic	PBE + U	12	0.10	42.66	-11.03	215.1	2.06
Orthorhombic	PBE + U	20	0.10	42.61	-11.05	214.3	2.06

The full results table of the 71 simulations can be found in Appendix B and Figure 4.09 provides a graphical representation of the complete set of results, showing the formation energy with respect to UO_2 and the volume change from the UO_2 cell.

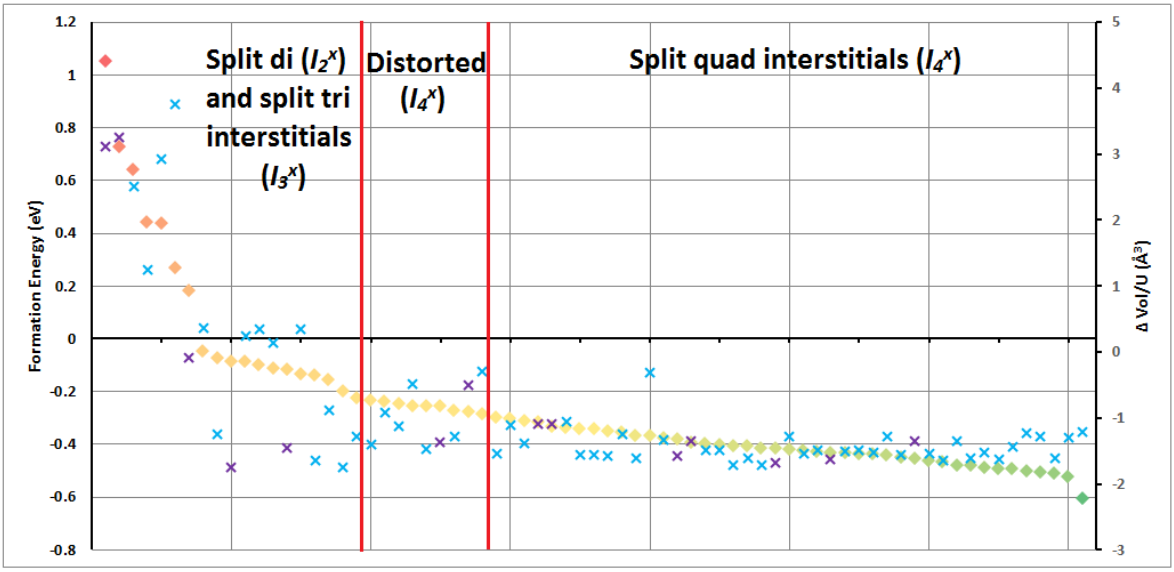

Figure 4.09 – Plot showing predicted formation energies for each calculated U_3O_7 phase (diamonds) and percentage change in volume relative to UO_2 per uranium atom (crosses). Purple cross markers indicate one or more U^{6+} ions were predicted in that system.

The simulations predict a narrower range of cluster types than was found in the U_4O_9 calculations (although this could possibly arise from the slightly smaller simulation cell). The least stable configurations contained (distorted and undistorted) I_2^x and I_3^x clusters, often accompanied by point O_i, however no pure O_i systems were found. A small number of systems containing distorted I_4^x clusters were found, having intermediate stability, and the most stable arrangements all contained undistorted I_4^x clusters, which align along (cubic) <100> directions (Figure 4.10 (a) and (b)). These results are in line with those reported by Andersson *et al* with their LSDA + U simulations [32]. The fact that no

systems containing only O_i were found shows that they are so unstable at this stoichiometry that they will not form at all. Interestingly, all traces of 2:2:2 Willis cluster chains are gone at U_3O_7 composition and attempts to stabilise them were ineffective, suggesting they are energetically unstable here despite their dominance at U_4O_9 and $UO_{2.125}$ stoichiometry.

In the vast majority of simulations oxidation of U^{4+} is to U^{5+}, although more systems, some surprisingly stable, are found to contain U^{6+} ions. I_4^x based systems never contain more than one U^{6+} whereas the less stable distorted I_4^x and I_2^x/I_3^x systems often contain more, three and five respectively for the two least stable configurations. These two highly unstable systems (E_{form} = 0.73-1.05 eV) also contain the highly oxidising peroxide ion (O_2^{2-}) that was observed in one of the U_4O_9 calculations and previously reported in DFT calculations by Andersson *et al* in their study of UO_2 oxidation [32]. The peroxide bond is slightly longer than in U_4O_9 at 1.479 Å but is unmistakeably a peroxide ion; Figure 4.10 (c) and (d) shows the least stable peroxide containing cell. The magnetisation of oxygen atoms in the peroxide ions has been checked and is confirmed to be zero, ruling out the superoxide ion (O_2^-). Thus, although U^{6+} is not indicative of peroxide ions the opposite is true with U^{6+} always accompanying O_2^-. The views along the *z* axis shown in Figure 4.10 (a) and (c) are showing {111} cubic fluorite planes, whereas (b) and (d) have been rotated to show the defects in a view where the cubic ordering is more clearly visible.

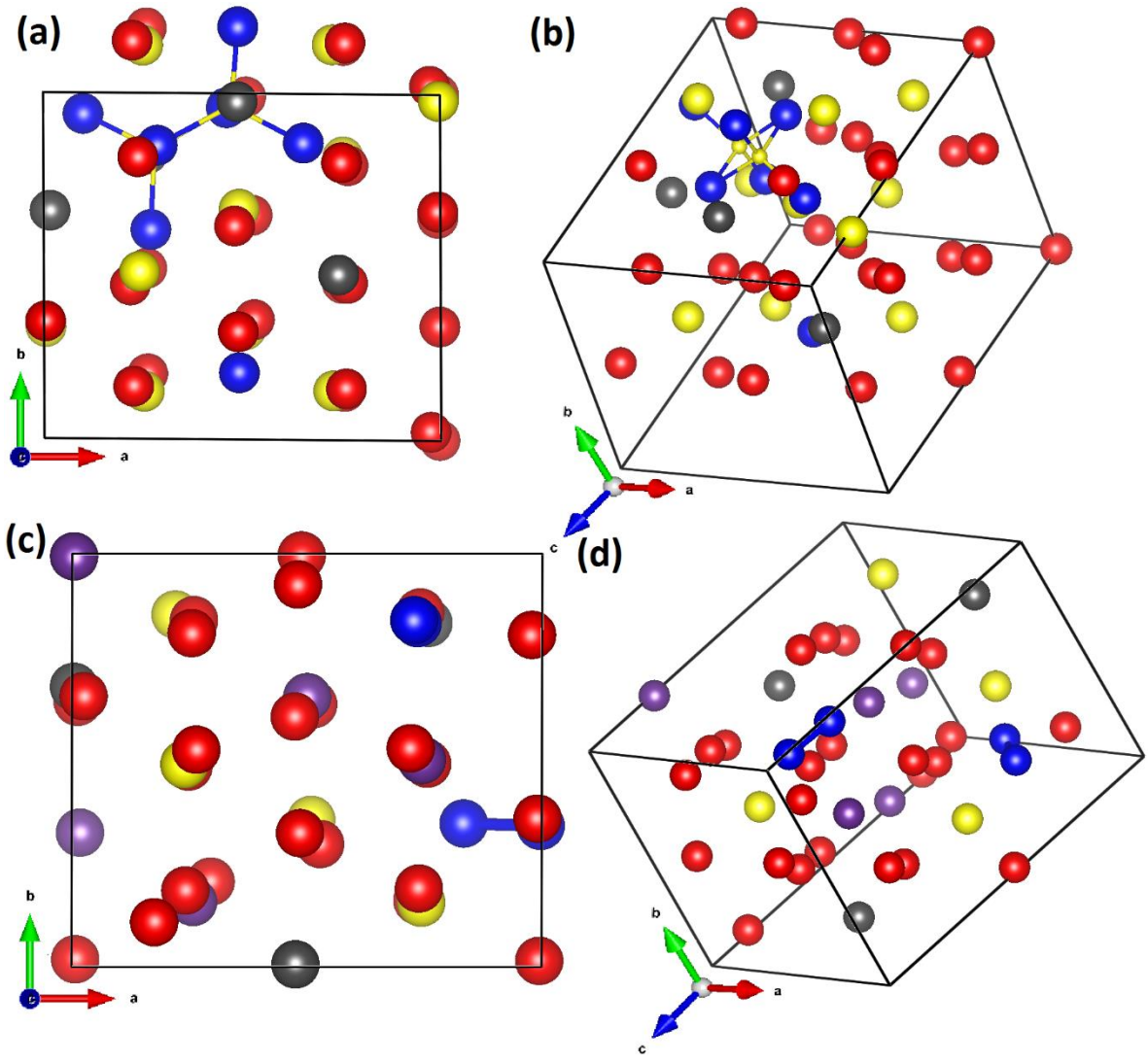

Figure 4.10 – Relaxed U_3O_7 phases. Quad interstitial cluster (a) view along *z* axis and (b) rotated to show cubic fluorite planes. Low stability peroxide containing phase (c) view along *z* axis and (d) rotated to show cubic fluorite planes. Grey spheres are U^{4+} ions, large yellow spheres are U^{5+}, purple are U^{6+}, red are lattice oxygen (i.e from UO_2), small yellow spheres are V_O and blue spheres are used to show defective oxygen species.

Although the U_3O_7 simulations show a slightly larger propensity for oxidation to U^{6+} the results show that U^{6+} is typically unstable at this composition and so, most likely, is unstable in fluorite based oxides in general.

The coordination of uranium atoms is similar to that found in U_4O_9, as sites that are not adjacent to defects mostly retain eight-fold coordination, albeit usually slightly distorted from perfect cubic coordination. No seven-coordinate sites were observed, and in close

proximity to defects there is a higher proportion of nine- and ten-fold coordination. Typical U^{5+} (and U^{4+}) coordination at sites adjacent to I_4^x clusters is ten-fold (six shorter and four longer bonds) (Figure 4.11 (a)), with one of the fluorite cube corners replaced by three O_i (from one half of a I_4^x cluster). This is not so different from the equivalent 2:2:2 Willis adjacent U^{5+} ions in U_4O_9, where two of the fluorite oxygen ions were withdrawn slightly from the uranium to give eight-fold coordination. In the highly unstable, peroxide containing simulations the fluorite cube corner oxygen is replaced by a O_2^{2-} ion, yielding a coordination number of nine (Figure 4.11(b)). This is more of a contrast to the U^{6+} systems in U_4O_9 which were characterised by formation of two shorter, collinear U-O bonds, resembling the uranyl ion.

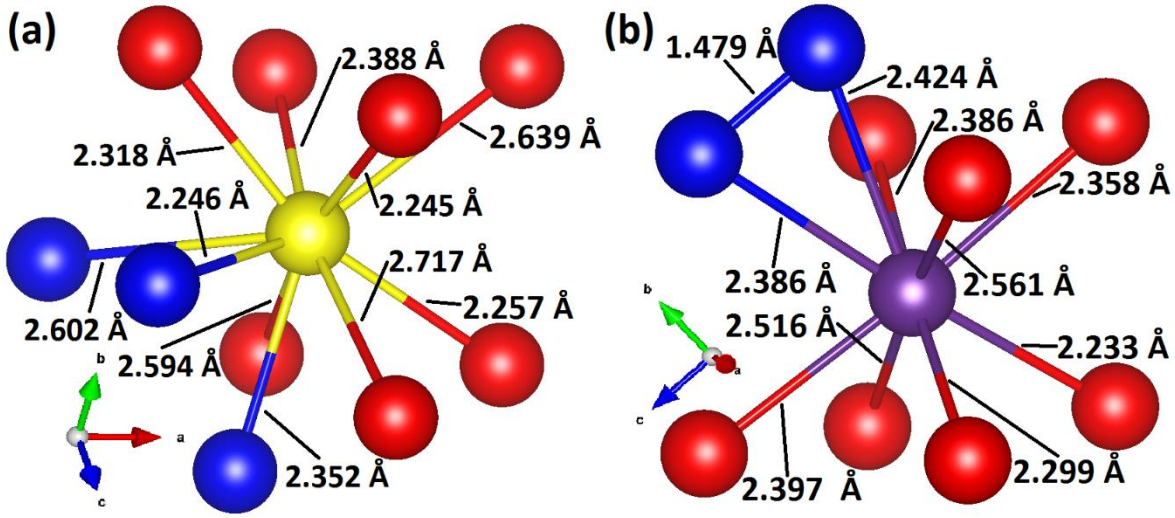

Figure 4.11 – Coordination of U^{5+} adjacent to a I_4^x cluster (a) and U^{6+} adjacent to a O_2^{2-} ion (b). Yellow spheres are U^{5+} ions, purple are U^{6+}, red are lattice oxygen (i.e from UO_2) and blue spheres are used to show defective oxygen species.

The average U-O bond length at U^{5+} sites is 2.436 Å, noticeably longer than the 2.294 Å found in U_4O_9 or 2.368 Å observed in UO_2. The same trend is apparent at U^{6+} sites where the mean bond length is 2.400 Å, compared to the 2.188 Å found in U_4O_9. The trend of shorter U^{6+}-O bonds, compared to U^{5+}-O bonds is retained though.

There is a strong positive correlation (r = 0.84) between U_3O_7 stability and volume change relative to the parent UO_2 lattice. The least stable systems show a marked volume increase while the most stable decrease. These findings are the opposite of that found in the U_4O_9 systems. They are also in contrast to the experimentally determined structure, where a

slight volume increase (1.85 %) compared to UO_2 is reported [31]. The origin of the slight lattice contraction found here arises from the larger lattice relaxation compared to U_4O_9, which involves greater displacement of oxygen ions from their lattice sites, as well as greater disruption to the uranium sublattice. The relaxation most likely is due to the higher proportion of U^{5+} ions in the lattice. The larger relaxation (compared to U_4O_9) allows for more efficient filling of space and a reduction of lattice strain thus giving a small overall reduction in the unit cell volume. In the same manner that was discussed for U_4O_9, the decrease in volume for the stable structures, compared to the increase reported experimentally suggests competing kinetically and thermodynamically stable structures. The COT-12 based U_3O_7 structures seen experimentally could be formed via kinetically controlled processes, whilst the I_4^x based U_3O_7 polymorphs predicted by the calculations here (and Andersson [32]) describe the most thermodynamically stable configuration. There is also the possibility, however, that the relatively small simulation cell used here (compared to the other defect simulations in this thesis) is preventing formation of cuboctahedral clusters.

In addition to the structural considerations the electronic band gaps of all U_3O_7 phases have been calculated, with the most stable systems found to have a gap between 1.41 and 1.67 eV. This is quite comparable to the result found for U_4O_9, 1.48 – 1.61 eV, and that calculated by He *et al* using the LSDA + U, 1.59 eV [172].

4.5 UO_2-$UO_{2.33}$ Structural Comparison

The comparatively small volume changes (considerably less than the difference between experimental and calculated pure UO_2) in the UO_{2+x} phases compared to the parent fluorite UO_2 lattice suggest there is relatively little distortion occurring. Indeed, the very presence of defect clusters may arise from the fact they can be introduced without a marked distortion of the lattice. Examining the structures of these phases (Figures 4.03, 4.06 and 4.10) reinforces this view, although it appears that with increasing oxygen content there is greater distortion from the original UO_2 structure, i.e. $UO_{2.125}$ is least distorted and U_3O_7 is most distorted. To provide a more detailed analysis of this relationship the radial distribution functions (RDFs) (Figure 4.12) and neutron diffraction patterns (Figure 4.13)

have been calculated for UO_2 and the energetically most stable $UO_{2.125}$ (labelled as $UO_{2.13}$), U_4O_9 and U_3O_7 systems.

The RDFs in Figure 4.12 provide detailed information on specific uranium and oxygen sublattice disorder. The U-U RDF shows the most similarity between all four structures with strong peaks for each in all the fluorite positions, meaning that it remains relatively unchanged during the oxidation process. This agrees well with experimental observations that the uranium sublattice is not affected as much during oxidation [18] (Figures 4.04 and 4.08). As expected, the $UO_{2.13}$ RDF departs from UO_2 the least and U_4O_9 and U_3O_7 do so slightly more. The same is true with the U-O RDFs, where the peaks broaden more significantly with increased stoichiometry as a wider variety of U-O bond lengths emerge, although there are still clearly stronger peaks at the fluorite locations. U_4O_9 has wider peaks in greater abundance, indicating a larger variety of bond lengths are found, consistent with greater local distortion. The O-O RDFs all show the largest discrepancy with the fluorite UO_2 function, indicative of the large distortions to the oxygen sublattice. The peaks broaden out with increasing oxygen stoichiometry, with comparable U_4O_9 and U_3O_7 RDFs which feature more additional small peaks between the fluorite ones compared to $UO_{2.13}$.

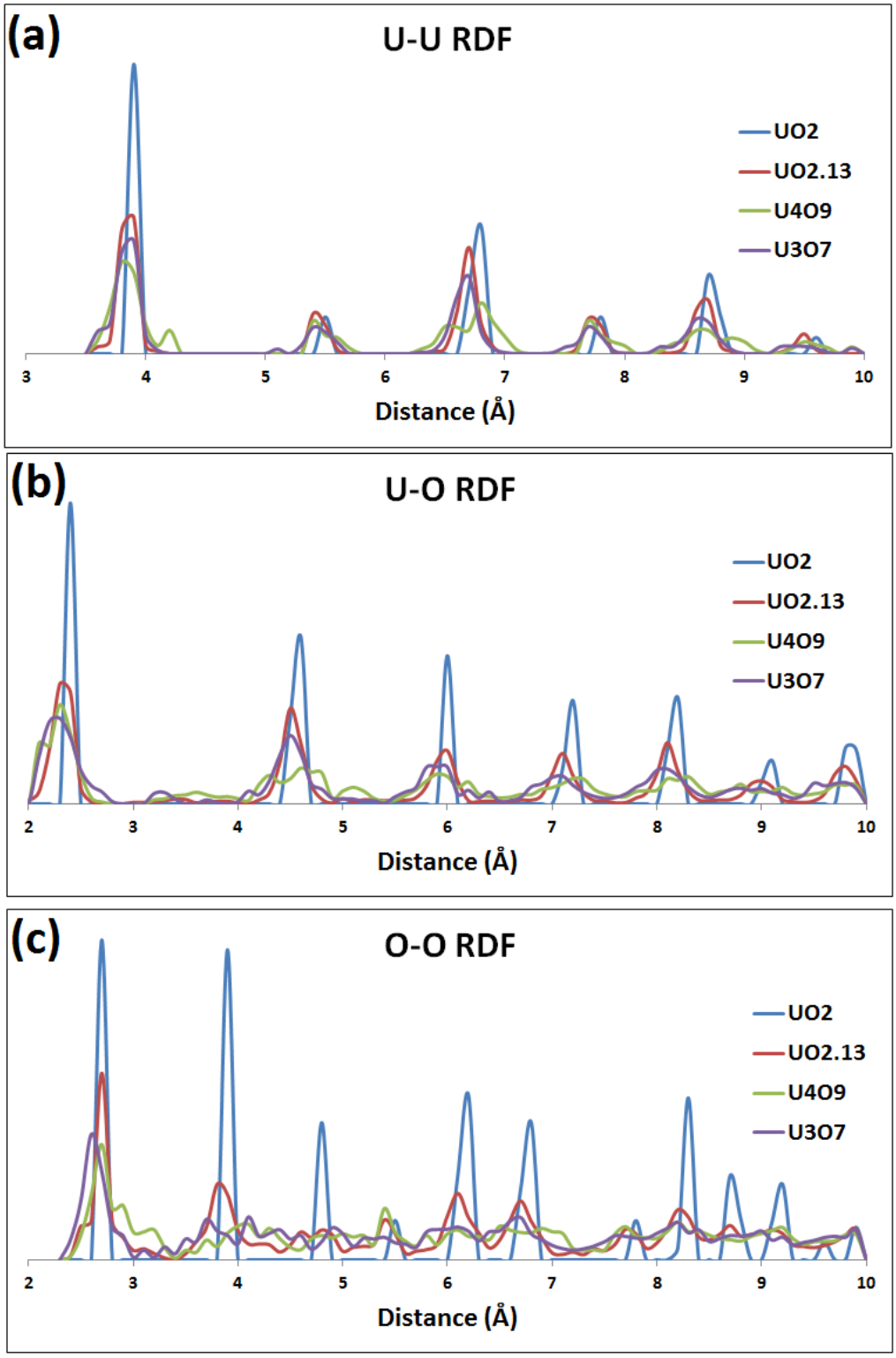

Figure 4.12 – PBE + U calculated radial distribution functions (RDFs) for fluorite based phases. (a), (b) and (c) show U-U, U-O and O-O RDFs respectively.

Examining Figure 4.13 it is clear that each hyperstoichiometric fluorite based phase has strong peaks close to the original fluorite peaks (UO_2). The $UO_{2.13}$ pattern is closest to UO_2, which is expected given the smaller amount of interstitial oxygen incorporated in the lattice. The U_4O_9 and U_3O_7 patterns are quite similar to one another in their distribution of peaks away from the pure fluorite ones, although U_4O_9 is actually more disordered at low 2θ (30 – 50 °).

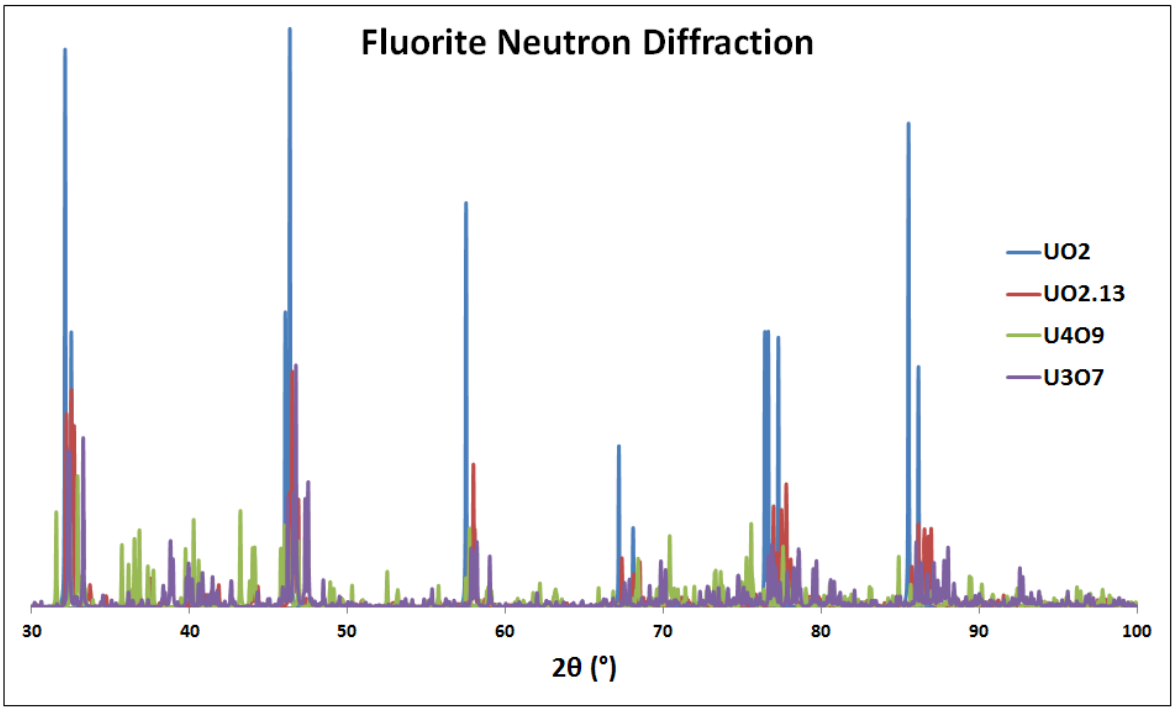

Figure 4.13 – Simulated neutron diffraction patterns for fluorite based phases from PBE + U calculations.

When the two types of clustering exhibited in the U_4O_9 and U_3O_7 phases are considered there is more local disorder (i.e. close to the defect clusters) in U_4O_9 than U_3O_7; as demonstrated in Figures 4.06 and 4.10 which show the coordination of uranium ions adjacent to defect clusters. In U_3O_7 the coordination number at such sites has increased to ten (from eight in UO_2), however seven of these oxygen ions remain largely at the cubic fluorite sites. The additional three oxygen ions then form an equilateral triangle, the centre of which is the original fluorite lattice site. By comparison, in U_4O_9 the equivalent site has eight-fold coordination but only four of the oxygen ions are in their original fluorite locations. The other four have been pushed outwards due to formation of the 2:2:2 Willis

cluster and now form a flattened tetrahedron (as opposed to the planar configuration of the fluorite based ions). At higher 2θ (> 50 °) the U_4O_9 and U_3O_7 patterns show better agreement with one another, consistent with comparable long range disorder in the structures.

Figures 4.14 and 4.15 compare the simulated neutron diffraction patterns of PBE + U predicted and experimentally determined U_4O_9 and U_3O_7 polymorphs.

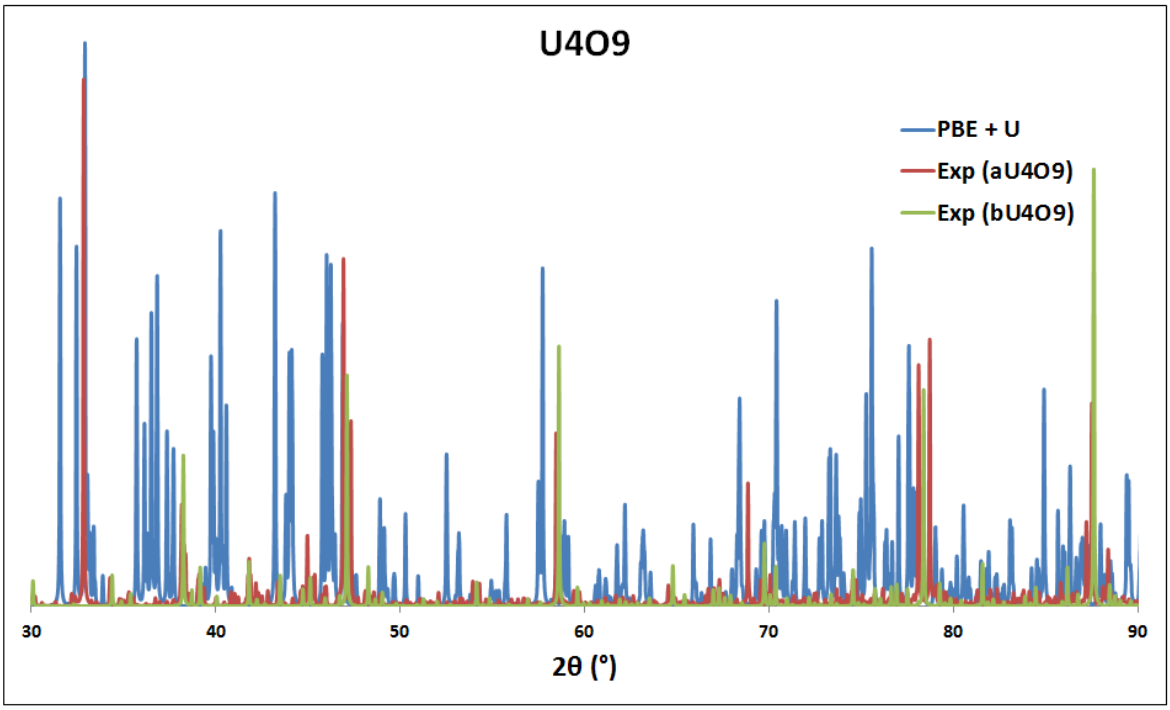

Figure 4.14 – Simulated neutron diffraction patterns for PBE + U calculated (2:2:2 Willis chain based) and experimentally determined (COT-12 based) U_4O_9 polymorphs.

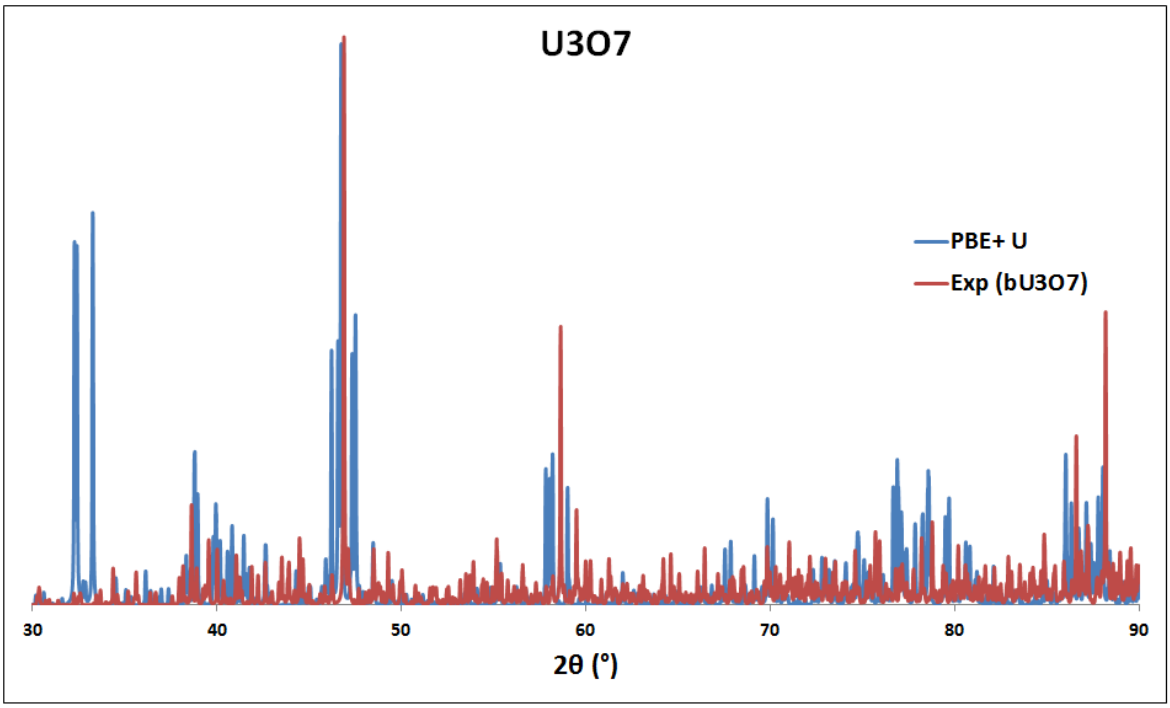

Figure 4.15 – Simulated neutron diffraction patterns for PBE + U calculated (I_4^x based) and experimentally determined (COT-12 based) U_3O_7 polymorphs.

The experimentally determined structures of the two oxide phases feature cuboctahedral based clustering arrangements, compared to the 2:2:2 Willis based U_4O_9 and I_4^x based U_3O_7 predicted by the calculations. In both instances there are considerably more peaks present in the predicted structures, suggesting greater disorder. The U_3O_7 pattern shows better agreement with experiment, with small groups of peaks around each major experimental peak. Although the calculated U_4O_9 pattern has peaks in line with those from the two experimental structures there are too many other peaks present to draw any significant similarities between the patterns. These large differences in neutron diffraction patterns are expected given the difference in structural composition between experiment and calculations here. As discussed in sections 4.4.2 and 4.4.4, the predicted volumes suggest the experimental structures are formed via kinetically controlled processes and the thermodynamically most stable products are located by the calculations.

4.6 Conclusions

UO_{2+x} fluorite based systems have been studied in the stoichiometry range $0.0625 < x < 0.33$, with single isolated defect clusters at lower amounts of excess oxygen to more complex arrangements of multiple clusters at higher levels of excess oxygen. In all of these defective fluorite materials there is a clear preference for charge compensation via oxidation to U^{5+}, although at $UO_{2.33}$ (U_3O_7) stoichiometry U^{6+} ions become more common in relatively stable systems.

The split interstitial family of clusters were found to be the most stable individual clusters in UO_2, with the I_2^x the most stable of these. Cuboctahedral clusters were generally found to be less stable, although the COT-13 was predicted to be more stable than the least stable split interstitial (I_4^x). 2:2:2 Willis clusters were found to be unstable with respect to I_2^x clusters, always relaxing to this configuration. The order of stability of defect clusters has been attributed mainly to lower local concentrations of U^{5+}. No U^{6+} ions were encountered in any of these simulations, which go up to a stoichiometry of 2.16 with the COT-13 system.

At $UO_{2.125}$ and $UO_{2.25}$ (U_4O_9) compositions, initial configurations of point O_i and I_2^x clusters were found to relax to chains of 2:2:2 Willis clusters. Although some unstable structures were found to contain U^{6+} none appeared in the stable ones, demonstrating the instability of U^{6+} at these stoichiometries. The defect chains cause fairly significant local distortions of the fluorite lattice (with comparatively less long range), resulting in the largest departure from the parent fluorite lattice for this system. COT-12 and I_4^x based U_4O_9 systems, equivalent to those reported in the literature, were also trialled and found to be less stable than the 2:2:2 Willis cluster chain phases.

At $UO_{2.33}$ (U_3O_7) stoichiometry single I_4^x clusters emerged from the simulations as the most stable U_3O_7 composition, with no sign of the 2:2:2 Willis clusters which were predicted for $UO_{2.125}$-$UO_{2.25}$ stoichiometry. This change in clustering behaviour, and the fact that I_4^x were earlier found to be the least stable cluster type in UO_2, provide clear evidence that the clusters are stoichiometry dependent, only forming at the appropriate composition. The excess charge introduced by additional oxygen is compensated by oxidation to U^{5+} in all of

the most stable systems. U^{6+} is formed in a minority of systems, suggesting U^{5+} is still energetically preferred at this stoichiometry but there is not as much of a barrier to U^{6+} formation as at U_4O_9 stoichiometry. The return to split-interstitial clustering is accompanied by slightly reduced local distortion from the fluorite lattice, reflected in the predicted neutron diffraction and RDF profiles of this phase.

The predicted volume changes relative to UO_2 for the most stable U_4O_9 and U_3O_7 are positive and negative respectively for the most stable systems, and the opposite for the least stable systems. Experimental results, in the literature, indicate a decrease in volume for U_4O_9 and increase for U_3O_7, leading to the tentative conclusion that the predicted phases in this thesis are the thermodynamically stable phases and the kinetic products are generally observed experimentally. Indeed, there remains the possibility that using larger simulation cells would reveal cuboctahedral defect clusters dominate. Although there is the possibility that the (relatively small) unit cell size has influenced the species found in these calculations.

Further oxidation of U_3O_7 leads to formation of U_2O_5, which can exist in both fluorite based and layered structures, thus the next chapter examines this phase.

Chapter 5

5 Layered U_2O_5

Experimental investigations report that U_2O_5 is the most difficult of the uranium oxides to stabilise and is consequently the least well characterised. Both fluorite based and layered U_2O_5 phases have been identified by using their respective densities and so the transition between the two types of structure clearly occurs at this stoichiometry. This chapter describes the reported U_2O_5 research and provides the results of simulations to evaluate the structure.

A paper has already been published concerning the study of δ-U_2O_5 in Dalton Transactions entitled "*Density Functional Theory Investigation of the Layered Uranium Oxides U_3O_8 and U_2O_5*" [73].

5.1 U_2O_5 Background

The highest oxygen stoichiometry found in fluorite based uranium oxides are α-, β- and γ-U_2O_5. The only significant experimental study of these materials is from Hoekstra *et al*, detailing their synthesis and structures [19]. α-U_2O_5 is prepared by heating a mixture of UO_2 and U_3O_8 at 673 K and 30 kbar and has a density of 10.5 gcm^{-3}, approximately 0.7 gcm^{-3} less than other fluorite based phases, suggesting it may be slightly closer to layered type oxides. β-U_2O_5 was prepared by heating the same mixture in excess of 1073 K at 40-50 kbar and was determined to have a hexagonal structure with a=b=3.813 Å and c=13.180 Å and density of 11.15 gcm^{-3}. γ-U_2O_5 was somewhat more problematic to synthesize, requiring temperatures in excess of 1073 K and greater than 60 kbar pressure, normally forming with the β- modification. Indexing the XRD pattern yielded a monoclinic cell with a=5.410, b=5.481, c=5.410 Å and β=90.49 ° and it was determined to have a density of 11.36 gcm^{-3}. The atomic coordinates and space groups of these materials are still unknown,

although given the densities they presumably follow the same pattern of O_i defect clusters in fluorite UO_2 cells. The {001} plane of the hexagonal β- polymorph is most likely equivalent to the {111} UO_2 plane as the uranium sublattice has a hexagonal arrangement in that orientation and the relation is observed for hexagonal γ-U_3O_8.

There are no published atomic coordinates for the fluorite based U_2O_5 polymorphs in the literature, meaning a UO_2 supercell with additional O_i is required to investigate this type of structure. To apply the same methodology used for modelling fluorite U_4O_9 and U_3O_7 phases at least 36 atoms are required to give a reasonable sized simulation cell. Using the cubic 48 atom cell a total of 483 calculations would be required to cover every unique starting configuration, too large a number to model at present with the resources available. Even using the orthorhombic 36 atom cell (used for U_3O_7 in Chapter 4) a total of 254 simulations are needed to examine every starting arrangement, again impractical for us to model with DFT at present. Thus, fluorite U_2O_5 has not been modelled and U_3O_7 marks the upper limit of the fluorite materials simulated here.

The first of the layered type structures discussed in the literature is δ-U_2O_5 and it is the only reported layered U_2O_5 polymorph (Figure 5.01). Details of its synthesis could not be obtained however it has a density of 8.22 gcm^{-3} and crystallises in the orthorhombic *Pnma* space group with a= 6.849, b=8.274 and c=31.706 Å [182]. This 22 formula unit cell contains uranium ions in a mixture of six- (distorted octahedral) and seven-fold (distorted pentagonal bipyramidal) coordinate positions. There is a slight bending of the interlayer U-O bonds; which can be observed in Figure 5.01, resulting in some O-U-O chains only being partially eclipsed. The structure is very similar to U_3O_8 (Chapter 6), essentially an oxygen deficient version of this higher oxide.

No thermodynamic information has been gathered experimentally for U_2O_5, nor has there been any further structural investigation since the original experiments of Hoekstra [19] and Kovba [182]. Early XPS studies have suggested a mixture of U^{4+} and U^{6+} ions [183] but more recent experiments have proposed U_2O_5 is composed entirely of U^{5+} ions [184]. There is only one computational study of δ-U_2O_5 in the literature, which reported it to be thermodynamically unstable (with respect to U_3O_8) with the highest formation energy of any uranium oxide [32].

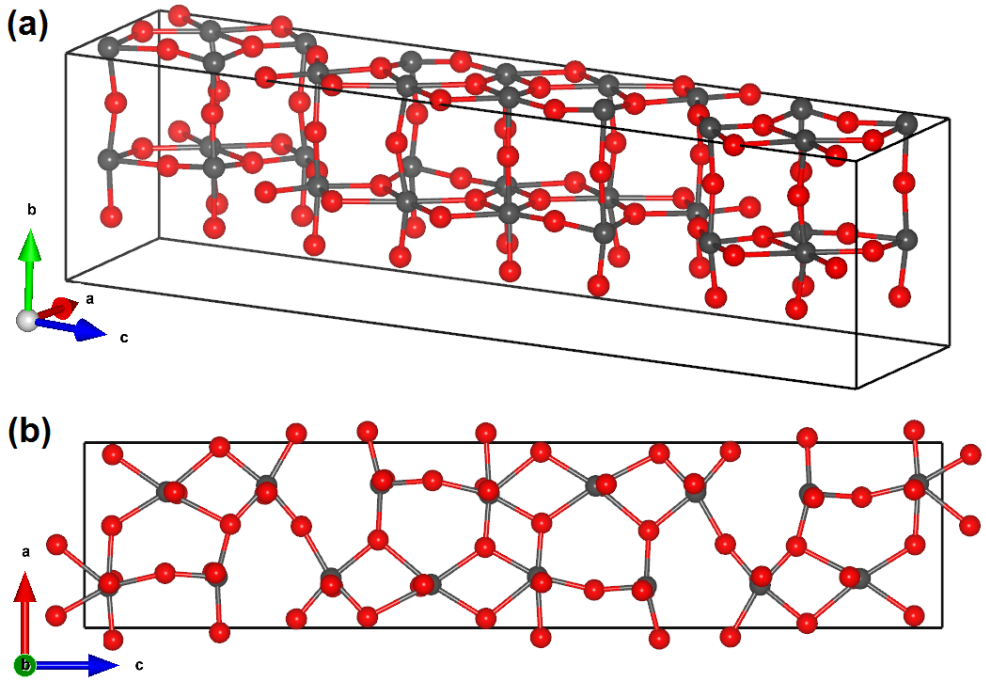

Figure 5.01 – The experimentally determined structure of δ-U_2O_5 (a) orientated to show the layers and (b) orientated along the *y* axis to show the equatorial uranium coordination [182].

Due to the difficulty in synthesising layered U_2O_5 at the time of writing, a number of alternative M_2O_5 (where M is an actinide or transition metal) structures have been investigated, replacing the metal ion with uranium. As these structures have not been reported experimentally for uranium oxides no discussion of their synthesis and background can been provided.

Table 5.01 – Predicted properties of U_2O_5. Space groups are calculated to a tolerance of 0.001 Å for both the initial (experimental) and final (relaxed) structures using Materials Studio [192]. Reported energies are formation energy per uranium ion relative to UO_2*. Δ% is the percentage difference between a calculated structure and experiment and is not presented for any of the M_2O_5 structures (where M is a metal ion other than uranium).

Study	Phase	Method	Lattice Parameters (Å)			Lattice Parameters (°)			Vol/U (Å^3)	Space Group	E_{Form} (eV)
			a (Δ%)	*b* (Δ%)	*c* (Δ%)	*α*	*β*	*γ*			
Kovba [182]	**δ-U_2O_5**	Exp	6.85	8.27	31.71	90.0	90.0	90.0	56.15	*Pnma*	-
		PBE + U	7.02 (2.5)	8.42 (1.8)	31.46 (-0.8)	90.0	90.0	90.0	58.15	*Pnma*	-0.86
Forbes [185]	**Np_2O_5**	Exp‡	8.17	6.58	9.31	90.0	116.1	90.0	56.23	*P2/c*	-
This Work		PBE + U	8.16	6.82	9.41	90.0	116.0	90.0	58.80	*P1*	-0.95
(α) Gruehn [186]	**Nb_2O_5**	Exp‡	3.98	3.83	12.79	90.0	90.8	90.0	48.72	*C2/m*	-
This Work		PBE + U	4.21	4.35	14.89	105.7	90.0	90.0	65.69	*P1*	-0.83
(β) Zibrov [187]		Exp‡	5.22	4.70	5.93	90.0	108.6	90.0	34.46	*C2*	-
This Work		PBE + U	7.85	5.48	5.34	90.2	109.1	90.1	54.20	*P1*	-0.57
(γ) Andersson [188]		Exp‡	28.51	3.83	17.48	90.0	120.8	90.0	51.23	*C2/m*	-
This Work		PBE + U	31.26	4.26	18.97	90.0	124.8	90.0	64.82	*P1*	-0.57
Zibrov [189]	**Ta_2O_5**	Exp‡	12.79	4.85	5.53	90.0	104.3	90.0	41.56	*C2/c*	-
This Work		PBE + U$^+$	14.28	5.30	6.14	90.0	104.0	90.0	56.42	*C2/c*	-0.70
Cocciantelli [190]	**V_2O_5**	Exp‡	9.95	3.59	10.04	90.0	90.0	90.0	44.8	*Pnma*	-
This Work		PBE + U	11.65	4.35	10.64	90.0	89.3	90.0	67.33	*P1*	-0.34
Filonenko [191]		Exp‡	7.11	3.57	6.28	90.0	90.1	90.0	39.92	*$P2_1/m$*	-
This Work		PBE + U	6.61	4.03	7.32	90.0	79.7	90.0	47.94	*Pm*	-0.31

‡ = Experimental data refers to the lattice parameters of parent M_2O_5 structure.

$^+$ = Imaginary vibrational modes were identified in this structure

* - $E_{\text{Form}} = E_{UO_2} - (E_{U_2O_5} - E_U - \frac{5}{2}E_O)$ (see section 2.4.4)

5.2 Structure and Stability of Layered U_2O_5

In addition to δ-U_2O_5 the other structures investigated include those of Np_2O_5 [185], Nb_2O_5 [186-188], Ta_2O_5 [189] and V_2O_5 [190, 191] polymorphs. Their experimental lattice parameters are included in the present work; however they are not directly comparable to the simulation results as the native metal ion has been changed to uranium. All relaxed structures retain the coordination environments of the original M_2O_5 systems, although the symmetry is often lowered. FM and AFM (<100>, <010> and <001>) magnetic orderings were used for δ-U_2O_5 and for all of the M_2O_5 structures with simulation cells of 28 atoms or less. The results from the PBE + U simulations found no energetic preference; indeed the resulting structures are almost identical. Despite the small structural differences between FM and AFM δ-U_2O_5 imaginary vibrational modes were found in the AFM, therefore only the FM results are included for all the structures here. See Appendix C for AFM (Np) U_2O_5 and δ-U_2O_5 results. The structural properties and relative energies of the various systems are collated in Table 5.01 whilst their relaxed structures are shown in Figures 5.02-5.06.

5.2.1 *Pnma* δ-U_2O_5

The coordination of uranium ions in δ-U_2O_5 remains the same on relaxation as the experimentally determined structure, with the bent axial bonds straightening out slightly (Figure 5.02 (a) and (b)). The axial bonds range between 2.105 and 2.107 Å, which is too long to be a uranyl bond and comparable to the axial bonds in α- and γ-U_3O_8 [73]. The layers stack in an eclipsed fashion such that the coordination of a given uranium ion is identical to the one directly above or below. The equatorial bonds are also similar to those in U_3O_8 and the structure as a whole is akin to an oxygen deficient U_3O_8 cell. As is customary with the PBE + U the cell volume is marginally overestimated, due to small expansions of the *a* and *b* lattice parameters. All uranium ions are predicted to be U^{5+}, consistent with uniform axial bond lengths at each uranium site, although two different types of coordination (distorted octahedral and distorted pentagonal bipyramidal) is less expected in light of this (Figure 5.02(c)).

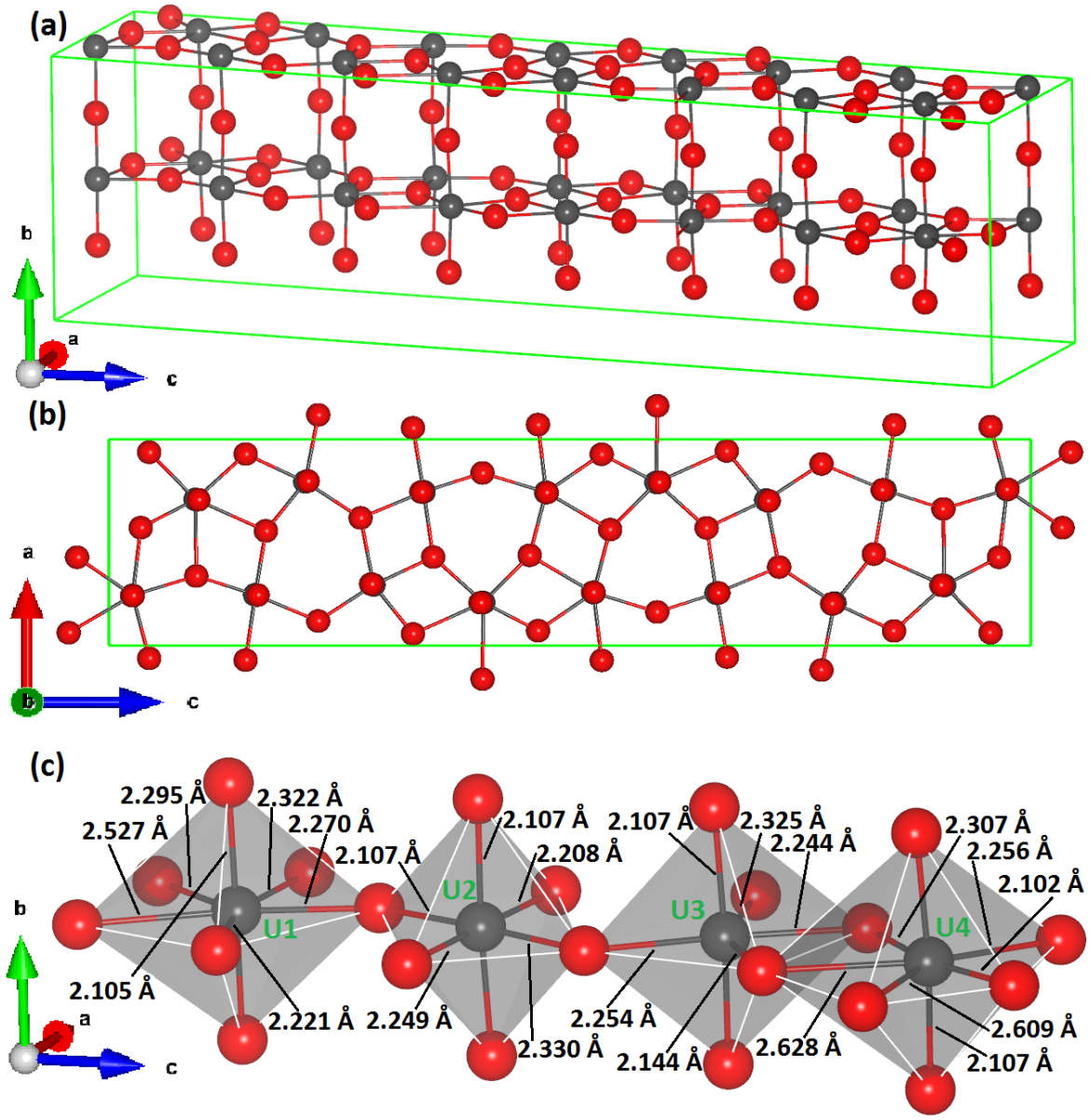

Figure 5.02 - PBE + U predicted structure of δ-U_2O_5: (a) *Pnma* unit cell, (b) top down view of unit cell and (c) uranium coordination at U1-4 (left to right). Black spheres are U ions (all 5^+), red are O and the unit cell is highlighted in green.

5.2.2 Np_2O_5 Structure

The Np_2O_5 structure [185] consists of three different metal sites, two have pentagonal bipyramidal coordination (U1 and U2) and one has octahedral coordination (U3) (Figure 5.03 (c)). There are two layers in the four formula unit monoclinic cell, with both containing two U3 sites and one of each pentagonal bipyramidal site. The stacking of layers

gives alternating octahedral and pentagonal bipyramidal coordination (Figure 5.03 (a)). Viewing the structure down the *x* axis (Figure 5.03 (b)), U3 eclipse one another whereas U1 and U2 are shifted apart slightly along the *y* axis. The consequence of this is slightly longer, tilted axial bonds at the U3 sites and shorter axial bonds at U1 and U2 that are perpendicular to the layers. At 1.973 Å the shorter axial bonds at pentagonal bipyramidal sites are slightly longer than a uranyl ion bond (1.7 - 1.9 Å).

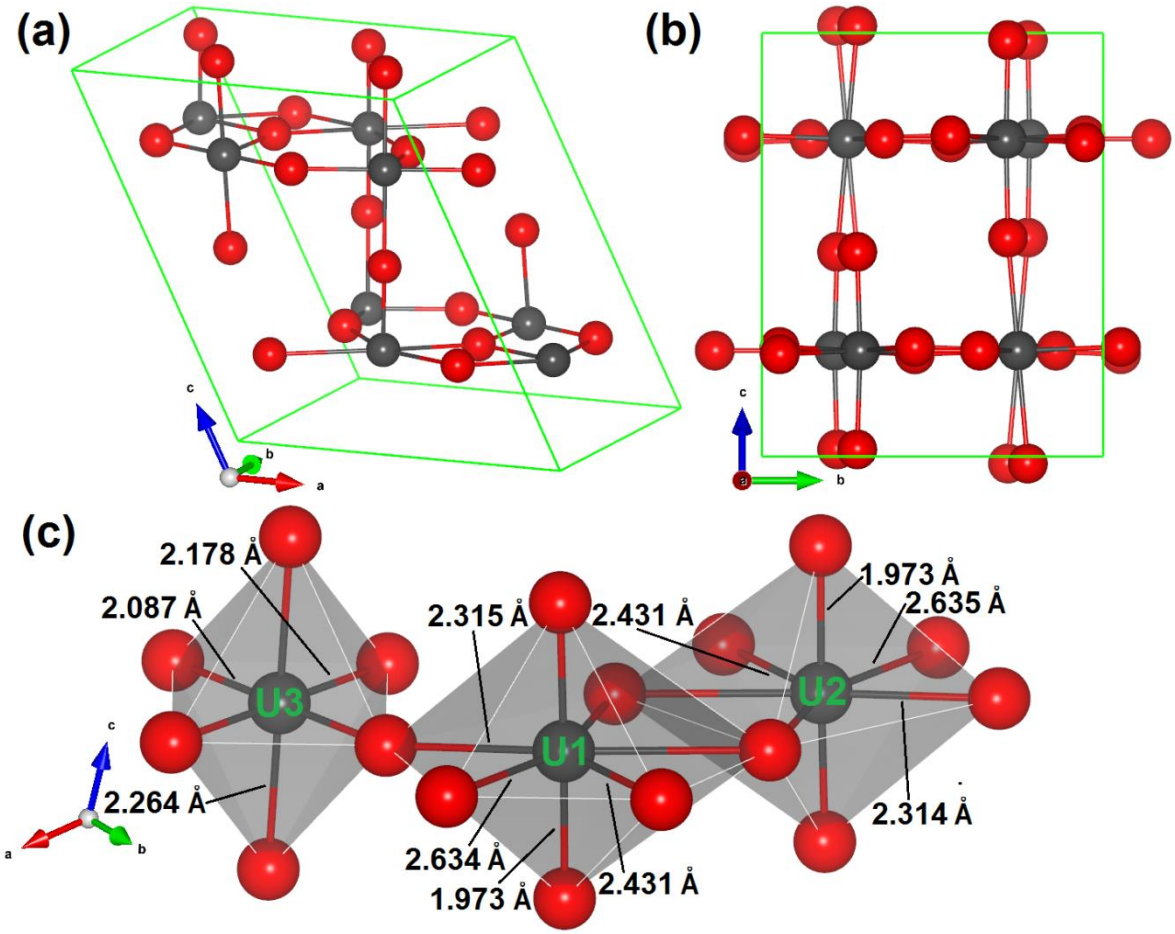

Figure 5.03 – PBE + U predicted structure of U_2O_5 (Np_2O_5): (a) *P1* unit cell, (b) view along the *x* axis and (c) coordination at each uranium site. Black spheres are U ions (all 5^+), red are O and the unit cell is highlighted in green.

All uranium ions are predicted to be U^{5+} and the coordination is again similar to the higher U_3O_8 oxide. Agreement with the experimental lattice parameters and volume is excellent considering it is a neptunium oxide structure, and is considerably better than for any of the other metal oxides, most likely due to the better match of the uranium and neptunium

atomic radii (both 175 pm). The monoclinic cell shape is fully retained upon relaxation, with the β angle particularly well reproduced, although the space group shifts from *P2/c* to the lower symmetry *P1* group.

5.2.3 Nb_2O_5 Structures

There are three different Nb_2O_5 structures that have been arbitrarily designated as α- [186], β- [187] and γ- [188] polymorphs in this work to match the nomenclature of the other phases. The α- and β-Nb_2O_5 structures both contain two formula units whereas the γ-structure has a considerably larger 16 formula unit cell. All three systems have monoclinic symmetry and metal ions in six-fold coordination but the symmetry differs quite significantly between structures. α-Nb_2O_5 has a single type of uranium atom in distorted octahedral coordination leading to a *C2/m* structure with large voids at the centre of the unit cell (Figure 5.04 (a) and (b)). β-Nb_2O_5 also contains a single type of metal atom but in trigonal antiprismatic coordination that yields *C2* symmetry and a tilted layered structure (Figure 5.04 (c) and (d)). γ-Nb_2O_5 contains eight different metal sites, all in octahedral coordination but with varying amounts of distortion. The structure is highly similar to α-Nb_2O_5, with *C2/m* symmetry and large voids surrounded by four octahedra (Figure 5.04 (e) and (f).

On minimisation all three polymorphs relax to the lower symmetry *P1* space group, however the energy differs quite significantly. In α- and γ-polymorphs the axial bond lengths are approximately 2.1 and 2.2 Å respectively, slightly longer than uranyl bonds (1.7 -1.9 Å). In γ-Nb_2O_5, these are all tilted relative to the equatorial plane whereas in α-Nb_2O_5 they are all perpendicular to it. In the α- and β-Nb_2O_5 based systems all uranium ions are predicted to be U^{5+} whereas in the γ-Nb_2O_5 structure one of the uranium sites (four uraniums in total) is predicted to be U^{4+}, with another predicted as U^{6+}, balancing the charge. The U^{4+} sites have the most distorted octahedral coordination whereas the U^{6+} are some of the least distorted positions. Agreement with the experimental lattice parameters for all structures is poorer than the Np_2O_5 structure, due to the larger discrepancy in atomic

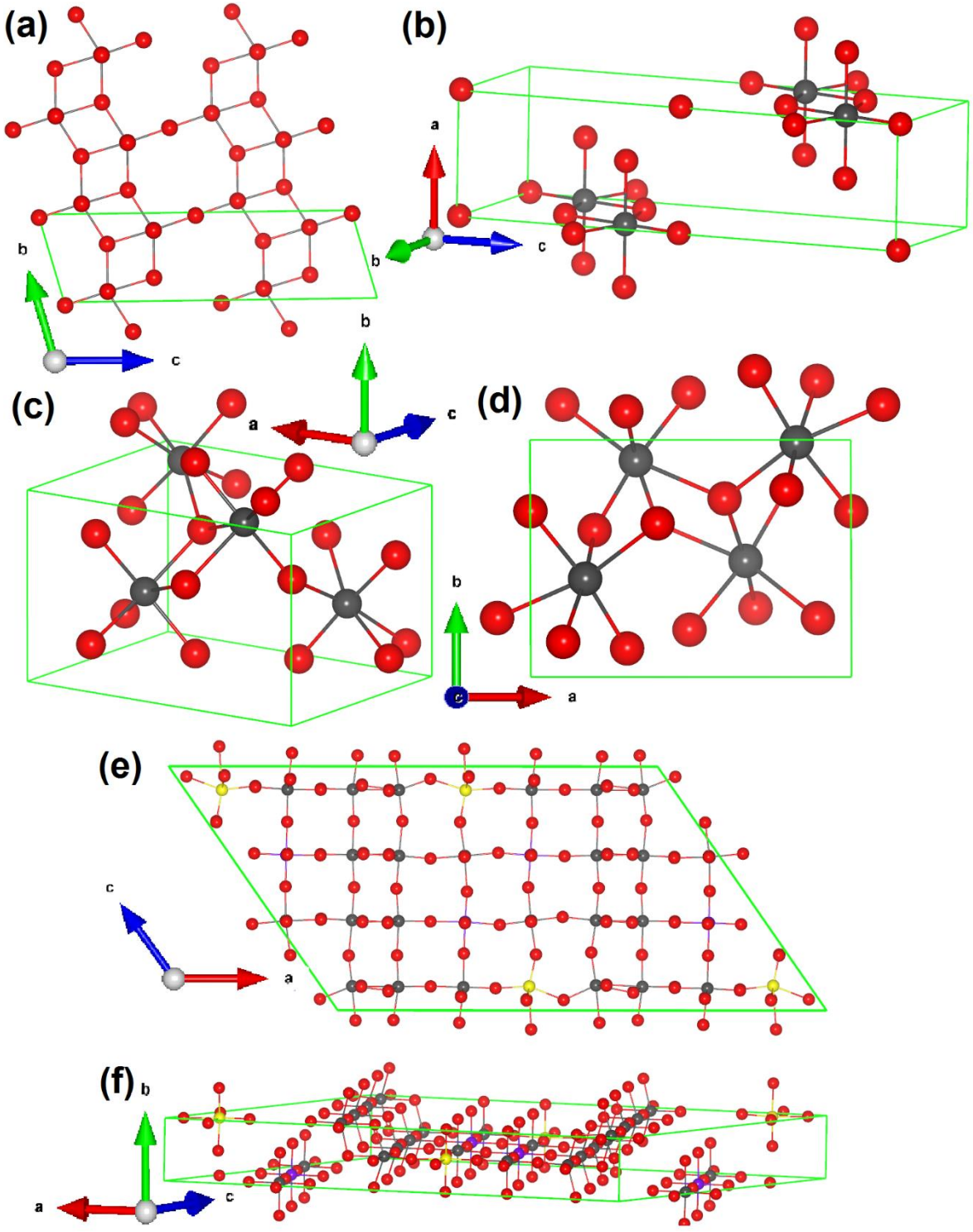

Figure 5.04 – PBE + U predicted structures of U_2O_5 (Nb_2O_5): (a) α-Nb_2O_5 view along the *x* axis, (b) α-Nb_2O_5 unit cell, (c) β-Nb_2O_5 unit cell, (d) β-Nb_2O_5 view along the *z* axis, (e) γ-Nb_2O_5 view along the *y* axis and (f) γ-Nb_2O_5 unit cell. Black spheres are U^{5+} ions, yellow are U^{4+}, purple are U^{6+}, red are O and the unit cell is highlighted in green. Note the large structural voids in the α- and β- polymorphs.

radii (145 pm compared to 175 pm) and the apparent preference of U^{5+} for seven-fold coordination. The monoclinic unit cell angles are also poorly reproduced, with the angle in α-Nb_2O_5 switching to α. The α- and γ-Nb_2O_5 structures have unreasonably high volumes per uranium ion compared to the other layered oxides, due to the large voids present in these polymorphs.

5.2.4 Ta_2O_5 Structure

A single unique Ta_2O_5 polymorph has been identified in the literature [189], it crystallises in a four formula unit cell with the *C2/c* space group and monoclinic symmetry. Although there are other polymorphs they are identical to Nb_2O_5. There is a single type of metal ion present in distorted octahedral coordination. The layers are tilted, in a similar manner to β-Nb_2O_5, with the axial bonds deviating significantly from orthogonal to the equatorial plane. Figure 5.05 shows the PBE + U relaxed structure.

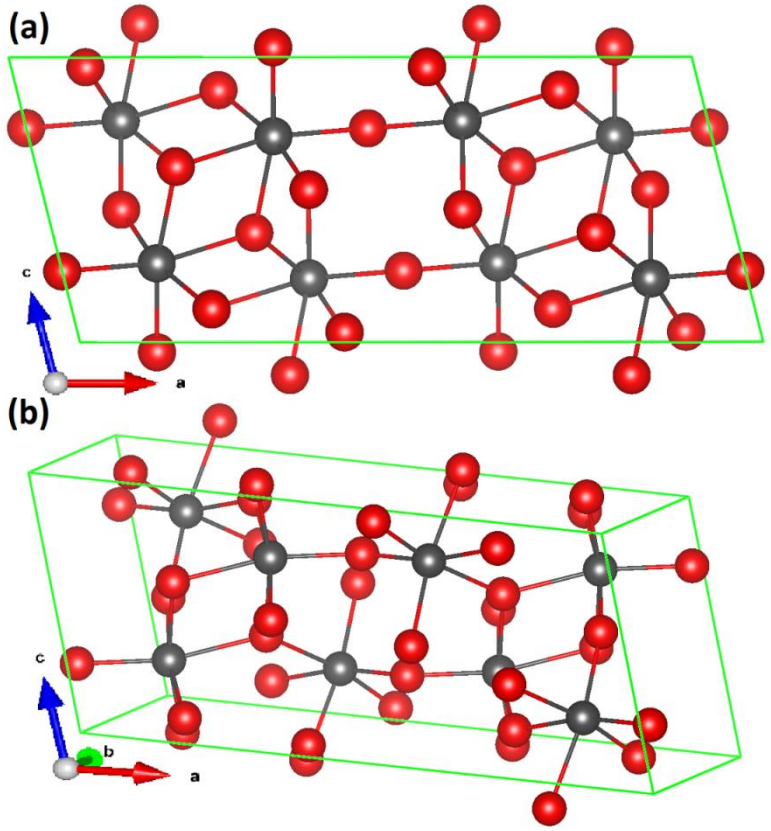

Figure 5.05 - PBE + U predicted structure of U_2O_5 (Ta_2O_5): (a) view along the *y* axis and (b) *P1* unit cell. Black spheres are U ions (all 5^+), red are O and the unit cell is highlighted in green.

The simulation retains the *C2/c* space group but predicts very different lattice parameters to the Ta_2O_5 structure, again due to the large difference in atomic radii (145 pm compared to 175 pm for uranium) and preference for U^{5+} to be in seven-fold coordination. The monoclinic symmetry and β angle are, however, well retained in the calculation. The axial bonds on each site are different lengths, 2.090 and 2.250 Å, and all uranium ions are predicted to be U^{5+}. The predicted volume per uranium ion is also in line with other layered oxide structures. The Ta_2O_5 based simulation is also the only one for which negative vibrational frequencies were predicted.

5.2.5 V_2O_5 Structures

Two V_2O_5 polymorphs have been found, designated arbitrarily here as α- [190] and β-V_2O_5 [191]. The α- polymorph crystallises in an orthorhombic *Pnma* four formula unit cell with two types of metal site, both in distorted octahedral positions. The layers are flat but the axial U-O bonds are bent such that they are not perpendicular to the layers. It also contains large structural voids, although they are shaped slightly differently to those in the α- and γ-Nb_2O_5 structures. In the β-V_2O_5 structure there are two types of metal ion which are both in distorted hexagonal bipyramidal sites, where the equatorial bonds extend above and below the equatorial plane in a similar manner to α-UO_3 [72]. The unit cell is monoclinic $P2_1/m$ and also features bent axial bonds relative to the equatorial plane. The β-V_2O_5 structure is essentially oxygen deficient α-UO_3 (Chapter 7), with octahedral coordination at each site instead of hexagonal bipyramidal.

On minimisation the α- and β-V_2O_5 structures relax to the lower symmetry *P1* and *Pm* space groups respectively but retain their original coordination (Figure 5.06). The difference with the experimental lattice parameters is largest for these two oxides, unsurprisingly, as vanadium has the smallest atomic radii of all the structures examined here (135 pm) and so there is the largest relaxation compared to the experimental data. The uranium ions are also all in six coordinate positions compared to the preference of U^{5+} for seven coordinate (Chapter 6). The α-V_2O_5 structure becomes slightly monoclinic on relaxation and the large voids are maintained, resulting in a very large volume per uranium ion. The tilted axial U-O bonds are 2.218 and 2.268 Å at each uranium site and both are U^{5+}. The β angle in β-V_2O_5 is almost orthorhombic to begin with but relaxes to 79.7 °,

along with a splitting of the uranium ions from two unique sites to four. Single U^{4+} and U^{6+} ions and two U^{5+} ions are predicted as the charge configuration, with slightly longer axial bonds at the U^{4+} site and slightly shorter at U^{6+}.

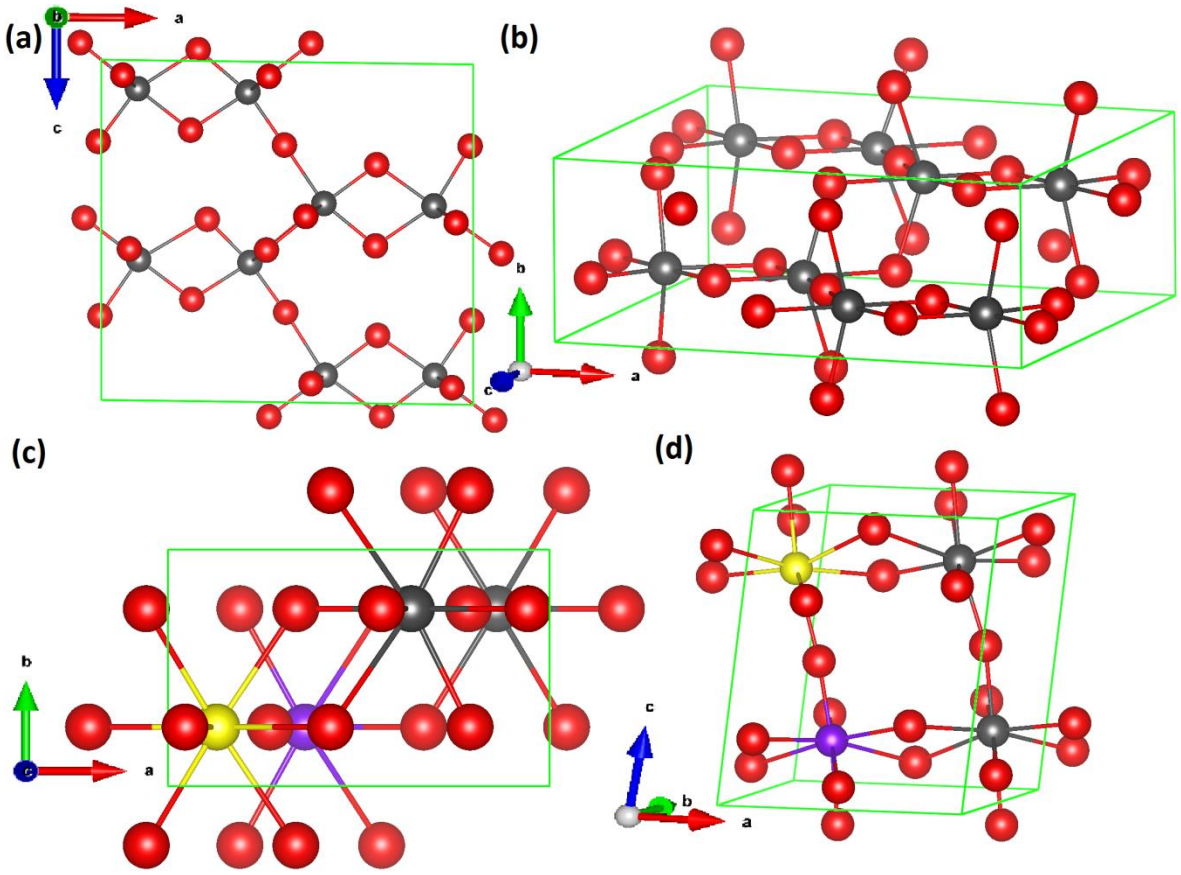

Figure 5.06 - PBE + U predicted structures of U_2O_5 (V_2O_5): (a) α-V_2O_5 view along the *y* axis, (b) α-V_2O_5 unit cell, (c) β-V_2O_5 view the along *z* axis and (d) β-V_2O_5 unit cell. Black spheres are U^{5+} ions, yellow are U^{4+}, purple are U^{6+}, red are O and the unit cell is highlighted in green. Note the large voids in the α-V_2O_5 structure.

5.2.6 Stability

The relative energies of the simulated U_2O_5 phases are provided in Table 5.01 and are linked to a number of factors; including the uranium charge, uranium coordination and the presence of structural voids or pores. There appears to be a larger geometrical strain in the systems originating from a smaller ion than uranium. In Chapter 6 it is established that U^{5+} is more stable in pentagonal bipyramidal coordination and the structures originating from smaller metal ions typically differ from this more significantly.

All systems were fully relaxed, however the original coordination is retained in each case and a general order of stability of Np > Nb/Ta > V based structures is established. The Np_2O_5 structure is actually most stable overall, almost 0.1 eV more stable than δ-U_2O_5. Np has the same ionic radius as U and the coordination of δ-U_2O_5 (a mix of distorted pentagonal bipyramidal and octahedral) is also found here. As with δ-U_2O_5 the structure is essentially oxygen deficient U_3O_8 (Chapter 6). All the other structures feature uranium atoms entirely in six coordinate positions and so are consequently less stable. Perhaps the most surprising result is the a-Nb_2O_5 structure which, despite having a relatively large volume (65.69 $Å^3$/U) and Nb having a slightly smaller atomic radius than U (-6 %), is only 0.03 eV less stable than δ-U_2O_5. After this the Ta_2O_5 structure is found to be the next most energetically stable (although it does contain imaginary vibrational frequencies and so is dynamically unstable) as the parent Ta ion is the same size as Nb. Entirely U^{5+} ions are predicted and the relaxed volume (56.42 $Å^3$/U) is very close to that found in δ-U_2O_5. At the other end of the scale, of the V_2O_5 structured oxides (V is 13 % smaller than U and so there is greater structural relaxation) the β- polymorph is least stable due to the presence of U^{4+} and U^{6+} ions and the relatively small volume of 47.94 $Å^3$/U. The α-V_2O_5 structure is slightly more stable as, although it has a particularly large volume (67.33 $Å^3$/U), entirely U^{5+} ions are predicted. The β- and γ-Nb_2O_5 structures are found to be of comparable stability to one another. The stability of β- is lowered due to the trigonal prismatic coordination environment whilst in the γ-Nb_2O_5 structure it is the presence of U^{4+} and U^{6+} ions and a relatively large volume of 64.82 $Å^3$/U. Based on these results it would be expected that U_2O_5 can crystallise in the Np_2O_5 structure, but due to the relative instability of the U_2O_5 stoichiometry compared to the other oxides it has not been synthesised or reported experimentally. The difficulty in synthesising layered U_2O_5 is likely to stem from the fact that the structure is essentially oxygen deficient U_3O_8 and U^{5+} is more stable in pentagonal bipyramidal coordination (Chapter 6). The instability of δ-U_2O_5 (and (Np) U_2O_5) likely arises from the presence of octahedrally coordinated uranium ions, it is highly favourable for this polymorph to gain more oxygen so that U^{6+} can occupy octahedral sites and U^{5+} pentagonal bipyramidal ones.

5.3 Elastic Properties

Elastic constants and bulk moduli for all polymorphs, except for the γ-Nb_2O_5 structure (due to the size of the structure and limited time available), have been predicted and are provided in Tables 5.02 and 5.03. There are no reported values for these in the literature, except for the published results from this work on δ-U_2O_5 [73], and so these form the first predicted values for the other U_2O_5 structures examined.

The first point of interest is the negative elastic constants predicted in the Np_2O_5 and α-V_2O_5 structures; which are notably absent from Ta_2O_5 despite the predicted negative vibrational modes in this structure. Although negative elastic constants can be indicative of dynamical instability, it is not necessarily the case [193] and evidently calculation of vibrational frequencies is also essential given the example of the Ta_2O_5 structure. A structure is considered unstable if the determinant of the C_{11}:C_{33} elastic matrix is negative or any of the lead diagonal elastic constants (C_{11}-C_{66}) are large negative values [194]. Applying this to the Np_2O_5 and α-V_2O_5 based structures it emerges that the former is dynamically stable whilst the latter is not. A further test to confirm this is to satisfy the condition in Equation 5.01 [194]:

$$\left(C_{ij}\right)^2 < C_{ii}C_{jj} \qquad \textbf{Equation 5.01}$$

where in the example of Np_2O_5 C_{ij} is C_{12} and C_{ii} and C_{jj} are C_{11} and C_{22} respectively.

Table 5.02 – Predicted elastic constants of U_2O_5 polymorphs. Independent elastic constants for orthorhombic cells are included.

Phase	U Charge Configuration	Elastic Constants (GPa)								
		C_{11}	C_{12}	C_{13}	C_{22}	C_{23}	C_{33}	C_{44}	C_{55}	C_{66}
δ-U_2O_5	U^{5+}	271.4	29.5	148.0	513.6	27.9	246.5	27.7	27.1	60.6
Np_2O_5	U^{5+}	217.6	130.4	-2.4	279.5	22.1	395.1	61.2	26.7	22.7
α-Nb_2O_5	U^{5+}	452.8	24.8	32.6	212.4	134.4	295.7	22.8	17.6	26.0
β-Nb_2O_5	U^{5+}	120.5	72.8	65.3	194.3	60.4	80.0	98.9	68.9	61.9
Ta_2O_5	U^{5+}	165.1	36.4	22.6	86.9	53.1	94.5	30.2	87.6	23.9
α-V_2O_5	U^{5+}	195.5	73.0	86.2	179.0	43.9	56.3	-2.3	-148.9	-31.0
β-V_2O_5	$U^{4+}/U^{5+}/U^{6+}$	298.2	132.8	128.8	253.8	87.3	330.1	51.1	64.9	33.5

Table 5.03 – Predicted bulk moduli of U_2O_5 polymorphs. Details of bulk moduli (*B*) calculation can be found in section 2.4.1.

Phase	U Charge Configuration	*B* (GPa)	Vol/U ($Å^3$)	E_{Form} (eV)
δ-U_2O_5	U^{5+}	156.8	58.15	-0.86
Np_2O_5	U^{5+}	132.5	58.80	-0.95
α-Nb_2O_5	U^{5+}	149.4	65.69	-0.83
β-Nb_2O_5	U^{5+}	88.0	54.20	-0.57
Ta_2O_5	U^{5+}	63.4	56.42	-0.70
α-V_2O_5	U^{5+}	93.0	67.33	-0.34
β-V_2O_5	$U^{4+}/U^{5+}/U^{6+}$	175.5	47.94	-0.31

In the stable materials the predicted bulk moduli are of comparable magnitude to those in U_3O_8 [73], with uranium charge configuration bearing no influence on the elastic properties. Volume per uranium atom also has little influence on the bulk modulus, demonstrated by α-Nb_2O_5 and a-V_2O_5. Equally the predicted formation energy is not correlated with B, as the relatively unstable β-V_2O_5 polymorph is predicted to have a bulk modulus in line with the highly stable δ-U_2O_5 and Np_2O_5 structures, although slightly higher. The key influence on B is the structural motifs present in the material. The δ-U_2O_5, Np_2O_5 and α-Nb_2O_5 structures have similar bulk moduli to the U_3O_8 polymorphs because they are structurally similar; with pentagonal bipyramidal or octahedral coordination and relatively straight, elongated uranyl-like axial U-O bonds. As was found in U_3O_8, the largest elastic constants are those corresponding to compression along the axial bond axis: C_{22} in δ-U_2O_5, C_{22}/C_{33} in Np_2O_5 and C_{11} in α-Nb_2O_5.

In the polymorphs with lower bulk moduli the axial bonds deviate more significantly from perpendicular to the layers (or are non-existent in β-Nb_2O_5). These results also show good agreement with UO_3, where the same elastic constant/axial bond relationship was identified and phases without uranyl bonds had bulk moduli of between 150 and 170 GPa [72].

5.4 Electronic Properties

There has been no experimental determination of the electronic properties of U_2O_5 and the only computational work in the literature is that published from this thesis [73]. The partial DOS for each U_2O_5 structure are in Figure 5.07 and Table 5.04 shows the predicted band gaps.

Table 5.04 – Predicted band gaps of U_2O_5 polymorphs.

Phase	U Charge Configuration	Band Gap (eV)	Vol/U (Å^3)	E_{Form} (eV)
δ-U_2O_5	U^{5+}	1.60	58.15	-0.86
Np_2O_5	U^{5+}	2.32	58.80	-0.95
α-Nb_2O_5	U^{5+}	2.14	65.69	-0.83
β-Nb_2O_5	U^{5+}	2.33	54.20	-0.57
γ-Nb_2O_5	$U^{4+}/U^{5+}/U^{6+}$	0.39	64.82	-0.57
Ta_2O_5	U^{5+}	2.23	56.42	-0.70
α-V_2O_5	U^{5+}	1.23	67.33	-0.34
β-V_2O_5	$U^{4+}/U^{5+}/U^{6+}$	1.55	47.94	-0.31

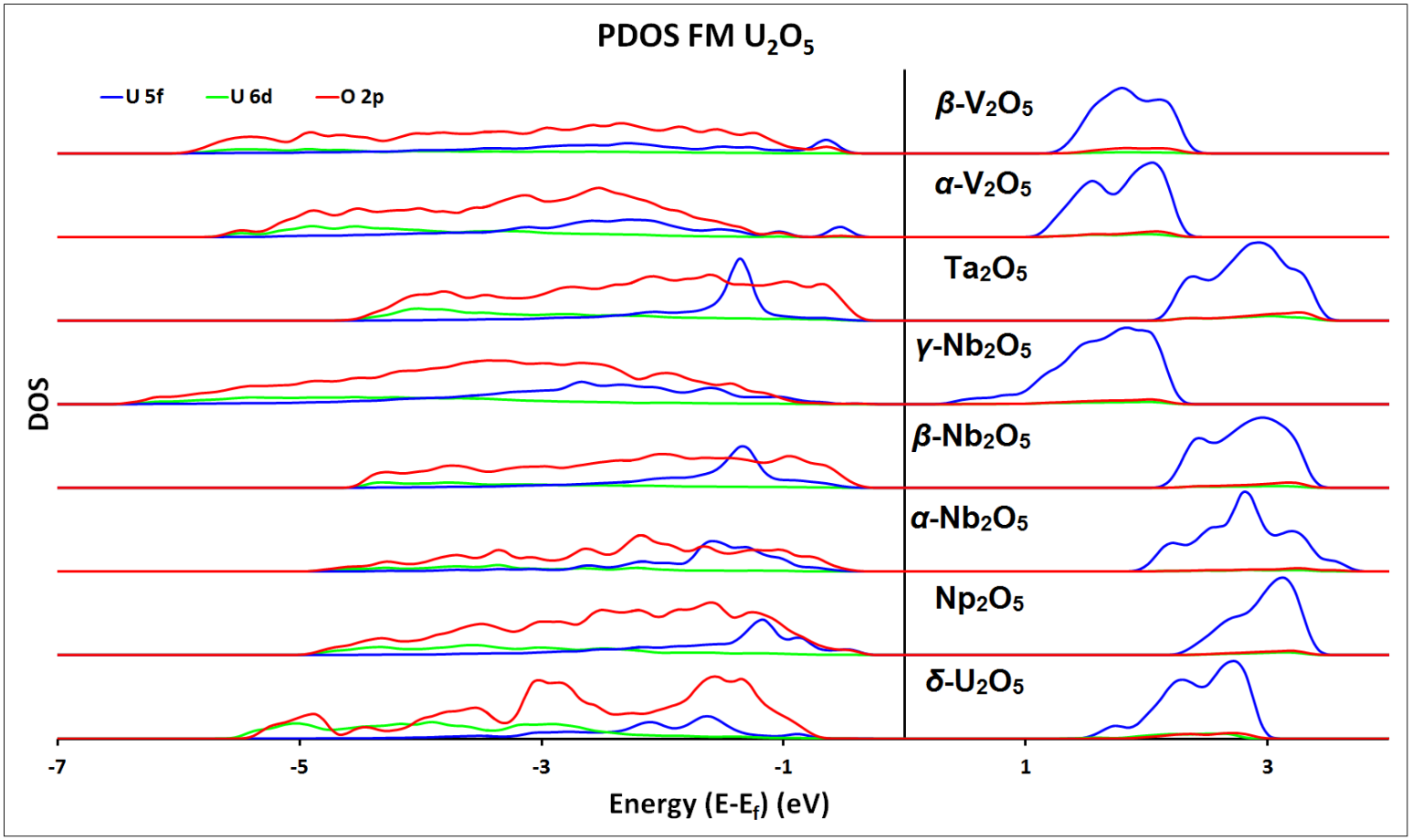

Figure 5.07 – PBE + U calculated partial DOS for U_2O_5 structures. O 2*p* states are in red, U 5*f* are in blue and U 6*d* are in green. Contributions from other states are negligible and so are omitted. Only spin up states are included here as the spin up and spin down channels are extremely similar. The energy of the highest occupied state was set to zero eV (i.e. E = E - E_f).

Only DOS from uranium 6*d* and 5*f* and oxygen 2*p* states have been included in the DOS as other states have relatively minor contributions to the DOS, particularly around the band gap. Almost every structure is predicted to be a charge transfer insulator, with a conductance band composed of U 5*f* states and valence band comprised mainly of O 2*p* states. All structures feature a notable U 5*f* peak that contributes to the valence band, in the Np_2O_5 structure in particular this is very close to the top of the band, but the main contributor is still the O 2*p* states. In the two V_2O_5 based structures, however, there are very small U 5*f* peaks at the tops of the valence bands, suggesting possible Mott-Hubbard insulating behaviour in these phases (as observed in UO_2). The presence of U 5*f* states in the valence band suggests a degree of covalent mixing with O 2*p* (fully ionic bonding would feature no overlapping states). The position of the U 5*f* peaks in the two most stable polymorphs (δ-U_2O_5 and Np_2O_5) matches well with that of the U^{5+} 5*f* peak in U_3O_8 [73]. There is very little overall contribution from U 6*d* states, with most of it confined to the lower valence band and the most significant 6*d* contributions to the DOS are found in δ-U_2O_5.

The predicted band gaps of the different U_2O_5 polymorphs cover a fairly wide range. There does not appear to be much relationship with relative stability or the volume per uranium atom of the phase, although the three most stable phases all have band gaps of 1.6 eV or higher. The Np_2O_5 and α-Nb_2O_5 band gaps (2.32 and 2.14 eV) are comparable the PBE + U predicted values for U_3O_8 (2.0 – 2.2 eV) [73], whereas at 1.60 eV δ-U_2O_5 is closer in line with the experimentally determined U_3O_8 value (1.76 eV) [172].

5.5 Conclusions

The paucity of experimental data on the U_2O_5 composition, combined with the large number of potential configurations associated with applying the defect models used for U_4O_9 and U_3O_7, have made it impossible to simulate fluorite based U_2O_5 at this stage. However, a number of layered type structures have been simulated, including δ-U_2O_5 and Np_2O_5, Nb_2O_5, Ta_2O_5 and V_2O_5 structures.

All of the most stable systems are predicted to contain entirely U^{5+} ions, with only two of the least stable systems found to contain U^{4+} and U^{6+}, and even then U^{5+} is also present.

The calculations reveal the most stable structures are those that contain well defined axial bonds, volume per uranium ions close to that of δ-U_2O_5, only U^{5+} ions, mostly seven-coordinate uranium sites and whose parent M_2O_5 structure contains a metal ion with an ionic radius close to that of uranium. The δ-U_2O_5 structure is actually found to be second most stable, after Np_2O_5, and is closely followed by α-Nb_2O_5, despite the large structural voids present in the latter polymorph. The δ-U_2O_5 and (Np) U_2O_5 polymorphs are structurally similar to U_3O_8, containing mixtures of pentagonal bipyramidal and octahedral coordination with slightly shorter axial bonds. To this end it would be expected that uranium can crystallise with the Np_2O_5 structure, however it has not been observed experimentally as the structural investigations in the literature for this composition date back to the 1960s and the composition is meta-stable with respect to U_3O_8, making synthesis and storage problematic. The stoichiometry is clearly worthy of synthetic investigation though as the Np_2O_5 structure is found to be a stable phase.

The bulk moduli of the most stable polymorphs (130 -160 GPa) are also very similar to U_3O_8, as would be expected given their close structural resemblance. The calculated elastic constants also share a relationship with U_3O_8 in that the largest predicted constants correspond to compression along the axial U-O bonds, demonstrating increased mechanical strength along that axis.

In keeping with the higher layered oxides U_3O_8 [73] and UO_3 [72], all of the U_2O_5 polymorphs are predicted to be charge transfer insulators with VBs made up of oxygen 2*p* states and CBs made up of uranium 5*f* states. The contributions to either of these bands from uranium 6*d* states are minimal. There is slightly more variation in predicted band gaps, with δ-U_2O_5 predicted to be 1.60 eV, which is relatively close to the experimentally determined α-U_3O_8 band gap of 1.76 eV [172]. However the Np_2O_5 and α-Nb_2O_5 structures are found to have band gaps of 2.32 and 2.14 eV respectively, which are much closer in line with the PBE + U computed band gaps for U_3O_8 (2.05 – 2.23 eV) [73], suggesting that perhaps these two structures are more representative of the U_2O_5 composition.

The following chapter examines the various polymorphs of U_3O_8 which, as described in this chapter, are structurally very similar to δ- and (Np) U_2O_5.

Chapter 6

6 Layered U_3O_8

U_3O_8 is the first isolatable layered oxide of the U-O system; U_4O_9, U_3O_7 and U_2O_5 all oxidise to it over time or disproportionate to UO_2 and U_3O_8 depending on the conditions. It is commonly produced from UO_2 oxidation, as the kinetically controlled product [195] (UO_3 is the thermodynamically controlled product) [196], but it can also form from reduction of UO_3 at high temperatures [197]. There are three closely related polymorphs [31, 198, 199] with well-defined structures reported in the literature and so simulation of the phase is relatively straightforward. Here simulations of all three polymorphs are presented and predictions are made of their fundamental properties, with detailed discussion of each polymorph in section 6.2.

All of the work presented here has been published previously in Dalton Transactions in a paper titled "*Density Functional Theory Investigation of the Layered Uranium Oxides U_3O_8 and U_2O_5*" [73].

6.1 U_3O_8 Background

The inherent stability and significance of U_3O_8 to the nuclear fuel cycle (Chapter 1) have led to numerous experimental investigations of its structural [31, 198-202], thermodynamic [19, 195, 203-207] and electronic [114, 172, 183, 208-212] properties, as well as a number of computational studies [32, 197, 213-216]. The stoichiometry, U_3O_8, suggests a mixed-valence oxide and dictates that the uranium charge configuration is either one U^{4+} and two U^{6+} or two U^{5+} and one U^{6+}. Older experimental studies propose the former [183, 217], whilst more recent work suggests the latter [114, 184]. Computational studies using interatomic potentials with an averaged charge of $U^{5.33+}$ gave the best structural fit with experiment [214], a result that was corroborated by DFT simulations from Geng *et al* [215].

More recent calculations using DFT + U, however, suggest a preferred configuration of U^{5+}/U^{6+} [197, 216]. He *et al* [172] used spectroscopic ellipsometry (SE) to determine the band gap of α-U_3O_8, finding it to be an insulator with an indirect band gap of 1.76 eV. Their accompanying LDA + U calculations predicted a value of 2.43 eV.

The current chapter presents the results from simulations of the U_3O_8 polymorphs and compares them with the available experimental and computational data. The PBE + U methodology is applied here as described in Chapter 2, however the PBE was also used for some initial calculations to test its effects on the system. Additionally, both FM and AFM (<100>, <010> and <001>) magnetic orderings were applied for each polymorph but there was found to be no energetic preference and the predicted structures were identical and so only the FM results are reported here (AFM results can be found in Appendix C). Some of the DFT studies in the literature report non-magnetic (NM) structures [197, 215, 216], however as all the calculations employed here are spin-polarised, this is not a phenomenon that was possible to reproduce.

6.2 Structural Properties

A total of five U_3O_8 polymorphs were found in the literature and are all discussed here: *Amm2* and *C222* α-U_3O_8, *Cmcm* and *P2₁/m* β-U_3O_8 and *P-62m* γ-U_3O_8. Table 6.01 contains all of their predicted structural properties and gives their relative stabilities in terms of formation energy with respect to UO_2.

6.2.1 α-U_3O_8

As the most common polymorph, α-U_3O_8 is synthesized from isothermal heating of UO_2 to 900 K in dry air [31]. It is structurally very similar to α-UO_3, having been described as an oxygen deficient version of this polymorph with ordered oxygen vacancies [218]. It is reported to crystallise in the *Amm2* (or *C2mm*) space group in a 22 atom (two formula unit) orthorhombic cell with each uranium ion in pentagonal bipyramidal coordination [31, 200, 202, 219] (Figure 6.01(a)). There is an alternative structure in the literature, reported by Andresen [198], which has the *C222* space group and one of the two uranium sites has octahedral coordination (Figure 6.01(c)). In both structures the axial interlayer bonds are

perpendicular to the layers in eclipsed configuration. The theoretical density is in good agreement with experiment, 8.39 and 8.43 gcm^{-3} respectively, a good indication of relatively few defects.

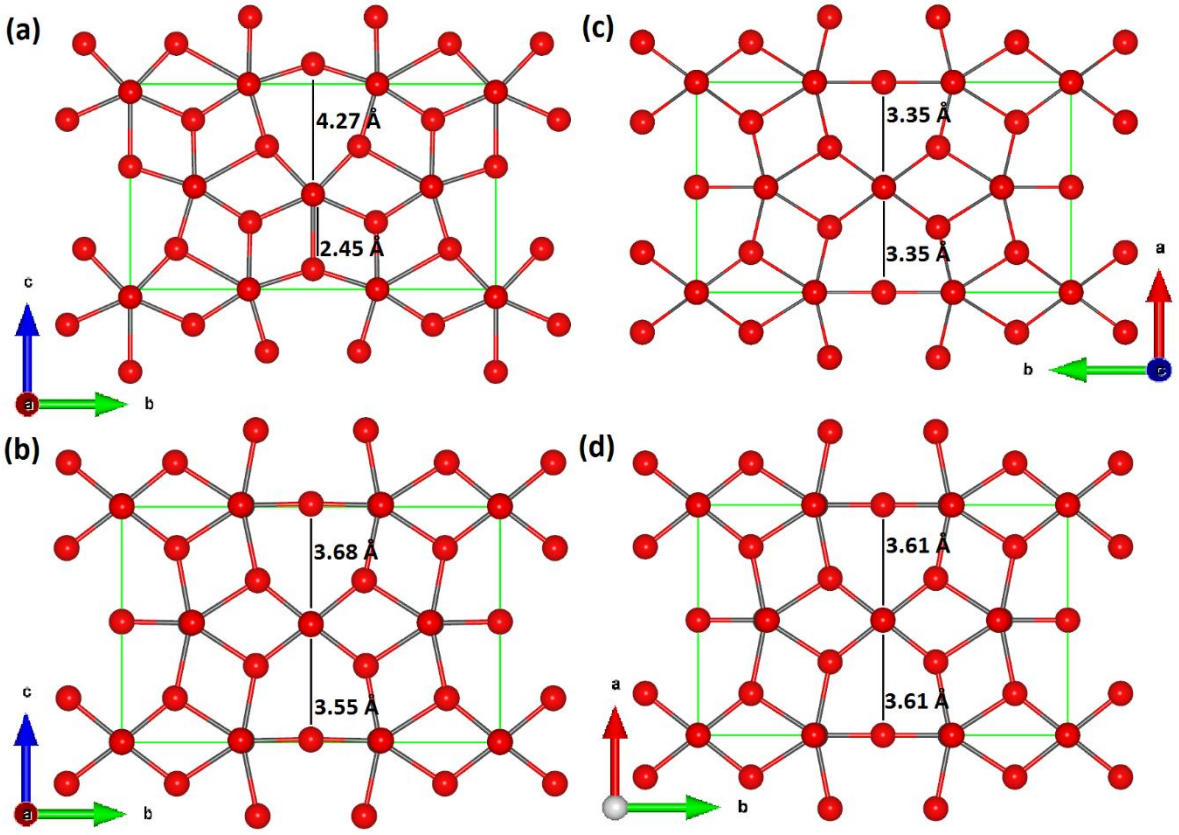

Figure 6.01 - α-U_3O_8: (a) experimentally observed *Amm2* structure, (b) PBE + U relaxed *Amm2* structure, (c) experimentally observed *C222* structure and (d) PBE + U relaxed *Cmmm* structure. Black spheres represent uranium ions, red oxygen ions and the unit cell is highlighted in green.

The calculated structural properties of the *Amm2* and *C222* polymorphs can be found in Table 6.01 and their predicted structures in Figures 6.01 and 6.02. The *C222* polymorph (which relaxes to *Cmmm* on minimisation) is predicted to be the lowest energy structure and contain no imaginary vibrational modes. The U^{5+}/U^{6+} charge configuration is also preferred; U^{4+}/U^{6+} was only stabilised for the *Amm2* polymorph and has a significantly higher formation energy (+0.4 eV/U) as well as a number of imaginary vibrational frequencies. The U^{5+} ions are found at pentagonal bipyramidal sites and the U^{6+} ions at octahedral sites.

Table 6.01 – Predicted properties of U_3O_8. Space groups are calculated to a tolerance of 0.001 Å using Materials Studio [192]. Reported energies are formation energy per uranium ion relative to UO_2*. Magnetic moments are indicative of uranium charge and there are two U2 sites. Results reported from the literature all have FM structures. Δ% is the percentage difference between a calculated structure and experiment.

Study	Phase	Method	Mag. Mom. (μ_B)		Lattice Parameters (Å)				Vol/U (Å^3)	β (°)	Space Group	E_{Form} (eV)
			U1	U2	*c/a*	*a* (Δ%)	*b* (Δ%)	*c* (Δ%)				
Loopstra [200]	***Amm2*** **α-U_3O_8**	Exp	-	-	-	4.15	11.97	6.72	55.58	90.0	*Amm2*	-
Wen [197]		HSE	0.00	1.10	-	4.09 (-1.4)	11.86 (-0.9)	6.64 (-1.1)	53.68	90.0	-	-
		PBE + U	0.00	1.10	-	4.21 (1.5)	11.60 (-3.1)	7.22 (7.5)	58.68	90.0	-	-
Yun [220]		PW91 + U	0.00	1.00	-	4.21 (1.5)	11.61 (-3.1)	7.20 (7.2)	58.65	90.0	-	-
Geng [215]		PBE	0.70	0.70	-	4.16 (0.3)	11.57 (-3.3)	7.03 (4.7)	56.39	90.0	-	-
This Work		PBE + U	2.00	0.05	-	4.24 (2.2)	13.06 (9.1)	6.60 (-1.7)	60.92	90.0	*Amm2*	-0.70
			0.00	1.09	-	4.21 (1.4)	11.60 (-3.1)	7.22 (7.5)	58.72	90.0	*Amm2*	-1.09
		PBE	0.75	0.72	-	4.16 (0.3)	11.84 (-1.0)	6.84 (1.8)	56.12	90.0	*Amm2*	-
Andresen [198]	***C222*** **α-U_3O_8**	Exp	-	-	-	6.70	11.95	4.14	55.30	90.0	*C222*	-
This Work		PBE + U	0.00	1.08	-	7.22 (7.7)	11.59 (-3.0)	4.20 (1.5)	58.67	90.0	*Cmmm*	-1.10
Loopstra [199]	***Cmcm*** **β-U_3O_8**	Exp	-	-	-	7.07	11.45	8.30	55.98	90.0	*Cmcm*	-
This Work		PBE + U	0.01	1.13	-	7.21 (2.0)	11.64 (1.7)	8.45 (1.7)	59.06	90.0	*Cmcm*	-1.12
Chodura [221]	***P2$_1$/m*** **β-U_3O_8**	Exp	-	-	-	11.93	6.72	8.29	55.38	90.0	*P2$_1$/m*	-
Wen [197]		HSE	0.00	1.10	-	12.04 (0.9)	6.60 (-1.8)	8.19 (-1.2)	54.23	90.0	-	-
		PBE + U	0.00	1.10	-	11.60 (-2.8)	7.04 (4.8)	8.34 (0.6)	56.76	90.0	-	-
This Work			0.02	1.11	-	12.28 (3.0)	6.85 (1.9)	8.45 (1.9)	59.20	90.0	*P1*	-1.08
Desgranges [31]	***P-62m*** **γ-U_3O_8**	Exp	-	-	0.61	6.82	6.82	4.15	55.76	120.0	*P-62m*	-
Wen [197]		HSE	0.85	0.85	0.61	6.73 (-1.3)	6.73 (-1.3)	4.09 (-1.5)	53.52	-	-	-
		PBE + U	0.84	0.84	0.61	6.84 (0.3)	6.84 (0.3)	4.17 (0.4)	56.31	-	-	-
This Work		PBE + U	1.06	0.65	0.60	7.03 (3.0)	7.03 (3.0)	4.20 (1.2)	59.86	122.5	*Amm2*	-0.77
			0.00	1.09	0.62	6.83 (0.1)	6.83 (0.1)	4.20 (1.2)	56.60	116.3	*Amm2*	-1.08

* - $E_{Form} = E_{UO_2} - (E_{U_3O_8} - E_U - \frac{8}{3}E_O)$ (see section 2.4.4)

A PBE calculation was also performed on the *Amm2* unit cell to compare its effects with the PBE + U and, as reported by Geng *et al* [215], a delocalised uranium charge of 5.33+ was found on each uranium site. Although it reproduced the experimental structure to a greater degree of accuracy compared to the PBE + U (the uranium coordination is the same as in Figure 6.01 (a)) and predicted no sublattice distortions (as in Figure 6.01 (b)), imaginary vibrational frequencies were found, indicating the structure is dynamically unstable. This structure was still predicted even when applying the PBE to the PBE + U minimised structure, demonstrating the strong preference of the PBE for delocalised charge and the coordination shown in Figure 6.01 (a).

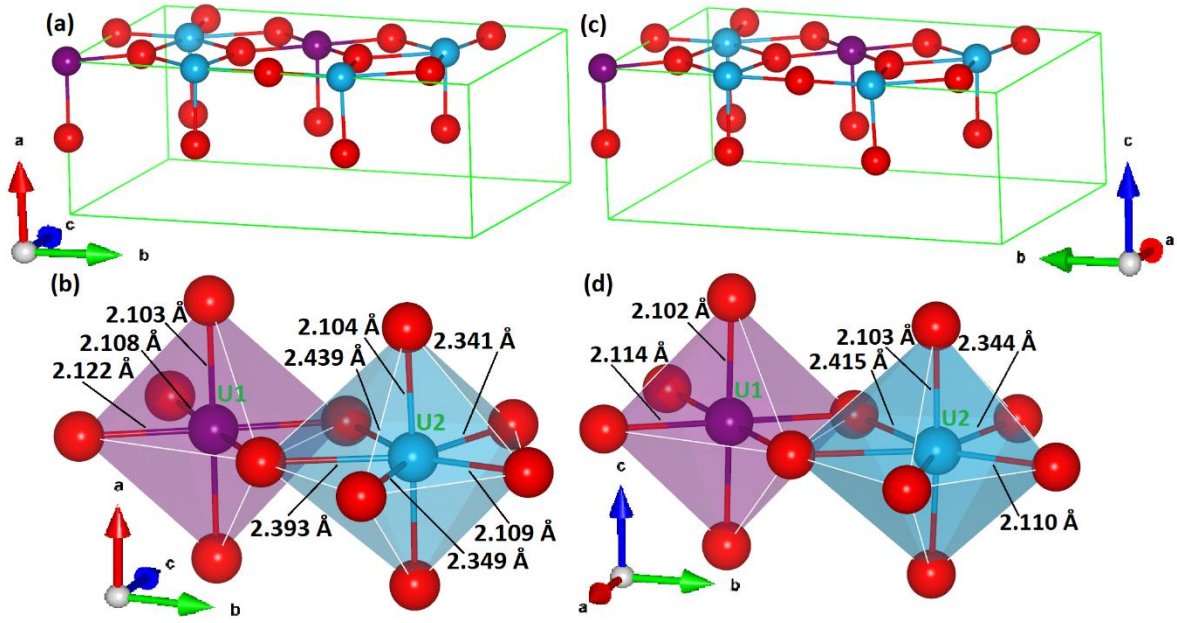

Figure 6.02 – PBE + U predicted structure if α-U_3O_8 (a) *Amm2* unit cell, (b) uranium coordination in *Amm2* structure, (c) *Cmmm* unit cell and (d) uranium coordination in *Cmmm* structure. U^{6+} in purple, U^{5+} in blue, oxygen in red and the unit cell is highlighted in green.

Now referring only to the PBE + U U^{5+}/U^{6+} results, for both the *Amm2* and *C222* structures the volume shows a slight overestimation, 5.7 and 6.1 % respectively. This arises predominantly from the overestimation of *a* by 0.5 Å, a result also found in the calculations of Wen *et al* [197]. On minimising the *Amm2* structure a distortion of the oxygen sublattice is predicted (Figure 6.02 (b)) whereby the coordination at U1 sites is lowered to octahedral such that the cell now strongly resembles the *C222* structure. Despite this coordination

change the original *Amm2* symmetry is retained due to the differences highlighted in Figures 6.01 (b) and (d). The *C222* structure displays no distortion on minimisation however it does relax to the higher symmetry *Cmmm* space group. These strikingly similar relaxed structures (Figures 6.01 (b) and (d) and 6.02); only differ slightly in atomic positions and volume, equating to a 0.05 eV energy difference. The *Cmmm* structure is the (slightly) energetically favoured one, however as the *Amm2* system relaxed to essentially the same structure it is clear that Andresen's *Cmmm* structure is preferred. An imaginary vibrational frequency is predicted for the *Amm2* polymorph that only concerns displacement of the oxygen ions involved in the structural distortion, further reinforcing the preferential status of the *Cmmm* modification. The axial U-O bonds in α-U_3O_8 are predicted to be 2.10 Å (Figure 6.02 (b) and (d)), in close agreement with 2.07 Å reported experimentally. This distance is almost the same as that found in the comparable *a*-UO_3 structure [72].

Previous DFT studies of α-U_3O_8 focussed solely on the *Amm2* (or *C2mm*) polymorph and did not report the oxygen sublattice distortion predicted here [172]. Wen *et al* predict six tightly bound oxygen ions at each oxygen site and a seventh at a greater distance of 2.55-2.72 Å [197], compared to the completely dissociated 3.55 Å predicted in this work (Figure 6.01 (b)). The structure from the U^{4+}/U^{6+} charge configuration predicted here is closer in line with that of Wen *et al*, however the seventh oxygen is still at a larger distance of 3.11 Å. Considering all of this information, it is reasonable to suggest that that the oxygen in α-U_3O_8 is thermally activated and can hop between sites such that the experimentally determined *Amm2* system is in fact an averaged structure of two almost degenerate minima in the *Cmmm* cell.

6.2.2 β-U_3O_8

β-U_3O_8, the high temperature polymorph, is produced by heating α-U_3O_8 to 1623 K in air or oxygen and slowly cooling to room temperature [199]. The primary polymorph discussed in the literature is *Cmcm* however a $P2_1/m$ structure is also available [221], both are orthorhombic and have 44 atom (four formula unit) cells. β-U_3O_8 contains three distinct uranium sites, with two assuming pentagonal bipyramidal coordination and the third in

octahedral coordination; in a similar structure to the *Cmmm* and relaxed *Amm2* α-U_3O_8 polymorphs.

A distinct structural feature of β-U_3O_8 is the tilting of the axial U-O bonds relative to the equatorial plane, in a similar fashion to the U_2O_5 polymorphs discussed in Chapter 5, although less pronounced at an average deviation from straight of 5 °. The bending is more significant in the *Cmcm* polymorph and alternates direction in order to maintain more or less eclipsed axial bonding. As with the α- polymorph, good agreement is shown between the experimental and theoretical densities at 8.38 and 8.33 gcm^{-3} respectively, suggesting relatively few defects are present [19].

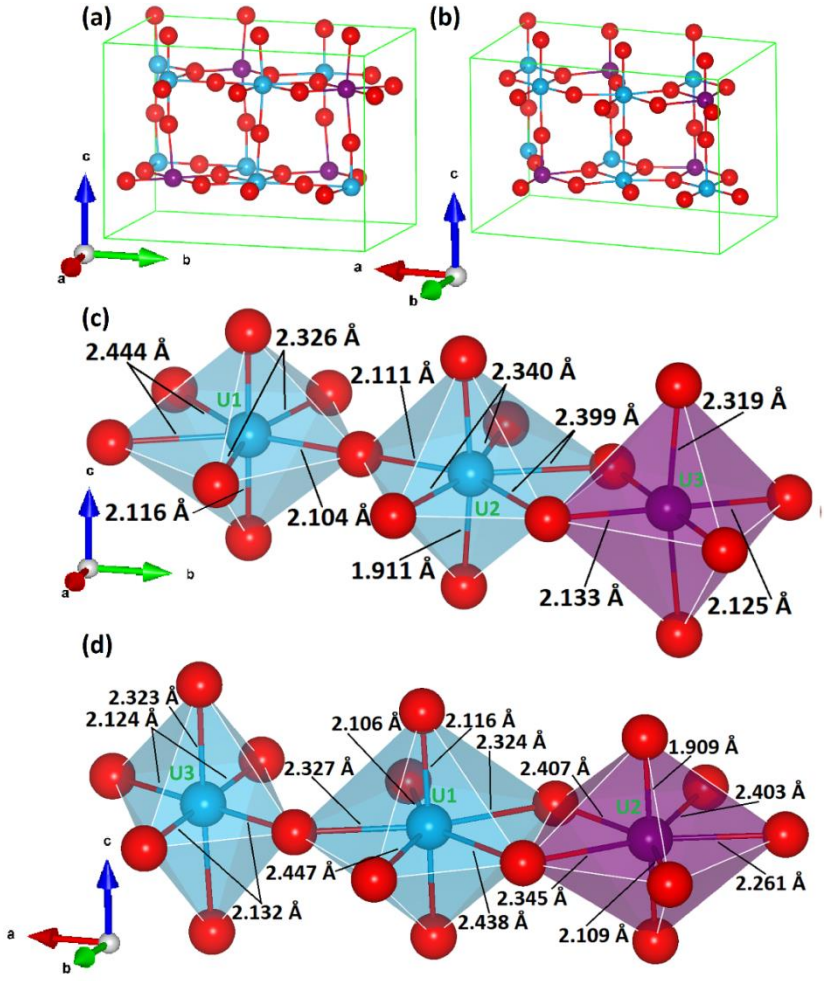

Figure 6.03 – PBE + U predicted structure of β-U_3O_8 (a) *Cmcm* unit cell, (b) *P1* unit cell, (c) uranium coordination in *Cmcm* structure and (d) uranium coordination in *P1* structure. U^{6+} ions are in purple, U^{5+} in blue, oxygen in red and the unit cell is highlighted in green.

Examining the results of the simulations (Table 6.01 and Figure 6.03) the similarities with α-U_3O_8 are still very apparent and the *Cmcm* polymorph is found to be energetically most stable. Both calculations predict U^{5+}/U^{6+} charge configurations and the PBE + U slightly overestimates the volume at 5.5 % and 6.9 % for the *Cmcm* and *P2₁/m* structures respectively. The lattice expansion is more isotropic and hence the relatively large distortion of the *a* lattice parameter in α-U_3O_8 is not found for β-U_3O_8. In the *Cmcm* calculation the uranium coordination and oxygen sublattice remain undistorted from their experimental configuration (comparable to *Cmmm* α-U_3O_8) and the *Cmcm* symmetry is retained (Figure 6.03 (a)). The *P2₁/m* polymorph relaxes to the lower symmetry *P1* group, adopting a monoclinic (β = 86.5 °) cell, accompanied by a large oxygen sublattice relaxation as the octahedral uranium site switches from U2 to U3 (Figure 6.03 (d)). The uranium charges remain unchanged though, yielding a U^{6+} ion in pentagonal bipyramidal coordination and U^{5+} in octahedral coordination, in contrast to the other U_3O_8 polymorphs examined so far. Additionally this *P1* structure is predicted to contain a number of imaginary vibrational modes, further adding to its lack of stability compared to the *Cmcm* polymorph. The tilting of axial bonds is retained in both structures, with no significant change in the *P1* polymorph but a slight increase in U1 site tilting and slight decrease in U2 and U3 site bending in *Cmcm* β-U_3O_8. Examining simulations from the literature, Wen *et al* used the *P2₁/m* polymorph but again do not report the same structural distortions found in this work [197]. Whilst the U2 site is found to be octahedral here they predict a loosely bonded seventh oxygen ion at 3.00 Å.

β-U_3O_8 is predicted to have a wider range of axial U-O bond distances than the other polymorphs (1.91 – 2.32 Å), although the average is still similar at around 2.10 Å. This does not seem to be related to the uranium charge, as the shortest axial bond is at a U^{5+} site in the *Cmcm* structure and at the U^{6+} site in the *P1* structure. It also appears to be unrelated to how tilted the axial bond is relative to the equatorial plane, as it is the most tilted bond in the *P1* structure but not in the *Cmcm*. It was not possible to stabilise alternative charge configurations in either of the β-U_3O_8 calculations.

6.2.3 γ-U_3O_8

γ-U_3O_8, or the high pressure polymorph, is reported to form after heating α-U_3O_8 to 473-573 K (or UO_2 to 900 K) at high oxygen partial pressure (> 16, 000 atm) [31, 222]. It crystallises in the relatively high symmetry hexagonal *P-62m* space group in a single formula unit (11 atom) cell. There is a single type of uranium site in the experimentally determined structure that has pentagonal bipyramidal coordination, in a markedly similar arrangement to *Amm2* α-U_3O_8. In keeping with β-U_3O_8 though there is a slight tilting of the axial U-O bonds relative to the equatorial plane (4.1 °). No experimentally measured density could be obtained for this polymorph but the theoretical density sits halfway between α- and β-U_3O_8 at 8.36 gcm^{-3}.

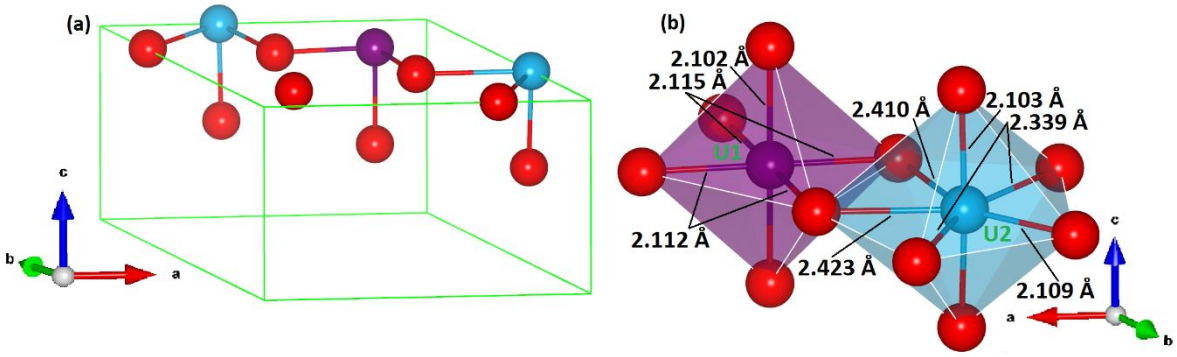

Figure 6.04 – PBE + U predicted structure of γ-U_3O_8 (a) *P-62m* unit cell and (b) uranium coordination at the two uranium sites (note that only a single type of uranium site is observed experimentally). U^{6+} ions are in purple, U^{5+} in blue, oxygen in red and the unit cell is highlighted in green.

The predicted structural properties of γ-U_3O_8 are given in Table 6.01 and Figure 6.04 shows the PBE + U predicted structure. Although it was not possible to stabilise a U^{4+}/U^{6+} charge configuration in this polymorph a partially delocalised system was obtained (referred to as $U^{5+}/U^{5.5+}$, containing one of the former and two of the latter) that was considerably less energetically stable than U^{5+}/U^{6+} and contained imaginary vibrational modes, emphasising the preference for formal charge. The relaxed structure bears strong resemblance to previous polymorphs (the exception being *P1* β-U_3O_8) as the oxygen sublattice relaxes to split the uranium sites into octahedral U^{6+} and pentagonal bipyramidal U^{5+}. There is also significant straightening of the axial U-O bonds on minimisation, deviating from straight by

only 0.20 ° and 1.51 ° in the relaxed structure for U^{6+} and U^{5+} respectively. Agreement with the experimentally determined volume is slightly better than the previous polymorphs, overestimating by only 1.5 %. The hexagonal symmetry, however, is broken in each calculation with the γ angle predicted to be 116 ° in the U^{5+}/U^{6+} configuration and 122 ° in the $U^{5+}/U^{5.5+}$ system. The symmetry also changes to *Amm2* on minimisation and the predicted energy per uranium ion to within 0.05 eV of the *Amm2* α-U_3O_8 structure. Again, previous simulations do not indicate any distortion of the oxygen sublattice [197], reporting the longest bond length to be 2.59 Å compared to complete dissociation (3.59 Å) to octahedral coordination that is found in the present work. The axial bonding is also most similar to in α-U_3O_8, with no formation of shorter axial bonds at either uranium site.

6.3 Elastic Properties

There is no experimentally recorded or DFT predicted bulk modulus for U_3O_8 however Ball *et al* used ionic potentials (with an averaged $U^{5.33+}$ charge) to predict some of the elastic constants for *Amm2* α-U_3O_8, although oddly do not provide enough information for calculation of the bulk modulus [213]. In this work the full set of elastic constants have been predicted and bulk moduli calculated using the PBE + U for each U_3O_8 polymorph and are presented in Table 6.02. In the interests of space only the nine independent elastic constants for orthorhombic cells have been provided, however the monoclinic symmetry of the relaxed γ-U_3O_8 systems has been taken into consideration when calculating the bulk moduli.

As discussed previously, *Amm2* α-U_3O_8 and *P1* β-U_3O_8 are both predicted to contain imaginary vibrational frequencies and so are expected to be dynamically unstable. In addition to this the U^{4+}/U^{6+} α-U_3O_8 configuration is predicted to have a negative C_{55} elastic constant which, as established in section 3.5.3, is further indication of instability. A number of the other elastic constants in this phase are predicted to be lower than in the equivalent U^{5+}/U^{6+} structure and so a lower bulk modulus overall is achieved. Comparing with the two γ-U_3O_8 charge configurations, a slightly lower bulk modulus is found in the partially delocalised ($U^{5+}/U^{5.5+}$) system for the same reasons. So deviation from a U^{5+}/U^{6+} charge configuration in U_3O_8 serves to reduce the elastic constants and bulk modulus overall.

Table 6.02 – Predicted elastic constants and bulk moduli of U_3O_8 polymorphs. Independent elastic constants for orthorhombic cells are included. EM refers to interatomic potential based energy minimisation. Details of bulk moduli (*B*) calculation can be found in section 2.4.1.

Study	Phase	Method	U Charge Configuration	Elastic Constants (GPa)									*B* (GPa)	Vol/U (Å^3)	E_{Form} (eV)
				C_{11}	C_{12}	C_{13}	C_{22}	C_{23}	C_{33}	C_{44}	C_{55}	C_{66}			
Ball [213]	*Amm2* α-U_3O_8	EM	$U^{5.33+}$	373.0	279.8	-	372.6	-	683.4	57.0	-	-	-	57.92	-
This Work		PBE	$U^{5.33+}$	523.4	27.8	30.2	245.4	198.2	248.4	32.1	31.3	33.4	168.1	56.12	-
		PBE + U	U^{4+}/U^{6+}	470.1	1.5	18.7	126.6	72.1	226.4	22.2	-24.0	31.5	92.5	60.92	-0.70
			U^{6+}/U^{5+}	505.3	42.5	26.9	373.9	139.9	258.2	31.8	34.4	25.7	165.8	58.72	-1.09
	Cmmm α-U_3O_8	PBE + U	U^{6+}/U^{5+}	268.0	142.2	29.2	386.3	38.6	505.9	35.7	34.3	26.3	169.4	58.67	-1.10
	Cmcm β-U_3O_8	PBE + U	U^{6+}/U^{5+}	244.1	136.2	3.2	370.2	24.4	388.1	39.8	29.2	22.1	140.6	59.06	-1.12
	P1 β-U_3O_8	PBE + U	U^{6+}/U^{5+}	208.8	191.7	6.7	263.3	18.6	376.0	56.5	22.1	20.9	136.8	59.20	-1.08
	Amm2 γ-U_3O_8	PBE + U	U^{6+}/U^{5+}	311.3	181.9	35.4	255.0	31.2	504.8	78.1	26.8	31.2	181.4	56.60	-1.08
		PBE + U	$U^{5+}/U^{5.5+}$	129.2	260.6	27.5	175.8	46.9	504.4	10.4	30.2	28.1	154.9	59.86	-0.77

The elastic constants and bulk moduli for *Amm2* and *Cmmm* α-U_3O_8 are generally very similar, which is expected given how alike the two relaxed structures are. The *Cmmm* polymorph is predicted to have a slightly higher bulk modulus and has a slightly lower volume per uranium ion. γ-U_3O_8 is predicted to have a slightly higher bulk modulus still, in keeping with its lower volume. The largest volume per uranium ion is found for the β-U_3O_8 polymorphs and they are also found to have the lowest bulk moduli of the group. Thus with highly related structures like the U_3O_8 polymorphs an inverse relationship between bulk modulus and volume emerges. The bulk moduli predicted for U_3O_8 are considerably lower than the 209 GPa found for UO_2 [22] (volume is 40.9 Å/U ion) and compare favourably with UO_3 polymorphs that do not contain uranyl type bonds [72].

The elastic properties can be more precisely linked to the structures themselves, as the largest elastic constant (i.e. largest resistance to compression) is found along the axis parallel to the axial U-O bonds. In *Amm2* α-U_3O_8 this refers to the C_{11} elastic constant (*a* axis) but in all other polymorphs this is the C_{33} elastic constant, corresponding to the *c* axis. This behaviour was also observed in section 3.5.3 with the elastic constants of the layered U_2O_5 polymorphs.

6.4 Electronic Properties

The DOS and band gap of U_3O_8 have been studied fairly extensively using DFT [172, 197, 215, 216] and recently He *et al* used spectroscopic ellipsometry (SE) to determine the band gap of α-U_3O_8 as 1.76 eV (and averaged result from the Cody, Tauc and T-L methods) [172]. The DOS have been calculated for each polymorph studied in this thesis and are presented in Figure 6.05, the predicted band gaps are given in Table 6.02 and values from the literature are provided for comparison.

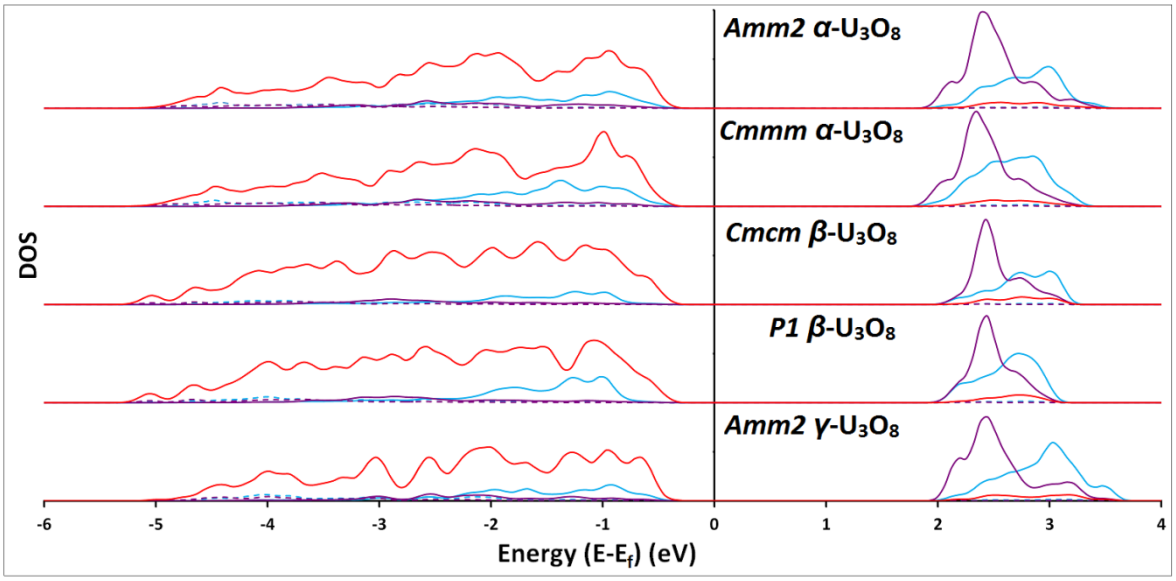

Figure 6.05 – PBE + U predicted partial DOS for U_3O_8 polymorphs. O 2*p* states are in red, U^{5+} states are in blue and U^{6+} states are in purple, 5*f* states are designated with solid lines and 6*d* are shown with dashed lines. Contributions from other states are negligible and so are omitted. Only spin up states are included here as the spin up and spin down channels are extremely similar. The energy of the highest occupied state was set to zero eV (i.e. E = E - E_f).

The partial DOS includes uranium 5*f* and 6*d* states and oxygen 2*p* states as contributions from other states were all found to be negligible. Equatorial and axial oxygen signals were not separated as they differed only in intensity (rather than energy of occupied states), corresponding to the different proportions of each. All U_3O_8 polymorphs are found to be clear charge transfer insulators with valence bands largely composed of O 2*p* states and conductance bands comprised mainly of U 5*f* states. 6*d* states generally show minor contributions to each band, most of which is located in the lower valence band and arises from U^{5+} ions. U^{5+} is consistently predicted to occupy the upper conductance band states and U^{6+} the lower conductance band states, implying higher ionicity on the U^{6+} ions. Additionally, there are small contributions from the U^{5+} 5*f* states to the valence band in all polymorphs but almost no U^{6+} 5*f* contributions. The presence of U^{5+} 5*f* states in the valence band suggests covalent mixing with the oxygen 2*p*. This accords well with the latest XPS results, which report covalent mixing in the actinide oxides is closely related to U-O bond distance and closed-shell systems screen the nuclear charge more effectively, thus reducing covalent character (i.e. less covalency is expected in the U^{6+}-O interaction than the U^{5+}-O

interaction) [223, 224]. Comparing the results with UO_3 [72] (Chapter 7), the U^{6+} in U_3O_8 closely corresponds to that of α-UO_3, the polymorph described as "uranium deficient α-U_3O_8", demonstrating similarities in the DOS of two types of oxide. Despite the presence of two U^{5+} sites in each polymorph the U^{6+} peaks are consistently stronger.

Table 6.03 – Calculated and experimentally determined band gaps of U_3O_8 polymorphs from the present work and the literature.

Study	Phase	Method	U Charge	Band Gap (eV)	Vol/U (Å^3)	E_{Form} (eV)
He [172]	***Amm2* α-U_3O_8**	Experiment	-	1.76	55.55	-
		LDA + U	U^{5+}/U^{6+}	2.43	53.91	-
Wen [197]		HSE	U^{5+}/U^{6+}	0.80	53.68	-
		PBE + U	U^{5+}/U^{6+}	1.20	58.68	-
Yun [216]		PW91 + U	U^{5+}/U^{6+}	0.63	58.65	-
Geng [215]		PBE	$U^{5.33+}$	2.20	56.39	-
This work		PBE + U	U^{4+}/U^{6+}	0.71	60.92	-0.70
		PBE + U	U^{5+}/U^{6+}	2.05	58.72	-1.09
		PBE	$U^{5.33+}$	1.37	56.12	-
	***Cmmm* α-U_3O_8**	PBE + U	U^{5+}/U^{6+}	2.01	58.67	-1.10
Wen [197]	***P1* β-U_3O_8**	HSE	U^{5+}/U^{6+}	1.60	54.23	-
		PBE + U	U^{5+}/U^{6+}	1.20	56.76	-
This Work		PBE + U	U^{5+}/U^{6+}	2.12	59.20	-1.08
	***Cmcm* β-U_3O_8**	PBE + U	U^{5+}/U^{6+}	2.23	59.06	-1.12
Wen [197]	***Amm2* γ-U_3O_8**	HSE	U^{5+}/U^{6+}	0.00	53.52	-
		PBE + U	U^{5+}/U^{6+}	0.00	56.31	-
This Work		PBE + U	U^{5+}/U^{6+}	2.19	56.60	-1.08
		PBE + U	$U^{5+}/U^{5.5+}$	0.84	59.86	-0.77

The PBE + U calculations from this thesis overestimate the α-U_3O_8 band gap by around 0.25 eV, although this result is still closer to the experimentally determined one than any of the simulations in the literature (Table 6.03). In the systems where U^{4+} or $U^{5.5+}$ ions were predicted the band gaps are significantly lower than the experimental or U^{5+}/U^{6+} results (0.71 and 0.84 eV respectively); reinforcing the argument that that the U^{5+}/U^{6+} configuration is correct. The α-U_3O_8 PBE calculation ($U^{5.33+}$) also yields a lower band gap (1.37 eV) compared to the equivalent PBE + U calculation. This value is significantly lower than the 2.2 eV reported by Geng *et al* in their equivalent calculation [215]. *Cmcm* β-, *P1* β- and *Amm2* γ-U_3O_8 are all predicted to have slightly higher band gaps than α-U_3O_8, between 2.12 and 2.23 eV.

Considering the predicted band gaps from the literature, there is quite a spread of results depending mainly on the choice of functional. In α-U_3O_8, the LDA + U overestimates the band gap by the greatest margin whilst the HSE and PW91 + U underestimate it most significantly. Wen *et al*s PBE + U result differs significantly from the present work, considerably underestimating the band gap, however they do not report the same structural distortion observed here. Geng *et al*s PBE calculation also differs substantially from the one presented here, overestimating by around 0.5 eV, compared to an underestimation of 0.39 eV. The *P1* β-U_3O_8 predicted band gap is 0.82 eV higher than the equivalent calculation from Wen *et al* and 0.50 eV higher than their HSE calculation. The largest difference, however, is seen for γ-U_3O_8 where they predict a metallic phase with both calculations whilst the simulations from this work predict the same insulating state as the other polymorphs, maintaining the close relationship the three polymorphs have demonstrated in other areas.

6.5 Thermodynamic Properties

This section discusses various thermodynamic properties of the stable U_3O_8 polymorphs, i.e. those that are predicted to contain no imaginary vibrational frequencies and meet the stability criteria for elastic constants. Thus the predicted thermodynamic properties of *Cmmm* α-, *Cmcm* β- and *Amm2* γ-U_3O_8 are presented in Figure 6.06. The formation enthalpy has been normalised with respect to the most stable polymorph (*Cmcm* β-U_3O_8) such that $\delta Hf = \Delta H_x - \Delta H_{\beta\text{-U3O8}}$, where x is the phase in question (Figure 6.06 (a)). Pressure has then been introduced and varied from -25 to 125 kbar to simulate a range of conditions from high temperature (negative pressure) to high pressure. Taking the predicted vibrational frequencies it was then possible to estimate the Helmholtz free energy (Figure 6.06 (b)) and vibrational entropy (Figure 6.06 (c)).

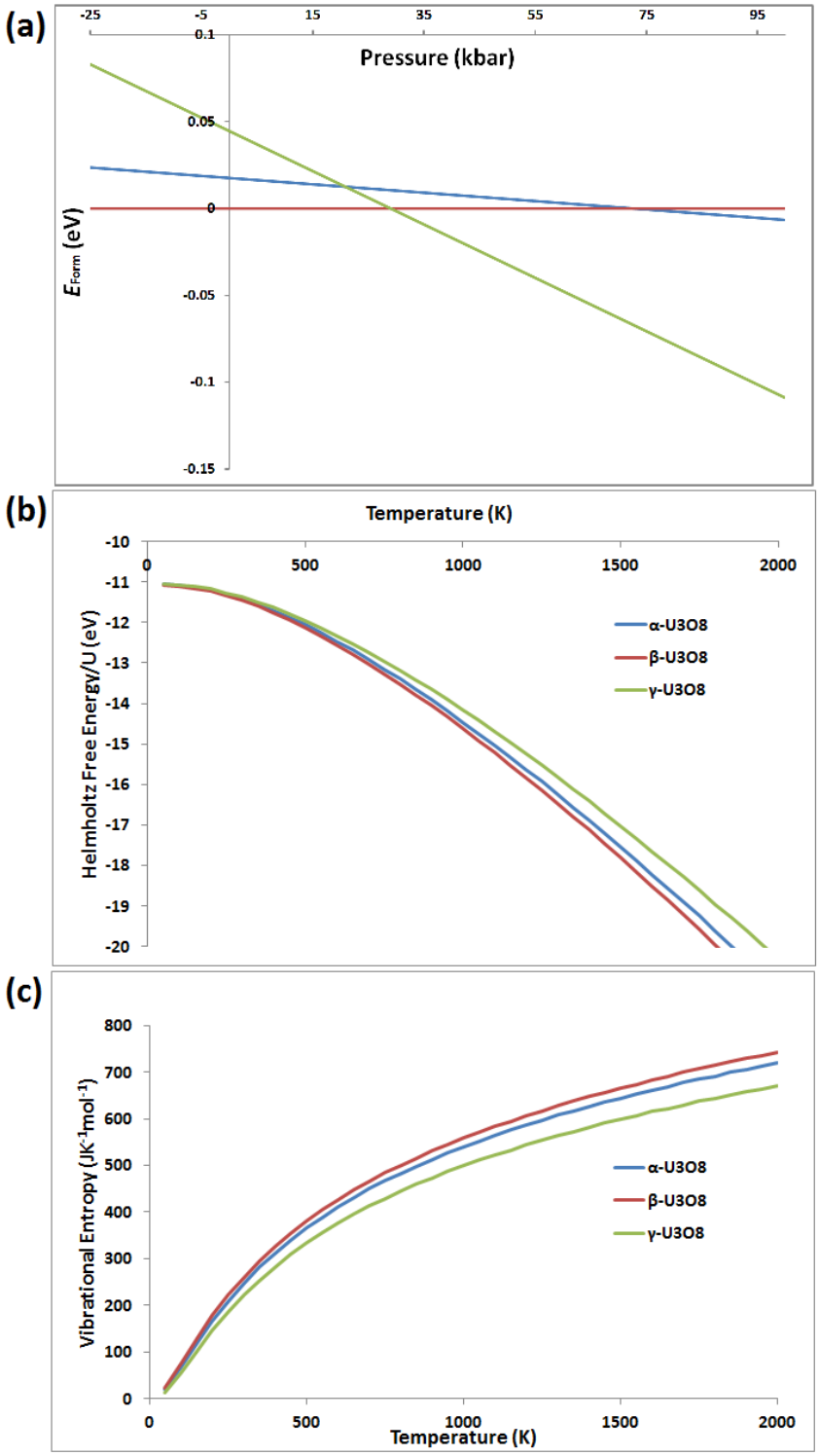

Figure 6.06 – (a) calculated enthalpies of formation as function of pressure, relative to *Cmcm* β-U_3O_8, (b) Helmholtz free energy as a function of temperature and (c) vibrational entropy as a function of temperature.

The plots demonstrate good qualitative agreement with experiment. Figure 6.06 (a) shows γ-U_3O_8 is predicted to be most stable at high pressure, logical considering it has the smallest predicted volume per uranium ion. The calculations predict it to be stabilised above 25 kbar (at 0 K) compared to the experimental value of greater than 16 kbar (although the experimental data was collected at higher temperature) [222]. Generally acknowledged as the high temperature polymorph, β-U_3O_8 is predicted to be most stable at negative pressure (used here to represent high temperature). Considering only the enthalpic contributions the calculations predict β-U_3O_8 to be most stable at 0 K, despite having a higher zero point energy. However, the difference with α-U_3O_8 is so minimal (0.025 eV) that a polycrystalline sample is highly likely to contain equal amounts of both polymorphs at low temperatures, with the synthesis conditions (i.e. kinetics) determining which polymorph dominates. This behaviour reflects the experimental observations of Loopstra [199] and Hoekstra [203] well.

The calculations predict that β-U_3O_8 has the highest vibrational entropy (Figure 6.60 (c)), which stabilises the polymorph at higher temperatures compared to α-U_3O_8 (Figure 6.60 (b)). γ-U_3O_8 is predicted to have the lowest vibrational entropy and consequently is found to be least stable at high temperatures.

6.6 Conclusions

Five different structures for three polymorphs of U_3O_8 have been simulated, two of which for the first time (*Cmmm* α-U_3O_8 and *Cmcm* β-U_3O_8). The PBE + U provides an adequate description of the phase, albeit with slight volume expansion. It is also an improvement on the PBE, which falsely predicts itinerant uranium *f* electrons. There was also no energetic preference between FM and AFM structures (presented in Appendix C), suggesting the possibility of paramagnetism in U_3O_8.

Cmmm α-, *Cmcm* β- and *Amm2* γ-U_3O_8 have been identified as the stable forms of each polymorph and all three were found to contain octahedrally coordinated U^{6+} ions and U^{5+} ions in pentagonal bipyramidal coordination. The *Amm2* α- and *P1* β-U_3O_8 polymoprhs were both found to be energetically less stable than their counterparts and contain imaginary vibrational frequencies.

In two systems U^{4+}/U^{6+} (*Amm2* α-U_3O_8) and $U^{5+}/U^{5.5+}$ (γ-U_3O_8) charge configurations were retained, but were found to be considerably less stable than U^{5+}/U^{6+} as well as having unreasonably low band gaps and bulk moduli. They were also both found to contain imaginary vibrational modes, the U^{4+}/U^{6+} system containing the most.

The elastic constants of U_3O_8 have been calculated for the first time, with bulk moduli of 169, 141 and 181 GPa for the stable α-, β- and γ- polymorphs respectively. A larger bulk modulus was found to be linked to a smaller volume per uranium ion and vice versa. Predicted bulk moduli were found to be similar in magnitude to related UO_3 polymorphs (150 GPa and above), i.e. those containing no uranyl type bonds. In a similar manner to U_2O_5, the largest predicted elastic constants are those that correspond to compression parallel to the axial U-O bonds, indicating greater mechanical strength in this dimension.

All polymorphs are predicted to be charge-transfer insulators (in the same way as U_2O_5 and UO_3) with band gaps of 2.01, 2.23 and 2.19 eV for the stable α-, β- and γ- polymorphs respectively. The partial DOS for each structure show minimal contributions from uranium 6*d* states to the VB, and almost none in the CB. The VB is predominantly composed of oxygen 2*p* states and the CB uranium 5*f* with clearly distinct peaks for U^{5+} and U^{6+} ions. The U^{6+} peaks are found to occupy lower energy states than U^{5+}, implying greater iconicity at the more highly charged site. U^{5+} ions also show a greater degree of covalent mixing between uranium 5*f* and oxygen 2*p* orbitals than U^{6+} and there is also considerably more 5*f*-2*p* mixing than 6*d*-2*p*.

Finally, the α- and β- polymorphs are predicted to be in competition at low temperatures, with the exact polymorph formed dependent on the synthesis conditions. Although β-U_3O_8 is predicted to be thermodynamically more stable α-U_3O_8 is more commonly observed experimentally, suggesting it forms via a kinetically controlled process. As the temperature is increased β-U_3O_8 dominates as it is stabilised by its higher vibrational entropy. γ-U_3O_8 is predicted to be the most stable polymorph at high pressures and is destabilised compared to the other two at high temperatures.

As mentioned earlier in this chapter, U_3O_8 bears some structural similarities to α-UO_3 (essentially an oxygen deficient version) and thus the following chapter considers the various polymorphs of UO_3.

Chapter 7

7 Layered UO_3

UO_3 marks the end point of the U-O system, as with an oxidation state of U^{6+} ($5f^{\,0}$ configuration) all valence electrons have been removed. It also displays more polymorphism than any of the other oxides, with a reported seven crystalline polymorphs and one amorphous phase [19, 174]. In addition to the relevance of this phase to the nuclear fuel cycle discussed in Chapter 1, the UO_3 polymorph formed is characteristic of the particular production method used and so a detailed understanding of the UO_3 system has potential use in nuclear forensics [225]. Detailed discussion of the different polymorphs is provided in section 7.2.

All of the UO_3 results have been published previously in Inorganic Chemistry in an article entitled "*Ab Initio Investigation of the UO_3 Polymorphs: Structural Properties and Thermodynamic Stability*" [72].

7.1 UO_3 Background

The U^{6+} ion displays a variety of coordination environments across the UO_3 polymorphs and, unique to this stoichiometry, some of the oxides feature so-called uranyl bonds, i.e. shorter axial bonds named such due to their presence in the uranyl (UO_2^{2+}) ion. The γ-UO_3 polymorph is the most thermodynamically stable uranium oxide and this, along with some of the other modifications, have been investigated fairly extensively beyond structural determinations in terms of their thermodynamic [129], electronic [172, 223, 224, 226] and optical [225] properties. There are also a handful of computational studies in the literature, mainly dealing with structural and electronic properties [172, 215, 227].

The extensive non-stoichiometry of the fluorite based uranium oxides is well documented and has been discussed in Chapter 4, however layered oxides, particularly UO_3, also display

disorder. In his report on the preparation and characterisation of UO_3 polymorphs, Cornman describes the difficulty in achieving a stoichiometric sample [228]. The oxides he produced all had O/U ratios between 3.03 and 3.07 with the exception of ζ-UO_3, which was found to be 3.23. The particularly high ratio in this case was attributed to the presence of ~1 wt % sulphate, occurring due to the production method which involved sulphamic acid. U^{6+} is the soluble form of uranium and UO_3 compounds are renowned for formation of hydrolysis and hydration products under ambient conditions [222, 229, 230]. Additionally, it is challenging to prepare some UO_3 polymorphs without the presence of others [225, 231], so producing a stoichiometric sample with no hydration products is an even greater challenge. There are also issues with hypostoichiometry; Girgis *et al* synthesised six UO_3 polymorphs with O/U ratios between 2.97 - 3.00, suggesting a small amount of uranium interstitials or (more likely) oxygen vacancies [226].

This chapter presents results from simulations of the α-, β-, γ-, δ- and η-UO_3 polymorphs and compares them with the available data from experiments and simulations in the literature. There have also been multiple reports on the synthesis of ε- [232, 233] and ζ-UO_3 [226, 228] but their simulation has been neglected due to insufficient structural data. The lack of valence electrons makes modelling these materials relatively straightforward compared to the lower uranium oxides as charge configurations and competing magnetic structures can be safely ignored.

7.2 Structural Properties

This section discusses the synthesis and structural properties of the five UO_3 polymorphs with sufficient data for simulation in the literature. Validity of structures has been confirmed by calculating the vibrational frequencies and checking for imaginary modes. The results are presented in Table 7.01 along with their relative stabilities in terms of formation energy with respect to UO_2.

Table 7.01 – Predicted properties of the UO_3 polymorphs, *C2mm* α-UO_3 refers to the experimental structure (with an imaginary frequency ($^+$)) and *C2* α-UO_3 is the adjusted structure (with no imaginary frequencies). Space groups are calculated to a tolerance of 0.001 Å using Materials Studio [192]. Reported energies are formation energy per uranium atom with respect to UO_2^+. Δ % is the percentage difference between the calculated structure and experiment.

Phase	Method	Lattice Parameters (Å)				*c*/*a* Ratio (Δ %)	Vol/U (Å^3)	Uranyl Bond (Å)		Space Group	E_{Form} (eV)
		a (Δ %)	*b* (Δ %)	*c* (Δ %)	*β* (°)			U1	U2		
***P-3m1* α-UO_3**	**Exp [234]**	3.97	3.97	4.17	120.0	1.05	56.92	2.08	-	*P-3m1*	-
	PBE + U	3.85 (-3.1)	3.85 (-3.1)	4.18 (0.4)	120.0	1.09 (3.6)	53.64 (-5.8)	2.09	-	*P-3m1*	-0.82
($^+$)*C2mm* α-UO_3	**Exp [219]**	3.91	6.94	4.17	90.0	-	56.55	2.08	2.08	*C2mm*	-
	PBE + U	3.96 (1.3)	6.81 (-1.9)	4.18 (0.2)	90.0	-	56.31 (-0.41)			*C2mm*	-0.59
***C2* α-UO_3**	**Exp [219]**	3.91	6.94	4.17	90.0	-	56.55	2.08	2.08	*C2*	-
	PBE + U	3.89 (-0.7)	6.61 (-4.7)	4.18 (0.4)	90.0	-	53.69 (-5.1)	2.09	2.09	*C2*	-0.81
β-UO_3	**Exp [235]**	10.34	14.33	3.91	99.0	-	57.22	-	-	$P2_1$	-
	PBE + U	10.81 (4.6)	14.33 (0.0)	4.19 (7.2)	90.8	-	64.95	-	-	$P2_1$	-1.21
***I4₁* γ-UO_3**	**Exp [196]**	6.90	6.90	19.98	90.0	2.89	59.46	1.80	1.89	$I4_1$	-
	PBE + U	7.03 (1.8)	7.03 (1.8)	20.68 (3.4)	90.0	2.94 (1.6)	63.82 (7.1)	1.78	1.87	$I4_1$	-1.46
***Fddd* γ-UO_3**	**Exp [196]**	9.79	19.93	9.71	90.0	2.02	59.16	1.76	1.88	*Fddd*	-
	PBE + U	9.94 (1.2)	20.68 (4.2)	9.93 (3.1)	90.0	2.08 (2.9)	63.79 (8.7)	1.78	1.87	*Fddd*	-1.46
δ-UO_3	**Exp [231]**	4.17	4.17	4.17	90.0	-	72.25	-	-	*Pm3m*	-
	PBE + U	4.20 (0.8)	4.20 (0.8)	4.20 (0.8)	90.0	-	73.89 (2.3)	-	-	*Pm3m*	-1.26
η-UO_3	**Exp [174]**	7.51	5.47	5.22	90.0	-	53.62	1.85/1.80		$P2_12_12_1$	-
	PBE + U	7.76 (3.3)	5.56 (1.6)	5.34 (2.3)	90.0	-	57.60 (7.4)	1.84/1.82		$P2_12_12_1$	-1.31

* - $E_{\text{Form}} = E_{UO_2} - (E_{UO_3} - E_U - 3E_O)$ (see section 2.4.4)

7.2.1 α-UO_3

α-UO_3 bears a close structural relation to α-U_3O_8 with uranium vacancies and is usually prepared by heating uranyl peroxide to 673 – 773 K [236]. Using XRD Zachariasen determined it crystallises in a four atom hexagonal unit cell in the *P-3m1* space group [234]. This was later refined to an orthorhombic two formula unit cell, first by Loopstra (*C2mm*) [219] and second by Greaves (*C222*) [218]. Zachariasen and Loopstra experimentally determined densities of 7.04 and 7.25 gcm^{-3} respectively, which differ significantly from Loopstra's theoretical density of 8.39 gcm^{-3}. This led Greaves to conclude that α-UO_3 is an imperfect structure with approximately 12 % of uranium lattice sites vacant, reducing the theoretical density to 7.44 gcm^{-3}, much closer in line with the observed densities. Subsequently the structure reported by Greaves is complex, involving partial occupancy of both uranium and oxygen sites, and thus hindering efforts to simulate it in this work. Consequently only the hexagonal *P-3m1* (Figure 7.01 (a)) and orthorhombic *C2mm* (Figure 7.01 (b)) modifications are considered here. Both structures feature hexagonal bipyramidal coordination with two distinct oxygen sites; O1 form the axial U-O bonds and O2 the equatorial ones, the equatorial bonds lying in the {001} (*ab*) plane. In the *C2mm* polymorph the equatorial oxygen ions all lie in this plane but in *P-3m1* α-UO_3 they are all reported to lie slightly above and below the plane, distorting the coordination slightly. Neither experimental structure is reported to contain uranyl bonds.

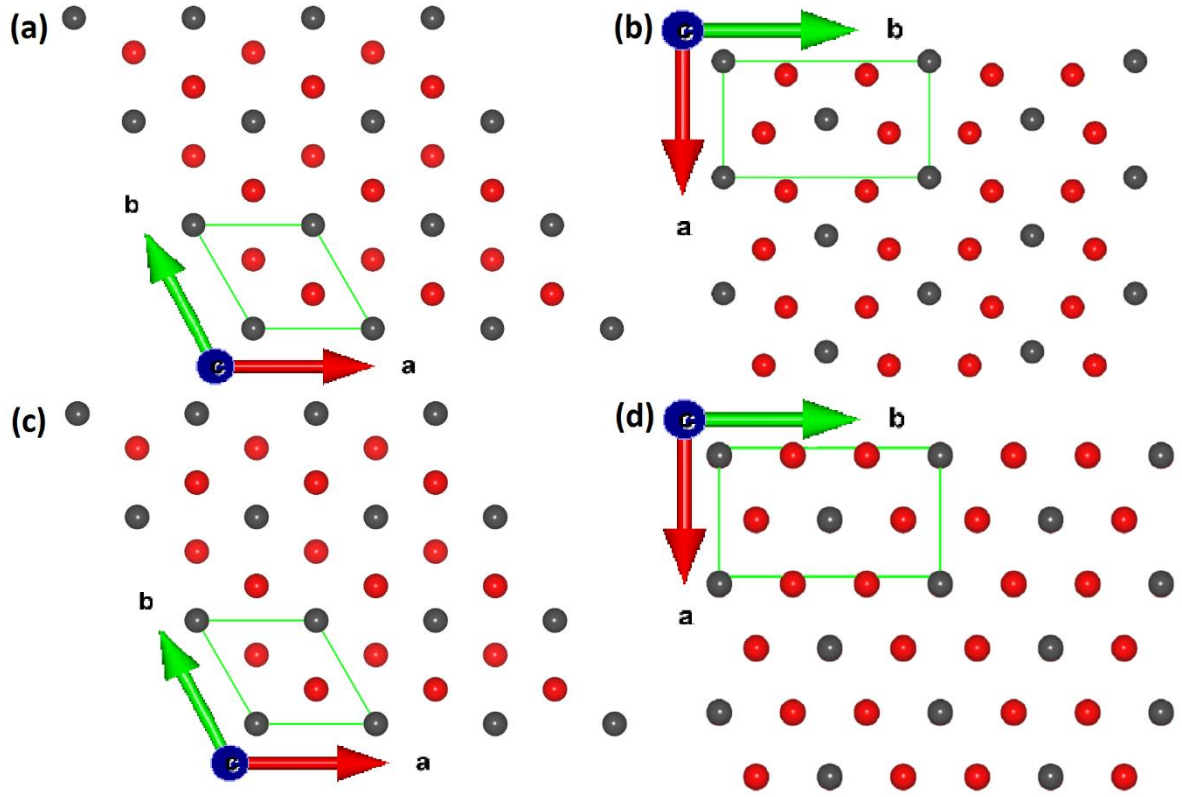

Figure 7.01 – Structures of α-UO_3 polymorphs: (a) experimentally observed *P-3m1* structure, (b) experimentally observed *C2mm* structure, (c) PBE + U *P-3m1* structure and (d) PBE + U *C2mm* (*C2*) structure. Uranium ions are in black, oxygen in red and the unit cell is highlighted in green.

The calculated structural properties of *P-3m1* and *C2mm* α-UO_3 are given in Table 7.01 and their predicted structures can be found in Figures 7.01 (c) and (d) and 7.02 (a) and (c). The *P-3m1* modification is found to be the energetically most stable structure and its overall structural reproduction is very good, maintaining the same space group and coordination as reported experimentally. The unit cell volume is slightly underestimated, which is very unusual for PBE + U calculations, which are renowned for overestimating lattice parameters. The predicted volume (53.64 $Å^3$/U) agrees well with the LSDA + U result of He *et al* (53.91 $Å^3$/U) [172] while Pickard *et al* report a greater underestimation of 51.83 $Å^3$/U using the LSDA [227]. The *c*/*a* ratio for *P-3m1* α-UO_3 in the present work is overestimated by 3.6 %, arising from the slight underestimation of the *a* lattice parameter.

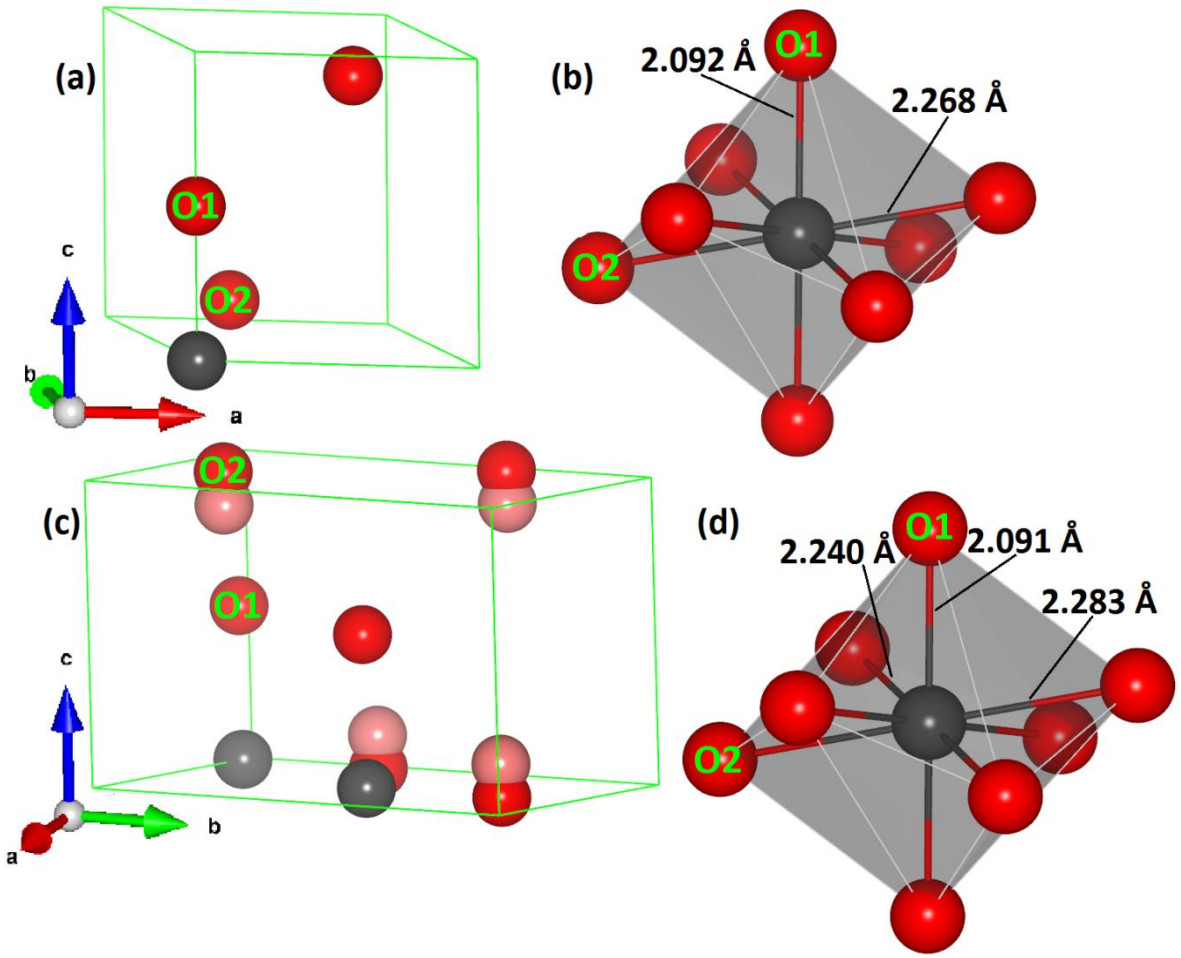

Figure 7.02 – PBE + U predicted structures of α-UO_3 polymorphs: (a) *P-3m1* hexagonal unit cell, (b) uranium coordination in *P-3m1* α-UO_3, (c) *C2mm*/*C2* orthorhombic unit cell and (d) uranium coordination in *C2* α-UO_3. Black spheres are uranium atoms, red are oxygen and the unit cell is highlighted in green. Pink spheres show the adjusted (*C2*) equatorial oxygen positions.

The experimentally derived orthorhombic *C2mm* structure was also well reproduced in the calculations; albeit with a distortion to more isotropic coordination (Figure 7.01 (b) and (d)), closer in line with the *P-3m1* structure (Figure 7.01 (a) and (c)). However, *C2mm* α-UO_3 yielded a single imaginary frequency which was removed by displacing the equatorial oxygen ions along the *z* axis; such that they occupy positions above and below the {001} (*ab*) plane (Figure 7.02 (c)), resulting in a reduced symmetry *C2* structure. This new arrangement is more similar to the *P-3m1* structure, which also features equatorial oxygen ions shifted above and below the plane in puckered hexagonal bipyramidal coordination. On relaxation, the resemblance of the *C2* structure to the *P-3m1* becomes even more

striking, with a tiny energetic preference for the latter (0.01 eV/U) and a difference in predicted volume of less than 0.05 $Å^3$/U (Table 7.01). By way of comparison, the *C2mm* structure was found to be 0.22 eV/U less stable than either of the other configurations. It is clear that six oxygen ions coordinating in the same plane destabilise the system; removing this structural frustration by shifting the oxygen ions out of the plane eliminates the imaginary vibrational frequency, along with stabilising the system considerably.

The predicted axial bond length in both structures is well reproduced, 2.09 Å compared to 2.08 Å observed experimentally, reinforcing the observation that no uranyl bonds are present. The equatorial bonds are 2.27 Å (*P-3m1*) and 2.24 and 2.28 Å (*C2*) (2.40, 2.02 and 2.16 Å in experiment respectively) (Figure 7.02 (b) and (d)). This represents a decrease in anisotropy in the *C2* polymorph, shifting further towards the *P-3m1* modification. The space groups for the hexagonal (*P-3m1*) and orthorhombic (*C2*) polymorphs are in a supergroup-subgroup relation and so are linked by symmetry. Considering the preference for more isotropic bonding and "puckered" over planar equatorial coordination it is logical that the *C2mm* polymorph is a thermally averaged structure. So in α-UO_3 the equatorially coordinated oxygen ions exist above and below the plane but have enough thermal energy to shift their relative positions such that the equilibrium site lies precisely in the {001} (*ab*) plane (i.e. red spheres in Figure 7.02 (c)). This fully explains the lower calculated stability and the imaginary vibrational frequency for *C2mm* α-UO_3.

7.2.2 β-UO_3

β-UO_3 is produced by calcining the product of the reaction of uranyl nitrate and ammonia at 723 – 773 K, γ-UO_3 forms at lower temperatures and so heating must be rapid. β-UO_3 was determined to crystallise in a $P2_1$ monoclinic unit cell (Figure 7.03 (a), (b) and (c)) by XRD and neutron diffraction [235, 237]. The structure is semi-layered and contains five unique uranium and 15 oxygen sites: U1-3 are found on the {010} (*ac*) plane and are connected by O1-5 to form a single UO layer; U4 and U5 are situated midway between these layers, interconnected by O12-15; the remaining O6-11 bridge the two types of layer. The uranium coordination, as reported in the original experimental data, is either distorted octahedral (U3, U4 and U5) or irregular seven-fold (U1 and U2), with each featuring a single short U-O bond (1.51 – 1.79 Å) and five or six U-O bonds at least 0.5 Å longer (Figure 7.03 (a)).

However, analysing the experimentally derived structure with bond cut-offs set according to reported shortest and longest bonds it is revealed that there is only a single distorted octahedral site (U3) with the other uranium ions all in irregular seven-fold coordination (Figure 7.03 (a)).

The distorted coordination means no uranium sites feature uranyl groups, even when there are two shorter bonds present (e.g. U4) they are not collinear. Good agreement is found between experimentally determined and calculated densities for β-UO_3, 8.25 and 8.30 gcm^{-3} respectively [238]. This work forms the first computational investigation of β-UO_3, as there are none pre-existing in the literature.

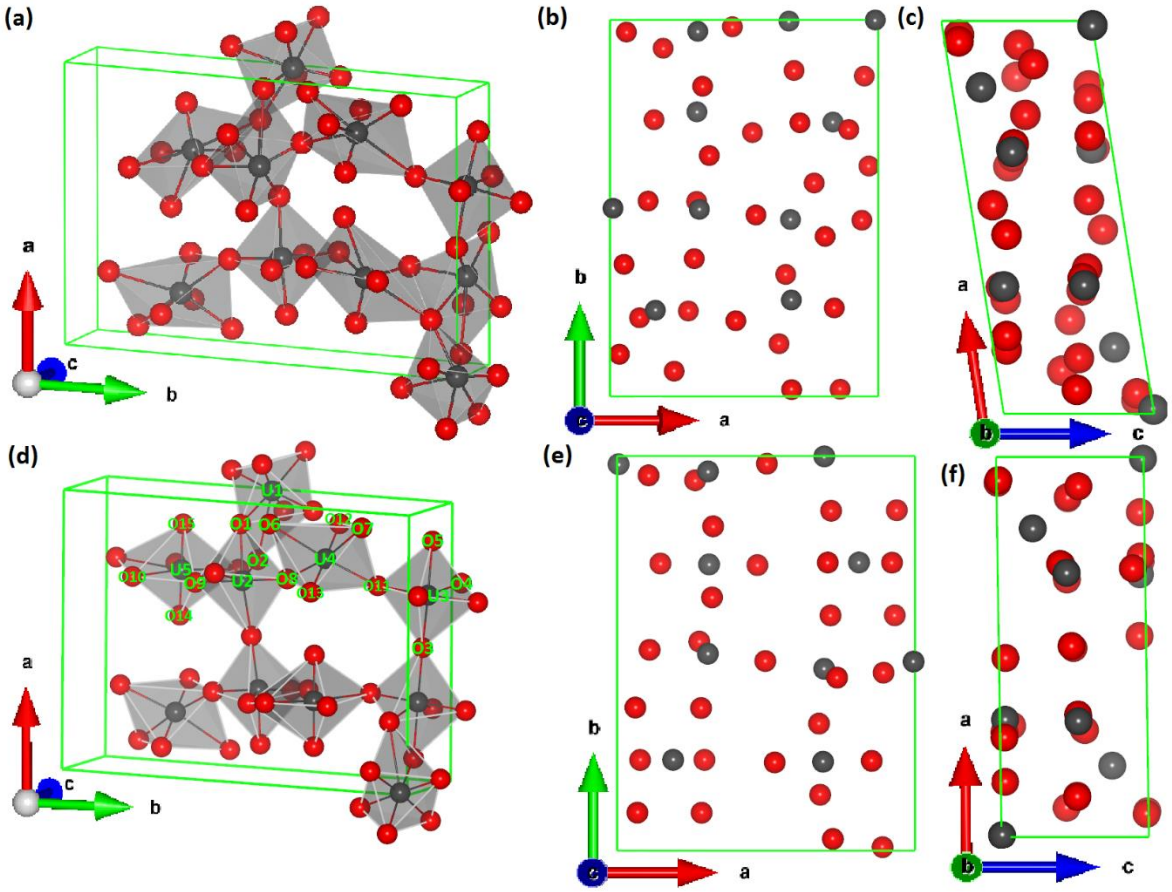

Figure 7.03 – The β-UO_3 unit cell: (a), (b) and (c) observed experimental structure and (d), (e) and (f) PBE + U calculated structure. (a) and (d) show the coordination at the uranium sites, (b) and (e) show the projection along the *z* axis and (c) and (f) show the projection along the *y* axis. Black spheres are uranium atoms, red are oxygen and the unit cell is highlighted in green.

The calculated structural properties of β-UO_3 are given in Table 7.01 and Figure 7.03 (c), (d) and (e) displays the predicted structure. The lattice parameters are overestimated slightly, *a* by 4.6 %, *b* by 0.1 % and *c* by 7.2 %, although this equates to a 13.5 % cell volume increase due to the underestimation of the monoclinic angle at 90.8 ° (compared to 99.0 °). Despite the change in the β angle the cell remains monoclinic on minimisation, although there are significant changes to the bond lengths and uranium coordination at U2 and U4 sites (Figure 7.03). In the relaxed structure, the bond lengths are more consistent with those expected for uranium oxides than the experimentally reported ones. For instance there are none shorter than 1.76 Å, compared to the 1.51 Å short bond reported by Debets [235]. At U1, U4 and U5 sites collinear uranyl type bonds emerge, with lengths ranging between 1.76 and 1.81 Å. Across the cell there is only a slight increase in average bond length on minimisation (0.9 %); reflecting a decrease in anisotropy (similar to that observed in *C2* α-UO_3), and demonstrating a preference for more homogenous U-O bonding. This behaviour is also reflected in the coordination changes at U2 and U4 sites, where the loosely bound oxygen is lost to yield distorted octahedral coordination. Taking these observations into consideration it is likely that β-UO_3 is also a defective structure, although the better agreement between experimentally determined and theoretical densities suggest to a lesser extent than in α-UO_3.

7.2.3 γ-UO_3

γ-UO_3 is acknowledged to be the most thermodynamically stable UO_3 polymorph, and indeed uranium oxide, at oxygen pressures below ten atm [205]. The synthesis is described as burning uranyl nitrate hexahydrate in air at 673 – 873 K or heating other UO_3 modifications to 723 K in 40 atm O_2 [204]. The structure was first determined using XRD by Engmann, who assigned a tetragonal $I4_1$ structure, although with γ = 90.34 ° it is formally monoclinic [239]. Loopstra later used neutron diffraction over a range of temperatures, identifying an orthorhombic *Fddd* structure below 293 K (Figure 7.04 (a) and (b)) and tetragonal $I4_1$ above 373 K (Figure 7.05 (a) and (b)). The two structures are extremely similar though, with the former space group being a maximal subgroup of the latter [196]. The orthorhombic cell is double the size of the tetragonal cell, with twice as many atoms, and they both contain two distinct uranium sites and three independent

oxygen sites. U1 sites adopt distorted octahedral coordination and U2 distorted dodecahedral coordination; O1 sites form short equatorial bonds with U2 and axial bonds with U1; O2 ions coordinate equatorially with U1 and form an alternative short equatorial bond with U2; finally O3 form both the axial and long equatorial bonds with U2 (as there is very little change on relaxation coordination is only shown in Figure 7.05 for the relaxed structures). The axial bonds are short enough to consider "uranyl" at 1.76 – 1.89 Å. This bonding and coordination regime is shared by Engmann's monoclinic structure. The theoretical densities for the *Fddd* and $I4_1$ structures are identical (8.00 ± 0.02 gcm^{-3}) and compare very favourably with the experimentally determined value from Engmann's structure (8.02 gcm^{-3}) [239]. Computationally, the tetragonal $I4_1$ polymorph has been simulated using the LSDA + U by He *et al*, showing good agreement with the experimentally observed volume (-3 %), although no other structural information was provided [172].

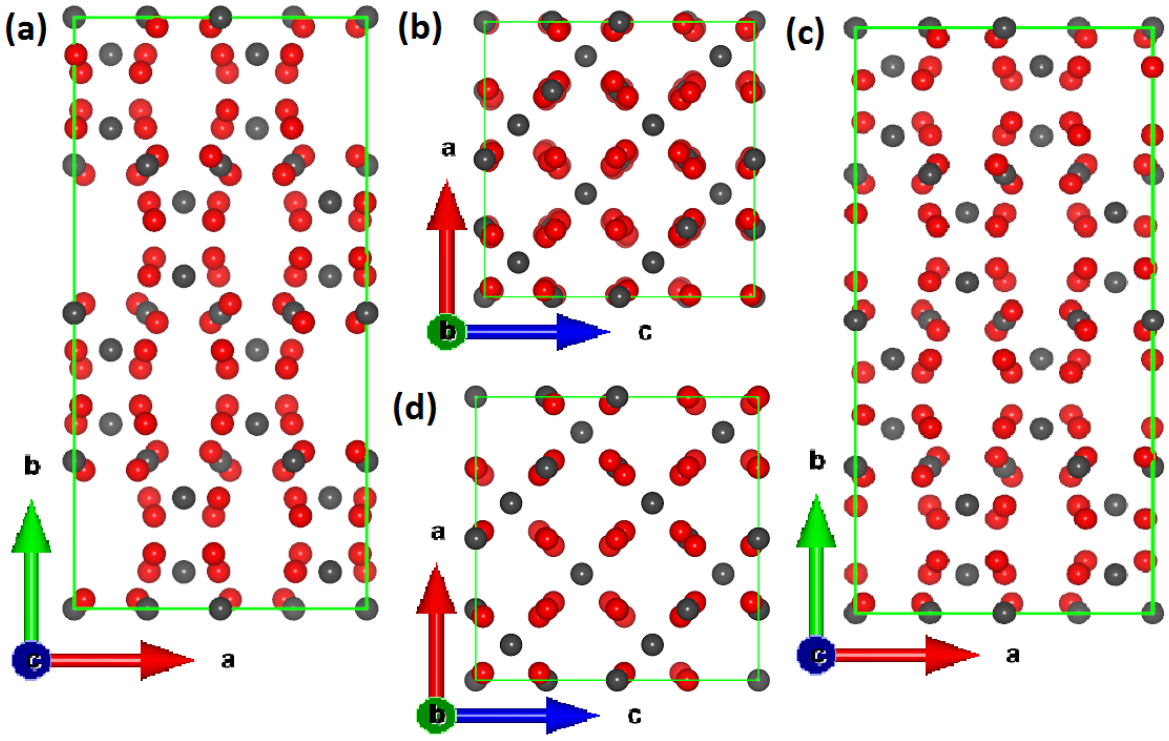

Figure 7.04 – The *Fddd* γ-UO_3 unit cell: (a) and (b) experimentally determined structure, (c) and (d) PBE + U calculated structure. Black spheres are uranium atoms, red are oxygen and the unit cell is highlighted in green.

The monoclinic structure of Engmann was found to relax to a tetragonal cell, retaining $I4_1$ symmetry, and have the same energy and bond lengths as Loopstra's tetragonal $I4_1$ modification. This leads to the conclusion that the monoclinic polymorph is not genuine and it was simply the tetragonal phase that had been identified, indeed the reported monoclinic angle is very small at 90.34 °. Thus only the predicted structural data have been provided for the tetragonal $I4_1$ and orthorhombic *Fddd* structures (Table 7.01), their predicted structures can be found in Figures 7.04 (c) and (d) and 7.05 (c) and (d).

The relaxed $I4_1$ and *Fddd* structures agree well with experiment and are extremely similar; the predicted volumes and energies per uranium ions are almost identical and the minimised bond lengths are practically indistinguishable. Indeed, the *Fddd* structure is related to the $I4_1$ by a 45 ° rotation and √2 expansion in *x* and *y*, accompanied by the reduction in symmetry associated with shifting from a tetragonal to orthorhombic cell. As the only experimental difference was the temperature the two structures were observed at it follows that these simulations did not distinguish between them well as no temperature effects were included.

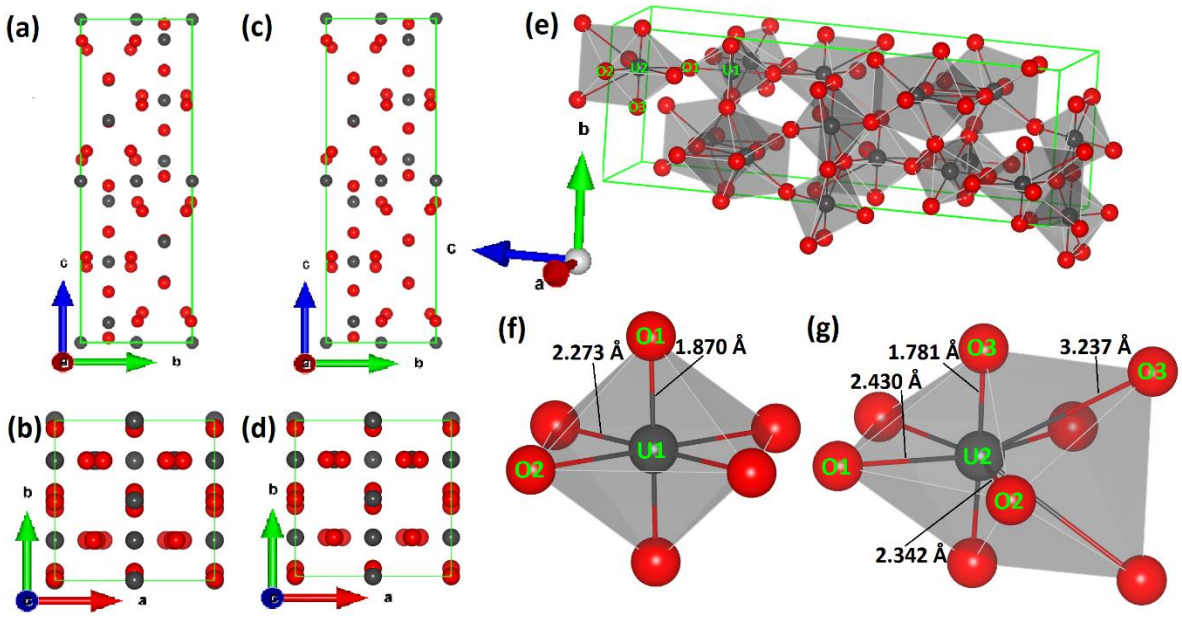

Figure 7.05 – The $I4_1$ γ-UO_3 unit cell: (a) and (b) experimentally determined, (c) and (d) PBE + U calculated and (e) PBE + U calculated showing coordination. (f) shows the octahedral coordination at U1 and (g) shows the dodecahedral coordination at U2. Black spheres are uranium atoms, red are oxygen and the unit cell is highlighted in green.

The predicted lattice parameters and volume were overestimated (7.1 and 8.7 % for $I4_1$ and *Fddd* respectively), compared to the 3.0 % underestimation of He *et al* with the LSDA + U [172]. This volume expansion corresponds to overestimation of each lattice parameter by less than 3.5 and 4.5 % for the $I4_1$ and *Fddd* structures respectively. The *c*/*a* ratio was also slightly overestimated (1.6/2.9 % for $I4_1$/*Fddd*), however this value was not reported by He. On minimisation the equatorially coordinated U-O bonds were predicted to lengthen slightly, more so at U2 than U1 sites, with the largest increase found for U2-O3 bonds. In the experimental structure these are already the longest bonds (3.04/3.01 Å for $I4_1$/*Fddd*) and so the increase to 3.24 Å signifies particularly weak coordination. The axial bonds are predicted to decrease slightly to 1.78/1.87 Å (U1/U2), maintaining the uranyl type coordination. γ-UO_3 is the first UO_3 phase which gains bond anisotropy on minimisation, especially at U2 sites, and the change is the same for both polymorphs.

The thermal lability between the two configurations implies the presence of disorder, which can also explain the overestimation of lattice parameters and subsequent deviation of the simulated systems from the experimental *c*/*a* ratio, as the disorder is absent from these calculations of stoichiometric materials.

7.2.4 δ-UO_3

The δ- polymorph is produced by hydrothermally reacting γ-UO_3, yielding β-$UO_2(OH)_2$, and then heating to 648 K. δ-UO_3 crystallises in the *Pm-3m* space group in the ReO_3 structure [231], with theoretically and experimentally determined densities of 6.99 and 6.57 gcm^{-3} respectively [19]. There are only single types of uranium and oxygen sites, with perfect octahedral coordination at each uranium ion and so a clear lack of uranyl type bonding, or indeed formal layers. This comparatively simple composition has led to δ-UO_3 being the most simulated modification of UO_3 [172, 215, 227].

Table 7.01 shows the predicted structural properties of δ-UO_3 and Figure 7.06 (b) and (c) show the predicted structure; which is essentially indistinguishable from the experimental one as the coordination and high symmetry is retained. The unit cell was well reproduced, with a small 2.3 % predicted increase in cell volume and 0.8 % overestimation of the bond length. By comparison the LSDA + U and LSDA calculations of He [172] and Pickard

[227] both underestimate the cell size slightly, but overall also show good agreement with experiment

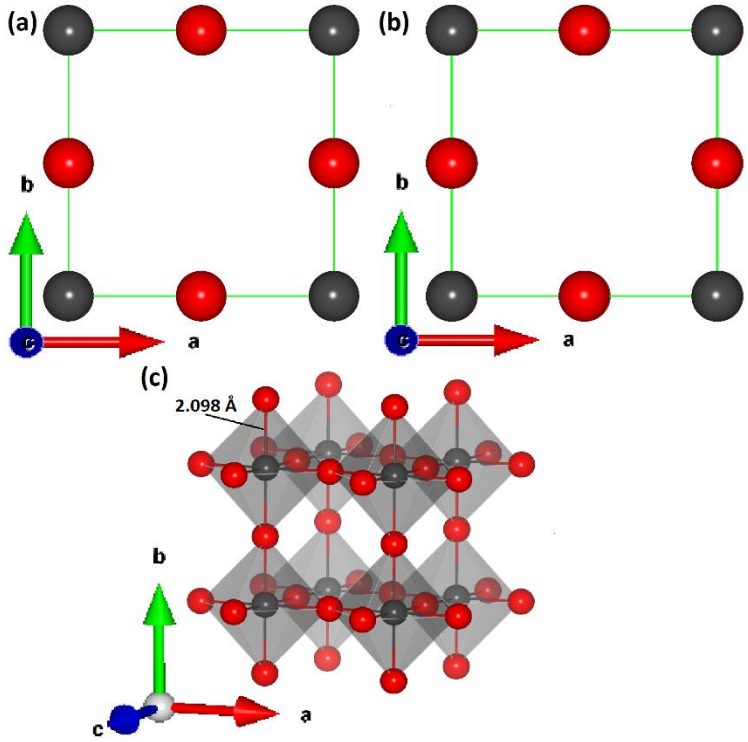

Figure 7.06 – Structure of *Pm-3m* δ-UO_3: (a) experimental unit cell, (b) PBE + U calculated unit cell and (c) uranium coordination in calculated structure. Black spheres are uranium atoms, red are oxygen and the unit cell is highlighted in green.

7.2.5 η-UO_3

The final polymorph to be simulated (η-UO_3) was originally identified by Siegel *et al* [174], who used XRD to derive the lattice parameters and determine an orthorhombic $P2_12_12_1$ structure. The cell contains four formula units with a single type of uranium ion in seven-fold (puckered pentagonal bipyramidal) coordination. It is another modification that contains collinear uranyl type axial bonds, although the distorted coordination polyhedra results in a slight bond length disparity (1.84 amd 1.85 Å). Of the three distinct oxygen sites; O1 only feature in the longer axial bonds, O2 form the shorter axial bond as well as one equatorial site and the O3 sites only participate in equatorial coordination, with three bonded to each uranium ion. No precise synthesis details for η-UO_3 are provided, however it is described as the high pressure polymorph, produced at 1373 K and 30 kbar [174]. In

keeping with this reputation is has the highest density of any UO_3 polymorph, or layered uranium oxide, with a calculated and measured value of 8.86 gcm^{-3} [19].

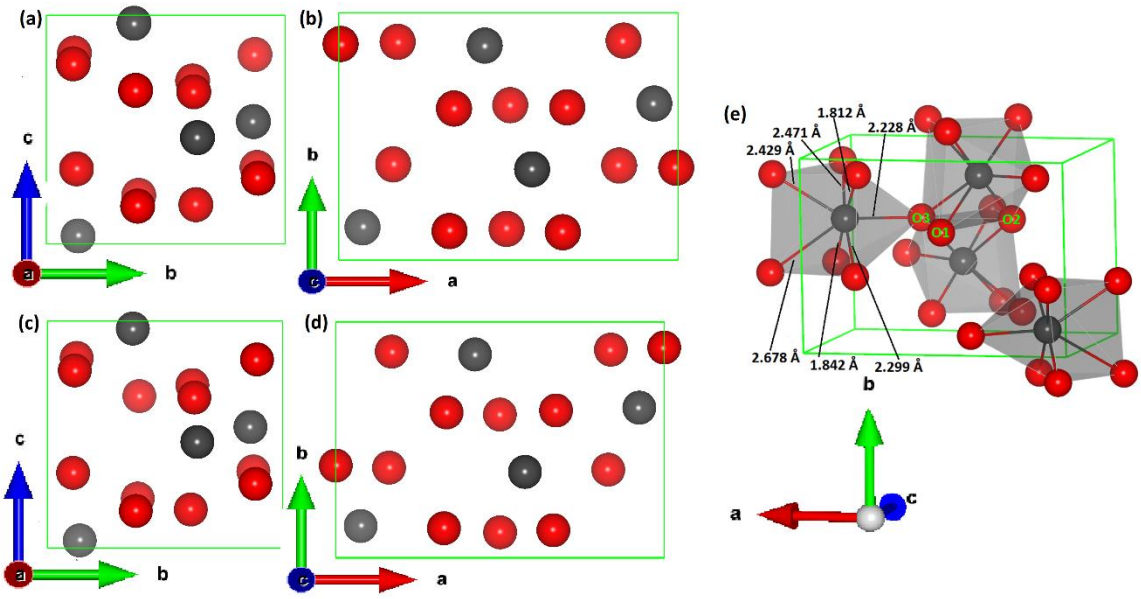

Figure 7.07 – Structure of $P2_12_12_1$ η-UO_3: (a) and (b) experimentally observed unit cell, (c) and (d) PBE + U calculated unit cell and (e) PBE + U calculated uranium coordination. Black spheres are uranium atoms, red are oxygen and the unit cell is highlighted in green.

The predicted structural information for η-UO_3 is shown in Table 7.01 and Figure 7.07 (c), (d) and (e) displays the predicted structure, demonstrating the good overall agreement with experiment. There is a slight overestimation of the observed lattice parameters ($\leq$ 3.5 %) and volume ($\leq$ 7.4 %) but the symmetry and space group are well retained in the simulation. Pickard *et al*'s LSDA calculation predicts slightly better agreement for the experimental lattice parameters than in this thesis but then offers little other structural insight. The predicted uranyl bond lengths are the closest at < 1 % difference with experiment, compared to a mean difference of 3.2 % for equatorial bonds. The uranyl bonds also become slightly more symmetrical on relaxation, although are still not exactly the same length at 1.82 and 1.84 Å. Overall the bonding comparison is closest to γ-UO_3, as a small increase in anisotropy is observed on minimisation when the equatorial oxygen ions are also accounted for. As with the β- and γ- systems the more irregular coordination, slightly larger discrepancy between calculated and reported lattice parameters and the shift

towards more symmetrical uranyl bonding on relaxation indicates the presence of disorder in this polymorph.

7.2.6 Further Structural Considerations

The structures of the UO_3 polymorphs have generally been well reproduced, particularly those without uranyl type bonds such as α- and δ-UO_3. The U^{6+}-O^{2-} system is complex, with more structural variation in terms of bond lengths and coordination environments than any other examined in this thesis. This is especially true of β-, γ- and η-UO_3 which contain short range, uranyl type bonds; mid-range bonds (as observed in α- and δ-UO_3); and weaker long range bonds, that are in excess of 3 Å in the case of γ-UO_3. The major discrepancies between simulation and experiment have been rationalised in terms of intrinsic disorder and defects that are absent from the calculations.

In a layered type material such as UO_3 with such a variety of bond lengths, it is entirely possible that dispersion (or van der Waals) interactions contribute to the bonding scheme. If this were the case then it would be necessary to include them within the simulation to provide a more accurate model. To test this, the DFT-D3 method of Grimme [59] has been used for γ-UO_3 (as the system with the widest variety of bond lengths), and no real improvement on the standard PBE + U calculations was found. The DFT-D3 lattice parameters for $I4_1$ γ-UO_3 are a=b=6.99 Å, c=20.68 Å, α=β=γ=90° (compared to a=b=7.02 Å, c=20.68 Å, α=β=γ=90° with PBE + U). The inclusion of van der Waals interactions is important in discretely layered materials (e.g. TiS_2 and V_2O_5) where the layers are held together by dispersion forces. In the same way it would be expected that they have more significant contributions to discretely layered uranium minerals, such as schoepite or studtite. However in all UO_3 modifications (and other layered uranium oxides) the layers are linked by the bridging oxygen atoms that form the axial U-O bonds, and so the inclusion of vdW does not improve the model compared to the PBE + U.

So the idea that defect chemistry and non-stoichiometry are responsible for the discrepancy in the lattice parameters produced by the stoichiometric models is reinforced. The idea is well documented: Greaves reported non-stoichiometry in α-UO_3 [218], Hoekstra reported a $UO_{2.9}$ phase [204] and Cornman described synthesised samples with compositions ranging

between 3.03 and 3.07 [228]. Even preparation of a pure phase is challenging; Weller *et al* reported their δ-UO_3 synthesis yielding small amounts of α-UO_3 [231] and Sweet *et al* described synthesising 82 % β-UO_3 with 18 % α-UO_3 in their experiments [225]. Furthermore, as U^{6+} is the soluble form of uranium, UO_3 phases are much more susceptible to formation of hydrolysis and hydration products under ambient conditions [225, 229].

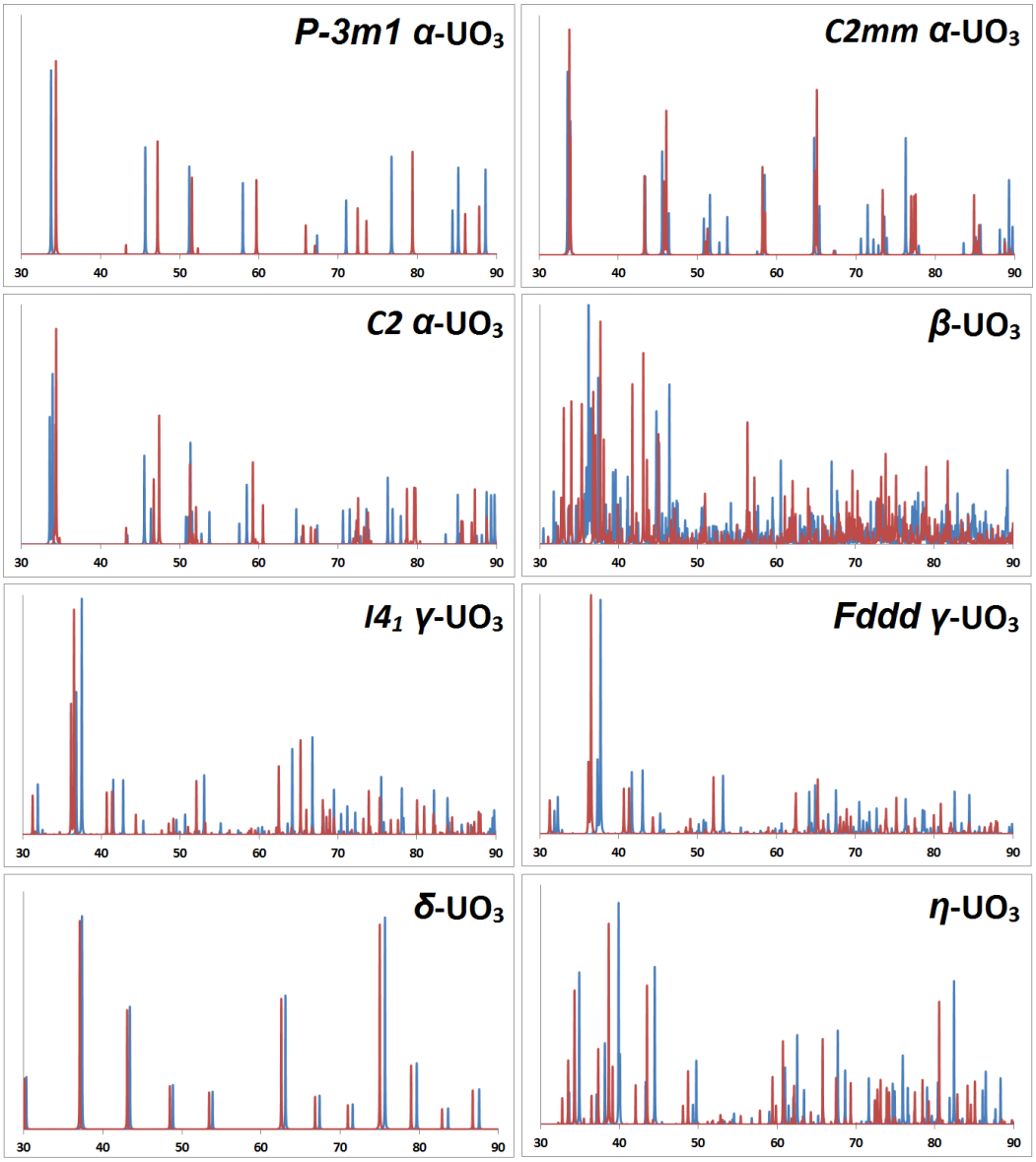

Figure 7.08 – Calculated neutron diffraction patterns for UO_3 polymorphs. Intensity (*y* axis) is in arbitrary units and so has not been labelled. The *x* axis shows angle (2θ) and is in degrees (°). The simulated patterns from experimental and predicted structures are shown in blue and red respectively.

In the present section further evidence of the generally good agreement between the simulated an experimentally observed UO_3 phases is demonstrated through simulated neutron diffraction patterns. Although a number of the UO_3 structures were originally derived using neutron diffraction, the varying complexity of patterns, and different wavelengths that they were recorded at, makes direct comparison difficult. Thus Figure 7.08 contains the simulated patterns based on the predicted and experimental structures, so that all patterns are produced using the same method [89] and so are directly comparable with one another.

The primary observation is that the number of peaks, and their relative intensities, are found to be similar, between almost all of the experimental and predicted structures. The only system where this breaks down slightly is β-UO_3, which is to be expected given this polymorph displayed the greatest reduction in anisotropy on relaxation; with multiple uranium sites changing coordination and the change in monoclinic angle changing the unit cell shape. In the other patterns the principle difference between calculation and experiment is a shift in the angle (2θ), which arises from the difference in lattice parameters (and bond lengths) and scales with how closely the predicted results match experiment.

Accordingly, the smallest shift is observed where experimental and PBE + U results are in closest agreement with one another. So the structure with the smallest (slightly lower 2θ) is seen for δ-UO_3, incidentally this system also shows the best match between intensities for experimental and calculated structures, as well as the positions of peaks reported in the original experimental work [231]. This close match between experiment and theory is indicative of a highly ordered structure. The α-UO_3 neutron diffraction patterns also shows a close match between experiment and theory, although this time the predicted peaks are shifted to higher 2θ, reflecting the underestimation of the lattice parameters in these simulations. In much the same way the γ- and η-UO_3 peaks are slightly more shifted (and show slightly more difference in intensities) and then even more so in β-UO_3. These UO_3 systems also show greater discrepancy with their experimentally recorded neutron diffraction patterns in the literature [196, 235]. This disparity between the recorded experimental neutron diffraction patterns and our simulated patterns from the experimentally derived structures is a strong indication that these three oxides (the only

three to contain uranyl bonding) are inherently more disordered and defective than the UO_3 polymorphs without uranyl bonds.

The neutron diffraction patterns also provide a useful tool for highlighting the similarities of competing structures for the α- and γ- compositions. Examining the two γ-UO_3 polymorphs it is clear that they are crystallographically extremely similar, with almost identical distributions of peaks, the main difference being the relative intensities. This is representative of the different symmetries of the two structures as the Miller planes are aligned differently, affecting the intensity of the detected signal. The patterns for the different α-UO_3 structures also show a strong match, with notable similarities between the *C2* and *P-3m1* as well as *C2* and *C2mm* structures, as the *C2* is essentially a hybrid of the *P-3m1* and *C2mm* structures.

7.3 Elastic Properties

The results from this work are the first (computational or experimental) regarding the elastic constants of UO_3 phases [72]. Elastic constants and bulk moduli have been calculated for the full set of polymorphs and are presented in Table 7.02.

There is quite significant variation in the predicted bulk moduli for the UO_3 polymorphs, ranging from around 75 to 171 GPa, depending on the precise structure of the material. The highest bulk moduli are comparable to those in U_2O_5 and U_3O_8 (Chapters 5 and 6) and are found for the two polymorphs that do not contain uranyl bonds, α- and δ-UO_3 (171 and 151 GPa respectively), and so are also most structurally similar to the lower layered uranium oxides. β-, γ- and η-UO_3 are predicted to have bulk moduli of 72, 75 and 89 GPa respectively, so the presence of uranyl bonds seem to approximately half the bulk modulus. There also appears to be an inverse relationship between density and bulk modulus, or a positive correlation between the presence of uranyl bonds and density. The uranyl-lacking α- and δ-modifications have densities of 7.04 and 6.57 gcm^{-3} whilst the uranyl-containing α- and δ- modifications are 8.25, 8.00 and 8.86 gcm^{-3} respectively. Thus based on these findings it is possible for the presence of uranyl bonds in a uranium oxide to be determined from the bulk modulus; if it is measured to be under 100 GPa then it is likely to contain uranyl bonds, if it is 150 GPa or higher then it probably does not contain uranyl bonds.

Table 7.02 – PBE + U predicted elastic constants and bulk moduli of uranium oxide polymorphs. Independent elastic constants for cubic (3), hexagonal (5) and orthorhombic (9) cells are included but monoclinic (13) are not. Details of bulk modulus calculation can be found in section 2.4.1.

Phase	Elastic Constants (GPa)									Bulk Modulus (GPa)	Vol/U ($Å^3$)	E_{Form} (eV)
	C_{11}	C_{12}	C_{13}	C_{22}	C_{23}	C_{33}	C_{44}	C_{55}	C_{66}			
***P-3m1* α-UO_3**	246.5	179.8	41.5	-	-	519.8	-	50.7	-	170.9	53.64	-0.82
***C2* α-UO_3**	222.1	182.8	37.6	253.0	43.9	521.1	37.0	50.5	49.9	164.5	53.69	-0.81
β-UO_3	115.6	22.2	43.9	142.8	45.0	167.1	16.7	45.9	-7.4	72.0	64.95	-1.21
***$I4_1$* γ-UO_3**	162.1	63.4	39.5	162.2	39.5	107.4	28.9	39.1	38.9	74.8	63.82	-1.46
***Fddd* γ-UO_3**	142.8	39.5	82.6	107.1	40.3	143.7	38.8	38.9	49.2	74.9	63.79	-1.46
δ-UO_3	387.6	33.2	-	-	-	-	27.3	-	-	151.3	73.89	-1.26
η-UO_3	172.7	55.2	60.7	120.8	70.3	150.8	29.1	63.7	46.5	89.2	57.60	-1.31

In U_2O_5 and U_3O_8 (Chapters 5 and 6) it was noted that the largest individual elastic constants are those that describe compression parallel to the axial bond axis. This is harder to determine in UO_3 due to the tilting of polyhedra within layers and higher index axial bond directions, however the observation appears to also hold true for this stoichiometry. α-UO_3 is the most straightforward polymorph in this respect, with layers aligning in {001} planes with axial bonds parallel to the *z* axis. C_{33} would therefore be expected to be the largest elastic constant and this is indeed found to be the case. The β-, γ- and η-UO_3 polymorphs feature uranyl type bonds aligning in *x*, *y* and *z* directions, or with components in each of these directions, and consequently are found to have relatively similar C_{11}, C_{22} and C_{33} elastic constants. Although only the C_{11} elastic constant has been provided for δ-UO_3 the cubic symmetry and lack of any distinction between axial and equatorial bonding results in $C_{11}=C_{22}=C_{33}$.

7.4 Electronic Properties

UO_3 consists entirely of U^{6+}, and consequently has a $5f^0$ electron configuration. This is confirmed by the DOS calculations, which predict each polymorph to be a charge transfer insulator with a VB composed mainly of oxygen 2*p* states and CB comprised primarily of uranium 5*f* states. As with the other uranium oxides, there is almost no contribution from 6*d* states to the CB and only very small contributions to the (mainly lower) VB. These findings are illustrated in Figure 7.09. There are also small uranium 5*f* contributions to the VB and oxygen 2*p* contributions to the CB; which may be attributed to hybridisation, or in other words the degree of covalency in the U-O bonds. These results show good agreement with the experimental results of Bagus *et al*, who report that a closed shell system (such as U^{6+}) screens the 6*d* orbitals more effectively than an open shell one (i.e. U^{4+} or U^{5+}) [223, 224]. Examining the PDOS for UO_2, U_2O_5 and U_3O_8 (in Chapters 3, 5 and 6 respectively) it can be seen that this relationship holds true across the full set of calculations. In charge-transfer insulating U_3O_8 5*f* states from U^{6+} ions do not contribute much to the VB but more significant contributions from U^{5+} are observed. Similarly 5*f* states from U^{5+} ions in charge-transfer insulating U_2O_5 show slightly greater VB contributions, in line with the higher proportion of U^{5+} in this oxide. Then in UO_2 the insulating behaviour has shifted to Mott-

Hubbard, as the top of the VB is composed of U^{4+} 5*f* states, as expected for the most open-shell system in the series.

The predicted band gaps for each UO_3 polymorph are listed in Table 7.03 and compared with data from the literature where available. Although the band gap of UO_2 was slightly underestimated and for U_3O_8 it was slightly overestimated the PBE + U generally performs very well for the UO_3 polymorphs, in particular for the β-, γ- and δ-UO_3 modifications. The notable exception to this is α-UO_3, where it is considerably underestimated in *P-3m1* and *C2* structures (around 60 % of the experimental value). The *C2mm* polymorph is significantly lower than either of the other two structures, at only 25 % of the experimentally determined value, augmenting the argument for out-of-plane equatorial oxygen ions in α-UO_3.

Table 7.03 – Calculated and experimentally determined band gaps of UO_3 phases from the present work and literature.

Study	Phase	Method	Band Gap (eV)	Vol/U (Å^3)	E_{Form} (eV)
He [172]	α-UO_3	Experiment	2.63	56.92	-
	P-3m1 α-UO_3	LSDA + U	0.94	53.91	-
		HSE	3.10	59.33	-
This Work		PBE + U	1.59	53.64	-0.82
	C2mm α-UO_3	PBE + U	0.64	56.31	-0.59
	C2 α-UO_3	PBE + U	1.54	53.69	-0.81
Idriss [240]	β-UO_3	Experiment	2.17	57.22	-
This Work		PBE + U	2.11	64.95	-1.21
He [172]	γ-UO_3	Experiment	2.38	59.35	-
		LSDA + U	2.35	57.72	-
This Work	*I4$_1$* γ-UO_3	PBE + U	2.40	63.82	-1.46
	Fddd γ-UO_3	PBE + U	2.39	63.79	-1.46
Idriss [240]	δ-UO_3	Experiment	2.17	72.25	-
He [172]		LSDA + U	2.19	71.21	-
		HSE	3.21	69.27	-
Geng [215]		PBE	1.60	72.41	-
This Work		PBE + U	2.19	73.89	-1.26
	η-UO_3	PBE + U	2.67	57.60	-1.31

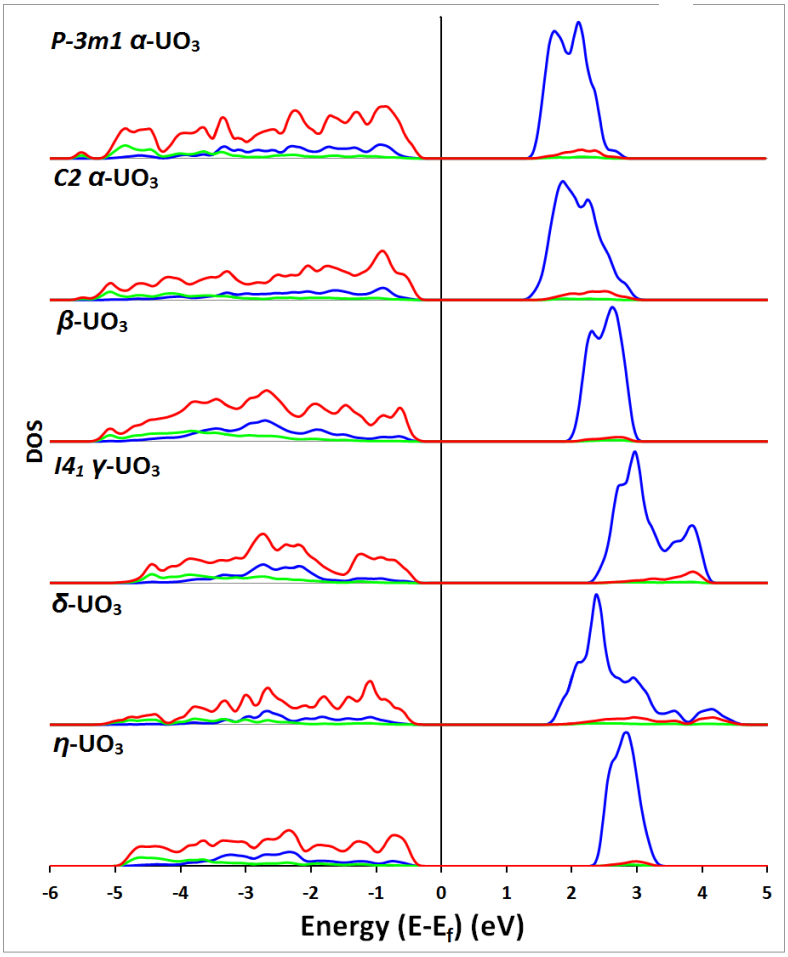

Figure 7.09 – PBE + U calculated PDOS for the UO_3 polymorphs. Oxygen 2*p* states are shown in red, uranium 5*f* states are in blue and uranium 6*d* states are in green. Contributions from other states are negliglible and so are omitted from this diagram. Only spin up states are included here as the spin up and spin down channels are identical. The energy of the highest occupied state was set to zero eV (i.e. $E = E - E_f$).

There does not appear to be a strong relationship between the presence of uranyl bonds and the band gap. Although α- and δ-UO_3 (non-uranyl oxides) are predicted in the PBE + U calculations to have lower band gaps (1.59 and 2.19 eV) than the uranyl-containing γ- and η-UO_3 oxides (2.39 and 2.67 eV) β-UO_3 is predicted to have uranyl bonds on three out of five sites and yet have a band gap of 2.11 eV. There also does not appear to be any relation between the predicted band gap and the volume or stability of a system.

Comparing with the calculated band gaps from the literature it appears that the PBE + U is the superior methodology for UO_3 polymorphs. Although it performs comparably with the

LSDA + U for some systems it comes a lot closer to the experimental value for α-UO_3, although this is still a 40 % underestimate.

7.5 Thermodynamic Stability

The enthalpic contribution to the thermodynamic stability of the UO_3 polymorphs has been predicted over a range of pressures, in the same manner as for U_3O_8 in section 6.4. This time the formation enthalpy has been compared to γ-UO_3 (the thermodynamically most stable polymorph) such that $\delta Hf = \Delta H_x - \Delta H_{\gamma\text{-}UO3}$, where x is the phase in question. The pressure has been varied between -25 and 125 kbar (Figure 7.10) to provide a wide range of enthalpy values and simulate conditions from high temperature (negative pressure) to high pressure (approaching 125 kbar).

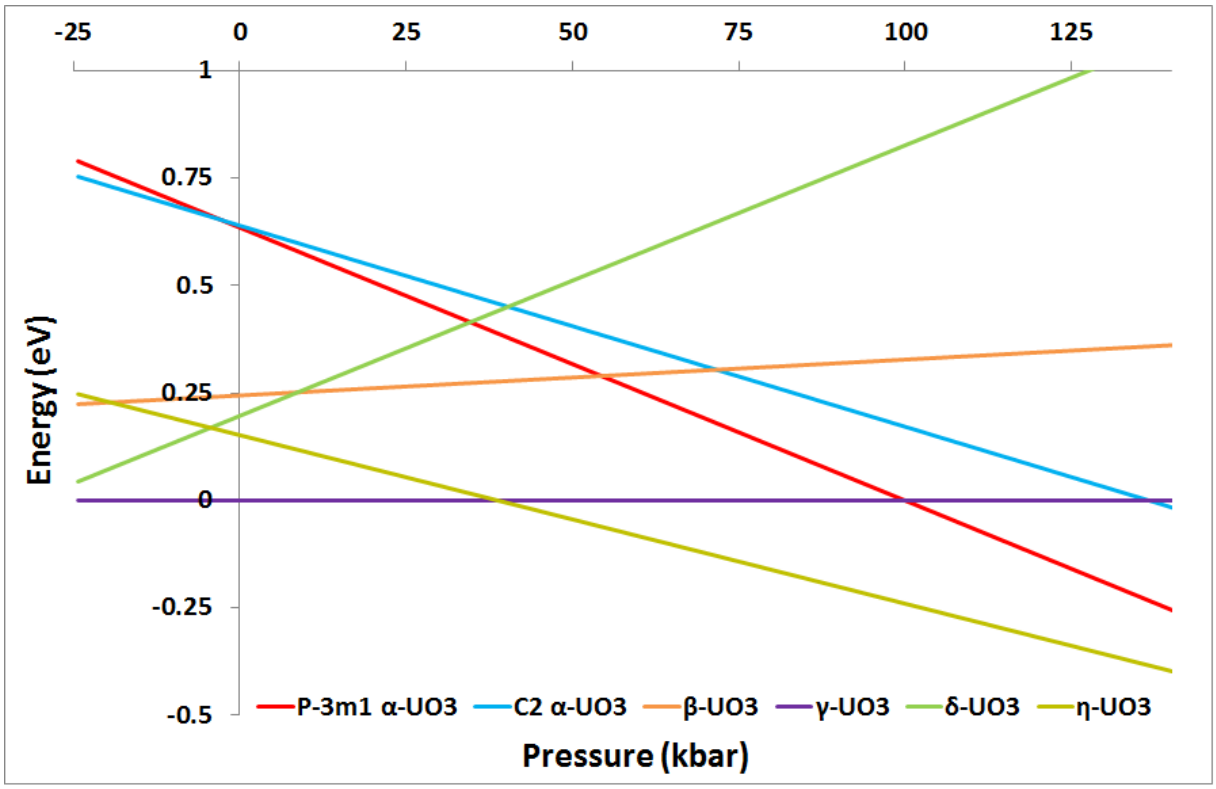

Figure 7.10 – Calculated formation energy (E_{Form}) for UO_3 polymorphs with PBE + U as a function of pressure, results are relative to γ-UO_3 (the thermodynamically most stable phase).

At zero pressure the results follow the PBE + U calculated order of stability exactly as the enthalpy is equal to the predicted energy. It is clear at this point that γ-UO_3 is the most stable polymorph and α-UO_3 is the least stable, in accordance with the experimental measurements [205]. γ-UO_3 is predicted to remain most stable up to 39.5 kbar, at which point it is destabilised with respect to η-UO_3, the densest system and also described as the high pressure polymorph (it was first synthesised at 30 kbar and 1373 K) [174]. So although the pressure is overestimated in the calculations a good qualitative fit with the experimental data is found. The two α-UO_3 polymorphs featured in the diagram are almost degenerate under the normal DFT conditions but the small difference in volume results in the *C2* polymorph being stabilised at negative pressure and *P-3m1* stabilising with increasing pressure. δ-UO_3 shows a large decrease in stability with increasing pressure, against the common trend, most likely arising from the particularly low density of this polymorph (6.57 gcm^{-3}). In support of this β-UO_3 is the second least dense polymorph and also shows slight destabilisation with increasing pressure. The stability appears to be less related to the presence or absence of uranyl bonds than the elastic properties, with no clear trend emerging.

7.6 Conclusions

A total of eight separate structures for five different polymorphs of UO_3 have been simulated, covering a wide range of coordination environments. Dispersive interactions were found to have a negligible effect on the structures by comparing van der Waals corrected DFT and the PBE + U. The best structural agreement with experiment was achieved for the systems without uranyl bonds (i.e. α- and δ-UO_3) although the systems with uranyl bonds (β-, γ- and η-UO_3) were also generally well reproduced. The β-, γ- and η-UO_3 systems also contain a greater variety of different bond lengths than the oxides with no uranyl bonds and the larger discrepancy with experiment is explained in terms of a higher degree of non-stoichiometry, reinforced by the predicted neutron diffraction profiles.

The experimentally observed *C2mm* α-UO_3 structure was found to be dynamically unstable as it contains imaginary vibrational frequencies. These soft modes were removed by applying small displacements to the equatorial oxygen ions that lowered the symmetry to

C2 and produced a structure that very closely resembles the *P-3m1* α-UO_3 polymorph. The conclusion from this is that the *C2mm* polymorph is a thermally averaged structure and the *P-3m1* modification is more representative of the actual material.

Multiple structures were also examined for γ-UO_3, although the monoclinic modification was quickly ruled out as a viable structure as it relaxed to the $I4_1$ tetragonal cell. The $I4_1$ and *Fddd* structures are almost identical on relaxation, only differing in overall cell symmetry, as the predicted formation energies and bond lengths are practically the same. As the two structures were recorded at different temperatures and the DFT calculations used here are performed at 0 K it is logical that they are hard to distinguish without including temperature in the simulations (e.g. *ab initio* MD).

Small differences between the predicted neutron diffraction patterns for the experimental and calculated structures suggest that the UO_3 structures are defective. This supports the experimental evidence of hypo- and hyperstoichiometry as well as significant presence of hydration and hydrolysis products.

The elastic constants and bulk moduli have also been predicted for each polymorph. The bulk modulus is linked to the presence or absence of uranyl type bonds (as well as the density). The oxides with uranyl bonds (β-, γ- and η-UO_3) are found to have lower bulk moduli (< 100 GPa) than those without (> 150 GPa). The two structures without uranyl bonds (α- and δ-UO_3) have bulk moduli in the same range as U_2O_5 and U_3O_8, in keeping with their similar structures. Although slightly harder to examine, the highest elastic constants are found for compression parallel to the axial bonds, as was found for the other layered oxides.

The experimentally determined band gaps are very well reproduced, with the exception of α-UO_3 which is significantly underestimated, and the PDOS reveal UO_3 to be a charge transfer insulator. There are small contributions from U 5*f* states to the O 2*p* dominated VB and to the U 5*f* dominated CB from O 2*p* states, indicating a small degree of covalency in the bonding. Although less is observed than in the lower oxides as U^{6+} displays a higher degree of ionicity. There are very limited contributions from U 6*d* orbitals to the PDOS, mainly occurring in the lower VB, showing that most of the bonding occurs through the 5*f* orbitals.

In line with experiments γ-UO_3 has been predicted as the most thermodynamically stable polymorph and α-UO_3 the least stable. η-UO_3 is correctly predicted to be the high pressure polymorph, although the transition pressure is overestimated. As the lowest density polymorph (by quite some margin), δ-UO_3 is predicted to destabilise considerably with increasing pressure.

This concludes the set of uranium oxides and thus all that remains is to compare the complete set of results and examine the trends that emerge across the group, presented in the next chapter.

Chapter 8

8 Conclusions and Future Work

The conclusions from the individual chapters are summarised here and combined to identify trends across the whole set of uranium oxides. The primary goals outlined in Chapter 1 have all been achieved: accurate reproduction of the observed UO_2 properties; simulation of point defects; defect clusters and U_4O_9/U_3O_7 phases; simulation of the layered oxides and assessment of the relative stability of each oxide phase.

There are individual sections discussing each type of property that has been calculated and section 8.6 provides details of future work for simulation of the uranium oxides, either proposing new work in the area or building on the models presented in this thesis.

8.1 DFT Model for the Uranium Oxides

In Chapter 3 a number of different GGA, meta-GGA and hybrid functionals were applied in the simulation of UO_2, chosen for this purpose due to the wealth of experimental information available compared to the other systems. It was quickly established that hybrid functionals are too computationally expensive to model the full range uranium oxides effectively and, although useful for structural properties, the rTPSS meta-GGA is unsuitable due to its inability to accurately calculate energies. Thus the PBE functional was selected as it performs best for prediction of system energies whilst maintaining a good level of accuracy.

A Hubbard coefficient (U) was required to accurately capture electronic properties; e.g. the Mott-Hubbard insulating state in UO_2 or formal charges on the uranium ions in U_3O_8. Although SOC and NCL magnetism were trialled in UO_2, it was found that SOC simply shifts the energy of the system without having any significant effects on the structure. The band gap is however improved to a 2.3 % underestimation of the experimental value (from

a 10.6 % underestimation). Although the experimentally determined magnetic structure of UO_2 was found to be most stable (3*k* NCL) the difference between different NCL magnetic states was extremely small (0.005 eV). Introducing 3*k* NCL magnetism also removes the tetragonal distortion predicted by a 1*k* CL structure.

Thus a 1*k* AFM CL magnetic structure was used to simulate UO_2, commonly used in other DFT studies, which provided a suitable description of the material. The notable (and well understood) drawback of this approach is the tetragonal distortion of the unit cell, arising due to alternating layers of uranium ions with opposing spins that show a slight attraction to one another, resulting in a slight contraction of the cell. However the effect is small and the predicted energies and other properties are not affected. This 1*k* AFM ordering was then maintained for all fluorite based structures that were simulated in the thesis (Chapters 3 and 4).

All CL AFM and FM magnetic orderings were trialled for the layered oxides of uranium (U_2O_5 and U_3O_8, as UO_3 is non-magnetic); however no energetic preference for either was found, raising the possibility of paramagnetism.

8.2 Structural Properties

A number of structures have been simulated across fluorite (UO_2, U_4O_9 and U_3O_7) and layered (U_2O_5, U_3O_8 and UO_3) type systems. Although U_2O_5 represents the transition point between fluorite and layered structures there is no structural data for the fluorite based oxides and building a representative set of fluorite based phases is impractical, so only layered U_2O_5 has been modelled.

The first structural observation is the uranium charge composition across the oxides. Stoichiometric UO_2 and UO_3 are composed entirely of U^{4+} and U^{6+} ions respectively, but the phases between these must contain a mixture of charges. It emerges that as additional oxygen is incorporated in the UO_2 lattice U^{4+} is oxidised to U^{5+}; at U_2O_5 composition all uranium ions are U^{5+} and then at U_3O_8 stoichiometry the composition is a mixture of U^{5+} and U^{6+} (illustrated in Figure 8.01). In the U_4O_9 systems a small number of configurations were found to contain U^{6+} however these were all found to be less stable. At U_3O_7 composition more systems were found to contain U^{6+}, a number of them relatively stable,

however given the most stable U_2O_5 systems are entirely U^{5+}, it is predicted to be unlikely that U^{6+} containing U_3O_7 would form experimentally.

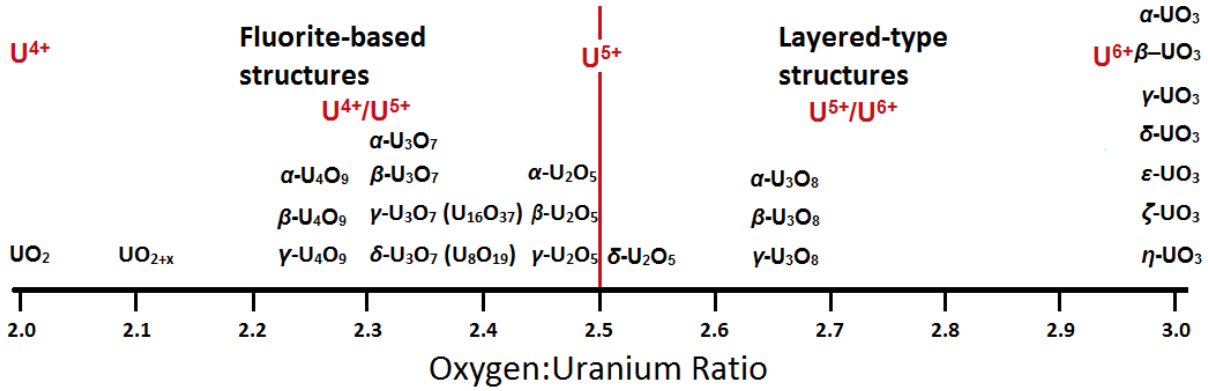

Figure 8.01 – Charge composition of fluorite and layered uranium oxide phases, as calculated from the results throughout this thesis and in agreement with available experimental data [114].

Defect structures in UO_2 have been studied extensively here. They are largely confined to the oxygen sublattice, with relatively little disturbance to the uranium sublattice up to the fluorite-layered transition. Even beyond this point the U_3O_8 and α-UO_3 oxides show remarkable similarity with hexagonally packed uranium ions that strongly resemble the UO_2 {111} plane. This fits with experimental data as the {111} surface is the most stable for UO_2 and studies report on epitaxial growth of U_3O_8 on UO_2 {111} surfaces. A number of isolated defect clusters in UO_2 have been simulated; including 2:2:2 Willis, cuboctahedral and split interstitial clusters. The split interstitial clusters are found to be more stable than cuboctahedral clusters, with split di-interstitials and 13 atom cuboctahedral clusters the most stable in each group, and a single 2:2:2 Willis cluster is found to relax to a split di-interstitial cluster. Once $UO_{2.125}$ stoichiometry is reached, however, edge-sharing chains of 2:2:2 Willis clusters are found to be the most stable defect arrangement. This behaviour is maintained at U_4O_9 stoichiometry, with structures based on multiple cuboctahedral or split quad-interstitial clusters being identified as less stable. At U_3O_7 stoichiometry the Willis cluster chains are predicted to be replaced by isolated split quad-interstitial clusters. The predicted volume changes relative to UO_2 for the most stable U_4O_9 and U_3O_7 phases are positive and negative respectively (the opposite is true for the least stable systems). The experimental observations indicate volume contraction for U_4O_9

and expansion for U_3O_7 and so the conclusion has been drawn that the predicted systems most likely represent the thermodynamically stable oxides whilst the kinetic oxidation products are typically obtained experimentally. Although additional simulation work is required here to more directly compare the experimentally determined and computationally identified phases and consider a broader range of defect clusters.

Although defects in the layered oxides have not been explicitly simulated in this work there are experimental reports of non-stoichiometry in the literature (particularly around UO_3 composition) [204, 218, 225, 228, 229] and evidence from the calculations point towards this being the case. Experiments also describe the ease with which UO_3 hydrolysis and hydration products form [225, 229]. The competing structures for different UO_3 polymorphs (most notably α- and γ-) imply the presence of thermally labile oxygen ions. Discrepancies with experiment over bond lengths (particularly in β-UO_3) and coordination environments are also a good indicator of disorder in these materials.

In terms of the bonding and coordination in the uranium oxides, fluorite UO_2 is cubic, but as it is oxidised this changes as additional oxygen is incorporated into the lattice. In fluorite U_4O_9 the eight-fold coordination is maintained at most uranium sites, however close to defect regions is distorted such that half of the coordinated cube is compressed into a flattened tetrahedron, rather than a single plane. In U_3O_7 there is even less distortion from the pure fluorite structure with planar, equilateral triangles of oxygen atoms (from the split quad-interstitial clusters) replacing a corner of the coordination cube. Shifting to the layered structures, the most stable U_2O_5 polymorphs and U_3O_8 all contain a mixture of pentagonal bipyramidal and octahedrally coordinated uranium ions, with U^{6+} preferring octahedral coordination. In all of these structures the axial bonds are found to be shorter than the equatorial ones, typically around 2.1 Å, although they are not as short as a uranyl bond (1.7 – 1.9 Å). In UO_3 no two polymorphs have the same coordination and, except for δ-UO_3, they are all layered structures with shorter axial bonds. There is distorted hexagonal bipyramidal (α-), distorted pentagonal bipyramidal (β- and η-), distorted octahedral (β- and γ-), perfect octahedral (δ-) and irregular dodecahedral (γ-) coordination. β-, γ- and η-UO_3 all contain uranyl axial bonds (< 1.9 Å) whilst the axial bonds in α-UO_3 are comparable to those in U_2O_5 and U_3O_8 (~2.1 Å) and the undistorted octahedral nature of δ-UO_3 means there is no axial/equatorial distinction.

8.3 Elastic Properties

The computationally expensive nature of calculating elastic constants (and vibrational frequencies) in this work has resulted in limiting to the stoichiometric systems derived from experimental data, and does not include systems built from defect structures.

As would be expected, the considerably denser (~ 11 gcm^{-3}) fluorite UO_2 has a larger bulk modulus than any of the layered oxides, predicted to be around 215 GPa. The layered oxides, with densities around 8 gcm^{-3}, are predicted to have significantly lower bulk moduli; U_2O_5 around 130 – 155 GPa and U_3O_8 approximately 140 – 165 GPa. The UO_3 polymorphs that do not contain uranyl bonds are highly comparable to these at 150 – 170 GPa, whilst those with uranyl bonds are in the range 70 – 90 GPa. So if a uranium oxide sample is unidentified, basic structural information such as whether it is fluorite or layered and whether it contains uranyl bonds can be determined from the bulk modulus as there are three clearly defined ranges. A further observation of the layered oxides is that they have the largest elastic constants (i.e. greatest resistance to compression) along the axis parallel to the axial bonds. This is observed in every structure containing layers and so is not observed in the cubic δ-UO_3 polymorph.

8.4 Electronic Properties

Density of states calculations have been performed for all systems with structures obtained from the literature and their band gaps have been evaluated. The predicted band gaps start at around 2.1 eV for UO_2 and then decrease with increasing oxygen stoichiometry (1.4 – 1.7 eV for U_4O_9 and U_3O_7) before starting to increase again at the layered transition, with U_2O_5 polymorphs between 1.6 and 2.3 eV. These results agree well with experimental and computational results in the literature [172]. U_3O_8 band gaps are predicted to be comparable to UO_2 at around 2.0 – 2.2 eV, although this an overestimate of the experimentally determined value of 1.76 eV. Finally UO_3 displays a fairly broad range at 1.6 – 2.7 eV, although the lower end of this (1.6 eV for α-UO_3) is about 40 % lower than recorded experimentally.

The Mott-Hubbard insulating nature of UO_2 was correctly described by the simulations, with the CB and upper VB all composed of uranium 5*f* states. All other oxides were predicted to be charge transfer insulators with CBs composed of uranium 5*f* states and VBs of oxygen 2*p* states. In all cases contributions from uranium 6*d* are found to be negligible, with the overwhelming amount of states in the CB/VB coming from 5*f* orbitals. In U_3O_8 separate CB peaks are present for U^{5+} and U^{6+} ions, with U^{6+} occupying the lower CB states, indicating higher ionicity.

The DOS can be used to extract information concerning the bonding in a particular system and a trend is observed across the full set of simulated oxides. Essentially, the larger the overlap of uranium states with oxygen, the greater the degree of covalent interaction between the two ions. The closed shell U^{6+} ion ($5f^0$) has the most effective orbital screening and so very little mixing is found in UO_3 or for the U^{6+} ions in U_3O_8. However, the U^{5+} ($5f^1$) in U_3O_8 and U_2O_5 contribute more to the oxygen dominated VB. The extreme case is in U_2O_5, where a small peak emerges. In U^{4+} ($5f^2$) the insulating behaviour has shifted to Mott-Hubbard type and the upper VB is now composed entirely of uranium states and shows improved overlap with oxygen states. So overall the results suggest a decrease in covalency as UO_2 is oxidised.

8.5 Thermodynamic Properties

The layered U_3O_8 and UO_3 phases, for which there are a number of competing polymorphs (three and five have been simulated respectively), have had their thermodynamic stabilities assessed with respect to pressure. This was a relatively straightforward procedure that involved treating the most stable polymorph in each case as zero and then substituting the predicted energies into the thermodynamic relation H = U + PV. As the energy and volume were known quantities that had been predicted for each polymorph pressure was simply varied between -25 and 125 kbar to provide a large range over which to assess the relative stabilities of the different polymorphs. Good qualitative agreement was found between all of the computational predictions and experiments in the literature.

The β-U_3O_8 polymorph was found to infinitesimally more stable than α-U_3O_8, with a larger energy gap to the γ- polymorph. The conclusion here being that a polycrystalline sample is

likely to contain both the α- and β- polymorphs at low temperatures with β-U_3O_8 starting to dominate as the temperature increases. γ-U_3O_8 is, however, expected to stabilise at higher pressures, overtaking β-U_3O_8 above 25 kbar.

At the UO_3 composition γ- and α-UO_3 are predicted to be the thermodynamically most and least stable polymorphs respectively; and above 40 kbar η-UO_3 is predicted to become the most stable polymorph. The two least dense polymorphs (β- and γ-UO_3) are the only ones to destabilise with increasing pressure, thus density seems closely linked to stability under pressure as η-UO_3 is the densest polymorph by some margin.

Building on these results a plot of the thermodynamic stability across the whole range of uranium oxides simulated in this study has been constructed (Figure 8.02). The oxygen chemical potential (μ_O) has been used instead of pressure as it provides an idea of stability as the oxygen concentration is varied. Thus formation energies (E_{Form}) are presented, normalised with respect to UO_2, and adjusted for the oxygen content of each phase. The result of which is that at $\mu_O = 0$ is $E_{Form} = E_{UO2n} - E_U - nE_O$.

At low oxygen concentration the most stable phase is predicted to be UO_2 and at high concentration it is γ-UO_3, as would be expected, and in agreement with experiment. The fluorite based $UO_{2.125}$, U_4O_9 and U_3O_7 phases are all predicted to be unstable with respect to other oxides, more or less across the full range of μ_O. Again, this is an expected result given their low reported stability and status as intermediate oxidation products of UO_2. The unanticipated result though is that U_2O_5 (Np_2O_5 structure) is predicted to be the most stable phase over a wide oxygen concentration range (μ_O of -1.8 to -1.0). It is found to be more stable than U_3O_8 which, along with UO_2 and UO_3, is considered one of the most stable oxides experimentally. The structure is the most stable of the neptunium oxides and so, given the similar ionic radius, it is not unexpected that it is predicted to be a stable structure for uranium. Hence, the results suggest that the Np_2O_5 structure is indeed a stable uranium oxide polymorph and presumably has not yet been synthesised because of difficulty in its preparation. Therefore it should be a good target for experiment. A more conventional set of results can be seen in Figure 8.03, which shows an identical plot but only with structures calculated from structures obtained directly from experimental data (i.e. without U_4O_9, U_3O_7 and $(Np)U_2O_5$).

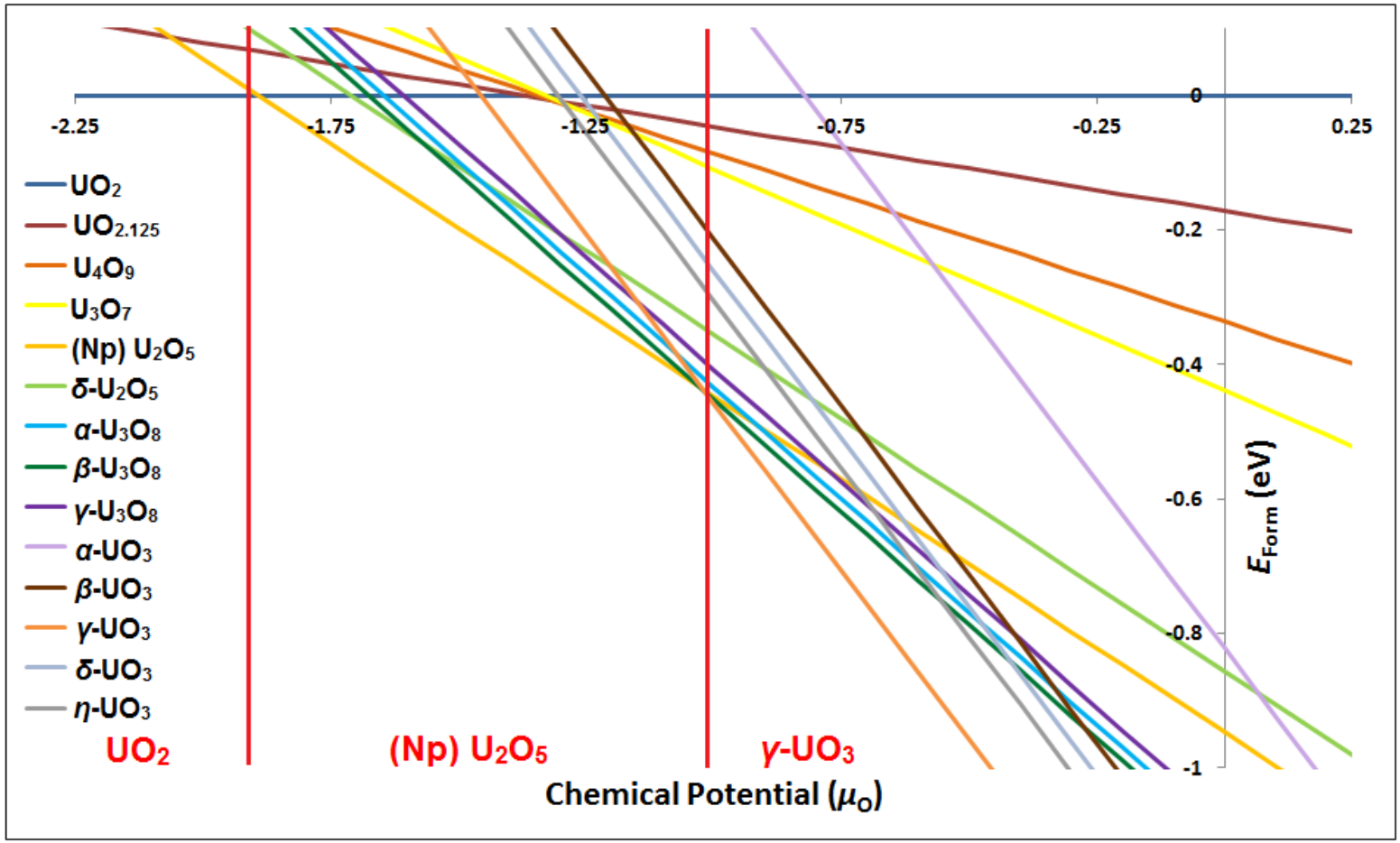

Figure 8.02 – PBE + U predicted thermodynamic stability of full range of simulated uranium oxides. Calculated energy of formation (E_{Form}) is presented as a function of oxygen chemical potential μ_O and results are all relative to UO_2. For clarity the most stable phases have been labelled in red.

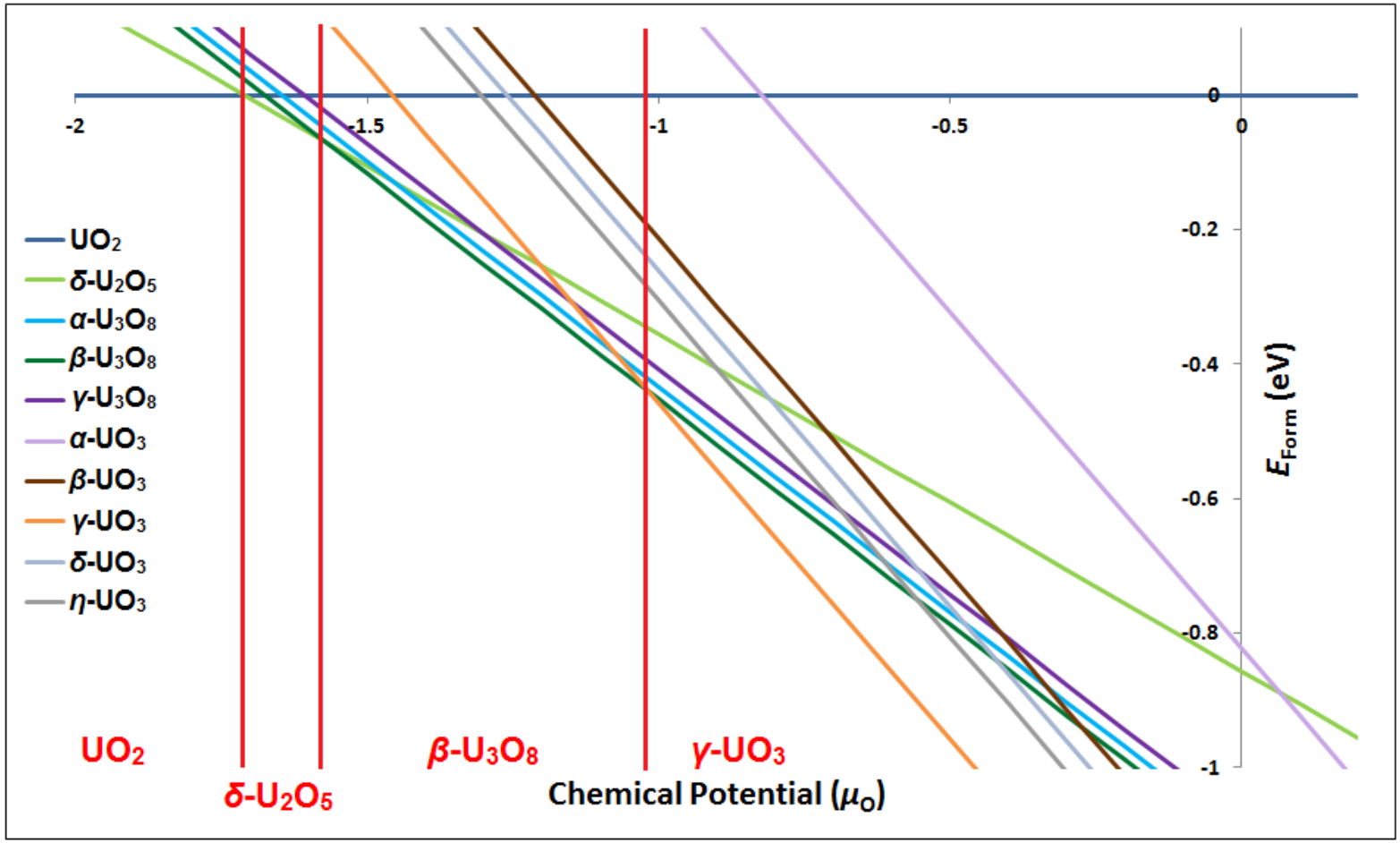

Figure 8.03 – PBE + U predicted thermodynamic stability of simulated uranium oxides derived directly from experimental data between UO_2 and UO_3 stoichiometry. Calculated energy of formation (E_{Form}) is presented as a function of oxygen chemical potential μ_O and results are all relative to UO_2. For clarity the most stable phases have been labelled in red.

Examining Figure 8.03 three major regions of stability emerge: UO_2 at low oxygen concentration (< -1.7), (β-) U_3O_8 over intermediate oxygen concentrations (-1.5 to -1.0) and (γ-) UO_3 at higher oxygen concentrations (> -1.0). There is also a narrow window of δ-U_2O_5 stability (-1.7 to -1.5) between UO_2 and U_3O_8. These results agree far better with experimental observations than the full set, although the brief stability of δ-U_2O_5 is intriguing given the apparent difficulty in synthesising this polymorph.

It is well known that γ-UO_3 is the thermodynamically stable form at that composition and the other polymorphs gradually convert to it. This is apparent from the plots, where each UO_3 polymorph has a similar gradient but γ- is the most stable, indicating that if the others are to be accessed it is by kinetically controlled processes [129]. This theory was also proposed earlier with regard to the experimentally observed U_4O_9 and U_3O_7 structures compared to the predicted ones. However, U_4O_9 and U_3O_7 are not predicted to be stable compared to any of the other phases at any oxygen concentration.

Thus applying the same argument to the (Np) U_2O_5 structure it is proposed that this is a thermodynamically stable material that has not been observed yet experimentally due to kinetic formation of δ-U_2O_5 and U_3O_8 as intermediates on the way to the thermodynamically stable γ-UO_3 oxide. Thus implying that with a suitable synthetic technique (Np) U_2O_5 could be isolated.

8.6 Future Work

There is clearly much work that remains to be done. In this final section future work has been split into three sections that expand on each of the main aims set out in Chapter 1.

8.6.1 UO_2 Methodology

The experimentally observed properties of UO_2 have been satisfactorily reproduced with the methodology applied here; however in recent years new DFT techniques have emerged for the simulation of localised *f* electron systems. The most prominent of these is by far occupational matrix control, which is a straightforward addition to the DFT code which fixes the orbitals that valence electrons occupy during minimisation. The atomic structure can then be relaxed and the electrons afterwards, in order to reach the electronic ground

state [97, 241]. The problem with occupational matrix control is that it requires modelling all possible configurations and hence a large number of calculations are required.

Occupational matrix control was not applied in this work due to the large number of simulations required, too many at this time. In a pure UO_2 lattice all the uranium ions are U^{4+} ($5f^2$) and so there are two valence electrons at each uranium site. If all uranium ions are considered equivalent this gives 21 different possible arrangements of filling the 5*f* orbitals with two electrons and so 21 separate calculations. Extending this methodology to defective UO_2 becomes even more complex as all uranium ions are no longer equivalent and some are U^{5+} and so a vastly greater number will be required to explore every electronic configuration explicitly. If more time and resources become available then this would be the most sensible way of expanding the calculations of UO_2 in the future as meta-GGA and hybrid functionals were not found to improve the predicted properties significantly enough to justify their use.

8.6.2 Defective UO_{2+x}

Considerable progress has been made here in simulating the UO_{2+x} region, particularly U_4O_9 and U_3O_7 phases using an approach that involves a systematic search of defect configurations. The next step would be to maintain these stoichiometries but use larger simulation cells so that a greater range of clustering schemes could be examined, for example multiple cuboctahedral clusters. This would be especially useful for U_3O_7 as slightly smaller cells were used here than in U_4O_9.

It would also be very useful to simulate fluorite based U_2O_5 phases, applying the same methodology as used here for U_4O_9 and U_3O_7, to investigate the stability of this phase compared to layered U_2O_5 and the type of defect clustering regime that is favoured. Fluorite U_2O_5 was omitted here due to the huge number of configurations required if every symmetry inequivalent arrangement were to be considered (483 in a 2 x 2 x 1 supercell). An alternative approach could involve taking a smaller number of these configurations and minimising them to see which types of cluster start to dominate. When this has been established all unique combinations of these larger clusters can be identified and minimised as there will be considerably fewer. Alternatively *ab initio* MD could be employed to

identify the most stable defect arrangements instead. This provides the advantage that oxygen can be continually added to the system after it has reached equilibration to investigate the structural transitions between different polymorphs ($U_4O_9 \rightarrow U_3O_7 \rightarrow U_2O_5 \rightarrow U_3O_8$).

Using the information obtained on UO_{2+x} in the current study, as well as any future work, there is a larger dataset of structures and charge configurations that could be used to derive more robust interatomic potentials. These would be useful for simulating defects in UO_2 as well as mixed valence uranium oxides.

8.6.3 Layered Uranium Oxides

The first point to consider here is the (Np) U_2O_5 structure that was identified as the energetically most stable at U_2O_5 stoichiometry, as this has not been reported experimentally. This means that experimental work of synthesising U_2O_5 phases is the most sensible approach to shine further light on this problem. An additional computational approach to layered U_2O_5 in general is to remove oxygen ions from U_3O_8 so that it has U_2O_5 stoichiometry and relax the structure.

A further extension to the simulation of the layered uranium oxides is to model the $U_{13}O_{34}$ phase, excluded from the present work as it was not identified until relatively late in the project and the calculations were very slow to converge. Although less stable (with respect to U_3O_8) than the other oxides reported here it has been isolated experimentally and has an orthorhombic cell with *Amm2* symmetry and a = 4.143, b = 51.532 and c = 6.740 Å [182]. The uranium coordination is a mixture of six- (distorted octahedral) and seven-fold (distorted pentagonal bipyramidal), with a higher proportion of seven-fold coordination than δ-U_2O_5. Overall the structure is somewhere between that of δ-U_2O_5 and U_3O_8, with a O/U ration of 2.62 and so it would a be useful intermediate structure to investigate, particularly for the uranium charge configuration.

Then there is the problem of defective UO_3; an issue identified both experimentally [226, 228] and in this thesis. The most likely type of point defect present is oxygen vacancies (or possibly uranium interstitials), which could be simulated in the UO_3 polymorphs considered here with relative ease. This would be a useful exercise to check if agreement

with the predicted band gaps improved with addition of defects, particularly in α-UO_3 where there is the largest discrepancy between experiment and theory. An alternative, and equally useful, approach would be to introduce oxygen interstitials (or uranium vacancies) to layered U_3O_8 systems and see if the two methods converged on a similar result.

There are also the hydration and hydrolysis products of UO_3, a cause of hyperstoichiometry experimentally, which have not been investigated computationally at the time of writing. These are known to form rapidly under ambient conditions [222, 229, 230] and so would be a useful avenue of future research.

In summary, this work has demonstrated that DFT can make considerable progress in simulating the structural, elastic, electronic and magnetic properties of uranium oxides. It is also clear that many questions remain and so the field will no doubt continue to be a fruitful area of research.

Bibliography

1. Hahn, O., The discovery of fission, *Scientific American*, **1958**, 198(2), 76-84.
2. Matthews, J.R., Technological Problems and the Future of Research on the BASIC Properties of Actinide Oxides. *Journal of the Chemical Society-Faraday Transactions Ii*, **1987**, 83, 1273-1285.
3. Grimes, R.W. and W.J. Nuttall, Generating the Option of a Two-Stage Nuclear Renaissance. *Science*, **2010**, 329(5993), 799-803.
4. Hore-Lacy, I., *Nuclear Energy in the 21st Century* **2012**, 3rd Ed., London, World Nuclear Association.
5. International Atomic Energy Agency, *Nuclear Energy Development in the 21st Century: Global Scenarios and Regional Trends*. **2010**, Vienna.
6. International Energy Agency, *Contribution of Renewables to Energy Security*. **2007**.
7. Zinkle, S.J. and Was, G.S., Material challenges in nuclear energy, *Acta Materialia*. **2013**, 61, 735-758.
8. Nerikar, P., T. Watanabe, J.S. Tulenko, S.R. Phillpot, and S.B. Sinnott, Energetics of intrinsic point defects in uranium dioxide from electronic-structure calculations. *Journal of Nuclear Materials*, **2009**, 384(1), 61-69.
9. International Atomic Energy Agency, *Safe Handling and Storage of Plutonium*. **1998**, Vienna.
10. Sokolov, F., K. Fukuda, and H.P. Nawada, *Thorium fuel cycle - Potential benefits and challenges*. **2005**, Vienna.
11. Fridman, E. and S. Kliem, Pu recycling in a full Th-MOX PWR core. Part I: Steady state analysis. *Nuclear Engineering and Design*, **2011**, 241(1), 193-202.
12. World Nuclear Association, 2014. *The Nuclear Fuel Cycle* [Online]. London: World Nuclear Association. Available from: http://www.world-nuclear.org/info/Nuclear-Fuel-Cycle/Introduction/Nuclear-Fuel-Cycle-Overview/ [Accessed 08/12/2014 2014].
13. Driscoll, R.J.P., D. Wolverson, J.M. Mitchels, J.M. Skelton, S.C. Parker, M. Molinari, I. Kahn, D. Geeson, and G.C. Allen, A Raman Spectroscopic Study of Uranyl Minerals from Cornwall, UK. *RSC Advances*, **2014**.
14. World Nuclear Association, *Uranium from Mine to Mill*. **2014** London.
15. Hopper, C.M., L.M. Petrie, L.J. Ott, and C.V. Parks, *Design Parameters for a Natural Uranium UO3- or U3O8-Fueled Nuclear Reactor*. **2002**, Oak Ridge, Tennessee, USA.
16. International Atomic Energy Agency, *Safety of Conversion Facilities and Uranium Enrichment Facilities*. **2010**, Vienna (SSG-5).

17. McEachern, R.J. and P. Taylor, A review of the oxidation of uranium dioxide at temperatures below 400 degrees C. *Journal of Nuclear Materials*, **1998**, 254(2-3), 87-121.

18. Allen, G.C. and N.R. Holmes, A Mechanism for the UO2 to Alpha-U3O8 Phase-Transformation. *Journal of Nuclear Materials*, **1995**, 223(3), 231-237.

19. Hoekstra, H.R., S. Siegel, and Gallaghe.Fx, Uranium-Oxygen System at High Pressure. *Journal of Inorganic & Nuclear Chemistry*, **1970**, 32(10), 3237-3248.

20. Idiri, M., T. Le Bihan, S. Heathman, and J. Rebizant, Behavior of actinide dioxides under pressure: UO2 and ThO2. *Physical Review B*, **2004**, 70(1), 014113-014121.

21. Frazer, B.C., G. Shirane, D.E. Cox, and C.E. Olsen, Neutron-Diffraction Study of Antiferromagnetism in UO2. *Physical Review*, **1965**, 140(4A), 188-190.

22. Fritz, I.J., Elastic Properties of UO2 at High-Pressure. *Journal of Applied Physics*, **1976**, 47(10), 4353-4358.

23. Allen, G.C., I.S. Butler, and N.A. Tuan, Characterization of Uranium-Oxides by Micro-Raman Spectroscopy. *Journal of Nuclear Materials*, **1987**, 144(1-2), 17-19.

24. Faber, J. and G.H. Lander, Neutron-Diffraction Study of UO2 - Antiferromagnetic State. *Physical Review B*, **1976**, 14(3), 1151-1164.

25. Baer, Y. and J. Schoenes, Electronic-Structure and Coulomb Correlation-Energy in UO2 Single-Crystal. *Solid State Communications*, **1980**, 33(8), 885-888.

26. Allen, G.C. and P.A. Tempest, Ordered Defects in the Oxides of Uranium. *Proceedings of the Royal Society of London Series a-Mathematical Physical and Engineering Sciences*, **1986**, 406(1831), 325-344.

27. Read, M.S.D. and R.A. Jackson, Derivation of enhanced potentials for uranium dioxide and the calculation of lattice and intrinsic defect properties. *Journal of Nuclear Materials*, **2010**, 406(3), 293-303.

28. Devey, A.J., First principles calculation of the elastic constants and phonon modes of UO(2) using GGA plus U with orbital occupancy control. *Journal of Nuclear Materials*, **2011**, 412(3), 301-307.

29. Willis, B.T.M., Defect Structure of Hyper-Stoichiometric Uranium-Dioxide. *Acta Crystallographica Section A*, **1978**, 34(JAN), 88-90.

30. Allen, G.C. and P.A. Tempest, Linear Ordering of Oxygen Clusters in Hyper-Stoichiometric Uranium-Dioxide. *Journal of the Chemical Society-Dalton Transactions*, **1982**, (11), 2169-2173.

31. Desgranges, L., G. Baldinozzi, G. Rousseau, J.-C. Niepce, and G. Calvarin, Neutron Diffraction Study of the in Situ Oxidation of UO(2). *Inorganic Chemistry*, **2009**, 48(16), 7585-7592.

32. Andersson, D.A., G. Baldinozzi, L. Desgranges, D.R. Conradson, and S.D. Conradson, Density Functional Theory Calculations of UO2 Oxidation: Evolution

of UO2+x, U4O9-y, U3O7, and U3O8. *Inorganic Chemistry*, **2013**, 52(5), 2769-2778.

33. Born, M. and J.R. Oppenheimer, On the Quantum Theory of Molecules. *Annalen der Physik*, **1927**, 84, 457-484.

34. Thomas, L.H., The Calculation of Atomic Fields. *Mathematical Proceedings of the Cambridge Philosophical Societ*, **1927**, 23, 542-548.

35. Fermi, E., Un metodo statistico per la determinazione di alcune priorietA dell'atome,. *Rend. Accad. Naz. Lincei*, **1927**, 6(6) 602-607.

36. Dirac, P.A.M., Note on exchange phenomena in the Thomas-Fermi atom. *Mathematical Proceedings of the Cambridge Philosophical Society*, **1930**, 26, 376-385.

37. Hohenberg, P. and W. Kohn, Inhomogeneous Electron Gas. *Physical Review B*, **1964**, 136(3B), B864-B871.

38. Kohn, W. and L.J. Sham, Self-Consistent Equations Including Exchange and Correlation Effects. *Physical Review*, **1965**, 140(4A), 1133-1138.

39. Becke, A.D., Density-Functional Thermochemistry .3. The Role of Exact Exchange. *Journal of Chemical Physics*, **1993**, 98(7), 5648-5652.

40. Lee, C.T., W.T. Yang, and R.G. Parr, Development of the Colle-salvetti Correlation-Energy Formula into a Functional of the Electron-Density. *Physical Review B*, **1988**, 37(2), 785-789.

41. Barth, U.V. and L. Hedin, Local Exchange-Correlation Potential for Spin Polarized Case .1. *Journal of Physics Part C Solid State Physics*, **1972**, 5(13) 1629-1642.

42. Ceperley, D.M. and B.J. Alder, Ground-State of the Electron-Gas by a Stochastic Method. *Physical Review Letters*, **1980**, 45(7), 566-569.

43. Vosko, S.H., L. Wilk, and M. Nusair, Accurate Spin-Dependent Electron Liquid Correlation Energies for Local Spin-Density Calculations - a Critical Analysis. *Canadian Journal of Physics*, **1980**, 58(8), 1200-1211.

44. Perdew, J.P. and A. Zunger, Self-Interaction Correction to Density-Functional Approximations for Many-Electron Systems. *Physical Review B*, **1981**, 23(10), 5048-5079.

45. Martin, R.M., *Electronic Structure: Basic Theory and Practical Methods*. **2004**, 1st Ed., Cambridge, Cambridge University Press.

46. Becke, A.D., Density-Functional Exchange-Energy Approximation with Correct Asymptotic-Behavior. *Physical Review A*, **1988**, 38(6), 3098-3100.

47. Perdew, J.P. and Y. Wang, Accurate and Simple Analytic Representation of the Electron-Gas Correlation-Energy. *Physical Review B*, **1992**, 45(23), 13244-13249.

48. Perdew, J.P., K. Burke, and M. Ernzerhof, Generalized gradient approximation made simple. *Physical Review Letters*, **1996**, 77(18), 3865-3868.

49. Perdew, J.P., A. Ruzsinszky, G.I. Csonka, O.A. Vydrov, G.E. Scuseria, L.A. Constantin, X.L. Zhou, and K. Burke, Restoring the density-gradient expansion for exchange in solids and surfaces. *Physical Review Letters*, **2008**, 100(13), 136406-136409.

50. Perdew, J.P., A. Ruzsinszky, G.I. Csonka, L.A. Constantin, and J.W. Sun, Workhorse Semilocal Density Functional for Condensed Matter Physics and Quantum Chemistry. *Physical Review Letters*, **2009**, 103(2), 179902-179905.

51. Sun, J.W., M. Marsman, G.I. Csonka, A. Ruzsinszky, P. Hao, Y.S. Kim, G. Kresse, and J.P. Perdew, Self-consistent meta-generalized gradient approximation within the projector-augmented-wave method. *Physical Review B*, **2011**, 84(3), 035117-035126.

52. Becke, A.D. and E.R. Johnson, A simple effective potential for exchange. *Journal of Chemical Physics*, **2006**, 124(22) 221101-221104.

53. Zhao, Y. and D.G. Truhlar, A new local density functional for main-group thermochemistry, transition metal bonding, thermochemical kinetics, and noncovalent interactions. *Journal of Chemical Physics*, **2006**, 125(19) 194101-194118.

54. Tao, J.M., J.P. Perdew, V.N. Staroverov, and G.E. Scuseria, Climbing the density functional ladder: Nonempirical meta-generalized gradient approximation designed for molecules and solids. *Physical Review Letters*, **2003**, 91(14), 146401-146404.

55. Adamo, C. and V. Barone, Toward reliable density functional methods without adjustable parameters: The PBE0 model. *Journal of Chemical Physics*, **1999**, 110(13), 6158-6170.

56. Heyd, J., G.E. Scuseria, and M. Ernzerhof, Hybrid functionals based on a screened Coulomb potential. *Journal of Chemical Physics*, **2003**, 118(18), 8207-8215.

57. Zhao, Y. and D.G. Truhlar, The M06 suite of density functionals for main group thermochemistry, thermochemical kinetics, noncovalent interactions, excited states, and transition elements: two new functionals and systematic testing of four M06-class functionals and 12 other functionals. *Theoretical Chemistry Accounts*, **2008**, 120(1-3), 215-241.

58. Aryasetiawan, F. and O. Gunnarsson, The GW method. *Reports on Progress in Physics*, **1998**, 61(3), 237-312.

59. Grimme, S., J. Antony, S. Ehrlich, and H. Krieg, A consistent and accurate ab initio parametrization of density functional dispersion correction (DFT-D) for the 94 elements H-Pu. *Journal of Chemical Physics*, **2010**, 132(15) 154104-154122.

60. Anisimov, V.I., F. Aryasetiawan, and A.I. Lichtenstein, First-principles calculations of the electronic structure and spectra of strongly correlated systems: The LDA+U method. *Journal of Physics-Condensed Matter*, **1997**, 9(4), 767-808.

61. Hubbard, J., Electron Correlations in Narrow Energy Bands .4. Atomic Representation. *Proceedings of the Royal Society of London Series a-Mathematical and Physical Sciences*, **1965**, 285(1403), 542-560.

62. Dudarev, S.L., G.A. Botton, S.Y. Savrasov, C.J. Humphreys, and A.P. Sutton, Electron-energy-loss spectra and the structural stability of nickel oxide: An LSDA+U study. *Physical Review B*, **1998**, 57(3), 1505-1509.

63. Liechtenstein, A.I., V.I. Anisimov, and J. Zaanen, Density-Functional Theory and Strong-Interactions - Orbital Ordering in Mott-Hubbard Insulators. *Physical Review B*, **1995**, 52(8), R5467-R5470.

64. Kotani, A. and T. Yamazaki, Systematic Analysis of Core Photoemission Spectra for Actinide Di-Oxides and Rare-Earth Sesqui-Oxides. *Progress of Theoretical Physics Supplement*, **1992**, (108), 117-131.

65. Weaver, P., **2011**. Computational Studies of Interstitial-type Oxide Ion Conductors for Applications in Solid Oxide Fuel Cells. *Department of Chemistry*. University of Bath, Bath.

66. Payne, M.C., M.P. Teter, D.C. Allan, T.A. Arias, and J.D. Joannopoulos, Iterative Minimization Techniques for Ab Initio Total-Energy Calculations - Molecular-Dynamics and Conjugate Gradients. *Reviews of Modern Physics*, **1992**, 64(4), 1045-1097.

67. Monkhorst, H.J. and J.D. Pack, Special Points for Brillouin-Zone Integrations. *Physical Review B*, **1976**, 13(12), 5188-5192.

68. Singh, D.J. and L. Nordström, *Planewaves, Pseudopotentials and the LAPW Method*. **2006**, 2nd Ed., New York, Springer.

69. Blochl, P.E., Projector Augmented-Wave Method. *Physical Review B*, **1994**, 50(24), 17953-17979.

70. Kresse, G. and J. Furthmuller, Efficiency of ab-initio total energy calculations for metals and semiconductors using a plane-wave basis set. *Computational Materials Science*, **1996**, 6(1), 15-50.

71. Lander, G.H., J. Faber, A.J. Freeman, and J.P. Desclaux, Neutron-Diffraction Study of UO2 - Paramagnetic State. *Physical Review B*, **1976**, 13(3), 1177-1182.

72. Brincat, N.A., S.C. Parker, M. Molinari, G.C. Allen, and M.T. Storr, Ab Initio Investigation of the UO3 Polymorphs: Structural Properties and Thermodynamic Stability. *Inorganic Chemistry*, **2014**, 53(23), 12253-12264.

73. Brincat, N.A., S.C. Parker, M. Molinari, G.C. Allen, and M.T. Storr, Density functional theory investigation of the layered uranium oxides U3O8 and U2O5. *Dalton transactions (Cambridge, England : 2003)*, **2015**, 44(6), 2613-2622.

74. Leach, A.R., *Molecular modelling - principles and applications*. **2001**, 2nd Ed., Harlow, UK: Pearson Eduction.

75. Fletcher, R. and C.M. Reeves, Function Minimization by Conjugate Gradients. *Computer Journal*, **1964**, 7(2), 149-154.

76. Fletcher, R. and M.J.D. Powell, A Rapidly Convergent Descent Method for Minimization. *Computer Journal*, **1963**, 6(2), 163-168.

77. Norgett, M.J. and R. Fletcher, Fast Matrix Methods for Calculating Relaxation About Defects in Crystals. *Journal of Physics Part C Solid State Physics*, **1970**, 3(11), L190-L193.

78. Broyden, C.G., Convergence of Single-Rank Quasi-Newton Methods. *Mathematics of Computation*, **1970**, 24(110), 365-382.

79. Fletcher, R., A New Approach to Variable Metric Algorithms. *Computer Journal*, **1970**, 13(3), 317-322.

80. Goldfarb, D., A Family of Variable-Metric Methods Derived by Variational Means. *Mathematics of Computation*, **1970**, 24(109), 23-26.

81. Shanno, D.F., Conditioning of Quasi-Newton Methods for Function Minimization. *Mathematics of Computation*, **1970**, 24(111), 647-656.

82. Pulay, P., Convergence Acceleration of Iterative Sequences - the Case of SCF Iteration. *Chemical Physics Letters*, **1980**, 73(2), 393-398.

83. Hebbache, M. and M. Zemzemi, Ab initio study of high-pressure behavior of a low compressibility metal and a hard material: Osmium and diamond. *Physical Review B*, **2004**, 70(22) 224107-224112.

84. Kittel, C., *Introduction to Solid State Physics.* **2004**, 8th Ed., John Wiley & Sons.

85. Le Page, Y. and P. Saxe, Symmetry-general least-squares extraction of elastic data for strained materials from ab initio calculations of stress. *Physical Review B*, **2002**, 65(10) 104104-104117.

86. Ravindran, P., L. Fast, P.A. Korzhavyi, B. Johansson, J. Wills, and O. Eriksson, Density functional theory for calculation of elastic properties of orthorhombic crystals: Application to TiSi2. *Journal of Applied Physics*, **1998**, 84(9) 4891-4904.

87. Fast, L., J.M. Wills, B. Johansson, and O. Eriksson, Elastic-Constants of Hexagonal Transition-Metals - Theory. *Physical Review B*, **1995**, 51(24), 17431-17438.

88. Dudarev, S.L., D.N. Manh, and A.P. Sutton, Effect of Mott-Hubbard correlations on the electronic structure and structural stability of uranium dioxide. *Philosophical Magazine B-Physics of Condensed Matter Statistical Mechanics Electronic Optical and Magnetic Properties*, **1997**, 75(5), 613-628.

89. Powder Cell code, Ver. 2.3, **2014**, Berlin, Germany, BAM.

90. Geng, H.Y., Y. Chen, Y. Kaneta, M. Iwasawa, T. Ohnuma, and M. Kinoshita, Point defects and clustering in uranium dioxide by LSDA+U calculations. *Physical Review B*, **2008**, 77(10) 104120-104139.

91. Huber, K.P. and G. Herzberg, *Constants of Diatomic Molecules.* **1979**, 1st Ed., New York, Van Nostrand.

92. Herzberg, G., Forbidden Transitions in Diatomic Molecules .2. The 3-Sigma-U+ -3-Sigma-G(-) Absorption Bands of the Oxygen Molecule. *Canadian Journal of Physics*, **1952**, 30(3), 185-210.

93. Barrett, C.S., M.H. Mueller, and Hitterman R.L., Crystal Structure Variations in Alpha Uranium at Low Temperatures. *Physical Review*, **1963**, 129(2), 625-629.

94. Soderlind, P., First-principles elastic and structural properties of uranium metal. *Physical Review B*, **2002**, 66(8) 085113-085119.

95. Gryaznov, D., E. Heifets, and E. Kotomin, Ab initio DFT plus U study of He atom incorporation into UO(2) crystals. *Physical Chemistry Chemical Physics*, **2009**, 11(33), 7241-7247.

96. Andersson, D.A., T. Watanabe, C. Deo, and B.P. Uberuaga, Role of di-interstitial clusters in oxygen transport in UO(2+x) from first principles. *Physical Review B*, **2009**, 80(6) 060101-060104.

97. Dorado, B., B. Amadon, M. Freyss, and M. Bertolus, DFT plus U calculations of the ground state and metastable states of uranium dioxide. *Physical Review B*, **2009**, 79(23), 235125-235132.

98. Andersson, D.A., J. Lezama, B.P. Uberuaga, C. Deo, and S.D. Conradson, Cooperativity among defect sites in AO(2+x) and A(4)O(9) (A=U,Np,Pu): Density functional calculations. *Physical Review B*, **2009**, 79(2), 024110-024121.

99. Barrett, S.A., A.J. Jacobson, B.C. Tofield, and B.E.F. Fender, The Preparation and Structure of Barium Uranium Oxide BaUO3+X. *Acta Crystallographica Section B-Structural Science*, **1982**, 38(NOV), 2775-2781.

100. Padel, A. and C. Denovion, Elastic Constants of Uranium and Plutonium Carbides, Nitrides and Oxides. *Journal of Nuclear Materials*, **1969**, 33(1), 40-51.

101. Ikushima, K., S. Tsutsui, Y. Haga, H. Yasuoka, R.E. Walstedt, N.M. Masaki, A. Nakamura, S. Nasu, and K. Onuki, First-order phase transition in UO2: U-235 and O-17 NMR study. *Physical Review B*, **2001**, 63(10), 104404-104414.

102. Momin, A.C., E.B. Mirza, and M.D. Mathews, High-Temperature X-ray Diffractometric Studies on the Lattice Thermal-Expansion Behavior of UO2, ThO2 and (U0.2Th0.8)O2 Doped with Fission-Product Oxides. *Journal of Nuclear Materials*, **1991**, 185(3), 308-310.

103. Wachtman, J.B., M.L. Wheat, H.J. Anderson, and J.L. Bates, Elastic Constants of Single Crystal UO2 at 25 Degrees C. *Journal of Nuclear Materials*, **1965**, 16(1), 39-41.

104. Brandt, O.G. and C.T. Walker, Ultrasonic Attenuation and Elastic Constants of Uranium Dioxide. *Physical Review*, **1968**, 170(2), 528-541.

105. Clausen, K., W. Hayes, M.T. Hutchings, J.E. Macdonald, R. Osborn, and P. Schnabel, Investigation of Oxygen Disorder, Thermal Parameters, Lattice-Vibrations and Elastic-Constants of UO2 and ThO2 at Temperatures up to 2930-K. *Revue De Physique Appliquee*, **1984**, 19(9), 719-722.

106. Tsuboi, M., M. Terada, and T. Shimanouchi, Optically Active Lattice Vibrations of Alpha-Uranium Trioxide. *Journal of Chemical Physics*, **1962**, 36(5), 1301-1310.

107. Dolling, G., R.A. Cowley, and A.D.B. Woods, Crystal Dynamics of Uranium Dioxide. *Canadian Journal of Physics*, **1965**, 43(8), 1397-1413.

108. Schoenes, J., Electronic-Transitions, Crystal-Field Effects and Phonons in UO2. *Physics Reports-Review Section of Physics Letters*, **1980**, 63(6), 301-336.

109. Axe, J.D. and G.D. Pettit, Infrared Dielectric Dispersion and Lattice Dynamics of Uranium Dioxide and Thorium Dioxide. *Physical Review*, **1966**, 151(2), 676-670.

110. Faber, J., G.H. Lander, and B.R. Cooper, Neutron-Diffraction Study of UO2 - Observation of an Internal Distortion. *Physical Review Letters*, **1975**, 35(26), 1770-1773.

111. Allen, S.J., Spin-Lattice Interaction in UO2 .I. Ground-State and Spin-Wave Excitations. *Physical Review*, **1968**, 166(2), 530-539.

112. Yu, S.W., J.G. Tobin, J.C. Crowhurst, S. Sharma, J.K. Dewhurst, P. Olalde Velasco, W.L. Yang, and W.J. Siekhaus, f-f origin of the insulating state in uranium dioxide: X-ray absorption experiments and first-principles calculations. *Physical Review B*, **2011**, 83(16) 165102-165109.

113. Jollet, F., T. Petit, S. Gota, N. Thromat, M. GautierSoyer, and A. Pasturel, The electronic structure of uranium dioxide: an oxygen K-edge x-ray absorption study. *Journal of Physics-Condensed Matter*, **1997**, 9(43), 9393-9401.

114. Kvashnina, K.O., S.M. Butorin, P. Martin, and P. Glatzel, Chemical State of Complex Uranium Oxides. *Physical Review Letters*, **2013**, 111(25), 253002-253006.

115. Allen, G.C., P.A. Tempest, and J.W. Tyler, Coordination Model for the Defect Structure of hyperstoichiometric UO2+x and U4O9. *Nature*, **1982**, 295(5844), 48-49.

116. Desgranges, L., M. Gramond, C. Petot, G. Petot-Ervas, P. Ruello, and B. Saadi, Characterisation of uranium vacancies in hyper stoichiometric uranium dioxide. *Journal of the European Ceramic Society*, **2005**, 25(12), 2683-2686.

117. Martin, G., P. Garcia, L. Van Brutzel, B. Dorado, and S. Maillard, Effect of the cascade energy on defect production in uranium dioxide. *Nuclear Instruments & Methods in Physics Research Section B-Beam Interactions with Materials and Atoms*, **2011**, 269(14), 1727-1730.

118. Govers, K., S. Lemehov, M. Hou, and M. Verwerft, Comparison of interatomic potentials for UO2. Part I: Static calculations. *Journal of Nuclear Materials*, **2007**, 366(1-2), 161-177.

119. Govers, K., S. Lemehov, M. Hou, and M. Verwerft, Comparison of interatomic potentials for UO2 Part II: Molecular dynamics simulations. *Journal of Nuclear Materials*, **2008**, 376(1), 66-77.

120. Catlow, C.R.A., Point-Defect and Electronic Properties of Uranium-Dioxide. *Proceedings of the Royal Society of London Series a-Mathematical Physical and Engineering Sciences*, **1977**, 353(1675), 533-561.

121. Taller, S.A. and X.M. Bai, Assessment of structures and stabilities of defect clusters and surface energies predicted by nine interatomic potentials for UO2. *Journal of Nuclear Materials*, **2013**, 443(1-3), 84-98.

122. Laskowski, R., G.K.H. Madsen, P. Blaha, and K. Schwarz, Magnetic structure and electric-field gradients of uranium dioxide: An ab initio study. *Physical Review B*, **2004**, 69(14), 140408-140411.

123. Tiwary, P., A. van de Walle, and N. Gronbech-Jensen, Ab initio construction of interatomic potentials for uranium dioxide across all interatomic distances. *Physical Review B*, **2009**, 80(17), 174302-174308.

124. Jollet, F., G. Jomard, B. Amadon, J.P. Crocombette, and D. Torumba, Hybrid functional for correlated electrons in the projector augmented-wave formalism: Study of multiple minima for actinide oxides. *Physical Review B*, **2009**, 80(23), 235109-235106.

125. Prodan, I.D., G.E. Scuseria, and R.L. Martin, Covalency in the actinide dioxides: Systematic study of the electronic properties using screened hybrid density functional theory. *Physical Review B*, **2007**, 76(3), 033101-033104.

126. Benedict, U., G.D. Andreetti, J.M. Fournier, and A. Waintal, X-ray-Powder Diffraction Study of the High-Pressure Behavior of Uranium-Dioxide. *Journal De Physique Lettres*, **1982**, 43(6), L171-L177.

127. Wang, J.W., R.C. Ewing, and U. Becker, Electronic structure and stability of hyperstoichiometric UO2+x under pressure. *Physical Review B*, **2013**, 88(2) 024109-024124.

128. Prodan, I.D., G.E. Scuseria, and R.L. Martin, Assessment of metageneralized gradient approximation and screened Coulomb hybrid density functionals on bulk actinide oxides. *Physical Review B*, **2006**, 73(4), 045104-045113.

129. Guillaumont, R., T. Fanghänel, J. Fuger, I. Grenthe, V. Neck, D.A. Palmer, and M.H. Rand, *Update on the Chemical Thermodynamics of Uranium, Neptunium, Plutonium, Americium and Technetium*. **2003**, Amsterdam: Elsevier.

130. Schwarz, K., 2011. *Magnetism (FM, AFM, FSM)*, **2011**, Wien, Austria.

131. Blackburn, E., R. Caciuffo, N. Magnani, P. Santini, P.J. Brown, M. Enderle, and G.H. Lander, Spherical neutron spin polarimetry of anisotropic magnetic fluctuations in UO2. *Physical Review B*, **2005**, 72(18), 184411-184420.

132. Amoretti, G., A. Blaise, R. Caciuffo, J.M. Fournier, M.T. Hutchings, R. Osborn, and A.D. Taylor, 5F-Electron States in Uranium-Dioxide Investigated Using High-Resolution Neutron Spectroscopy. *Physical Review B*, **1989**, 40(3), 1856-1870.

133. Dorado, B. and P. Garcia, First-principles DFT plus U modeling of actinide-based alloys: Application to paramagnetic phases of UO2 and (U,Pu) mixed oxides. *Physical Review B*, **2013**, 87(19) 195139-195145.

134. Santini, P., S. Carretta, G. Amoretti, R. Caciuffo, N. Magnani, and G.H. Lander, Multipolar interactions in f-electron systems: The paradigm of actinide dioxides. *Reviews of Modern Physics*, **2009**, 81(2), 807-863.

135. Dorado, B., M. Freyss, and G. Martin, GGA plus U study of the incorporation of iodine in uranium dioxide. *European Physical Journal B*, **2009**, 69(2), 203-209.

136. Mott, N.F. and M.J. Littleton, Conduction in Polar Crystals. I. Electrolytic Conduction in Solid Salts. *Transactions of the Faraday Society*, **1938**, 34(15), 485-499.

137. Gupta, F., G. Brillant, and A. Pasturel, Correlation effects and energetics of point defects in uranium dioxide: a first principle investigation. *Philosophical Magazine*, **2007**, 87(16-17), 2561-2569.

138. Iwasawa, M., Y. Chen, Y. Kaneta, T. Ohnuma, H.Y. Geng, and M. Kinoshita, First-principles calculation of point defects in uranium dioxide. *Materials Transactions*, **2006**, 47(11), 2651-2657.

139. Matzke, H., Atomic Transport-Properties in UO2 and Mixed Oxides (U, Pu)O2. *Journal of the Chemical Society-Faraday Transactions Ii*, **1987**, 83, 1121-1142.

140. Freyss, M., Petit, T., and Crocombette, J.P., Point defects in uranium dioxide: Ab initio pseudopotential approach in the generalized gradient approximation. *Journal of Nuclear Materials*, **2005**, 347(1-2), 44-51.

141. Yu, J.G., R. Devanathan, and W.J. Weber, First-principles study of defects and phase transition in UO2. *Journal of Physics-Condensed Matter*, **2009**, 21(43), 435401-435410.

142. Dorado, B., G. Jomard, M. Freyss, and M. Bertolus, Stability of oxygen point defects in UO(2) by first-principles DFT plus U calculations: Occupation matrix control and Jahn-Teller distortion. *Physical Review B*, **2010**, 82(3), 035114-035124.

143. Andersson, D.A., P. Garcia, X.Y. Liu, G. Pastore, M. Tonks, P. Millett, B. Dorado, D.R. Gaston, D. Andrs, R.L. Williamson, R.C. Martineau, B.P. Uberuaga, and C.R. Stanek, Atomistic modeling of intrinsic and radiation-enhanced fission gas (Xe) diffusion in UO2 +/- x: Implications for nuclear fuel performance modeling. *Journal of Nuclear Materials*, **2014**, 451(1-3), 225-242.

144. Crocombette, J.P., Influence of charge states on energies of point defects and clusters in uranium dioxide. *Physical Review B*, **2012**, 85(14), 144101-144110.

145. Williams, N.R., **2014**. Atomistic Simulation of Uranium Dioxide Interfaces. *Department of Chemistry*, University of Bath, Bath.

146. Morelon, N.D., D. Ghaleb, J.M. Delaye, and L. Van Brutzel, A new empirical potential for simulating the formation of defects and their mobility in uranium dioxide. *Philosophical Magazine*, **2003**, 83(13), 1533-1550.

147. R.A. Jackson, A.D. Murray, J.H. Harding and C.R.A. Catlow, the calculation of defect parameters in UO_2. *Philosophical Magazine A*, **1986**, 53(1), 27-50.

148. Grimes, R.W. and C.R.A. Catlow, The Stability of Fission-Products in Uranium-Dioxide. *Philosophical Transactions of the Royal Society a-Mathematical Physical and Engineering Sciences*, **1991**, 335(1639), 609-634.

149. Kapshukov, II, N.V. Lyalyushkin, L.V. Sudakov, A.S. Bevz, and O.V. Skiba, Preparation of Hypostoichiometric UO2-X at Low-Temperatures and Study of Some Properties. *Journal of Radioanalytical and Nuclear Chemistry-Articles*, **1990**, 143(1), 213-220.

150. Chikalla, T.D., C.E. McNeilly, and R.E. Skavdahl, The Plutonium-Oxygen System. *Journal of Nuclear Materials*, **1964**, 12(2), 131-141.

151. Wulff, M. and G.H. Lander, Magnetic-Structure and Pu Ground-State in Beta-Pu2O3. *Journal of Chemical Physics*, **1988**, 89(5), 3295-3299.

152. Dorado, B., P. Garcia, G. Carlot, C. Davoisne, M. Fraczkiewicz, B. Pasquet, M. Freyss, C. Valot, G. Baldinozzi, D. Simeone, and M. Bertolus, First-principles calculation and experimental study of oxygen diffusion in uranium dioxide. *Physical Review B*, **2011**, 83(3), 035126-035135.

153. Alberman, K.B. and J.S. Anderson, Oxyde des Urans. *Angewandte Chemie*, **1949**, 61(10), 416-416.

154. Willis, B.T.M., Positions of Oxygen Atoms in UO2.13. *Nature*, **1963**, 197(486), 755-756.

155. Catlow, C.R.A., **1974**. Defect Structures in Fluorite Crystals, *Theoretical Physics Division*, Atomic Energy Research Establishment, Harwell, 263.

156. Catlow, C.R.A., Defect Clusters in Doped Fluorite Crystals. *Journal of Physics C-Solid State Physics*, **1973**, 6(4), L64-L70.

157. Willis, B.T.M., Structures of UO2, UO2+x and U4O9 by Neutron Diffraction. *Journal De Physique*, **1964**, 25(5), 431-441.

158. Cheetham, A.K., B.E.F. Fender, and M.J. Cooper, Defect Structure of Calcium Fluoride Containing Excess Anions .1. Bragg Scattering. *Journal of Physics Part C Solid State Physics*, **1971**, 4(18), 3107.

159. Brincat, N.A., M. Molinari, S.C. Parker, G.C. Allen, and M.T. Storr, Computer Simulation of Defect Clusters in UO_2 and their Dependence on Composition. *Journal of Nuclear Materials*, **2015**, 456, 329-333.

160. Geng, H.Y., Y. Chen, Y. Kaneta, and M. Kinoshita, Ab initio investigation on oxygen defect clusters in UO(2+x). *Applied Physics Letters*, **2008**, 93(20) 201903-201905.

161. Bevan, D.J.M., O. Greis, and J. Strahle, A New Structural Principle in Anion-Excess Fluorite-Related Super-Lattices. *Acta Crystallographica Section A*, **1980**, 36(11), 889-890.

162. Bevan, D.J.M., I.E. Grey, and B.T.M. Willis, The Crystal-Structure of Beta-U4O9-γ. *Journal of Solid State Chemistry*, **1986**, 61(1), 1-7.

163. Geng, H.Y., Y. Chen, Y. Kaneta, and M. Kinoshita, Stability mechanism of cuboctahedral clusters in UO(2+x): First-principles calculations. *Physical Review B*, **2008**, 77(18), 180101-180104.

164. Wang, J., R.C. Ewing, and U. Becker, Average structure and local configuration of excess oxygen in UO2+x. *Scientific Reports*, **2014**, 1-4.

165. Andersson, D.A., F.J. Espinosa-Faller, B.P. Uberuaga, and S.D. Conradson, Stability and migration of large oxygen clusters in UO2+x: Density functional theory calculations. *Journal of Chemical Physics*, **2012**, 136(23), 234702-234711.

166. Cooper, R.I. and B.T.M. Willis, Refinement of the structure of beta-U4O9. *Acta Crystallographica Section A*, **2004**, 60, 322-325.

167. Desgranges, L., G. Badinozzi, D. Simeone, and H.E. Fischer, Refinement of the alpha-U(4)O(9) Crystalline Structure: New Insight into the U(4)O(9) -> U(3)O(8) Transformation. *Inorganic Chemistry*, **2011**, 50(13), 6146-6151.

168. Flotow, H.E., D.W. Osborne, and E.F. Westrum, Heat Capacity of Tetrauranium Enneaoxide (U4O9) from 1.6 Degrees to 24 Degrees K . Magnetic Ontribution to Entropy. *Journal of Chemical Physics*, **1968**, 49(5), 2438-2442.

169. Gotoo, K. and K. Naito, Study on U4O9- .I. An Anomaly of Heat Capacity Near Room Temperature. *Journal of Physics and Chemistry of Solids*, **1965**, 26(11), 1673-1677.

170. White, J.T. and A.T. Nelson, Thermal conductivity of UO2+x and U4O9-y. *Journal of Nuclear Materials*, **2013**, 443(1-3), 342-350.

171. Gotoo, K., S. Nomura, and K. Naito, Study on U4O9- .2. Magnetic Susceptibility of U4O9. *Journal of Physics and Chemistry of Solids*, **1965**, 26(11), 1679-1684.

172. He, H.M., D.A. Andersson, D.D. Allred, and K.D. Rector, Determination of the Insulation Gap of Uranium Oxides by Spectroscopic Ellipsometry and Density Functional Theory. *Journal of Physical Chemistry C*, **2013**, 117(32), 16540-16551.

173. Grau-Crespo, R., S. Hamad, C.R.A. Catlow, and N.H. de Leeuw, Symmetry-adapted configurational modelling of fractional site occupancy in solids. *Journal of Physics-Condensed Matter*, **2007**, 19(25), 256201-256216.

174. Siegel, S., H. Hoekstra, and E. Sherry, Crystal Structure of High-Pressure UO3. *Acta Crystallographica*, **1966**, 20, 292-295.

175. Tempest, P.A., P.M. Tucker, and J.W. Tyler, Oxidation of UO2 Fuel Pellets in Air at 503 and 543 K Studied Using X-ray Photoelectron-Spectroscopy and X-ray-Diffraction. *Journal of Nuclear Materials*, **1988**, 151(3), 251-268.

176. Nowicki, L., A. Turos, C. Choffel, F. Garrido, L. Thome, J. Gaca, M. Wojcik, and H. Matzke, Quasiepitaxial growth of a monoclinic phase on UO2 single crystals upon leaching in H2O. *Physical Review B*, **1997**, 56(2), 534-542.

177. Nowicki, L., F. Garrido, A. Turos, and L. Thome, Polytypic arrangements of cuboctahedral oxygen clusters in U3O7. *Journal of Physics and Chemistry of Solids*, **2000**, 61(11), 1789-1804.

178. Garrido, F., R.M. Ibberson, L. Nowicki, and B.T.M. Willis, Cuboctahedral oxygen clusters in U3O7. *Journal of Nuclear Materials*, **2003**, 322(1), 87-89.

179. Hoekstra, H.R., A. Santoro, and S. Siegel, The Low Temperature Oxidation UO2 U4O9. *Journal of Inorganic & Nuclear Chemistry*, **1961**, 18, 166-178.

180. Hoekstra, H., S. Siegel, and P. Charpin, Synthesis of UO2.37 at High Pressure. *Journal of Inorganic & Nuclear Chemistry*, **1968**, 30(2), 519-523.

181. Westrum, E.F. and F. Gronvold, Triuranium Heptaoxides - Heat Capacities and Thermodynamic Properties of Alpha- and Beta- U3O7 from 5 to 350 Degrees K. *Journal of Physics and Chemistry of Solids*, **1962**, 23(2), 39-53.

182. Kovba, L.M., N.I. Komarevtseva, and E.U. Kuz'mitcheva, On the Crystal Structures of U13 O34 and delta-U2 O5. *Radiokhimiya*, **1979**, 21, 754-757.

183. Pireaux, J.J., E. Thibaut, J. Riga, C. Tenretnoel, R. Caudano, and J.J. Verbist, Shake-Up Satellites in X-ray Photoelectron-Spectra of Uranium-Oxides and Fluorides - Band-Structure Scheme for Uranium-Dioxide, UO2. *Chemical Physics*, **1977**, 22(1), 113-120.

184. Teterin, Y.A. and A.Y. Teterin, The structure of the X-ray photoelectron spectra of light actinide compounds. *Uspekhi Khimii*, **2004**, 73(6), 588-631.

185. Forbes, T.Z., P.C. Burns, S. Skanthakumar, and L. Soderholm, Synthesis, structure, and magnetism of Np2O5. *Journal of the American Chemical Society*, **2007**, 129(10), 2760-2761.

186. Gruehn, R., Eine Weitere Neue Modifikation des Niobpentoxids. *Journal of the Less-Common Metals*, **1966**, 11(2), 119-126.

187. Zibrov, I.P., V.P. Filonenko, P.E. Werner, B.O. Marinder, and M. Sundberg, A new high-pressure modification of Nb2O5. *Journal of Solid State Chemistry*, **1998**, 141(1), 205-211.

188. Andersson, S., Crystal Structure of N-Nb2O5 Prepared in Presence of Small Amounts of LiF. *Zeitschrift Fur Anorganische Und Allgemeine Chemie*, **1967**, 351(1-2), 106-112.

189. Zibrov, I.P., V.P. Filonenko, M. Sundberg, and P.E. Werner, Structures and phase transitions of B-Ta2O5 and Z-Ta2O5: two high-pressure forms of Ta2O5. *Acta Crystallographica Section B-Structural Science*, **2000**, 56, 659-665.

190. Cocciantelli, J.M., P. Gravereau, J.P. Doumerc, M. Pouchard, and P. Hagenmuller, On the Preparation and Characterization of a New Polymorph of V2O5. *Journal of Solid State Chemistry*, **1991**, 93(2), 497-502.

191. Filonenko, V.P., M. Sundberg, P.E. Werner, and I.P. Zibrov, Structure of a high-pressure phase of vanadium pentoxide beta-V2O5. *Acta Crystallographica Section B-Structural Science*, **2004**, 60, 375-381.

192. Materials Studio. Ver. 5.5.0.0, **2010**, San Diego, Accelrys Software Inc.

193. Soderlind, P. and J.E. Klepeis, First-principles elastic properties of alpha-Pu. *Physical Review B*, **2009**, 79(10) 104110-104116.

194. Mouhat, F. and F.-X. Couder, *Necessary and Sufficient Elastic Stability Conditions in Various Crystal Systems*. **2014**, Chimie ParisTech.

195. Rousseau, G., L. Desgranges, F. Charlot, N. Millot, J.C. Niepce, M. Pijolat, F. Valdivieso, G. Baldinozzi, and J.F. Berar, A detailed study of UO2 to U3O8 oxidation phases and the associated rate-limiting steps. *Journal of Nuclear Materials*, **2006**, 355(1-3), 10-20.

196. Loopstra, B.O., J.C. Taylor, and A.B. Waugh, Neutron Powder Profile Studies of Gamma-Uranium Trioxide Phases. *Journal of Solid State Chemistry*, **1977**, 20(1), 9-19.

197. Wen, X.D., R.L. Martin, G.E. Scuseria, S.P. Rudin, E.R. Batista, and A.K. Burrell, Screened hybrid and DFT plus U studies of the structural, electronic, and optical properties of U3O8. *Journal of Physics-Condensed Matter*, **2013**, 25(2), 025501-025510.

198. Andresen, A.F., The Structure of U3O8 Determined by Neutron Diffraction. *Acta Crystallographica*, **1958**, 11(9), 612-614.

199. Loopstra, B.O., Structure of Beta-U3O8. *Acta Crystallographica Section B-Structural Crystallography and Crystal Chemistry*, **1970**, B 26, 656-657.

200. Loopstra, B.O., Neutron Diffraction Investigation of U3O8. *Acta Crystallographica*, **1964**, 17(6), 651-654.

201. Loopstra, B.O., Phase Transition in Alpha-U3O8 at 210 Degrees C. *Journal of Applied Crystallography*, **1970**, 94-96.

202. Loopstra, B.O., Crystal-Structure of Alpha-U3O8. *Journal of Inorganic & Nuclear Chemistry*, **1977**, 39(9), 1713-1714.

203. Hoekstra, H.R., S. Siegel, L.H. Fuchs, and J.J. Katz, The Uranium-Oxygen System - UO2.5 to U3O8. *Journal of Physical Chemistry*, **1955**, 59(2), 136-138.

204. Hoekstra, H.R. and S. Siegel, The Uranium-Oxygen System - U3O8-UO3. *Journal of Inorganic & Nuclear Chemistry*, **1961**, 18, 154-165.

205. Cordfunke, E.H. and P. Aling, System UO3+U3O8 - Dissociation Pressure of Gamma-UO3. *Transactions of the Faraday Society*, **1965**, 61(505P), 50-53.

206. Pillai, C.G.S., A.K. Dua, and P. Raj, Thermal conductivity of U3O8 from 300 to 1100 K. *Journal of Nuclear Materials*, **2001**, 288(2-3), 87-91.

207. Caneiro, A. and J.P. Abriata, Equilibrium Oxygen Partial-Pressure and Phase-Diagram of the Uranium Oxygen System in the Composition Range $2.61<x<2.67$ Between 844-K and 1371-K. *Journal of Nuclear Materials*, **1984**, 126(3), 255-267.

208. Allen, G.C., A.J. Griffiths, and C.W. Suckling, Electron-Spin Resonance-Spectra of Mixed Oxides Containing Uranium and Alkaline-Earth Metals. *Chemical Physics Letters*, **1978**, 53(2), 309-312.

209. Allen, G.C., J.A. Crofts, M.T. Curtis, P.M. Tucker, D. Chadwick, and P.J. Hampson, X-ray Photoelectron-Spectroscopy of some Uranium Oxide Phases. *Journal of the Chemical Society-Dalton Transactions*, **1974**, (12), 1296-1301.

210. Allen, G.C., P.A. Tempest, and J.W. Tyler, Oxidation of Crystalline UO2 Studied Using X-ray Photoelectron-Spectroscopy and X-ray-Diffraction. *Journal of the Chemical Society-Faraday Transactions I*, **1987**, 83, 925-935.

211. Vitova, T., K.O. Kvashnina, G. Nocton, G. Sukharina, M.A. Denecke, S.M. Butorin, M. Mazzanti, R. Caciuffo, A. Soldatov, T. Behrends, and H. Geckeis, High energy resolution x-ray absorption spectroscopy study of uranium in varying valence states. *Physical Review B*, **2010**, 82(23), 235118-235123.

212. Teterin, A.Y., M.V. Ryzhkov, Y.A. Teterin, K.I. Maslakov, T. Reich, and S.L. Molodtsov, Resonant Emission of UO2, U3O8, and UO2+x Valence Electrons Under SR Excitation Near the O-4,O-5(U) Absorption Edge. *Journal of Structural Chemistry*, **2011**, 52(2), 295-303.

213. Ball, R.G.J. and P.G. Dickens, Calculation of Structural and Defect Properties of Alpha-U3O8. *Journal of Materials Chemistry*, **1991**, 1(1), 105-112.

214. Ball, R.G.J. and P.G. Dickens, Computer-Simulation Study of Alkali-Metal Insertion into Alpha-U3O8. *Journal of Materials Chemistry*, **1991**, 1(3), 415-421.

215. Geng, H.Y., H.X. Song, K. Jin, S.K. Xiang, and Q. Wu, First-principles study on oxidation effects in uranium oxides and high-pressure high-temperature behavior of point defects in uranium dioxide. *Physical Review B*, **2011**, 84(17), 174115-174126.

216. Yun, Y., J. Rusz, M.T. Suzuki, and P.M. Oppeneer, First-principles investigation of higher oxides of uranium and neptunium: U(3)O(8) and Np(2)O(5). *Physical Review B*, **2011**, 83(7), 075109-075118.

217. Allen, G.C. and N.R. Holmes, Mixed-Valency Behavior in some Uranium-Oxides Studies by X-ray Photoelectron-Spectroscopy. *Canadian Journal of Applied Spectroscopy*, **1993**, 38(5), 124-130.

218. Greaves, C. and B.E.F. Fender, Structure of Alpha-UO3 by Neutron and Electron-Diffraction. *Acta Crystallographica Section B-Structural Science*, **1972**, 28(DEC15), 3609-3614.

219. Loopstra, B.O. and Cordfunke E.H.P., On Structure of Alpha-UO3. *Recueil Des Travaux Chimiques Des Pays-Bas*, **1966**, 85(2), 135-142.

220. Petot-Ervas, G., G. Baldinozzi, P. Ruello, L. Desgranges, G. Chirlesan, and C. Petot, *Influence of defect interactions on diffusion processes in UO2+x: a key issue for understanding the behaviour of spent nuclear fuel*. 28th Symposium on the Scientific Basis for Nuclear Waste Management, **2004,** San Francisco, CA. Materials Research Society, 203-209.

221. Chodura, B. and J. Maly, A Contribution to the Solution of the Structure of U3O8. *Journal of Inorganic & Nuclear Chemistry*, **1958**, 7(1-2), 177-178.

222. Colmenares, C.A., The oxidation of thorium, uranium and plutonium. *Progress in Solid State Chemistry*, **1975**, 9, 139-239.

223. Bagus, P.S. and E.S. Ilton, Theory for the XPS of Actinides. *Topics in Catalysis*, **2013**, 56(12), 1121-1128.

224. Bagus, P.S., C.J. Nelin, and E.S. Ilton, Theoretical modeling of the uranium 4f XPS for U(VI) and U(IV) oxides. *Journal of Chemical Physics*, **2013**, 139(24) 244704-244717.

225. Sweet, L.E., T.A. Blake, C.H. Henager, S.Y. Hu, T.J. Johnson, D.E. Meier, S.M. Peper, and J.M. Schwantes, Investigation of the polymorphs and hydrolysis of uranium trioxide. *Journal of Radioanalytical and Nuclear Chemistry*, **2013**, 296(1), 105-110.

226. Girgis, B.S. and N.H. Rofail, Reactivity of Various UO3 Modifications in the Fluorination to UF4 by FREON-12. *Journal of Nuclear Materials*, **1992**, 195(1-2), 126-133.

227. Pickard, C.J., B. Winkler, R.K. Chen, M.C. Payne, M.H. Lee, J.S. Lin, J.A. White, V. Milman, and D. Vanderbilt, Structural properties of lanthanide and actinide compounds within the plane wave pseudopotential approach. *Physical Review Letters*, **2000**, 85(24), 5122-5125.

228. Cornman, W.R., *Preparation and Characterization of the Polymorphs of UO3*. **1962**, Savannah River Laboratory, Aiken, South Carolina (TID-4500).

229. Wheeler, V.J., R.M. Dell, and E. Wait, Uranium Trioxide and the UO3 Hydrates. *Journal of Inorganic & Nuclear Chemistry*, **1964**, 26(11), 1829-1845.

230. Cordfunke, E.H.P. and P.C. Debets, Preparation and Properties of a New Monohydrate of Uranium Trioxide Epsilon-UO3.H2O. *Journal of Inorganic & Nuclear Chemistry*, **1964**, 26(10), 1671-1677.

231. Weller, M.T., P.G. Dickens, and D.J. Penny, The Structure of Delta-UO3. *Polyhedron*, **1988**, 7(3), 243-244.

232. Kovba, L.M., L.M. Vidavskii, and E.G. Lavut, Study of ε-UO3. *Zhumal Strukturnoi Khimii*, **1963**, 4(4), 627-629.

233. Johnson, J.A., **2013**. Studies of Reaction Processes for Voloxidation Methods. *Trace: Tennessee Research and Creative Exchange*, University of Tennessee, 133.

234. Zachariasen, W.H., Crystal Chemical Studies of the 5F-Series of Elements .1. New Structure Types. *Acta Crystallographica*, **1948**, 1(1-6), 265-269.

235. Debets, P.C., Structure of Beta-UO3. *Acta Crystallographica*, **1966**, 21, 589-593.

236. Kim, B.H., Y.B. Lee, M.A. Prelas, and T.K. Ghosh, Thermal and X-ray diffraction analysis studies during the decomposition of ammonium uranyl nitrate. *Journal of Radioanalytical and Nuclear Chemistry*, **2012**, 292(3), 1075-1083.

237. Debets, P.C., Interpretation of the X-ray Powder Pattern of Beta-UO3. *Journal of Inorganic & Nuclear Chemistry*, **1964**, 26(8), 1468-1470.

238. Cordfunke, E.H.P. and E.F. Westrum, The Thermodynamic Properties of Beta-UO3 and Gamma-UO3. *Thermochimica Acta*, **1988**, 124, 285-296.

239. Engmann, R. and P.M.D. Wolff, Crystal Structure of Gamma-U3. *Acta Crystallographica*, **1963**, 16(10), 993-996.

240. Idriss, H., Surface reactions of uranium oxide powder, thin films and single crystals. *Surface Science Reports*, **2010**, 65(3), 67-109.

241. Allen, J.P. and G.W. Watson, Occupation matrix control of d- and f-electron localisations using DFT plus U. *Physical Chemistry Chemical Physics*, **2014**, 16(39), 21016-21031.

Appendices

Appendix A – Example VASP Input Files

Set of example input files for VASP (with annotations), a twelve atom CL AFM UO_2 structure has been used.

INCAR

```
SYSTEM = urania_bulk

Startparameters
# NWRITE =      2          Determines verbosity when writing to output file (OUTCAR)
   ISTART =      1          Determines if wavefuntion is written to WAVECAR
   ICHARG =      1          Determines how initial charge density is constructed
   NPAR =        4          Parallelisation of atoms over CPU cores
   KPAR =        4          Parallelisation of k-points over CPU cores

 Electronic Relaxation
#  PREC    = Normal         Determines precision (overridden by individual settings here
#  ALGO    = Normal         Determines electronic minimisation algorithm
   ENMAX   = 500.00 eV      Maximum plane wave cut-off energy
   NELM    = 999            Maximum number of electronic steps per ionic iteration
   NELMIN  = 8              Minimum number of electronic steps per ionic iteration
   EDIFF   = 1E-06          Minimum energy change to break electronic relaxation loop
   GGA     = PE             Determines GGA functional used (PBE)
   ISPIN   = 2              Spin polarised calculation

 Ionic Relaxation
   EDIFFG =  -0.01          Minimum energy change to break ionic relaxation loop
   NSW    =     36          Maximum number of ionic steps per calculation
   NBLOCK =      1          Determines how often pair correlation function and DOS are calculated
   KBLOCK =     50          Determines how often pair correlation function and DOS are calculated
   IBRION =      2          Determines ionic relaxation algorithm (conjugate gradients)
   ISIF   =      3          Controls degrees of freedom allowed to relax (all) and stress tensor
   IWAVPR =      1          Determines how charge density is extrapolated between ionic steps
   ISYM   =      1          Controls whether symmetry is used

 DOS related values
   ISMEAR =     0           Determines how partial occupancies are set for each orbital
   SIGMA  =     0.10        Determines smearing width

 Miscellaneous:
   LORBIT =     11          Controls writing of output (PROCAR) with site projected
wavefunctions
   LASPH  = .TRUE.          Includes non-spherical contributions from gradient corrections

 DFT+U Calculations:
   LDAU   = .TRUE.          Turns on DFT + U
   LDAUTYPE = 2             Determines DFT + U type (Dudarev)
   LDAUL  = 3 -1            L quantum numbers for each species using DFT + U (f, not used)
   LDAUU  = 4.50 0.00       U portion of Hubbard coefficient for each species
   LDAUJ  = 0.54 0.00       J portion of Hubbard coefficient for each species
   LDAUPRINT = 2            Verbosity of output (in OUTCAR) – writes occupancy matrix
   LMAXMIX = 6              Mixing parameter (set for f electrons) to give faster convergence
```

```
 Magnetic Calculations:
   MAGMOM = 2 -2 2 -2 8*0
```
Magnetic moments for each species

KPOINTS

```
Automatic mesh
0
g
  4   4   4
  0.  0.  0.
```
Automatically generated *k* point mesh
Generate gamma centred grid
Subdivisions along reciprocal lattice vectors
Shift of mesh

POSCAR

```
U   O
   1.0
```
Atomic species
Scaling factor

```
5.4682000000000000  0.0000000000000000  0.0000000000000000
0.0000000000000000  5.4682000000000000  0.0000000000000000
0.0000000000000000  0.0000000000000000  5.4682000000000000
```
Matrix of lattice vectors

```
U    O
4    8
Direct
0.0000000000000000  0.0000000000000000  0.0000000000000000
0.0000000000000000  0.5000000000000000  0.5000000000000000
0.5000000000000000  0.0000000000000000  0.5000000000000000
0.5000000000000000  0.5000000000000000  0.0000000000000000
0.2500000000000000  0.2500000000000000  0.2500000000000000
0.7500000000000000  0.7500000000000000  0.2500000000000000
0.7500000000000000  0.2500000000000000  0.7500000000000000
0.2500000000000000  0.2500000000000000  0.7500000000000000
0.7500000000000000  0.7500000000000000  0.7500000000000000
0.2500000000000000  0.7500000000000000  0.7500000000000000
0.7500000000000000  0.2500000000000000  0.2500000000000000
0.2500000000000000  0.7500000000000000  0.2500000000000000
```
Atomic species
Numbers of each species
Atomic coordinates

Appendix B – Full U_4O_9 and U_3O_7 Results

Results tables for full set of U_4O_9 and U_3O_7 calculations.

Table A – Predicted properties of U_4O_9 phases in a 2 x 2 x 1 UO_2 supercell. Predicted formation energy is per O_i and volume change is from relaxed pure UO_2.

Configuration	$E_{formation}$ (eV)	Δ Volume (%)	Band Gap (eV)	U^{6+}
4 x O_i	0.487	-1.14	0.71	×
4 x O_i	0.438	-0.81	0.97	✓
4 x O_i	0.425	-0.83	0.97	✓
4 x O_i	0.370	-0.62	1.10	×
4 x O_i	0.319	-0.87	1.29	×
4 x O_i	0.309	-0.93	1.35	×
4 x O_i	0.273	-0.63	1.17	✓
4 x O_i	0.264	-1.33	1.16	×
4 x O_i	0.222	-0.54	1.03	×
Distorted clusters and O_i	0.181	0.93	1.37	✓
Distorted clusters and O_i	0.173	-0.47	1.10	×
Distorted clusters and O_i	0.171	-0.92	1.23	×
Distorted clusters and O_i	0.153	-0.39	1.16	×
Distorted clusters and O_i	0.110	-0.33	1.29	✓
Distorted clusters and O_i	0.090	-0.24	1.03	×
Distorted clusters and O_i	0.072	-0.39	1.16	×
Split-int clusters/distorted Willis chains	-0.016	0.33	1.03	×
Split-int clusters/distorted Willis chains	-0.018	-0.51	1.23	×
Split-int clusters/distorted Willis chains	-0.018	-0.43	1.16	×
Split-int clusters/distorted Willis chains	-0.020	-0.46	1.16	×
Split-int clusters/distorted Willis chains	-0.034	-0.08	1.41	×
Split-int clusters/distorted Willis chains	-0.048	-0.82	1.29	×
Split-int clusters/distorted Willis chains	-0.049	-0.36	1.29	×
Split-int clusters/distorted Willis chains	-0.068	-0.24	1.16	×
Split-int clusters/distorted Willis chains	-0.076	0.05	1.16	×
Split-int clusters/distorted Willis chains	-0.087	-0.44	1.10	×
Split-int clusters/distorted Willis chains	-0.117	-0.27	1.29	×
Split-int clusters/distorted Willis chains	-0.120	-0.45	1.22	×
Split-int clusters/distorted Willis chains	-0.138	-0.08	1.16	×
Split-int clusters/distorted Willis chains	-0.140	-0.37	1.35	×
Split-int clusters/distorted Willis chains	-0.166	-0.43	1.29	×
Split-int clusters/distorted Willis chains	-0.201	-0.41	1.16	×
Willis cluster chains	-0.202	-0.38	1.09	×
Willis cluster chains	-0.213	0.02	1.16	×
Willis cluster chains	-0.273	-0.14	1.10	×
Willis cluster chains	-0.333	-0.28	1.48	×
Willis cluster chains	-0.390	0.15	1.35	×
Willis cluster chains	-0.417	-0.56	1.42	×
Willis cluster chains	-0.430	0.22	1.36	×
Willis cluster chains	-0.484	0.27	1.48	×
Willis cluster chains	-0.516	0.37	1.48	×
Willis cluster chains	-0.520	0.68	1.30	×
Willis cluster chains	-0.526	0.16	1.48	×
Willis cluster chains	-0.638	0.79	1.61	×

Table B – Predicted properties of U_3O_7 phases in an orthorhombic UO_2 supercell. Predicted formation energy is per O_i and volume change is from relaxed pure UO_2.

Configuration	$E_{formation}$ (eV)	Δ Volume (%)	Band Gap (eV)	U^{6+}
Split di and tri interstitials	1.049	3.11	1.50	5
Split di and tri interstitials	0.727	3.24	1.43	2
Split di and tri interstitials	0.639	2.52	1.56	×
Split di and tri interstitials	0.442	1.25	1.42	×
Split di and tri interstitials	0.439	2.93	1.18	×
Split di and tri interstitials	0.267	3.75	1.43	×
Split di and tri interstitials	0.182	-0.10	1.41	1
Split di and tri interstitials	-0.046	0.37	1.79	×
Split di and tri interstitials	-0.074	-1.24	1.42	×
Split di and tri interstitials	-0.087	-1.76	1.35	1
Split di and tri interstitials	-0.088	0.25	1.60	×
Split di and tri interstitials	-0.100	0.35	1.28	×
Split di and tri interstitials	-0.112	0.15	1.23	×
Split di and tri interstitials	-0.117	-1.47	1.74	3
Split di and tri interstitials	-0.133	0.35	1.41	×
Split di and tri interstitials	-0.139	-1.64	1.03	×
Split di and tri interstitials	-0.155	-0.88	1.22	×
Split di and tri interstitials	-0.201	-1.75	1.41	×
Split di and tri interstitials	-0.225	-1.28	1.35	×
Distorted split quad interstitials	-0.234	-1.41	1.22	×
Distorted split quad interstitials	-0.236	-0.92	1.48	×
Distorted split quad interstitials	-0.246	-1.12	1.41	×
Distorted split quad interstitials	-0.256	-0.49	1.48	×
Distorted split quad interstitials	-0.256	-1.47	1.22	×
Distorted split quad interstitials	-0.256	-1.38	0.90	1
Distorted split quad interstitials	-0.273	-1.28	1.48	×
Distorted split quad interstitials	-0.275	-0.51	1.16	1
Distorted split quad interstitials	-0.284	-0.30	1.67	×
Split quad interstitials	-0.300	-1.55	1.22	×
Split quad interstitials	-0.303	-1.10	1.85	×
Split quad interstitials	-0.313	-1.38	1.16	×
Split quad interstitials	-0.314	-1.10	1.09	1
Split quad interstitials	-0.333	-1.10	1.03	1
Split quad interstitials	-0.337	-1.05	1.22	×
Split quad interstitials	-0.340	-1.56	1.22	×
Split quad interstitials	-0.341	-1.55	1.09	×
Split quad interstitials	-0.349	-1.57	1.22	×
Split quad interstitials	-0.355	-1.25	1.41	×
Split quad interstitials	-0.366	-1.62	1.22	×
Split quad interstitials	-0.368	-0.31	1.54	×
Split quad interstitials	-0.375	-1.33	1.35	×
Split quad interstitials	-0.383	-1.58	1.09	1
Split quad interstitials	-0.396	-1.36	1.35	1
Split quad interstitials	-0.400	-1.48	1.22	×
Split quad interstitials	-0.404	-1.49	1.35	×
Split quad interstitials	-0.405	-1.71	1.80	×
Split quad interstitials	-0.407	-1.68	1.48	×
Split quad interstitials	-0.414	-1.28	1.35	×
Split quad interstitials	-0.416	-1.54	1.48	1
Split quad interstitials	-0.421	-1.49	1.35	×

Configuration	$E_{formation}$ (eV)	Δ Volume (%)	Band Gap (eV)	U^{6+}
Split quad interstitials	-0.424	-1.64	1.22	×
Split quad interstitials	-0.428	-1.50	1.16	×
Split quad interstitials	-0.434	-1.64	1.41	1
Split quad interstitials	-0.435	-1.50	1.35	×
Split quad interstitials	-0.436	-1.48	1.29	×
Split quad interstitials	-0.437	-1.53	1.41	×
Split quad interstitials	-0.443	-1.28	1.09	×
Split quad interstitials	-0.450	-1.55	1.22	×
Split quad interstitials	-0.454	-1.36	1.16	1
Split quad interstitials	-0.464	-1.55	1.35	×
Split quad interstitials	-0.469	-1.64	1.54	×
Split quad interstitials	-0.482	-1.34	1.42	×
Split quad interstitials	-0.482	-1.61	1.80	×
Split quad interstitials	-0.488	-1.52	1.48	×
Split quad interstitials	-0.492	-1.62	1.41	×
Split quad interstitials	-0.493	-1.44	1.35	×
Split quad interstitials	-0.501	-1.23	1.41	×
Split quad interstitials	-0.508	-1.27	1.41	×
Split quad interstitials	-0.511	-1.60	1.54	×
Split quad interstitials	-0.522	-1.30	1.86	×
Split quad interstitials	-0.605	-1.21	1.67	×

Appendix C – AFM U_2O_5 and U_3O_8 Results

Results tables including AFM U_2O_5 and U_3O_8 polymorphs.

Table C – Predicted properties of U_2O_5 polymorphs. Space groups are calculated to a tolerance of 0.001 Å for both the initial (experimental) and final (relaxed) structures using Materials Studio [192]. Reported energies are formation energy per uranium ion relative to UO_2. Δ% is the percentage difference between a calculated structure and experiment.

Study	Phase	Magnetism	Method	Lattice Parameters (Å)			Lattice Parameters (°)			Vol/U (Å^3)	Space Group	ΔH_f^0 (eV)
				a (Δ%)	b (Δ%)	c (Δ%)	α	β	γ			
Kovba [182]	**δ-U_2O_5**	-	Exp	6.85	8.27	31.71	90.0	90.0	90.0	56.15	*Pnma*	-
This Work		FM	PBE + U	7.02 (2.5)	8.42 (1.8)	31.46 (-0.8)	90.0	90.0	90.0	58.15	*Pnma*	-0.86
		AFM <010>	PBE + U	7.02 (2.5)	8.42 (1.8)	31.46 (-0.8)	90.0	90.0	90.0	58.15	*Pnma*	-0.85
		AFM <100>	PBE + U	7.02 (2.5)	8.42 (1.8)	31.46 (-0.8)	90.0	90.0	90.0	58.15	*Pnma*	-0.85
Forbes [185]	**Np_2O_5**	FM	Exp‡	8.17	6.58	9.31	90.0	116.1	90.0	56.23	*P2/c*	-
This Work		FM	PBE + U	8.16	6.82	9.41	90.0	116.0	90.0	58.80	*P1*	-0.95
		AFM <001>	PBE + U	8.16	6.82	9.41	90.0	116.0	90.0	58.80	*P1*	-0.95
		AFM <010>	PBE + U	8.16	6.82	9.41	90.0	116.0	90.0	58.80	*P1*	-0.95
		AFM <100>	PBE + U	8.16	6.82	9.41	90.0	116.0	90.0	58.80	*P1*	-0.95

Table D - Predicted properties of U_3O_8 polymorphs. Space groups are calculated to a tolerance of 0.001 Å for both the initial (experimental) and final (relaxed) structures using Materials Studio [192]. Reported energies are formation energy per uranium ion relative to UO_2. Δ% is the percentage difference between a calculated structure and experiment. Only the more energetically stable U^{5+}/U^{6+} charge configuration is considered here.

Study	**Phase**	**Method**	**Magnetic Order**	**Lattice Parameters (Å)**				**Vol/U (Å^3)**	**β (°)**	**Space Group**	**ΔH_f^0 (eV)**
				c/a	***a* (Δ%)**	***b* (Δ%)**	***c* (Δ%)**				
Loopstra [200]	***Amm2* α-U_3O_8**	Exp	-	-	4.15	11.97	6.72	55.58	90.0	*Amm2*	-
This Work		PBE + U	FM	-	4.21 (1.4)	11.60 (-3.1)	7.22 (7.5)	58.72	90.0	*Amm2*	-1.09
			AFM <010>	-	4.21 (1.4)	11.60 (-3.1)	7.22 (7.5)	58.72	90.0	*Amm2*	-1.08
			AFM <001>	-	4.21 (1.4)	11.60 (-3.1)	7.22 (7.5)	58.70	90.0	*Amm2*	-1.08
Loopstra [199]	***Cmcm* β-U_3O_8**	Exp	-	-	7.07	11.45	8.30	55.98	90.0	*Cmcm*	-
This Work		PBE + U	FM	-	7.21 (2.0)	11.64 (1.7)	8.44 (1.7)	59.06	90.0	*Cmcm*	-1.12
			AFM <100>	-	7.21 (2.0)	11.64 (1.7)	8.45 (1.7)	59.06	90.0	*Cmcm*	-1.12
			AFM <001>	-	7.21 (2.0)	11.64 (1.7)	8.45 (1.7)	59.07	90.0	*Cmcm*	-1.12
Desgranges [31]	***P-62m* γ-U_3O_8**	Exp	-	0.61	6.82	6.82	4.15	55.76	120.0	*P-62m*	-
This Work		PBE + U	FM	0.62	6.83 (0.1)	6.83 (0.1)	4.20 (1.2)	56.60	116.3	*Amm2*	-1.08
			AFM	0.62	6.83 (0.1)	6.83 (0.1)	4.20 (1.2)	56.59	116.3	*Amm2*	-1.08